AN EXPERIMENTAL INVESTIGATION OF HEAT

AND MOMENTUM TRANSFER IN SMOOTH AND ROUGH

TUBES AT VARIOUS PRANDTL NUMBERS

Thesis by

Duane F. Dipprey

In Partial Fulfillment of the Requirements

For the Degree of

Doctor of Philosophy

California Institute of Technology

Pasadena, California

1961

ACKNOWLEDGEMENTS

ABSTRACT

Results are presented from an experimental investigation of the relation between heat transfer and friction in smooth and rough tubes. Three rough tubes and one smooth tube were formed from electroplated nickel. The rough tubes contained a close-packed, granular type of surface with roughness-height-to-diameter ratios ranging from 0.0024 to 0.049. Measurements of the heat transfer coefficients (C_H) and the friction coefficients (C_F) were obtained with distilled water flowing through the electrically heated tubes. A Prandtl number range of 1.20 to 5.94 was investigated by adjusting the bulk temperature of the water. Results were obtained for Reynolds numbers from 6×10^4 to 5×10^5 and from 1.4×10^4 to 1.2×10^5 at the lowest and highest Prandtl number respectively.

A similarity rule for heat transfer was used to correlate, interpret and extend the experimental results. The results were compared with previously existing results, both theoretical and experimental. Increases in C_H due to roughness of as high as 270 percent were obtained. These increases were, in general, accompanied by even larger increases in C_F. An exception to this general behavior occurs at high Prandtl number in the region of transition between the "smooth" and the "fully rough" C_F characteristic.

TABLE OF CONTENTS

TABLE OF CONTENTS (Cont'd)

LIST OF TABLES

LIST OF FIGURES

LIST OF APPENDICES

I INTRODUCTION

The use of roughened bounding surfaces as a possible means of reducing the thermal resistance of a turbulent flow has been receiving increasing interest. As early as 1917, water flow experiments discussed by Stanton (Ref. 1, p. 176) showed significant improvements in heat transfer coefficients due to the use of roughened surfaces. In recent years, the heat exchanger size, shape, weight, pumping power and temperature restraints associated with the problems of rocket engine and nuclear reactor cooling have sharpened interest in the use of rough surfaces; the experimental and analytical investigations by Fortescue and Hall (Ref. 2), Grass (Ref. 3), Sheriff (Ref. 4) and Nunner (Ref. 5) have demonstrated that considerable reductions in coolant pumping power or in heat exchanger size are attainable. Surface roughening must of course compete with other means of achieving the same results such as swirl induction, Cf. Gambill, Bundy and Wansbrough (Ref. 6), or other types of secondary flow induction, Cf. Koch (Ref. 7).

In addition to ascertaining the advantages to be gained by the use of artificially roughened surfaces, it is important to understand the heat transfer behavior of surfaces where roughness occurs naturally. Natural roughness may occur either from the original manufacture of a surface or from subsequent chemical attack.

The large number of experimental conditions affecting heat transfer from rough surfaces and the general difficulty involved in attaining accuracy in heat transfer measurements have led to diverse

conclusions in the relatively few previously existing studies on the use of rough surfaces in heat exchanger design. The experiment referred to by Stanton (Ref. 1, p. 176) suggested that increases in heat transfer coefficient (C_H) can exceed the increases in friction coefficient (C_F) caused by surface roughening; whereas Cope (Ref. 8) indicated that for certain regions of operation the heat transfer coefficient may even decrease while the friction coefficient increases. Smith and Epstein (Ref. 9), in studying certain naturally rough pipes, were led to conclude that the small improvements in heat transfer observed in rough pipes could be easily offset by any amount of surface fouling that may accompany natural roughness. Nunner (Ref. 5) found substantial improvements in heat transfer characteristics of rough pipes at Prandtl number near 0.7 but conjectured that these would diminish for higher Prandtl numbers. This latter suggestion is contradicted by the results of the present experiments.

One of the principal intentions of the present investigation is to obtain a set of data experimentally relating the various pertinent dimensionless parameters with sufficient accuracy to permit its use in establishing and testing theoretical deductions concerning the mechanisms of heat and momentum transfer from rough surfaces. By limiting the experimental conditions to hydrodynamically and thermally fully established pipe flow with negligible radial fluid property variations and with roughness elements of a fixed type, the complete heat and momentum transfer problem is restricted to finding the relationships among the dimensionless groups, C_H, C_F, Re, Pr and ϵ/D. The heat transfer coefficient (C_H) and the friction

coefficient (C_F) may be thought of as dependent variables with Reynolds number (Re), Prandtl number (Pr), and pipe roughness-ratio (ϵ/D) as the independent variables. In none of the previously existing experiments with which the writer is familiar have Re, Pr and ϵ/D all been varied systematically to permit a complete test of theoretical predictions. Perhaps the most complete previous rough tube experiments, in which these same idealized conditions were approached, were performed by Nunner (Ref. 5). However these experiments, being conducted with air through-flow, were restricted to one Prandtl number.

The type of roughness used for the current experiments is a three-dimensional, close-packed, granular form not greatly dissimilar from the close-packed sand-grain surface used by Nikuradse (Ref. 10) for rough pipe friction measurements. The rough tubes for the present experiments were produced by electroplating nickel over mandrels coated with closely graded sand grains. The mandrel was subsequently dissolved out leaving a cast of the sand inside of the remaining nickel tube. The intention was to produce a series of tubes each having a particular scale of roughness and all having a roughness shape which remains geometrically similar as the scale is varied from tube to tube. The sand-grain type of roughness was desired in order to make direct use of the extensive correlations between velocity profiles and friction coefficients established by Nikuradse for this type of pipe surface. Further, the Reynolds number region of smooth-to-fully-rough C_F transition observed by Nikuradse for this type of roughness was expected to be, and later proved to be, of special interest for heat transfer. The use of nearly geometrically

similar roughness shapes permits characterization of the roughness by a single geometrical parameter, ϵ/D. Since the accurate measurement of the roughness height attained in the experimental tubes could not be made, the equivalent sand grain size (ϵ_s) as determined from the friction similarity law (Cf. Section II) was used to characterize the roughness. The three rough tubes tested herein exhibited equivalent roughness ratios (ϵ_s/D) equal to 0.0024, 0.0138 and 0.0488 respectively.

The present heat transfer experiments were conducted with water flowing upward through a nominally 0.4-inch-diameter tube which was heated by the passage of alternating-current electricity through the tube walls. Friction coefficients were determined from fluid flow rate and pressure drop measurements, and the heat transfer coefficients were determined from measurements of heating power, outside tube-wall temperature and fluid temperature. Fully established conditions were approximated by providing approximately 45 diameters of hydro-dynamic entrance length followed by 38 diameters of thermal entrance length ahead of the heat transfer coefficient measurement station. The effects of radial temperature gradients accompanying finite heat flux rates were eliminated by extrapolating the C_H results from tests with various wall-to-fluid temperature differences to the zero temperature difference condition. Prandtl number variations from 1.20 to 5.94 were achieved by setting the water bulk temperature at values from 80 to 290°F. Reynolds number was independently varied in the range from 1.4×10^4 to 5.2×10^5 by adjustment of water flow rate.

Allen (Ref. 11) has shown that some disagreement persists among recent experimental results on smooth tube heat transfer coefficients. Since a direct comparison between the rough tube and smooth tube heat

and momentum transfer characteristics is desired, a series of tests on a smooth tube, using the same tube construction and experimental methods used for the rough tubes, is included in the present experiments.

Although the present results are restricted to one type of roughness and to other simplifying conditions, it is expected that in many cases of practical interest the conditions of these experiments will be met closely enough to permit direct use of the data for heat exchanger design. With the possible exception of transverse fins with nearly square cavities, the particular type of roughness studied in the present work is shown to perform as well as or better than surfaces studied in the other experiments compared herein; hence the present results may be used as indicative of heat exchanger improvements available from the use of roughened surfaces. Further, it is expected that the results here obtained for fully established pipe flow can be directly employed in determining heat transfer coefficients for zero-pressure-gradient, turbulent boundary layers over similar rough surfaces; the same methods used to relate smooth tube and smooth plate heat transfer (Cf. Ref. 12, p. 215) should be valid for the rough surfaces. Hama (Ref. 13) has discussed the close relationship between pipe flow and boundary layer flow in connection with velocity profiles and shear stress distributions, and he has proposed that friction measurements for boundary layer flow over rough surfaces should be carried out in pipes to take advantage of the better accuracy attainable. The same arguments are assumed to apply to heat transfer measurements.

II FUNDAMENTALS

The discussion in this section is limited to the following conditions as approximated in the present experiments:

i) Fully turbulent (Re greater than about 2000), steady, pipe flow.

ii) Hydrodynamically fully established flow in which the mean fluid motions are invariant with axial station.

iii) Thermally fully established conditions whereby the radial temperature profile referenced to the local wall temperature is independent of axial location.

iv) Constant fluid properties, density (ρ), viscosity (μ), thermal conductivity (k), specific heat (c_p).

v) Surface roughness patterns which are statistically independent of circumferential or axial position provided that statistical samples are measured at points separated by distances much greater than the scale of the roughness elements.

vi) Roughness patterns which are statistically geometrically similar from tube to tube with only a geometrical scale factor being different.

The purpose here is to extend theoretical notions existing for heat and momentum transfer in smooth tubes and for momentum transfer in rough tubes to the problem of heat transfer in rough tubes. The theories for heat transfer in turbulent shear flow which have found practical application result from the use of similarity principles and an analogy between the turbulent diffusivities of heat and momentum. These theories--which must necessarily be based on empirical information--are useful principally because from them the essential

relationships between the various parameters may be derived. With the aid of these relationships, the experimental results may then be presented in their most general form.

For the prescribed simplifying conditions, a time averaging (Cf., e.g., Ref. 14) of the momentum equation for pipe flow gives

$$(\tau_o/\rho)(1 - y/R) = -\overline{u'v'} + \nu(du/dy) \tag{1}$$

where y is the distance from the wall, R is the tube radius and ν is the kinematic viscosity of the fluid. This equation may be thought of as a relation between the turbulent shear stress, $\rho\,\overline{u'v'}$, and the mean velocity profile ($u\{y\}$) with the shear stress at the wall (τ_o) as a parameter. No independent information is available for making equation 1 determinate short of solving the complete time-dependent Navier-Stokes equations. However, a description of the form of the $u\{y\}$ dependence and hence the $\overline{u'v'}\{y\}$ dependence over part of the flow is possible by following the similarity arguments presented by Townsend (Ref. 15, Chap. 9) as they apply to rough pipes.

First, use is made of the so called principle of Reynolds number similarity which states that there exists, in a turbulent flow at high Reynolds number, a region in which the direct effect of viscosity on the mean flow is negligible. In terms of equation 1, this implies

$$- \overline{u'v'}/(du/dy) >> \nu \tag{2}$$

In such a region the mean velocity and the principal turbulent components such as those involved in $\overline{u'v'}$ are dependent only on the conditions at the edges of the region. Townsend points out the

existence of a considerable amount of experimental evidence that this viscosity independence prevails in many types of turbulent flows notwithstanding the fact that a finite viscosity is involved in the creation of the large scale turbulent motion and in the final dissipation of the turbulent energy into heat. For the case of turbulent pipe flow, the Reynolds number similarity holds in regions outside of the immediate vicinity of the wall wherein the damping action of solid boundaries on the turbulent term $(\overline{u'v'})$ leaves the molecular term $(\nu \, du/dy)$ with a significant portion of the total shear stress.

From an over-all force balance on the flow, it can be shown that the shear stress is given by

$$\tau = (1 - y/R) \, \tau_o \qquad (3)$$

from which it is seen that for

$$y/R << 1.0 \qquad (4)$$

the shear stress is essentially equal to the wall value. The assumption is made that the fully turbulent central flow regime extends to a region close enough to the wall that the inequality 4 is valid and the bounding shear stress is τ_o. Then the statement of the Reynolds number similarity for this core region leaves only the wall shear stress (τ_o), the density (ρ), the tube diameter (D) and the roughness height (ϵ) as pertinent parameters on which the mean velocity distribution must depend. A dimensional analysis for $u\{y\}$ yields only the length scales D and ϵ and the velocity scale $\sqrt{\tau_o/\rho}$. Thus, the functional relationship

$$\frac{u - u_t}{\sqrt{\tau_o/\rho}} = f_1 \{y/D, \ \epsilon/D\} \tag{5}$$

must hold for the fully turbulent flow where u_t is an arbitrary trans-lation velocity which must be included for generality since the zero velocity at the wall cannot be used as a reference, the wall being outside of the region in which equation 5 is valid.

As a second step toward obtaining a form for the $u\{y\}$ function from similarity arguments, Townsend demonstrates that the production of turbulent energy by the mean flow occurs primarily within the con-stant stress region very near the wall. From this he is led to the ''law of the wall'' which states that the velocity distribution is deter-mined entirely by the local conditions, y, τ_o, ρ and ν and, in the case of surface roughness of differing scale, also on ϵ. Thus by this law, the flow is independent of the external conditions such as the average velocity of the main flow or the pipe diameter. A dimensional analy-sis then gives directly

$$u/\sqrt{\tau_o/\rho} = f_2 \left\{ \frac{y\sqrt{\tau_o/\rho}}{\nu}, \ \frac{\epsilon\sqrt{\tau_o/\rho}}{\nu} \right\} \tag{6}$$

or for smooth pipes

$$u/\sqrt{\tau_o/\rho} = f_3 \left\{ \frac{y\sqrt{\tau_o/\rho}}{\nu} \right\} \tag{7}$$

Laufer's measurements (Ref. 16) of the mean velocities and the various time averaged turbulent components have adequately demonstrated that the ''law of the wall'' (Eq. 7) is valid throughout the constant stress region in smooth pipes. None of the assumptions made by Townsend in establishing the elimination of the outer flow parameters is violated by the presence of wall roughness; hence it is assumed that Laufer's

observations, by supporting the deductions based on the assumptions for the particular case of a smooth wall, also lend credibility to the more general deduction given in equation 6.

As a final step, a "region of overlap" is defined as that region within which viscous forces are negligible and constant shear stress can be assumed and thus in which both Reynolds number similarity and wall similarity should hold. Comparing equations 5 and 6, it follows that

$$f_1 \{y/D, \ \epsilon/D\} + u_t/\sqrt{\tau_o/\rho} = f_2 \{\frac{y\sqrt{\tau_o/\rho}}{\nu}, \ \frac{\epsilon\sqrt{\tau_o/\rho}}{\nu}\} \tag{8}$$

must hold for a finite variation in distance from the wall (y). Since the independent parametric groups associated with y on either side of equation 8 are different, this expression can be valid if and only if the functional forms are such that the y dependence can be separated from the other terms. Hence, the functional forms must be

$$f_1 = B \ \ell n \ (y/D) + f_4 \ \{\epsilon/D\} \tag{9}$$

and

$$f_2 = B \ \ell n \ (\frac{y\sqrt{\tau_o/\rho}}{\nu}) + f_5 \ \{\frac{\epsilon\sqrt{\tau_o/\rho}}{\nu}\} \tag{10}$$

where B is an absolute constant and f_4 and f_5 express the dependence on roughness scale, these also being constants for the smooth pipe case. The necessity of these logarithmic forms for the velocity profiles over smooth surfaces was first pointed out by C. B. Millikan (Ref. 17). Using equation 10 in equation 6, one obtains the velocity distribution in the region close to the wall but outside of the viscous region,

$$u/u_\tau \cong B \ln y* + A_1 \{\epsilon*\} \tag{11}$$

where

$$u_\tau \equiv \sqrt{\tau_o/\rho} \; , \quad y* \equiv \frac{y\sqrt{\tau_o/\rho}}{\nu} \tag{12}$$

and

$$\epsilon* \equiv \frac{\epsilon\sqrt{\tau_o/\rho}}{\nu} \tag{13}$$

and $A_1\{\epsilon*\}$ is a general function... Since

$$y* \cong \epsilon*(y/\epsilon)$$

equation 11 can be written

$$u/u_\tau \cong B \ln y/\epsilon + A\{\epsilon*\} \tag{14}$$

where $A\{\epsilon*\}$ is a different function. Equation 14 will be referred to as the "velocity similarity law" in the present discussion.

The expression for the fully turbulent "outer" flow can be given as a difference between the velocity at two points, y and y_1 which fall within the region of overlap,

$$(u - u_1)/u_\tau \cong B \ln (y/y_1) \tag{15}$$

From equation 15 it is seen that the shape of the velocity profile in this region is independent of either the roughness height or the roughness type or the Reynolds number. If one now assumes that this characteristic of the central flow maintains its validity outside of the constant stress layer and on out to the center of the pipe, one can write

$$(u_{CL} - u)/u_{\tau} = f_6 \{y/D\} \tag{16}$$

where u_{CL} is the mean velocity at the pipe center line. This assumption is certainly plausible since it is difficult to imagine how the effects, appearing in equation 5, of ϵ/D on velocity distribution can be in evidence near the center of the pipe while ϵ/D has no influence on the velocity distribution over a finite region nearer to the wall. Townsend made this assumption at the outset as part of the principle of Reynolds number similarity, i.e., he assumed that equation 5 contained no ϵ/D dependence. Although Townsend's premise for writing equation 5 without the ϵ/D dependence is probably justifiable; the present development of equation 16, which avoids the initial deletion of ϵ/D at the expense of having to make the additional assumption stated just prior to equation 16, is perhaps more satisfying. Regardless of the derivation, Nikuradse (Ref. 10) experimentally demonstrated the validity of equation 16 for a wide variation of ϵ/D, and in fact he showed that the logarithmic law, equation 15, is essentially valid almost to the pipe center. That is, equation 16 is empirically shown to be

$$(u_{CL} - u)/u_{\tau} = - B \ln (2y/D) \tag{17}$$

The logarithmic velocity laws which have received verification with both smooth and rough surfaces for free boundary layers (Ref. 13) and pipes (Ref. 10) are seen to be a direct consequence of the widely applicable assumptions: Reynolds number similarity, a region of essentially constant shear stress wherein viscous action is negligible, and the deductions from the law of the wall. Assumptions

concerning the detail nature of the turbulent flow components are not required; hence any consistent model for the turbulence structure which incorporates above mentioned assumptions should necessarily lead to the logarithmic laws as a byproduct. An interesting example of this is von Kármán's local similarity hypothesis for the turbulence. This hypothesis leads to the logarithmic law for the flow near the wall (Ref. 18, p. 392 and Ref. 19, p. 68) even though as indicated by Laufer (Ref. 16) the hypothesized local similarity may not exist.

A relationship for the friction factor may now be deduced following Nikuradse's treatment (Ref. 10). Neglecting the very thin region near the wall wherein the velocity deficiency law (Eq. 16) is invalid, a simple relation between the center line velocity and the mean discharge velocity is obtained. The latter is defined

$$u_m \equiv (2/R^2) \int_0^R u\{r\}\, r\, dr \tag{18}$$

where "r" is the radial location. Integrating equation 16 as prescribed by the definition in equation 18, noting that $y/D = (1/2)(1-r/R)$, and converting the variable of integration to $r/R \equiv \eta$ yields the definite integral

$$\beta \equiv \frac{u_{CL} - u_m}{u_\tau} = 2 \int_0^1 f_6 \{\tfrac{1}{2}(1-\eta)\}\, \eta\, d\eta \tag{19}$$

Thus, β is a constant independent of the qualities of the wall roughness. The friction factor is then defined

$$C_F \equiv 2\tau_o / \rho\, u_m^2 \tag{20}$$

Hence, by the definitions 12 and 20,

$$u_m/u_\tau \equiv 1/\sqrt{C_F/2} \qquad (21)$$

Assuming equation 17 to be valid from the pipe center to the wall region and using the wall law (Eq. 14),

$$u_{CL}/u_\tau = -B \ln(2\epsilon/D) + A\{\epsilon*\} \qquad (22)$$

and using the definitions of equations 19 and 21 with equation 22,

$$\frac{1}{\sqrt{C_F/2}} = -B \ln(2\epsilon/D) - \beta + A\{\epsilon*\} \qquad (23)$$

The constants B and β are applicable to both smooth and rough pipes and have been evaluated by Nikuradse (Ref. 10) as 2.5 and 3.75 respectively. By using the definition of Reynolds number,

$$Re \equiv D u_m/\nu \qquad (24)$$

and the definitions of equations 13 and 20 one obtains the identity

$$\epsilon* \equiv Re\sqrt{C_F/2}\ \epsilon/D \qquad (25)$$

From this, equation 23 can be rewritten

$$\frac{1}{\sqrt{C_F/2}} + B \ln(2\frac{\epsilon}{D}) + \beta = A\{Re\sqrt{\frac{C_F}{2}}\ \frac{\epsilon}{D}\} \qquad (26)$$

Equation 26, which will be referred to herein as the "friction similarity law," reduces the experimental problem of finding the general three-dimensional functionality

$$C_F\{Re, \epsilon/D\}$$

to that of finding the two-dimensional function $A\{\epsilon*\}$, thus greatly

extending the usefulness of a given amount of empirical information.
The identity of the $A\{\epsilon *\}$ function found (Cf. Ref. 10) by velocity pro-
file measurements with equation 14 and by friction measurements
with equation 26 over a wide range of Reynolds numbers and of rough-
ness ratios has put these similarity laws on a firm experimental
basis.

Using the velocity law in the form of equation 11 (with A_1 as
constant) to develop the friction law, the smooth pipe law evolves

$$\frac{1}{\sqrt{C_F/2}} - B \ln (Re \sqrt{C_F/2}) + \beta = A_1 - B \ln 2 \tag{27}$$

where the constant, A_1, on the right is determined experimentally.
In this case the problem of finding the relation $C_F\{Re\}$ has been re-
duced to that of experimentally determining this one constant. Equa-
tion 27 for smooth pipes can be put into the form of the more general
equation 26 by reordering the terms and letting

$$A\{\epsilon *\} = A_1 + B \ln \epsilon * \tag{28}$$

Thus, the friction similarity law (Eq. 26) is applicable both to smooth
tubes and to rough tubes with geometrically similar roughness ele-
ments.

The general $A\{\epsilon *\}$ function determined by Nikuradse for sand-
grain type roughness shows a region of smooth-type behavior (Eq. 28)
at low $\epsilon *$ values followed by a "transition" region, $3.55 \leq \epsilon * \leq 67.5$,
and a "fully rough" region, $\epsilon * > 67.5$, wherein A becomes a constant.
In the "smooth" region, the roughness elements are buried deep in
the laminar wall layer and create no effect on the flow which is nearly
stationary at the wall. In the "fully rough" region, reference to

equation 14 and equation 26 shows that both the velocity profile and friction coefficient become independent of Reynolds number, i.e. of viscosity, and hence that the Reynolds number similarity extends throughout the flow. A likely possibility here is that the flow separates from the roughness elements producing secondary cavity flows which result in a pressure drag on the element surfaces that far exceeds the viscosity-dependent surface shear forces.

The problem of heat transfer for flow in rough pipes with geometrically similar roughness is reduced, by means of a dimensional analysis on the relevant parameters (Cf., e.g., Ref. 20, p. 495), to finding the four-dimensional relationship

$$C_H \{Re, \ Pr, \ \epsilon/D\}$$

where C_H is the Stanton number given by

$$C_H \equiv \frac{\dot{q}_o}{\rho \, u_m \, c_p (T_w - T_L)} \tag{29}$$

where $\dot{q}_o$ is the radial heat flux at the wall, T_w is the wall temperature and the liquid temperature, T_L, is defined for experimental convenience as the mixed mean temperature,

$$T_L \equiv \frac{2}{R^2 u_m} \int_0^R T\{r\} \, u\{r\} r \, dr \tag{30}$$

The theoretical approach to the heat transfer problem in rough tubes will follow a similar development for smooth tubes in making use of a modified Reynolds analogy between heat and momentum transfer in turbulent flow. The general energy equation for pipe flow written in terms of time-averaged quantities assumes a simple form if the following assumptions are made:

i) The energy involved in the pressure work and viscous dissipation terms is negligible in comparison to the heat energy transferred.

ii) Axial temperature gradients are negligible compared to the radial temperature gradients.

iii) The flow is thermally fully established such that the the axial thermal gradient ($\partial T / \partial x$) is independent of radial position.

iv) The velocity is independent of radius insofar as it affects the radial heat flux distribution; thus it is assumed that $\dot{q}\{r\}/\dot{q}_o = r/R$.

The momentum and heat transfer equations can then be written (Cf. Appendix A of Ref. 14),

$$\tau_o/\rho \ (1 - y/R) = (\epsilon_M + \nu) \ du/dy \tag{31}$$

$$-(\dot{q}_o/\rho c_p)(1 - y/R) = (\epsilon_H + \nu/Pr) \ dT/dy \tag{32}$$

where

$$\epsilon_M \equiv \frac{-\overline{u'v'}}{du/dy} \tag{33}$$

and

$$\epsilon_H \equiv \frac{-\overline{T'v'}}{dT/dy} \tag{34}$$

are the turbulent diffusivities for momentum and heat respectively. The terms $\overline{u'v'}$ and $\overline{T'v'}$ are time averages of the products of the turbulent fluctuations in the axial velocity (u), the velocity radially away

from the wall (v) and the temperature (T). Next the assumption is made that the region of large changes in temperature and velocity occurs very close to the wall; this is the case for large Reynolds numbers (say greater than 10^4) and for Prandtl numbers greater than 0.7. With this assumption, y/R can be dropped with respect to 1.0 in equations 31 and 32. And next, the respective distances from the wall at which the velocity equals u_m and at which the temperature equals T_L are assumed to be the same. Finally, the Reynolds analogy, which states that

$$\epsilon_H = \epsilon_M$$

for the fully turbulent region of flow, is assumed to hold throughout the pipe.

A heat transfer similarity law is then derived by the following arguments. A dimensionless distance from the wall, y_2^*, is assumed which is far enough from the wall that viscous shear stresses are negligible, say $y_2^* = 100$, for either rough or smooth pipes. Re-solving equation 29 yields

$$\frac{1}{C_H} = \frac{\rho c_p u_m}{\dot{q}_o} (T_w - T_2) + \frac{\rho c_p u_m}{\dot{q}_o} (T_2 - T_L) \tag{35}$$

Using the nondimensionalizing groups from the law of the wall together with the assumptions of the previous paragraph, the integration of equations 31 and 32 between the distance from the wall, y_2, and the distance, y_m, at which both T_L and u_m are assumed to occur gives

$$\frac{u_m - u_2}{u_\tau} = \int_{y_2^*}^{y_m^*} \frac{dy^*}{\epsilon_M/\nu} \tag{36}$$

and

$$\frac{\rho c_p u_\tau}{\dot{q}_o} (T_2 - T_L) = \int_{y_2^*}^{y_m^*} \frac{dy^*}{\epsilon_M/\nu} \tag{37}$$

Subtracting equation 36 from 37, multiplying by u_m/u_τ and substituting with equation 21 yields

$$\frac{\rho c_p u_m}{\dot{q}_o} (T_2 - T_L) = \frac{2}{C_F} - \frac{u_2/u_\tau}{\sqrt{C_F/2}} \tag{38}$$

From equation 6,

$$u_2/u_\tau = f_7 \{y_2^*, \epsilon^*\} \tag{39}$$

Next a dimensional analysis using the parameters of the law of the wall, together with the parameters $\dot{q}_o$, c_p, ρ and k which must be added for the heat transfer problem, gives

$$(T_w - T_2) \frac{\rho c_p u_\tau}{\dot{q}_o} = f_8 \{y_2^*, \epsilon^*, Pr\} \tag{40}$$

or, multiplying this equation by u_m/u_τ and again substituting from equation 21,

$$(T_w - T_2) \frac{\rho c_p u_m}{\dot{q}_o} = \frac{1}{\sqrt{C_F/2}} f_8 \{y_2^*, \epsilon^*, Pr\} \tag{41}$$

Substituting equations 38 and 41 into equation 35 and reorganizing the latter, gives

$$\frac{(C_F/2C_H)-1}{\sqrt{C_F/2}} = f_8 \{y_2^*, \epsilon^*, Pr\} - f_7 \{y_2^*, \epsilon^*\} \tag{42}$$

Since y_2^* is a constant number independent of the parameters of the problem, it may be dropped from the functions and equation 42 becomes

$$\frac{(C_F/2C_H)-1}{\sqrt{C_F/2}} = f_9 \{\epsilon*, Pr\} \tag{43}$$

This equation will be referred to as the "heat transfer similarity law"; it does for the heat transfer problem what the friction similarity law does for the momentum transfer problem. In the heat transfer case, the general experimental job of finding the four-dimensional relation

$$C_H \{Re, Pr, \epsilon/D\}$$

is reduced to finding the three-dimensional relation

$$f_9 \{\epsilon*, Pr\}$$

For the case of a smooth wall the same analysis gives f_9 as a function of Prandtl number only. The essential assumptions leading to the heat transfer similarity law are the law of the wall, Reynolds analogy and the assumed coincidence of u_m and T_L.

A more descriptive and useful form of the f_9 function in equation 43 is afforded by the following similar but less direct derivation of the heat transfer similarity law. First the flow is divided into two regions by an imaginary cylinder passing through the tips of the roughness elements at y equal to ϵ. At this interface the axial velocity, temperature, shear stress and heat flux are defined as u_g, T_g, τ_o and $\dot{q}_o$ respectively. These are spatial means which are taken along the interface surface over an interval including many roughness elements in the same manner and in the same operation in which temporal averaging was done to develop equations 31 and 32. These statistical mean values are then independent

of axial or circumferential location in the pipe. That is, they are
independent of location with respect to a roughness element, and
the simple one-dimensional aspect of the problem is preserved.
Note that the same treatment is tacitly assumed in the development
of the previously discussed friction similarity law. By continuity,
the net flow through the interface, i.e. into and out of the roughness
cavities, is zero, and this motion is thought of as part of the turbu-
lent motion. Also the net axial fluid motion on the wall side of this
interface is assumed negligible. This will not be precisely true
for the three-dimensional roughness elements being considered,
but the net heat convected from each cavity in the axial direction
is still taken as insignificant compared to the radial heat flow out
of the cavity.

The definition for C_H in equation 29 is resolved into

$$\frac{1}{C_H} \equiv \frac{\rho c_p u_m}{\dot{q}_o} (T_w - T_g) + \frac{\rho c_p u_m}{\dot{q}_o} (T_g - T_L) \tag{44}$$

The central flow region is then treated by the same procedure given
by Rannie (Ref. 14) for use in smooth tubes within the assumptions
used previously. Making use of the proper nondimensionalizing
groups from the law of the wall (Eq. 6) and integrating equations
31 and 32 respectively, there follows

$$\frac{u_m - u_g}{u_\tau} = \int_{\epsilon^*}^{y_2^*} \frac{dy^*}{(\epsilon_M/\nu)+1} + \int_{y_2^*}^{y_m^*} \frac{dy^*}{(\epsilon_M/\nu)} \tag{45}$$

and

$$\frac{\rho c_p u_\tau}{\dot{q}_o} (T_g - T_L) = \int_{\epsilon^*}^{y_2^*} \frac{dy^*}{(\epsilon_M/\nu)+(\frac{1}{Pr})} + \int_{y_2^*}^{y_m^*} \frac{dy^*}{(\epsilon_M/\nu)} \tag{46}$$

Here again the y_2^* value is taken sufficiently far from the wall that the $1/Pr$ value and 1 are both negligible with respect to ϵ_M/ν, and the y_m^* value is the assumed common point where both u_m and T_L are attained. Subtracting equation 45 from 46, multiplying by u_m/u_τ and substituting from equation 21 yields an expression for the second term on the right hand side in equation 44,

$$\frac{\rho c_p u_m}{\dot{q}_o} (T_g - T_L) = \frac{2}{C_F} - \frac{u_g/u_\tau}{\sqrt{C_F/2}} + \frac{F\{Pr, \epsilon^*\}}{\sqrt{C_F/2}} \tag{47}$$

where

$$F\{Pr, \epsilon^*\} \equiv \int_{\epsilon^*}^{y_2^*} \left[\frac{1}{(\epsilon_M/\nu) + (1/Pr)} - \frac{1}{(\epsilon_M/\nu) + 1} \right] dy^* \tag{48}$$

The cavity flow on the wall side of the separating surface can be considered as a separate flow system with the cavity walls as one boundary and velocity, u_g, and shear stress, τ_o, representing the conditions at the open boundary. By the law of the wall (Eq. 6), the velocity at the location y equals ϵ can be written

$$\frac{u_g}{u_\tau} = \frac{u_g}{u_\tau} \{\epsilon^*\} \tag{49}$$

Further, by rewriting equation 1 for the constant stress region and differentiating equation 6, the turbulent shear stress can be written for y equals ϵ as

$$\frac{\overline{u'v'}}{u_\tau^2} = \frac{\partial(u/u_\tau)}{\partial y^*} - 1 = f_{10}\{\epsilon^*\}$$

Then from equation 49,

$$\frac{\overline{u'v'}}{u_\tau^2} = f_{11}\{\frac{u_g}{u_\tau}\}$$

Thus the conditions at the cavity opening are completely described by u_g and $u_\tau \equiv \sqrt{\tau_o/\rho}$.

Next the appropriate Reynolds number for the time mean cavity motion can be written

$$Re_c \equiv \frac{\epsilon u_g}{\nu} = \epsilon^* \frac{u_g}{u_\tau} \{\epsilon^*\} \tag{50}$$

and the appropriate Stanton number for the time mean heat exchange becomes

$$C_{Hc} \equiv \frac{\dot{q}_o}{\rho u_g c_p (T_w - T_g)} \tag{51}$$

and, by a dimensional analysis of the cavity flow,

$$C_{Hc} = C_{Hc} \{Re_c, Pr\} \tag{52}$$

The first term on the right of equation 44 is then written, again using equation 21,

$$\frac{\rho c_p u_m}{\dot{q}_o} (T_w - T_g) = \frac{1}{\sqrt{C_F/2}\,(u_g/u_\tau) C_{Hc} \{(u_g/u_\tau)\epsilon^*, Pr\}} \tag{53}$$

Using equations 47, 49 and 53 in equation 44 and rearranging terms gives the heat transfer similarity law again. This is written here as

$$\frac{(C_F/2C_H)-1}{\sqrt{C_F/2}} + 8.48 = g\{\epsilon^*, Pr\} \tag{54}$$

where

$$g\{\epsilon^*, Pr\} = F\{Pr, \epsilon^*\} - \frac{u_g}{u_\tau}\{\epsilon^*\} + 8.48$$

$$+ \frac{1}{\frac{u_g}{u_\tau}\{\epsilon^*\} C_{Hc} \left\{\epsilon^* \frac{u_g}{u_\tau}\{\epsilon^*\}, Pr\right\}} \tag{55}$$

Note that the $f_9\{\epsilon*, Pr\}$ function of equation 43 appears in equation 54

as $(g\{\epsilon*, Pr\} - 8.48)$. The term 8.48 was included to simplify the

form of certain limiting cases of equation 55.

The limiting $\epsilon*$ regions of the "fully rough" type and the "smooth"

type friction behavior discussed previously have simple forms for the

$g\{\epsilon*, Pr\}$ function. For the fully rough region, the Reynolds number

similarity extends to the tips of the elements, and beyond, such that

the F integral as defined in equation 48 becomes zero. The logarith-

mic velocity law is assumed to hold to y equals ϵ since the "region of

overlap" extends to this point, and since for sand grain roughness

Nikuradse (Ref. 10) found that $A\{\epsilon*\}$ becomes constant at 8.48, equa-

tion 14 gives

$$\frac{u_g}{u_\tau} = 8.48$$

Then, by equation 55,

$$g_{F.R.}\{\epsilon*, Pr\} = \frac{1}{8.48 \; C_{Hc}\{8.48\epsilon*, Pr\}} \tag{56}$$

Thus it is seen that, for the fully rough condition, $g_{F.R.}$ is essen-

tially the reciprocal of the cavity Stanton number. The cavity Stanton

number (C_{Hc}) and hence the pipe Stanton number (C_H) are expected

to be functions of viscosity and of Prandtl number by reason of the

viscous layer that must exist at the cavity walls even though the fric-

tion factor of the pipe (C_F) is essentially independent of molecular

processes.

For the smooth region, as $\epsilon*$ approaches zero, the last term

on the right hand side of equation 55 which represents the temperature

drop in the cavity $(T_w - T_g)$ becomes insignificant compared to the

first term on the right representing the temperature drop across the nearly undisturbed laminar boundary layer. Further, the velocity at the tips of the roughness elements (u_g) goes to zero, and the lower limit of the integral, F, shown in equation 48 also approaches zero. Thus, as expected, the smooth pipe law (Cf. Ref. 14) is approached:

$$\frac{(C_F/2C_H)-1}{\sqrt{C_F/2}} \approx g - 8.48 \approx F\{Pr\} \tag{57}$$

or

$$\left(\frac{2C_H}{C_F}\right)_S = \frac{1}{1 + \sqrt{C_F/2}\, F\{Pr\}}$$

where the subscript S refers to "smooth pipe". It is noted that here once again the use of the similarity law reduces the order of the problem by converting the unknown relation

$$C_{HS}\{Re,\ Pr\}$$

into the unknown relation

$$F\ \{Pr\}$$

Referring to equation 48 with ϵ^* equal zero, it is seen that the problem of determining $F\{Pr\}$ can be further resolved into that of finding

$$\frac{\epsilon_M}{\nu}\{y^*\}$$

This is accomplished in principle by measurement of the velocity profiles since by equation 31, for $y/R << 1$,

$$\frac{\epsilon_M}{\nu} = \frac{1}{d(u/u_\tau)/dy^*} - 1 \tag{58}$$

However, for Pr values appreciably greater than 1.0, the F integral becomes sensitive to values of ϵ_M/ν very close to the wall where sufficiently accurate measurements of the mean velocity profile are difficult if not impossible to obtain. By hypothesizing a "buffer region" joining a purely laminar region very near the wall to the region of the logarithmic velocity law further out, von Kármán (Ref. 21) generated a relatively simple form for $F\{Pr\}$,

$$F\{Pr\} = 5[(Pr-1) + \ln(1 + \frac{5}{6}[Pr-1])]$$ (59)

which gives good agreement with heat transfer measurements for Prandtl numbers between about 0.7 and 10. In order to improve this theory at higher Prandtl numbers, Rannie (Ref. 14), Reichardt (Ref. 22) and Deissler (Ref. 23) have used various mathematical models allowing for a continuous variation of ϵ_M/ν which becomes zero only right at the wall.

The validity of the assumptions leading to the heat transfer similarity law for rough pipes will next be considered. First the possible errors in the heat transfer similarity law for smooth pipes are of interest in that they will imply errors in the rough tube law which is based on the same assumptions. For Prandtl number equal to 1.0, the smooth pipe heat transfer equation takes on a simple form. As seen from the F integrand (Eq. 48),

$$F\{1.0\} = 0$$

and

$$(\frac{2C_H}{C_F})_S = 1.0$$ (60)

This result might have been expected from the fact that the dimension-less temperature and velocity profiles are the same, Cf. equations 31 and 32, for $Pr = 1$ and $\epsilon_H = \epsilon_M$. However, the definitions of the mean velocity (Eq. 18) and the mixed mean temperature (Eq. 30) used in the usual C_H and C_F definitions are not similar; equation 60 is obtained only by use of the simplifying, but slightly erroneous, assumption that T_L and u_m are reached at the same distance from the wall.

Reichardt (Ref. 22) has considered a first order correction for this assumption along with corrections for two other assumptions involved in the present theory for smooth tubes. First the assumption of $\epsilon_H = \epsilon_M$ is not expected to hold at appreciable distances out from the wall. This is based in part on reference to the Taylor vorticity transfer theory (Cf., e.g., Ref. 18, p. 389) which predicts that

$$\epsilon_H/\epsilon_M = 2.0$$

This prediction has been confirmed by observations in free turbulence. Reichardt argues that

$$\epsilon_H/\epsilon_M = 1.0$$

will occur only in the immediate neighborhood of the wall. Secondly, the heat flux rate does not vary linearly with radius near the wall since the velocity profile is not uniform in this region. And finally, the complete integrations of the temperature and velocity profiles must be used to eliminate the approximation discussed in the preceding paragraph. For the simple case of $Pr = 1$, Reichardt's theory gives

$$\left(\frac{2C_H}{C_F}\right)_S = \left(\frac{\epsilon_H}{\epsilon_M}\right)_m \cdot \frac{1}{(1+e)} \cdot \frac{u_m/u_{CL}}{(T_w-T_L)/(T_w-T_{CL})} \tag{61}$$

where the successive terms on the right represent the integrated effects of the various corrections to the present theory in the order in which they were discussed above. In smooth tube experiments, including the present experiments, it is found that

$$\left(\frac{2C_H}{C_F}\right)_{exp'l.} \approx 1.0 \tag{62}$$

for Pr $\approx$ 1.0 over a large range of Re values. Using this observation and Reichardt's computed values for the second and third terms on the right in equation 61, it is possible to compute the effective ratios of the eddy diffusivities as follows:

$$\left(\frac{\epsilon_H}{\epsilon_M}\right)_m \{Re = 10^4\} \cong 1.21$$

and

$$\left(\frac{\epsilon_H}{\epsilon_M}\right)_m \{Re = 10^6\} \cong 1.06$$

Thus the experimental result of equation 62 cannot be taken as a verification of the modified Reynolds analogy assumption; on the contrary, it tends to support Reichardt's reasoning that ϵ_H/ϵ_M increases from 1.0 at the wall to higher values nearer the pipe center.

The smooth tube theories of Rannie* (Ref. 14) and of von Kármán (Ref. 21) contain the heat transfer similarity law. As shown in the preceding discussion, the success of these theories in predicting experimental results (Cf. Sec. IV-B) is apparently due in part to the cancellation of errors introduced by the assumptions. The possibility exists

---

*Rannie's complete theory includes a first order correction for the assumption that u_m and T_L are coincident. With this correction his theory necessarily does not obey the heat transfer similarity law. Rannie's theory as used in this discussion refers to that part of his development which does not include the correction term.

that this cancellation will not be as complete for the case of rough tubes. In particular, the large difference between the velocity profile shapes for rough and smooth tubes operating at the same Reynolds number (Cf., e.g.., Ref. 19, p. 56) may make the assumption that u_m and T_L are reached at the same radius a poorer assumption for rough tubes. A check on the effects of this assumption is provided by carrying through the development of the theory without this simplification; this can be done readily as follows if fully rough operation is assumed.

No net axial flow through the roughness elements is assumed to occur on the wall side of the cylinder passing through the element tips, and further, for the fully rough condition, the terms ν and ν/Pr in equations 31 and 32 are assumed negligible throughout the flow inside of this cylinder. Defining an effective mean value of the eddy diffusivity ratio $(\epsilon_H/\epsilon_M)_m$ which is independent of radius, the velocity and temperature profiles in the central flow region are simply related as

$$T - T_g \approx \frac{-\dot{q}_o}{\rho c_p u_\tau^2 (\epsilon_H/\epsilon_M)_m} (u - u_g) \qquad (63)$$

Then using the definitions of u_m and T_L in equations 18 and 30 respectively, equation 63 is integrated to give

$$T_g - T_L = \frac{\dot{q}_o}{\rho c_p u_\tau^2 (\epsilon_H/\epsilon_M)_m} \eta\{\frac{\epsilon}{D}\} (u_m - u_g) \qquad (64)$$

where

$$\eta\{\frac{\epsilon}{D}\} \equiv \frac{\overline{(u/u_\tau)^2}/\overline{(u/u_\tau)} - (u_g/u_\tau)}{\overline{(u/u_\tau)} - (u_g/u_\tau)} \qquad (65)$$

and the bar signifies

$$\bar{\alpha} \{\frac{\epsilon}{D}\} \equiv 2 \int_{2\epsilon/D}^{1} \alpha \{\frac{r}{R} ; \frac{\epsilon}{D}\} (\frac{r}{R}) d(\frac{r}{R})$$

where α is an arbitrary dependent variable.

Using equation 14 for the fully rough condition and the constants for the sand grain roughness,

$$\frac{u}{u_{\tau}} \{\frac{r}{R} ; \frac{\epsilon}{D}\} = 2.5 \ln (1 - \frac{r}{R}) - 2.5 \ln(2\frac{\epsilon}{D}) + 8.48 \tag{66}$$

and, as given in the discussion leading to equation 56,

$$\frac{u_g}{u_{\tau}} = 8.48 \tag{67}$$

Substituting equation 64 into equation 44 and following the same steps used to generate equation 54 yields

$$\frac{\dfrac{C_F}{2C_H} - \dfrac{\eta\{\epsilon/D\}}{(\epsilon_H/\epsilon_M)_m}}{\sqrt{C_F/2}} + 8.48 = g \{\epsilon^*, Pr\}$$

$$+ 8.48 (1 - \frac{\eta\{\epsilon/D\}}{(\epsilon_H/\epsilon_M)_m}) \tag{68}$$

where the $g\{\epsilon^*, Pr\}$ function is the same as that used in equation 54. Equation 68 differs from the similarity law (Eq. 54) only insofar as $\eta\{\frac{\epsilon}{D}\}/ (\epsilon_H/\epsilon_M)_m$ differs from 1.0.

An evaluation of $\eta\{\frac{\epsilon}{D}\}$ from equations 65, 66 and 67 shows that

$$\eta\{\frac{\epsilon}{D}\} \approx 1.055 , \quad 0.01 \leqslant \frac{\epsilon}{D} \leqslant 0.1$$

and that $\eta\{\epsilon/D\}$ falls off rapidly to 1.0 for $\epsilon/D < 0.01.$* The term $(\epsilon_H/\epsilon_M)_m$ may be assumed to take on similar values; hence it is doubtful that any improvement in the heat transfer similarity law will be gained by using $\eta\{\epsilon/D\}/(\epsilon_H/\epsilon_M)_m$ values other than 1.0. And since the errors due to the various approximations in the heat transfer similarity law appear to be small and to tend toward cancellation for both the "smooth" and "fully rough" regions, it is assumed that the relation expressed by equation 54 is uniformly valid for all regions of operation including the transition region.

The fundamental notions presented in this section can now be summarized in terms of three similarity laws for rough pipes with geometrically similar roughness elements. All of these laws are ultimately dependent on the postulate of the "law of the wall" represented by equation 6, and they all have the property of reducing the respective problems of finding the functional dependence of a dependent variable on various independent variables to substitute problems containing one less independent variable. The three similarity laws together with the respective special forms for the "smooth" region and the "fully rough" region can be summarized as follows:

---

*The value of $\eta\{\epsilon/D\}$ for $\epsilon/D = 0.0$ has little physical significance since the fully rough condition requires that $Re \approx \infty$ for this case. The $\eta\{\epsilon/D\}$ term in equation 68 for fully rough pipe flow and the last term on the right of equation 61 for smooth pipe flow both represent corrections for the same assumption used in the derivation of the heat transfer similarity law. However, the relationship between the correction terms ends there. One of these correction terms cannot be obtained from the other as is indicated by the fact that the η term evaluated for fully rough conditions depends only on ϵ/D while the term in equation 61 depends on Re and Pr.

The Velocity Similarity Law

$$\frac{u}{u_\tau} - B \ln (y/\epsilon) = A \{\epsilon*\} \tag{14}$$

For the smooth region

$$A\{\epsilon*\} = A_1 + B \ln (\epsilon*)$$

For the fully rough region

$$A\{\epsilon*\} = A$$

The Friction Similarity Law

$$\frac{1}{\sqrt{C_F/2}} + B \ln (2 \frac{\epsilon}{D}) + \beta = A \{\epsilon*\} \tag{26}$$

For the smooth region

$$A \{\epsilon*\} = A_1 + B \ln (\epsilon*)$$

For the fully rough region

$$A \{\epsilon*\} = A$$

The Heat Transfer Similarity Law

$$\frac{(C_F/2C_H)-1}{\sqrt{C_F/2}} + A = g \{\epsilon*, Pr\} \tag{54}$$

For the smooth region

$$g\{\epsilon*, Pr\} = A + F \{Pr\}$$

For the fully rough region

$$g \{\epsilon*, Pr\} = \frac{1}{A \, C_{Hc} \{A\epsilon*, Pr\}}$$

The constants B and β are universal; the constant A_1 is applicable to smooth pipes; the function $A\{\epsilon*\}$ depends in general on the type of roughness as does the constant A; the functions $g\{\epsilon*, Pr\}$ must also be determined for each type of roughness, and the function $F\{Pr\}$ is that already determined for smooth pipes. The friction and velocity laws have been thoroughly tested and verified for rough tubes by Nikuradse (Ref. 10). The heat transfer similarity law for rough tubes-- to the writer's knowledge--has not been previously formulated in this manner. The experiments presented in this thesis are suitable for checking the validity of this law and such a check is made. The relation given herein between the heat transfer similarity parameter (g) in the fully rough region and the so-called cavity Stanton number (C_{Hc}) does not in itself provide any information; however, it does focus attention on the residual problem of finding an appropriate Stanton number for the cavity flow. A theoretical model of the cavity heat transfer will be presented in an appendix.

III EXPERIMENTAL APPARATUS AND METHOD

A. Fluid (Water) Properties

Distilled water was used as the working fluid in these experiments. At the start of the test program, a measurement of the electrical conductivity of the water using a Barnstead Purity Meter, Model PM-2, gave a reading of 1.0 parts per million (ppm) equivalent of sodium chloride in water. At the completion of one-half of the test program a reading of 2.6 ppm was obtained. This may be compared to a reading of 1.4 ppm made with the same meter on freshly double-distilled water. The entire enclosed test system was composed of stainless steel with the exception of the nickel tube and the receiver tank which was made of galvanized steel; hence, the low dissolved-salts impurity level shown by these measurements was readily maintained. However, since the water was pumped by nitrogen gas, it may be assumed that the water was nearly saturated with this gas at the temperatures and pressures of the various tests.

The properties of water used for reducing the data of these experiments were interpolated from tables of density, specific heat, kinematic viscosity, and Prandtl number as functions of temperature found in Eckert and Drake (Ref. 12, p. 500).

B. Experimental Tubes

The following characteristics were required of the tubes used in this experimental program:

i) A rough inner surface of continuous metal.

ii) Approximately 0.4-inch-diameter in order to utilize existing fluid pumping and metering equipment effectively.

iii) Approximately 37 inches of length in order to provide for established conditions.

iv) Wall strength sufficient to withstand fluid pressures of 350 psig.

v) A uniformly thin wall to suffice as an electrical heating element utilizing an available electrical source.

vi) A well established thermal conductivity of the material to permit calculation of inner wall temperatures from measurements on the outer wall.

The desired features were obtained by an electroforming construction process which has not been hitherto applied to making tubes for this purpose. In the process, nickel was electroplated onto a sand-covered mandrel, and the mandrel was subsequently dissolved with chemicals leaving a pure nickel shell which served as the test tube. More details on the basic tube construction are presented in Appendix I. Samples trimmed from the ends of the four tubes used in the tests are shown in Fig. 1. An almost exact cast of the original mandrel was obtained for all tubes, and, although the tube surfaces have an inverse imprint of a partially-filled sand surface, the tube surfaces have the general appearance of an array of sand grains. Close

examination reveals that, as expected, the cavities are slightly more concave in appearance and the protrusions are slightly more cusp-like than the respective features of a sanded surface.

The tube wall material was found to be of high purity, free of inclusions, and uniform throughout. Electrical resistivity measurements, discussed in Appendix II-A, reveal the nickel to be only slightly less pure than the 99.98 percent-pure electrolytic nickel reported on in Ref. 24, p. 427. Further, the nickel in all tubes and throughout each tube was found to have essentially the same resistivity, Cf. Appendix II-A. Figure 2 shows photomicrographs of etched samples taken from each tube. These samples, along with others not shown, reveal a very uniform nickel grain structure and show no evidence of inclusions or voids. The thermal conductivity of the wall material was determined, as shown in Appendix II-B, from the electrical resistivity measurements and from the measurements of thermal conductivity of the very pure nickel reported on in Ref. 24, p. 425. A semi-empirical relationship between the thermal conductivity and electrical resistivity suggested by Smith and Palmer (Ref. 25) was used in this determination.

Table 1 presents the significant dimensions of each of the four experimental tubes. The inside diameter of the tubes is defined as

$$D \equiv \left[\frac{4 \Delta V}{\pi \Delta x} \right]^{\frac{1}{2}} \tag{69}$$

where ΔV is the volume contained in the length Δx. The values used for the inside diameter in Table 1 were based on 12 outside diameter

measurements of the original mandrel with corrections for the mean sand protrusion. As a check, the diameter was also determined volumetrically as prescribed in equation 69 by means of burette measurements of the volumes of water required to fill successive lengths of the tube. And as another check, the inside diameter was indicated by measuring the outside diameter of the finished tube and subtracting the wall thickness. All three of these diameter measurements agreed within their respective limits of accuracy, and they showed the diameter to be uniform for each tube.

The effective tube-wall thickness used in determining the temperature drop in the wall is defined implicitly from

$$t\{x\} \equiv \frac{\rho_e}{\pi (d R_e/dx)(D-t\{x\})} \tag{70}$$

where ρ_e is the electrical resistivity of the wall material and dR_e/dx is the resistance per unit length of tube. This definition is developed in Appendix II-C. Values of wall thickness, computed by equation 70, agree closely with the thickness measured on photomicrographs taken from end samples of each tube. Table 1 contains wall thickness computed by equation 70 for a particular longitudinal station on each tube. As discussed in Appendix II-C, a slight longitudinal taper in the tube wall was observed on all tubes and is taken into account in the data reduction.

A qualitative indication of the relative degree of roughness attained on the four finished tubes is provided in Figures 3 and 4. Figure 3 shows photomicrographs of longitudinal and circumferential sections of each tube. For the smoother E-3 and D-3 tubes, a better resolution of the roughness is provided by records made with a

Brush Surface Analyzer; sample records are shown in Figure 4. It should be noted that these figures both represent planar cross sections of the surface and that, since the roughness elements are distributed in a two-dimensional pattern, the cross-section-cuts only occasionally pass directly through an element to give the true roughness height. For the same reason these figures give the appearance of a more random roughness pattern than that which actually exists in the intentionally roughened tubes.

The roughness ratio (ϵ/D) of each of the three rough tubes is operationally defined to obey the friction similarity law presented in Section II. Since the sand-grain roughness used in Nikuradse's experiments (Ref. 10) satisfies this law, the required definition is accomplished by assigning to each tube that sand-grain roughness ratio (ϵ_s/D) which gives the same friction factor for fully-rough conditions ($C_{F\ F.R.}$). These "hydraulic equivalent" sand-grain sizes are presented in Table 1. Also shown in Table 1 are the mean diameters of the sand grains used in making the mandrels for the respective tubes; determination of these grain diameters is discussed in Appendix I. The fact that the ratio of the diameter of the sand used in making the mandrel to the "hydraulic equivalent" sand diameter of the finished tube is not constant from tube to tube is an indication that the tubes do not have exactly geometrically-similar roughness elements. The reasoning behind his statement and the implications of the statement will be discussed in Section IV-F.

A drawing of the complete test-section assembly is shown in Figure 5, and photographs of one of the tubes taken before and after installation are shown in Figures 6 and 7. A continuous

electroformed-nickel tube forms the entrance section and the heated test section. By the method described in Appendix I, a one-inch-long smooth section was formed near the center of all of the rough tubes. Three equally spaced, 0.032-inch-diameter holes connecting the center of this smooth region to a small ring manifold constitute the pressure tap at the entrance to the heated test section. The downstream pressure tap having the same geometry is located in a smooth section 1/2-inch from the exit end of the rough tube. Copper blocks, silver-brazed to the nickel tube, serve as electrode attachment points and distributors of the electric current. The center block is extended to form part of a sliding seal. This seal together with a somewhat similar seal arrangement at the tube entrance end permits the tube to expand axially when heated while maintaining a pressure seal and electrical isolation. The exit end of the test section is electrically isolated by a special flange which also incorporates a thermal mixing chamber. The mixing chamber consists of a brass thermal equalizer which is isolated from the other metal parts by a teflon sleeve. The equalizer has drilled holes directing the flow first into an outer chamber and then back into the central passage.

Three wall-thermocouple stations are located in the heated test-section at the positions listed as E, F and G in Table 1. At each station, three thermocouples are mounted 120 degrees apart and are arranged to match the circumferential locations of the thermocouples at the other stations. Figure 5 shows a typical thermocouple station. The thermocouple junctions are formed by discharge welding 0.005-inch-diameter Chromel and Alumel wires to the

nickel tube leaving a 0.020-inch gap between the ends of the wires
such that a Chromel-nickel junction and a nickel-Alumel junction
are formed in series. The insulated leads are wrapped several turns
around the tube and are secured to the tube with high temperature
cement. A cover is provided for each set of thermocouples to pro-
tect the junctions from injury and to further insure that the leads
will approach the heated tube temperature and thereby minimize
heat conduction from the junctions. Also shown in Figure 5, item
14, is one of two voltage probes mounted on each tube at the loca-
tions indicated by A and B in Table 1. The voltage probes each
consist of a 1/2-inch "pig tail" of 0.010-inch-diameter Constantan
wire which is end welded to the nickel tube by electrical discharge.
The use of Constantan prevents appreciable variations in the re-
sistance of the voltage leads due to changes in tube operating tem-
perature.

C.   Test Facility and Instrumentation

A general view of the test facility from the front of the gage panel is shown in Figure 8, and Figure 9 shows a simplified schematic of the system. Appendix III contains complete hydraulic and electrical systems schematics along with designations of the more important equipment items and instruments.

The basic features of the facility may be described by referring to Figure 9. Electrical immersion heaters are used to heat the water in the reservoir tank to the test conditions; pumping the water through the mixing loop keeps the temperature uniform throughout the tank. During the tests, the introduction of pressure regulated nitrogen into the reservoir tank pumps the water upwards through the test section and into the receiver tank. The plumbing just upstream of the test tube entrance consists of a 12-inch straight run of one-inch-diameter guide tube (See item 3, Figure 5); ahead of this the flow turns 90 degrees in a "tee" fitting which mounts a thermocouple measuring the inlet flow temperature. For most of the tests, a 11-1/2-inch-long (29 diameters) segment of rough tube was inserted into the guide tube just ahead of the entrance section of the tube being tested. This additional entrance section, which has the diameter and roughness of the C-9 tube (See Table 1), was expected to improve the symmetry of the fluid velocity distribution at the test tube entrance. The water flow rate is controlled by combinations of settings of the reservoir-tank nitrogen regulator, the throttle valve, and the receiver-tank back-pressure regulator. Following the tests, the water is returned to the reservoir tank by pressurizing the receiver tank and venting the reservoir tank. The

system has provisions for maintaining the pressure above atmospheric pressure in all parts of the system; these permit operation at temperatures above 212°F. The tube heating is supplied through a 100 kva variable-tap-primary transformer with 2500 amperes capacity in the secondary circuit. Tube voltage-drop settings lower than those provided by the transformer are achieved by introducing an auxiliary resistance tube into the circuit, Cf. Appendix III, Fig. A-III-2. The electrodes on the test section and the mixing flange (see Fig. 5) are maintained at temperatures near that of the flowing water by means of electrical resistance heating tapes which are controlled by small variable transformers. The tapes are shown installed in Figure 7. Temperatures of the electrodes and the mixing flange are indicated by the output from thermocouples mounted on the respective metal parts.

Water flow rate is determined from measurements of the pressure differential between the reservoir and the throat of a calibrated venturi located at the reservoir exit. The differential pressures are monitored on one of several bellows-type differential pressure gages which can be connected to the venturi through selector valves, see Appendix III. The need for corrections due to differential head effects in the gage lines is eliminated by provisions for maintaining room temperature water in all vertical legs of the gage lines. Trapped air was bled from the lines prior to each test. In addition, horizontal lengths of line with volumes greater than that of the bellows chambers are located immediately adjacent to the venturi and tank fittings; this provision keeps heated reservoir water from being drawn into vertical gage lines when the starting or

stopping of the flow causes motion of the gage bellows.

The test-section pressure drop between the tube fittings (shown in Fig. 5) is measured by techniques identical to those described for the venturi pressure differential measurement. In this case, however, the column of water in the vertical test section, which forms a part of the gage circuit, was not necessarily at room temperature. For high temperature tests, the density difference between that of the water in the tube and the water in the rest of the gage circuit produces a small differential pressure at the gage under the no-flow condition. This effect was eliminated from the gage reading by flushing heated water from the reservoir through the test section prior to each test, stopping the flow, and adjusting the differential pressure gage to read "zero".

The electrical power supplied to the tube is measured by a wattmeter. A current transformer used to reduce the current and a potential transformer used to increase the potential bring the respective signals into the range of a standard wattmeter. A switch in the potential circuit permits the input to be taken either from voltage probes on the tube (see Fig. 5) or from similar probes mounted on the copper electrode blocks. Further redundancy in the power determination is provided by voltmeter and ammeter measurements. The complete power metering system is shown in Appendix III, Fig. A-III-2.

The bulk temperatures of the fluid entering and leaving the test section are monitored respectively by two immersion-type Chromel-Alumel thermocouples with the junctions fused into the bottom of glass wells, see Figure 10. The entrance thermocouple

is mounted in a ''tee'' with the glass well axis coincident with the tube axis. The junction is located approximately 12-inches upstream of the test tube entrance. The exit thermocouple, shown installed in Figure 7, is mounted in a similar manner with its junction approximately 1/2-inch downstream of the mixing chamber (see Fig. 5). The leads from the immersion thermocouples as well as the leads from the tube-wall thermocouples (discussed in Sec. III-B) are connected to copper wire extensions in a stirred ice-water bath. Each of the connections between thermocouple wire and copper wire is in a separate glass cell immersed in the bath. The copper extensions are connected into a switching network (see Fig. A-III-2, Appendix III) which is used to connect any of the eleven thermocouple circuits to a hand-balanced potentiometer-galvanometer. The switching network also provides a means for directly measuring the e.m.f. difference between any of the thermocouples and the outlet-water thermocouple.

D. Procedures

1. Test Operation

A series of 45 to 55 heat transfer tests was performed on each of four tubes. The test conditions for each series consisted of the combinations of 4 or 5 nominal water flow rates (0.20, 0.35, 0.60, 1.00 and 1.75 pounds per second), 4 nominal bulk fluid temperatures (80, 103, 149 and $290^\circ F$) and 2 or 3 heat flux rates in the range of 0.05 to 0.7 Btu per square inch-second. A set-up sheet prescribing the settings of the system needed to produce the desired test conditions was prepared for each test series. Prior to each test, the following operations were performed:

i) The reservoir water was preheated to the prescribed temperature and mixed.

ii) The electrodes and the mixing chamber on the test section were preheated to the computed local equilibrium temperature.

iii) The differential pressure gages for the test-section and venturi pressure-drop measurements (ΔP_{TS} and ΔP_v respectively) were selected; the respective gage lines and bellows chambers were bled free of air; and the gage indicators were adjusted to read "zero".

iv) The output voltage of the power transformer was set.

v) The nitrogen regulator on the reservoir tank was set to operating pressure, the back pressure regulator on the receiver tank was set, and the receiver tank pressure was brought up to this setting. For tests with water temperature less than the boiling point, the receiver tank

was simply vented to the atmosphere.

vi) The galvanometer indicator was set to read "zero" (using a special procedure described in Sec. III-D-2), and the potentiometer voltage was standardized.

The allowable test duration, limited by the capacity of the reservoir tank and the water flow rate, varied from 2 minutes 45 seconds to 15 minutes. The task of registering all of the necessary data in the short periods available was facilitated by the use of a dictating machine to record the data which were read aloud during the test. For the short duration tests, three operators were employed to read the various instruments in rapid succession. The principal operations during each test were as follows:

i) The remotely operated reservoir tank valve was opened allowing flow to start, and the throttle valve was adjusted to permit passage of the prescribed flow rate.

ii) The relays were closed bringing power to the test section.

iii) Following a delay during which approximately 10 percent of the total water supply was allowed to pass through the system and establish equilibrium conditions, the operators read in succession: the power metering instruments, the electrode and flange temperatures, each of the 10 differential temperatures (tube-wall and inlet-water minus outlet-water), the inlet-water temperature, two selected tube-wall temperatures, the pressure drops in the venturi and across the test section, and the pressures in the tube and in the reservoir tank.

iv) These readings were repeated if time allowed.

v) Power was cut off.

vi) Flow was shut down by the throttle valve.

vii) Zero readings on the differential pressure gages and the galvanometer were checked.

Following the test:

i) The water was chilled in the receiver tank if necessary for the succeeding tests.

ii) The water was returned to the reservoir tank.

iii) The data were recorded from the dictating machine onto a special data sheet showing the relative times at which the respective readings were taken.

2. Calibration

The three differential pressure recording gages (0-20, 0-100 and 0-300 inches-of-water) were calibrated in situ against manometers. The calibration system is shown schematically in Figure A-III-1 and pictorially in Figure 8. This system provides a means for nitrogen-purging the water out of the lines joining the manometer and the gage and out of the gage bellows chambers prior to calibration. Thus no spurious pressures are produced by unbalanced water columns. Nitrogen gas, regulated to selected pressures, is fed into the manifold connecting the high pressure sides of the manometer and the gage; the low pressure sides of each are vented to the atmosphere. The difference between the manometer and gage readings then provides the desired gage correction term. The more rugged, high level (0-25 and 0-50 psid) differential pressure gages

were calibrated against a 140-inch mercury manometer located in a
separate laboratory; the same techniques used in calibrating the
lower scale gages were used for the higher scale gages. Several
calibrations of the differential pressure gages were performed at
different times in the test program with no appreciable changes in
the gage corrections being observed.

The discharge coefficient for the flow metering venturi was
determined by operating the flow system in the normal manner ex-
cept that the flow was discharged into a weighing tank instead of
the receiver tank. Pressure differentials were measured by the
calibration-corrected gages used in the tests. Figure 11 presents
the calibration data as a dimensional form of the square of the dis-
charge coefficient plotted against $\dot{w}/\mu$ which can be thought of as
a dimensional form of the Reynolds number. In this term $\dot{w}$ is the
mass rate of fluid discharge and μ is the fluid viscosity. The curve
drawn through the points in Figure 11 gives the discharge coefficient
used for flow rate data reduction. The strange kink in this curve
at $\dot{w}/\mu$ equals 3000 feet is thought to be caused by a flow-separation
region occurring near the first entrance; this first entrance is
shown in the sketch of the venturi profile in Figure 11. As Reynolds
number is increased to the observed critical value, this separated
region is assumed to extend into the venturi throat thus partially
choking the passage and decreasing the discharge coefficient. Whether
or not this explanation is the correct one is of little consequence to
the present experiments since all that matters here is that the dis-
charge coefficient obtained is Reynolds number correlated, and this
is demonstrated to be the case by the agreement shown in Figure 11

between calibration measurements at differing temperatures, i.e.,
differing fluid viscosities. Note that cavitation effects are unlikely
since the pressure in the venturi throat was seldom, if ever, below
50 psia in the calibration tests.

A step-up transformer in the wattmeter potential circuit was
used to increase the voltage signal from potential drop in the heated
test-section by nominally a factor of 10. This novel use of an instru-
ment transformer required special care to avoid errors due to im-
pedances in the measuring circuit. A check by oscilloscope of the
transformer under load conditions showed the phase shift through
the transformer to be almost exactly 180 degrees indicating that the
transformer coil impedances are purely resistive. Thus the effec-
tive potential ratio across the transformer can be expressed with
good approximation by

$$\frac{\Delta E_2}{\Delta E_1} = n \left[1 - \frac{R_2 + R_{L2} + n^2 (R_1 + R_{L1})}{R_m} \right]$$

where n is the turns ratio and R_1, R_2, R_{L1}, R_{L2} and R_m are respec-
tively the resistances of the transformer primary coil, the trans-
former secondary coil, the leads from the transformer to the tube,
the leads from the transformer to the wattmeter and the wattmeter
potential coil. The wattmeter coil resistances were given by the
manufacturer and the other resistances were measured by the use
of a Kelvin bridge. The contribution to the transformer potential
ratio from the combined-resistance correction term ranged from
2 to 5 percent depending on the wattmeter scale being used. The
transformer potential ratio computed by the foregoing equation was

confirmed by the results of several auxiliary tests in which standard alternating-current (AC) instruments were used to measure the ratio directly while the transformer was subjected to loads similar to those used in the experiments.

The wattmeter was calibrated against standard direct-current (DC) instruments over the range of voltage and current combinations encountered in the experiments. Correction charts were prepared for use in the data reduction; none of the corrections exceeded 2 percent. Additional calibrations of the wattmeter and potential transformer combination against standard AC instruments under selected load combinations further substantiated the principal calibration techniques.

Auxiliary checks on the tube power measurement were provided in each test by redundant measurements with a voltmeter and an ammeter; these instruments were also calibrated against standard instruments. Oscilloscope measurements showed the power factor for the experimental tubes to be 1.00; this fact permits the product of the current and the voltage drop to be used directly as a measure of heating power. It was also observed that the tube resistance computed as the quotient of the AC voltage drop and the AC current agreed with DC tube resistance measurements (Cf. Appendix II-A). This observation tends to confirm computations which indicate that the AC phenomena of hysteresis-heating and skin-effect are negligible for the nickel tubes employed in the experiments.

Particular care in calibrating the thermocouples and the thermocouple e.m.f. measuring system was required in order to achieve the desired accuracy in the C_H determinations. The

calibration of the e.m.f. measuring system will be discussed first.
All of the tube-wall thermocouple wires are matched in length so
that their resistances are equal. In addition, matching resistors
are connected into the switching network, Cf. Fig. A-III-2, such
that the impedance presented to the potentiometer is the same whether
e.m.f. is being read from tube-wall thermocouples or the water-
immersion thermocouples or any of the difference combinations.
It is then possible to minimize the effects of stray "thermal e.m.f."
generated in the potentiometer-galvanometer circuit in the following
way: First, the potentiometer battery is switched out of the circuit
and across an external resistor which keeps the current drain on
the battery essentially uninterrupted. Then a resistance, which
matches the thermocouple network impedance but contains no e.m.f.
source, is switched across the potentiometer input posts in place of
the thermocouple network. In this state the potentiometer-galvanome-
ter circuit is complete with essentially the same resistances as exist
in normal operation, but the circuit contains only the stray e.m.f.'s.
Under these conditions, the galvanometer indicator is set to read
zero; if the same null position is used during the tests, the effects
of the stray e.m.f.'s are then automatically subtracted. Finally the
battery is switched back and the thermocouple system is reconnected.
The absence of stray e.m.f.'s in the switching network was demon-
strated by placing one of the hot junctions, normally used to measure
water temperature, into the same ice bath with the corresponding
cold junction; the measured e.m.f. in this thermocouple circuit,
which includes the switching network, was nil. The potentiometer
itself was calibrated against a higher-order-of-accuracy standard

potentiometer and was shown to have negligible error. Since the
thermocouple circuit impedance is large, approximately 320 ohms,
compared to the potentiometer impedance, it is permissible to use
the galvanometer as a deflection instrument over a small range.
This facilitates rapid successive readings of the differential e.m.f.'s.
A calibration of the galvanometer deflection showed a linear relation
to exist between the imposed e.m.f., unbalanced by the potentiometer,
and the deflection. The deflection coefficient is 7.7 microvolts per
millimeter over the allowable deflection range of $\pm$ 10 millimeters.
A final check of the thermocouple e.m.f. measurement system was
provided by each test wherein certain of the thermocouple e.m.f.
differences were obtained by taking readings from the individual
thermocouples and subtracting the results as well as by reading a
direct electrical difference in e.m.f.; the agreement found was
within the limits of the combined reading accuracies in all cases.

The glass-well immersion thermocouples were both cali-
brated by inserting them together with a standard mercury-in-glass
thermometer into a controlled furnace which was operated at tem-
peratures from 70 to $350^{\circ}F$. A comparison of the thermocouple
e.m.f.'s and the thermometer readings provided data used in com-
puting both the thermoelectric power of the exit-water thermocouple
and the isothermal difference in e.m.f. between the two immersion
thermocouples as functions of temperature. In addition, the abso-
lute e.m.f. level versus temperature for the inlet-water thermo-
couple was provided by the results of this calibration. The use of
these three functions to convert the thermocouple e.m.f.'s to tem-
peratures is discussed in Sec. III-D-3.

A series of nearly-isothermal-flow calibration tests was performed for each tube; these tests were carried out in the same way as the heat transfer tests except that no heating power was used. Each of the combinations of water temperature and flow rate, i.e. of Prandtl and Reynolds numbers, used in the hot-test series was included in this calibration series. The isothermal tests supplied the following information:

i) Test section pressure drop and flow rate from which $C_F\{Re\}$ for isothermal conditions was determined.

ii) The rise in the bulk water temperature due to frictional heating was obtained from the high flow rate calibration tests. This small energy rise, which is due primarily to the flow resistance of the outlet mixing-chamber, agrees with the pumping work computed from the estimated mixing chamber pressure drop.

iii) A spurious heat loss from the water was observed and evaluated. In these isothermal calibration tests the electrodes and the exit mixing flange were maintained at temperatures very near to the water temperature so that heat exchange at these points was assumed negligible; furthermore, the natural convection and radiation losses to the atmosphere are computed to be of only secondary importance. Nevertheless, at the highest water temperature (290°F) a very small but measurable "spurious heat loss" was observed. This heat loss is assumed to have the same magnitude in the corresponding hot tests. The difference between the surface temperatures of the tube and its attachments and the temperature

of the surroundings is nearly the same for the hot tests as for the corresponding calibration tests.

iv) The isothermal e.m.f. differences between the tube-wall thermocouples and the outlet-water thermocouple were established. Corrections to these measurements, required because of water temperature changes caused by frictional heat gains and spurious heat losses (see items ii and iii), were readily determined and applied.

The e.m.f.-temperature dependences of all of the wall thermocouples on any given tube are nearly identical. This should be expected since the thermocouple wires were taken successively from the same spools. The thermocouples for one of the tubes were made from wire coming from different spools than those used for the other tube-wall thermocouples. The e.m.f. at a given temperature for the thermocouples coming from the odd spools was considerably different than the e.m.f. of the others; this difference amounted to as much as 75 microvolts at some temperatures. Also the differences in isothermal e.m.f. between any of the tube-wall thermocouples and the glass-well thermocouples were as much as 100 microvolts.

In addition to the standard, non-heating, calibration test series, a set of calibrations was performed for each tube with conditions similar to those described in the previous paragraph except that temperatures of the electrodes and of the exit flange were purposely adjusted to various values differing from the water temperature. From the results of these tests it is possible to ascertain corrections for the effects of the small temperature mismatches which are unavoidable in the heat transfer tests.

3. Data Reduction

A major part of the data reduction was accomplished with a digital computer; consequently the reduction methods were devised to best utilize simple step-wise computer procedures. The over-all reduction was performed in three phases: preliminary, computer and final. Frequent reference will be made in this section to Appendix IV wherein certain of the reduction formulas are developed and the computer program formulation is presented.

In the preliminary reduction the following operations were performed on the original data:

i) Redundant measurements were checked for consistency, and in cases where more than one set of data on a given run were available, the best set was selected primarily on the basis of the smallest variations in tube power readings and secondarily on the closeness of the temperature match between the electrodes and the local bulk water.

ii) Gage calibration corrections were applied to the tube and venturi pressure drop measurements and the resulting values were converted to standard units.

iii) The electrical power readings taken before and after the main thermocouple readings were averaged; calibration corrections were applied; and the result was converted to standard units.

iv) The thermocouple e.m.f. corrections accounting for the frictional heating and the heat gain or loss from the electrodes or mixing flange were computed and

applied to the various differential e.m.f. measurements.
The method for arriving at these corrections is described
in Appendix IV-A.

The data read into the computer consist of corrected and converted values for test section pressure drop (ΔP_{TS}), venturi pressure drop (ΔP_v), tube power at the probes (W_p), inlet-water and outlet-water thermocouple e.m.f.'s (E_0, E_{11}), differential e.m.f. for the inlet-water and outlet-water thermocouples (as corrected in item iv above) ($\Delta_0 E_{11T}$), differential e.m.f.'s for each of the tube-wall thermocouples and the outlet-water thermocouple (as corrected in item iv above)($\Delta_x E_{11T}$), and test-section voltage drop and current (E_{TS}, I). The use of these data in the computer program and the computer operations are discussed in Appendix IV-C. Only the more important and/or unique steps in the computer phase of the data reduction will be discussed herein.

The flow rate was determined by use of the venturi calibration curve, the density of the fluid in the venturi (implied by E_0), and the venturi pressure drop (ΔP_v). The friction coefficient can be expressed in the form

$$C_F = K_1 \left[\frac{\rho \Delta P_{TS}}{\dot{w}^2} - \gamma \right] \tag{71}$$

where the constant K_1 contains various dimensional conversion factors in addition to the values of the diameter and the length of the roughened test section, and the constant $\gamma \equiv \rho (\delta \Delta P_{TS})/\dot{w}^2$ includes small corrections to the measured pressure drop (ΔP_{TS}) to account for 1) differences in dynamic pressure at the two smooth surface measuring stations, 2) the smooth pipe friction on the 1/2-inch-sections

adjacent to the measuring stations and 3) the small sudden-contraction and sudden-expansion pressure losses associated with the fact that the rough tube diameter and the diameter of the smooth measuring regions are not identical.

In order to obtain values of C_H, Re, and Pr based on local conditions, it is necessary to establish the stationwise value of the heat flux ($\dot{q}_o$) in terms of the integrated heat flux given by the measurement of test-section power at the probes (W_P). The value of the local mixed-fluid temperature (T_L) then depends on the total heat released up to the particular measuring station. In theory, the determinations of local $\dot{q}_o$ and local T_L result in inseparable, integral equations. The value of $\dot{q}_o$ depends on the local resistivity of the tube wall which, in turn, depends on the effective local wall temperature. This effective wall temperature, taken as the temperature in the center of the wall, is determined by 1) the local T_L, 2) the heat transfer film conductance (h) of the fluid, and 3) the thermal conductivity of the wall. Further the thermal conductivity must be evaluated at the local wall temperature. In treating this problem, the complete equations containing the various interactions were first put into dimensionless form. Then by evaluating the maximum excursions of the various dimensionless coefficients in terms of the parameters of these experiments and by expanding the various functional forms in Taylor's series, it was possible to produce linearized, separated expressions for $\dot{q}_o\{x\}$ and $T_L\{x\}$. Only first order corrections were retained to account for the various interactions. Since the correction terms are small and since the truncations of the series expansions restrict their use to conditions near to those observed

in the present experiments, the resulting expressions are of limited interest. Because of this, the complete derivation of the results will not be presented; only the results themselves will be shown. The resulting expressions have the form

$$\frac{W_{TS}}{\pi DL \, \dot{q}_{ox}} = M_x \left[1 + B_x \left(\frac{Q_x}{M_x^2} \right) + \Gamma_x \left(\frac{N_x}{M_x} \right) \right] \tag{72}$$

and

$$\frac{T_{11} - T_{Lx}}{T_{11} - T_0} = M_{xx} \left[1 - \frac{B_x (x/L)}{2(1 + \Gamma_x)} - \frac{\Gamma_x S_x}{(1 + \Gamma_x)} \right] \tag{73}$$

where subscript x refers to a particular local thermocouple station and W_{TS} is the power released in the test section, L is the length of the heated test section, T_{11} is the temperature of the mixed outlet water, T_0 is the temperature of the mixed inlet water and T_{Lx} is the mixed-mean water temperature at the thermocouple station. An equation similar to equation 72 relates the power measured at the probes (W_P) to W_{TS}. In these expressions, M_x, N_x, Q_x, M_{xx} and S_x represent various definite integrals depending only on the variation of wall thickness with longitudinal station and on the particular thermocouple station. For the limiting case of uniform wall thickness:

$$
\begin{aligned}
M_x &= 1.0 \\
N_x &= 0.0 \\
Q_x &= 1/2 - x/L \\
M_{xx} &= 1 - x/L \\
S_x &= 0.0
\end{aligned}
\tag{74}
$$

For the simple case of the present tubes where tube wall thickness has a weak linear dependence on longitudinal station, thickness is expressed

$$t\{x/L\} = t\{0\}\left[1 + \alpha (x/L)\right] \tag{75}$$

where α is constant. Using equation 75, the various definite integrals are evaluated to give algebraic expressions in terms of thermocouple station (x/L). The factors B_x and Γ_x involve the properties of the tube and the conditions of the test. The term

$$B_x \equiv \frac{(d\rho_e/dT)}{\rho_e \{T_{wx}\}} (T_{11} - T_0) \tag{76}$$

is determined with adequate accuracy from a knowledge of the resistivity of the wall material (ρ_e), a rough estimate of the wall temperature (T_{wx}) in terms of the inlet water temperature, and the measurement of the temperature rise of the water passing through the test section $(T_{11} - T_0)$. The term

$$\Gamma_x \cong B_x (D/4L) (1/\tilde{C}_H) \tag{77}$$

contains the first order correction for the effect of the error caused by estimating the local effective wall temperature to be equal to the local mixed fluid temperature. Hence Γ_x must depend on an approximation for the heat transfer coefficient noted by $\tilde{C}_H$. A crude preliminary estimate of $\tilde{C}_H$ in terms of the conditions of the test and the tube being used suffices for the determination of Γ_x.

The limiting cases are simple in form and may be of some general interest. For the case of uniform wall thickness, the list of item 74 may be substituted into equations 72 and 73. The remaining

correction terms, B_x and Γ_x, show the effects of the longitudinal variation in $\dot{q}_O$ caused by the rise in fluid temperature, hence by the rise in wall temperature and in resistivity. A second limiting case comes from assuming that wall resistivity is independent of temperature, i.e. $d\rho_e/dT = 0$. This gives B_x and Γ_x both equal to zero. Thus for a uniformly tapered wall equations 72 and 73 reduce to

$$\frac{W_{TS}}{\pi DL \dot{q}_{ox}} = M_x = \frac{1 - \alpha/2}{1 - \alpha(x/L)} \tag{78}$$

and

$$\frac{T_{11} - T_{Lx}}{T_{11} - T_0} = M_{xx} = 1 - \frac{(x/L)[1 - (\alpha/2)(x/L)]}{[1 - \alpha/2]} \tag{79}$$

where α is defined by equation 75.

The correction terms in equations 72 and 73 are small, less than 8 percent, for the conditions of the present experiments where $(d\rho_e/dT)/\rho_e$ is of the order of 0.003 $(^\circ F^{-1})$ and α is of the order of 0.08. Obviously in cases where variations in the wall thickness or the thermal coefficient of resistivity is greater than the respective values encountered in these experiments, the corrections will be greater and, in addition, retention of more correction terms may be necessitated.

Using then the simplified relations for $\dot{q}_{ox}$ and T_{Lx} in equations 72 and 73 respectively, the local values of C_H, Re and Pr were generated from the experimental data as part of the computer operation. Values of Pr, μ and c_p were determined from the known thermal dependencies of these fluid properties. The formula used to compute the local Stanton number was

$$C_{Hx} = \frac{(\pi/4)D^2 \dot{q}_{ox}}{\dot{w} \, c_p \, \Delta T_{fx}}$$

(80)

The wall-to-mixed-fluid temperature difference (ΔT_f) was derived from the measured and corrected e.m.f. difference between the wall thermocouple and the outlet-water thermocouple $(\Delta_x E_{11})$. By the methods described in Appendix IV-A, this e.m.f. was converted to the corresponding temperature difference $\Delta_x T_{11}$. By the preliminary data reduction, $\Delta_x T_{11}$ already contained corrections for 1) heat exchange between the fluid and the exit electrodes and between the fluid and the mixing flange, 2) heat added to the fluid by frictional heating and 3) spurious heat losses from the fluid. Thus there remained for the machine operation only to add the temperature rise due to electrically generated heat added to the fluid between the wall thermocouple location and the exit and to subtract the temperature drop in the wall of the tube in order to obtain ΔT_f, that is,

$$\Delta T_{fx} = \Delta_x T_{11} + (T_{11} - T_{Lx}) - \Delta T_w$$

(81)

The fluid temperature rise term $(T_{11} - T_{Lx})$ in equation 81 was determined from equation 73 once the total fluid temperature rise $(T_{11} - T_0)$ was established from the $\Delta_0 E_{11T}$ measurement. The expression used to compute wall temperature drop for use in equation 81 is developed in Appendix IV-B and is written

$$\Delta T_w = \Delta T_{wp} \left[1 - \frac{1}{6}(t/R) + \left(\frac{\alpha}{2} - \frac{\beta}{6}\right) \Delta T_{wp} \right]$$

(82)

where

$$\Delta T_{wp} \equiv \dot{q}_o t / 2 \, k \{ T_{ow} \} \tag{83}$$

$$\alpha \equiv \frac{dk/dT}{k \{ T_{ow} \}} \tag{84}$$

and

$$\beta \equiv \frac{d\rho_e/dT}{\rho_e \{ T_{ow} \}} \tag{85}$$

The outside wall temperatures used to evaluate $k \{ T_{ow} \}$ and $\rho_e \{ T_{ow} \}$ in equations 83, 84 and 85 were obtained directly from the wall thermocouple e.m.f.'s. For consistency, equation 82 in its entirety was applied to all tubes even though it is recognized that, for the case of the roughest tube, the small correction terms are probably overwhelmed by uncertainties in the effective wall drop caused by disturbances in the electrical current flux and uneven cooling at the liquid wall.

As part of the computer program, equations 81 and 80 were used to derive ΔT_{fx} and C_{Hx} respectively at each of the nine wall thermocouple locations. The first step in the final data reduction was to plot the individual C_{Hx} values as a function of thermocouple location. These plots display the degree to which the heat transfer coefficients are independent of circumferential location and the degree to which fully established conditions were obtained.

The computed average of the three C_{Hx} values at the farthest downstream thermocouple station, $\overline{C}_{H7}$, was used as the pertinent Stanton number from each test. Since it was not always possible to precisely match the mixed fluid temperature at the final thermocouple station to the nominal temperature an adjustment was applied to $\overline{C}_{H7}$ in order to correct for the deviation of the local Reynolds number and Prandtl number from the

nominal conditions. Application of this correction was done as part of the final data reduction. The correction was computed by means of the following approximation technique. It was first assumed that the expression

$$C_H = K \, Re^n \, Pr^m \tag{86}$$

is valid over a small range of Pr and Re with K, m, and n as constants. Then, since nominal flow rate was adequately achieved in the tests, the variation of Re from the nominal value is given solely by the variation of viscosity,

$$\frac{d\,Re/dT}{Re_N} = -\frac{d\mu/dT}{\mu_N}$$

Applying this to the differential variation of equation 86 gives

$$\frac{dC_H/dT}{C_{HN}} = \frac{m\{Re_N, Pr_N\}}{Pr_N} \, \frac{dPr}{dT} \, \{T_N\}$$

$$-\frac{n\{Re_N, \, Pr_N\}}{\mu_N} \, \frac{d\mu}{dT} \, \{T_N\} \tag{87}$$

where the subscript N refers to the nominal local bulk temperature and hence to the nominal local Re and Pr. Assuming that $(dP_r/dT)/Pr$ and $(d\mu/dT)/\mu$ are also constant for a small range of the variables, the average heat transfer coefficient at the nominal bulk temperature $(\overline{C}_H)$ can then be written

$$\overline{C}_{HN} = \overline{C}_{HE} \left[1 + \left(\frac{m\{Re_N, Pr_N\}}{Pr_N} \, \frac{dPr}{dT} \, \{T_N\} \right. \right.$$

$$\left. \left. -\frac{n\{Re_N, Pr_N\}}{\mu_N} \frac{d\mu}{dT} \, \{T_N\} \right) (T_N - T_E) \right] \tag{88}$$

where the subscript E here denotes the measured value and the subscript N refers to the nominal value. The values of $(dPr/dT)/Pr$ and $(d\mu/dT)/\mu$ are established for each of the nominal test temperatures from semi-log plots of the respective fluid properties versus temperature. The exponents m and n are adequately determined from slopes taken on log-log plots of the uncorrected C_H results.

The last operation of the final data reduction phase was to plot the downstream-station C_H values, adjusted to the nominal test temperature, against the wall-to-mixed-fluid temperature difference (ΔT_f). In general there were three points to each plot corresponding to results from three tests at fixed Re and Pr values but at differing heat flux rates. On each plot a straight line, estimated to best relate the three points, was drawn with the restriction that the slope of the line be non-negative; that is, if C_H appeared to decrease with increasing ΔT_f, the best zero-slope line was drawn. The intercept of the selected straight line with the ordinate $(\Delta T_f = 0)$ was then taken to represent the C_H value that would be obtained by using a fluid with constant properties and by maintaining thermally and hydrodynamically fully established flow conditions. Such an idealized C_H value was determined for each tube at each of the nominal Pr and Re combinations. This set of C_H values, taken together with the corresponding C_F values from the non-heating calibration tests, then constitutes the principal result of the experiments.

E. Confidence Limits Evaluation

The purpose of this section is to delineate and discuss the major sources of error or uncertainty in the C_F and C_H determinations of these experiments. The definition of the uncertainty limits will be of importance in comparing the present results with those of other experiments and with various theoretical models.

The evaluation of error limits must be based to some extent on the experimenter's judgment; hence such an evaluation is necessarily somewhat subjective. Nevertheless, an attempt has been made to set limits which are compatible with the observed degree of agreement among redundant measurements and the degree of reproducibility among repeated measurements. The error limits discussed in this section are taken to represent a high confidence coefficient, say 95 percent, for the reported values of the respective measurements. By way of definition, this means that the interval, formed by attaching the given error limits to the value of a parameter determined by the methods of these experiments, is expected to contain the true value of the parameter 95 percent of the time. The 95 percent value is stated here only for the sake of argument. It has the qualitative meaning that the estimated error limits are set wide enough to contain essentially all of the values obtained from a particular operation repeated many times. Another qualitative way of stating this is that the prescribed limits are expected to be two to three times as wide as that confidence interval which would be expected to contain the true value 50 percent of the time.

1. Friction Coefficients

The equation used for determination of the friction coefficients

can be expressed

$$C_F = K_1 \frac{D^5}{L_R} \left[\frac{\rho_{av} \Delta P_{TS}}{K \rho_o \Delta P_V} - \gamma \right] \tag{89}$$

where K_1 is a dimensionless constant, L_R is the length of the rough tube between the pressure taps, and the group $\gamma \equiv \rho_{av}(\delta \Delta P_{TS})/\dot{w}^2$ is a constant correction to the pressure drop accounting for the effects discussed in connection with equation 71 in Section III-D-3. The coefficient K is the venturi discharge coefficient herein defined so that

$$K \rho_o \Delta P_V \equiv \dot{w}^2 \tag{90}$$

In the non-heating tests used for the C_F determinations, the average fluid density in the test section (ρ_{av}) is the same as the density of the fluid passing the venturi (ρ_o). Hence the density cancels out of equation 89, and the uncertainties in the C_F determination can be ascertained from the uncertainties in the remaining measurements, D, L_R, ΔP_{TS}, K, and ΔP_V and in the computed correction, γ. The errors will be separated into two groups defined as follows: The systematic errors are those that are fixed for the set of tests on a given tube, and the random errors are those involved in parameters that must be re-evaluated in each test. The effects of the random errors are reduced by smoothing the final results in the $C_F\{Re\}$ plot; whereas the systematic errors are not so reduced.

The differential gages used for the measurements of ΔP_V and ΔP_{TS} were all calibrated several times during the test program with no time-dependent changes in the calibrations being observed. Further, in cases where deviations from the standard manometers existed, corresponding corrections were applied in the data reduction.

Systematic errors in the differential pressure measurements due to density variations in the gage lines were eliminated by the design of the equipment, Cf. Sec. III-C. The success of this design was indicated by the absence of gage zero-shift following low flow rate tests wherein these effects would have been most noticeable had they existed. Thus the primary errors remaining in the pressure-drop measurement are assumed to be limited to normally distributed reading errors which are taken as $\pm$ 0.4 percent of the gage full-scale level in all tests except for certain of the tests at the highest flow rate (1.75 lb per sec). For the high-flow-rate tests, the direct reading gages were used and a slight vibration existing in the system limited the reading accuracy to approximately $\pm$ 0.8 percent of full scale.

The largest value of the pressure-drop correction constant (γ) applied to any of the tubes amounted to 7 percent of C_F. Assuming that this roughly estimated correction could be in error by $\pm$ 10 percent, a possible systematic error of 0.7 percent could have been introduced to the C_F determination from this cause. This error source is negligible for the smooth tube. Since no prediction can be made concerning the statistical distribution of the error in the γ determination, this error will be combined with the other systematic errors by adding it directly rather than by using the root mean square combination used for errors assumed to be normally distributed.

The error in the mean curve used for the venturi discharge coefficient (K) is taken as $\pm$ 1.5 percent, this being judged from the plot of the venturi calibration data, Cf. Fig. 11. This error in K, which depends on combinations of random instrument reading errors

incurred during the venturi calibration tests, is assumed to be normally distributed. Since the same mean venturi calibration curve is selected for use in all tests, the error in K must be treated as a systematic error.

Another source of systematic error in the C_F determination is the measurement of the so-called volumetric diameter. As discussed in Section III-B, this diameter was determined by three independent means all of which gave agreement within their respective error limits. Of these methods, the measurement of the outside diameter of the sanded mandrel with corrections for the mean sand grain protrusion was selected as having the smallest uncertainty and was used to establish the volumetric tube diameters. The adjustment for the mandrel sand grain volume, taken to be 1/2 of the mean grain diameter, was subtracted from the mandrel diameter giving the estimate of volumetric internal diameter shown in Table 1. The principal uncertainty in rough tube volumetric diameter is taken as $\pm$ 1/3 of the grain volume correction or the maximum variation in mandrel measurements, whichever is larger. By this scheme the largest diameter uncertainty (Tube A-4) is $\pm$ 1.3 percent. The error in the smooth tube internal diameter is taken as $\pm$ 0.001 inch or $\pm$ 0.3 percent. Variations in tube diameter due to thermal expansion and pressure strain were computed to be negligible for the conditions of the experiments. The error in diameter determination is assumed to be normally distributed so that, if an error interval for D^5 of $\sqrt{5}$ times the error interval for D is used, the same confidence coefficient is maintained.

The percentage error in the length measurement is negligible in comparison with other errors in the C_F determination.

The combined systematic error in C_F becomes

$$\%\delta C_{F \text{sys.}} = \pm ([5(\%\delta D)^2 + (\%\delta K)^2]^{\frac{1}{2}} + 0.07[\%\delta\gamma]) \qquad (91)$$

where the operator ($\%\delta$) indicates that the variation of the operand is expressed as a percentage of its mean value. The largest systematic error is thus computed for the roughest tube (A-4) as follows:

$$\%\delta C_{F \text{sys.}} (A-4) = \pm ([5(1.3)^2 + (1.0)^2]^{\frac{1}{2}} + 0.07[10.0] = \pm 4.0$$

The combined random error is written

$$\%\delta C_{F \text{ran.}} = \pm[(\%\delta \Delta P_{TS})^2 + (\%\delta \Delta P_v)^2]^{\frac{1}{2}} \qquad (92)$$

The percentage error in the pressure drop measurements depends on the proportion of full scale registered by the gages and upon which gages were used. The poorest combination of readings used in these tests corresponds to $\%\delta P_{TS} = \pm 4.1$ and $\%\delta P_v = \pm 2.5$. This yields for the maximum random error encountered,

$$\%\delta C_{F \text{ran.}} = \pm 4.8$$

Except for three cases out of the 72 combinations of tube, flow rate, and bulk temperature in the complete set of isothermal C_F tests, reading errors in ΔP_{TS} and ΔP_v were both less than ± 2.5 percent for which

$$|\%\delta C_{F \text{ran.}}| \leqslant 3.5$$

As can be seen in the C_F {Re} curves presented in Figure 12, the

experimental points do fall within a band of approximately $\pm$ 3.5 percent about the mean curves, thus corroborating the above analysis. Further, since C_F is a weak function of Re, the shape of the smoothing curve is readily discerned, and it is assumed that the smooth curve drawn in Figure 12 represents an averaging process. Thus considering the random error associated with each of the data points and considering the number of points in a given region contributing to the local definition of the mean curve, it is estimated that the random error associated with the smoothed curves is only approximately $\pm$ 1.0 percent.

This random error for the curves is combined with the systematic error determined for each tube to yield the total estimated percentage error in the final $C_F\{Re\}$ functions. The estimated uncertainties in C_F are thus computed for each tube as:

Tube E-3 (smooth)	$\pm$ 2.5%
D-3	$\pm$ 3.4%
C-9	$\pm$ 3.6%
A-4	$\pm$ 4.2%

2. Heat-Transfer Coefficients

In these experiments, C_H is determined from

$$C_{Hx} = \frac{(\pi/4) \, D^2 \, \dot{q}_{ox}}{\dot{w} \, c_p \, [\Delta_x T_{11} + M_{xx} \Delta T_c - \Delta T_{wx}]} \tag{93}$$

where $[\Delta_x T_{11} + M_{xx} \Delta T_c - \Delta T_{wx}]$ is the wall-to-mixed-fluid temperature difference (ΔT_f) with $\Delta_x T_{11}$ as the measured temperature difference between the outside tube wall and the exit fluid, $M_{xx} \Delta T_c$ as the approximate temperature rise in the fluid between the wall-thermocouple station and the exit (Cf. equation 73), and ΔT_{wx} as the local temperature

drop through the wall. The term ΔT_c is identically $(T_{11} - T_0)$. The tube wall thermocouples are placed sufficiently far from the electrode blocks that the effects of end-conduction of heat along the tube wall introduces negligible error into the determination of C_H by equation 93. This conclusion is discussed in Appendix V. For purposes of determining the principal C_H error in equation 93, errors in $M_{xx} \Delta T_c$ are negligible with respect to errors in $\Delta_x T_{11}$; ΔT_{wx} is adequately approximated by $\dot{q}_{ox} t_x / 2k$, and the error contributions from measurements of the fluid density and the tube length are negligible. Note, the use of subscript x will be dropped for the remainder of this section when the meaning is clear without it. Making the above mentioned allowances, equation 90 can be written

$$\dot{w} = \rho_0^{1/2} [K \Delta P_v]^{1/2} \tag{94}$$

and equation 72 can be written

$$\dot{q}_o = \frac{K_2}{L} [W_P / D] \tag{95}$$

where K_2 is a dimensionless constant. Then using equation 95 in the preceding approximation for ΔT_w,

$$\Delta T_w = \frac{K_2}{2L} [W_P t / Dk] \tag{96}$$

Also from the definition of the thermoelectric power (e), one can write

$$\Delta_x T_{11} = \Delta_x E_{11} / e \tag{97}$$

Using the simplifying assumptions discussed above, substituting equations 94, 95, 96 and 97 into equation 93, taking the reciprocal and

rearranging, one obtains

$$\frac{1}{C_H} = K_3 \frac{(K\Delta P_v)^{1/2}}{D} \left[\frac{\Delta_x E_{11}}{e\ W_P} - \frac{K_2}{2L} \left(\frac{t}{Dk}\right) \right] \qquad (98)$$

where K_3 is another dimensional constant. A differentiation of the logarithm of equation 98 reveals that percentage errors in the heat transfer coefficients ($\%\,\delta C_H$) can be induced independently from any of the following percentage errors:

$$
\begin{array}{ll}
1/2\%\,\delta K & (1+\zeta)\%\,\delta e \\[4pt]
1/2\%\,\delta\Delta P_v & (1+\zeta)\%\,\delta W_P \\[4pt]
(1-\zeta)\%\,\delta D & \zeta\%\,\delta t \\[4pt]
(1+\zeta)\%\,\delta\Delta_x E_{11} & \zeta\%\,\delta k
\end{array} \qquad (99)
$$

where

$$\zeta \equiv \frac{\Delta T_w}{\Delta T_f} \cong \frac{2c_p t}{\pi D^2} \frac{\dot{w}\ C_H\{\epsilon/D,\ Re,\ Pr\}}{k\{T\}} \qquad (100)$$

It is noted that the ratio of the temperature drop in the wall to temperature drop in the fluid (ζ) serves to amplify the effect of most of the error sources involved in the experimental method used. For the most sensitive conditions of the high roughness (high C_H) and high flow rate, ζ equals 0.45. In addition to the eight error sources listed as expression 99, three sources of uncertainty in the results will be treated separately in terms of their direct effect on the final C_H values reported for the isothermal, fully developed conditions. These additional uncertainties stem from 1) an observed small discrepancy between the electrically and calorimetrically measured power, 2) an observed circumferential variation in heat transfer coefficient at the separate thermocouple points, possibly due to local

variations in wall thickness and local variations in flow conditions, and 3) an observed fall-off in heat transfer coefficient with longitudinal position indicating that the heat transfer conditions may not be quite fully established.

The error terms $\%\delta K$, $\%\delta P_v$ and $\%\delta D$ have been discussed in connection with the C_F error analysis. The term $\%\delta\Delta P_v$ is a reading error varying from 0.8 to 2.5 percent, depending on the gage being used for the $\dot{w}$ determination.

Considering the errors involved in the determination of ΔT_f, it is first noted that errors due to effects such as heat conduction along the thermocouple wires, spurious heat losses from the fluid, and frictional heat gains to the fluid are essentially canceled out by the technique used for calibrating the wall thermocouples against the outlet-water thermocouple in the non-heating tests. In addition, small corrections made for heat exchange at the electrodes during the hot tests are expected to negate this heat exchange as a source of error. An error implied in the ΔT_f determination by the small observed discrepancy between the electrically and calorimetrically determined power measurements will be discussed separately. Oscilloscope measurements revealed alternating-current (AC) e.m.f's of the order of 10 mv (rms) to be superposed on the direct-current (DC) e.m.f.'s in the thermocouple network. A special test was performed in which a signal generator was used to reproduce the observed AC voltage in the network while the thermocouple junctions were held at fixed temperatures. No net change in the galvanometer deflection due to the AC signal occurred even when the impressed AC voltage was changed from zero to three times the AC e.m.f.

prevalent in the experiments. Thus it is assumed that no errors in the thermocouple measurements were produced by the presence of the AC voltages. This conclusion is supported by Allen's investigation (Ref. 11, p. 208) of possible spurious AC effects on thermocouple measurements made under similar circumstances.

Four sources of error in the $\Delta_x E_{11}$ determination are significant. The thermocouple data reduction in Appendix IV-A gives

$$\Delta_x E_{11} = \Delta_x E_{11T} - \delta_x E_{11}$$

where $\Delta_x E_{11T}$ is the e.m.f. measured in the test and $\delta_x E_{11}$ is the same value measured during the non-heating calibration tests. The error in individual readings of the potentiometer-galvanometer is taken as $\pm$ 3 μv; this constitutes the principal error in the $\Delta_x E_{11T}$ measurement. Since $\delta_x E_{11}$ was determined for each thermocouple from an average of the results of many calibration tests, it is assumed that the error, $\delta(\delta_x E_{11})$, involved in the resulting $\delta_x E_{11} \{T\}$ calibration curve is reduced to $\pm 2\mu v$. These errors become important percentage-wise only at very low values of $\Delta_x E_{11}$. At large values of $\Delta_x E_{11}$, fluctuations in the galvanometer indicator, presumably due to small power fluctuations, were observed. This introduced a possible additional reading error which is taken to be plus or minus 0.9 percent and is designated $\% \delta G.F.$ Finally a small allowance was made for errors in the potentiometer-standard-cell voltage. In general the potentiometer showed no readable error when calibrated against a standard unit; however, a slight shift was noted in one such calibration, and, since no allowance was made for this in the data reduction, a variation in the differential e.m.f. determinations of plus or minus

0.3 percent, designated $\% \delta P.C.$, is included as a possible error.

On the basis of the preceding discussion the error, $\% \delta(\Delta_x E_{11})$, can be decomposed into the following four error elements:

$$(\frac{\Delta_x E_{11T}}{\Delta_x E_{11}}) \; \% \, \delta \, (\Delta_x E_{11T}) = \pm \; \frac{300}{\Delta_x E_{11}} \approx \pm \; \frac{300}{e \Delta T_f (1+\zeta)} \tag{101}$$

$$(\frac{\delta_x E_{11}}{\Delta_x E_{11}}) \% \, \delta(\delta_x E_{11}) \approx \pm \; \frac{200}{\Delta_x E_{11}} \approx \pm \; \frac{200}{e \Delta T_f (1+\zeta)} \tag{102}$$

$$\% \, \delta G.F. = \pm \, 0.9 \tag{103}$$

and

$$\% \, \delta P.C. = \pm \, 0.3 \tag{104}$$

where the final forms of equations 101 and 102 permit direct evaluation from the reduced data and where $(e \Delta T_f)$ is expressed in μv.

The use of the thermoelectric power curve, $e\{T\}$, in the thermocouple data reduction is described in Appendix IV-A. The error involved in the process of selecting the value of ''e'' from this curve for any given $\Delta_x E_{11}$ measurement can be shown to be negligible. The values used for the curve were taken from calibrations of the outlet-water thermocouple against a mercury-in-glass standard thermometer at $50°F$ intervals. The change in thermocouple e.m.f. divided by the change in temperature provides a value of ''e'' at the midpoint of each interval. The error involved in measuring the ''e'' values, taken together with the interpolation errors involved in the use of the resulting curve, is estimated as being

$$\% \, \delta e = \pm \, 0.6 \tag{105}$$

It is noted that the existence of the maximum observed in the $e\{T\}$ curve shown in Figure A-IV-1 is confirmed by other calibrations of Chromel-Alumel thermocouples reported in Reference 26, p. 31. The calibrations of Reference 26 cover a much larger temperature range and show the observed maximum to be a part of a perturbation which exists in an otherwise monotonically rising $e\{T\}$ curve.

The power measured by the wattmeter, connected either to the probes on the tube or to the electrode blocks, was used as the primary indication of heat flux $(\dot{q}_o)$. The total power delivered to the test section was also measured by a voltmeter and ammeter as discussed in Section III-D-2. In general, the electrical power measurements gave good agreement. For the tests on each tube, the mean discrepancy between the wattmeter and the voltmeter-ammeter measurements was less than 0.5 percent with a two-standard-deviation spread on the discrepancy measurement of less than $\pm$ 2.3 percent. This spread corresponds to the expected combined reading inaccuracies of the three meters. The mean discrepancy for all tests taken together was only 0.12 percent. These observations lead to the conclusion that essential agreement exists between the wattmeter and the voltmeter-ammeter measurements. As discussed in Section III-D-2, the AC voltage-drop-to-current ratio gave satisfactory agreement with the test-section resistance measured with very low, DC current. In this check, the higher power AC test results were adjusted for the effect of longitudinal resistance variations caused by the axial temperature gradient. In several cases, it was possible to obtain good wattmeter reading accuracy at the

probes as well as at the electrode blocks. The probes-to-test-section power ratio agreed with the computed ratio which again included the effects of axial temperature variations. This check on the relation between probes and test-section power measurements showed that the computed longitudinal variation in heat generation was essentially correct, and it further supported the validity of the wattmeter calibrations. The calorimetric power measurements, which were inherently less accurate than the electrical measurements, were on the average several percent lower than the electrical power measurements after all pertinent corrections were applied. This mean difference between the two types of power measurement was within the two-standard-deviation spread of the difference values, but the bias was evident in the results from all tubes. A special test simulating the conditions of one of the standard tests was performed using a large DC welding generator substituted for the AC power transformer as a heating source. In this test the power was measured by calibrated DC instruments with the result that the electrical power was again several percent greater than the calorimetric power. This result inferred that neither spurious effects in the AC electrical power measurements nor spurious AC effects on the thermocouple measurement of water temperature rise is the explanation for the electrical-calorimetric power discrepancy. The effect on the C_H determination of this apparent systematic discrepancy will be discussed subsequently; it is only noted here that the disagreement is not to be taken as an indication of additional error in the determination of $\dot{q}_o$ by the electrical power measurement. Considering then 1) the normal wattmeter reading error, 2) the possible increase in

reading error occurring when slight fluctuations in the power were observed, 3) the small systematic differences among the various electrical checks on the wattmeter, and 4) the direct calibrations of the wattmeter, the error in the power measurement used in the $\dot{q}_o$ determinations is estimated to be

$$\% \, \delta \, W_P = \pm \, 1.5 \tag{106}$$

An approximate form for the operational definition of the circumferential-mean wall thickness (Cf. Appendix II-C) is adequate for use in the error analysis. This approximation is given as

$$t \cong \frac{\rho_e}{\pi \, D(d \, R_e / dx)} \tag{107}$$

where ρ_e is the electrical resistivity of the wall material and $d \, R_e / dx$ is the resistance of the tube per unit length. The complete form of equation 107 is developed in Appendix II-C by substituting $\rho_e / (d \, R_e / dx)$ for the cross-sectional area of the tube. For the smooth tube this substitution has exact meaning by the definition of resistivity (ρ_e). The wall thickness of the E-3 (smooth) tube was determined by measuring the cross-sectional area directly. The uncertainty in the thickness so derived is taken as plus or minus 0.0004 inch or

$$(\% \, \delta t)_S = \pm \, 2.0 \tag{108}$$

However, for the rough tubes, ρ_e was determined separately, and the errors in the terms ρ_e, dR_e / dx and D appearing in equation 107 must be considered separately and then be combined. Doing this, the error in the computed mean thickness for the rough tubes is estimated as

$$(\% \delta t)_R = \pm 4.0 \tag{109}$$

The error in establishing the thermal conductivity of the tube wall by the method discussed in Appendix II-B depends primarily on the error in the measurement of electrical resistivity which is taken as ± 3.0 percent. This error, combined with assumed uncertainties in the method itself, yields an estimate for the error in the computed thermal conductivity of the tube,

$$\% \delta k = \pm 3.5 \tag{110}$$

The three sources of C_H uncertainty which are not evident from the data reduction formula (equation 93) must be considered before the complete C_H uncertainty can be developed. First of all, the existence of a systematic error in the calorimetric power measurement, presumably caused by either unaccounted for heat losses in the system or by poor mixing of the exit fluid prior to the thermocouple measurement, implies a small error in the C_H determination. An analysis of this effect is provided in Appendix VI. If a heat loss, not predicted by the calibration tests, occurs between the wall thermocouple stations and the exit, or if the outlet-water thermocouple, by reason of poor mixing, should read a temperature lower than the fluid mean temperature, there results an error in C_H,

$$\% \delta C_H = - 400 \frac{x}{D} C_H \frac{(W_{TS} - W_{TSC})}{W_{TS}} \tag{111}$$

where W_{TSC} is the measured calorimetric power. Note also that the operator $(\% \delta)$ is so defined that

$$\% \delta C_H \equiv 100 \frac{C_H(\text{measured}) - C_H(\text{correct})}{C_H(\text{correct})}$$

If, on the other hand, the calorimetric power error is due to extraneous heat losses between the entrance station and the station of the wall thermocouple, or if the inlet thermocouple reads erroneously too high, the C_H error becomes

$$\% \, \delta C_H = 400 \, \frac{(L-x)}{D} \, C_H \, \frac{(W_{TS}-W_{TSC})}{W_{TS}} \qquad (112)$$

The errors found in the calorimetric power measurements are considerable, as will be shown in the succeeding paragraph; however, the effect of these errors on the C_H determination, given by equations 111 and 112, is small.

Combining the results of all of the tests on each tube, the following mean percent-deviations of the calorimetric power from the electrical power were obtained; the spread shown represents the two-standard-deviation limits:

Tube	$100 \, (W_{TS}-W_{TSC})/W_{TS}$	
E-3 (smooth)	$+6.4 \pm 6.0$	
D-3	$+2.2 \pm 3.7$	
C-9	$+3.8 \pm 5.0$	(113)
A-4	$+3.0 \pm 4.0$	

The statistical distributions of the discrepancies are based on approximately 50 points in each case. The distributions are fairly symmetric except in the case of the smooth tube where a large peak occurs at

$$100 \, (W_{TS}-W_{TSC})/W_{TS} = \pm 3.5$$

with a long tail-off running to values as high as + 15.0 percent. Because the tests for all tubes were set up with heat flux computed to

give a certain ΔT_f range for each flow rate and since the heat transfer film conductance (h) for the smooth tube is relatively low, the smooth tube power settings were lower than those for the other tubes. Hence the fluid bulk temperature rise, ΔT_c, was consistently lower for the smooth tube leading to a relatively poorer accuracy in the W_{TSC} determination. The high sensitivity of the calorimetric power measurement to errors in the ΔT_c measurement is indicated by the fact that a systematic shift of 5 μv in $\Delta_o E_{11}$ could account for almost all of the observed deviations of W_{TSC} from W_{TS} for all tubes including the smooth tube. Since systematic shifts in the e.m.f. measurements of as high as 5 μv are not expected, such shifts can account for part but not all of the observed error in W_{TSC}. However, the errors in the $\Delta_o E_{11}$ e.m.f. measurement, discussed previously in this section, could easily account for the excess in the W_{TSC} error for the smooth tube over that for the rough tubes. Considering the aggregate of the tests, it is concluded that there exists a residual deficiency of the order of 3 percent in the calorimetric power determination which cannot be explained by errors in the e.m.f. measurement. Further this residual deficiency is about the same for all tubes, for all fluid bulk temperatures, and for all flow rates.

There is some indication that the calorimetric power anomaly is statistically slightly larger for the highest temperature, lowest flow rate condition. If this indication is correct, it would imply that some of the effect may be due to heat losses. It should be noted here that rough calculations of the expected heat loss by natural convection from the exterior of the test section indicate negligible effects from this cause. The calibration tests revealed spurious heat losses only

at the highest fluid temperature, 290°F, and in this case, the losses appeared to increase with flow rate. This dependence on flow rate would not be expected to attend natural-convection losses since, to a first order, such losses can be shown to depend on the tube surface temperature only. The supposition that natural-convection heat losses are negligible was supported also by one of the calibration tests at a water temperature of 290°F wherein a jet of air, with a velocity many times that predicted for natural convection, was played on the test section. The air jet produced only a barely discernible change in the heat loss. Moreover, in the heat transfer experiments, all heat losses occurring in the non-heating calibration tests are compensated. This leaves unaccounted for only those natural-convection losses attributable to the small increase in tube surface temperature due to electrical heating. These uncompensated losses should be small indeed.

Another possible cause of heat loss is axial conduction along the tube to the electrode blocks. An analytical discussion of this effect is presented in Appendix V. The largest heat loss to the electrodes compared to the total heat generated occurs in the situation of a smooth tube operating at high Pr and low Re, i.e., for the lowest heat transfer fluid film conductance (h). The end conduction for this extreme case could account for 0.8 percent of the total heat generated in the tube. For most other cases the computed end conduction would be much less than this amount. It is improbable that this effect can wholly explain the observed calorimetric power discrepancy.

The high pressure drop of the mixing chamber used in these experiments is expected to result in adequately mixed fluid leaving

the test section; however, it is conceivable that temperature non-
uniformities of a magnitude necessary to explain the power discrepancy
still persist in the fluid at the exit station. Errors of only 1 to 2 per-
cent of ΔT_f in the outlet-water temperature measurement would provide
the required explanation.

Since neither the cause nor the location of the calorimetric
power deficiency can be clearly ascertained and since the effects on
the computed C_H values is either positive or negative depending on
where the heat loss occurs (Cf. Eqs. 111 and 112), no compensating
adjustment in the C_H formulation is attempted. Hence the implied
C_H error, which will be designated $\% \delta H.L.$, must be included in
the error analysis. For this purpose, the possible error is com-
puted for the farthest downstream wall thermocouple station from
equations 111 and 112. Taking the foregoing discussion into account,
the power discrepancy, $(W_{TS}-W_{TSC})/W_{TS}$, is assumed to be 4
percent for the smooth tube and 3 percent for the rough tubes. It
is noted that the statistical spread in the W_{TSC} discrepancy displayed
in item 18 is not pertinent to the C_H error calculation. This spread
is caused primarily by errors in the ΔT_c measurement, but the con-
tributor to this spread which is pertinent to the C_H measurement is
already taken into account by the $\% \delta \Delta_x E_{11}$ errors of equations 101
and 102. The resulting C_H errors obtained for the smooth and the
rough tubes respectively are

$$(\% \delta \ H.L.)_S = \begin{bmatrix} +87 \\ -640 \end{bmatrix} C_H \tag{114}$$

and

$$(\%\delta \text{ H. L. })_R = \begin{bmatrix} +65 \\ -480 \end{bmatrix} C_H \qquad (115)$$

The maximum C_H error computed from equation 115 is plus 0.3 or minus 2.5 percent. This occurs for the roughest tube at low Pr and low Re. The $\%\delta$ H.L. error is regarded as existing as one or the other of the values shown depending on whether the effective heat loss occurs upstream or downstream of the wall thermocouple station. Hence this error probability is not continuously distributed.

Spatial variations in the liquid-side wall temperature are a second source of C_H error not evident from the data reduction formula. Such variations must necessarily exist for rough tube heat transfer tests wherein the tube wall serves as the heating element. One cause of liquid-side wall temperature variations is pictured by assuming that the wall is very thin and that the current density and hence the resistance heating and hence $\dot{q}_o$ are distributed nearly uniformly over the warped surface. Under these conditions the wall temperature, which will depend directly on the local heat transfer coefficient, would be expected to differ between the peaks and troughs of the roughness elements. Secondly, for finite but small wall thickness as used in these experiments, the tortuous electrical current paths must necessarily lead to local variations in current density distribution and thus to local variations in heat generation. This non-uniform heat generation, combined with effects of differing conduction paths between the heat source points and the liquid-side wall, leads to perturbations in the liquid-side wall temperature which cannot be expected to compensate those produced by the first cause mentioned. These variations in liquid-side wall temperature diminish as the wall-thickness-to-roughness-height ratio is increased or

as the thermal conductivity of the wall is increased. The same effects that produce variations in the liquid-side wall temperature are expected to produce similar variations in the outside wall temperature. The latter variations are not exactly the same as the former, but they are assumed to exhibit a similar statistical spread. A measure of this spread was obtained from a comparison of the C_{Hx} values computed from the data of each of the three thermocouples located at each of the two downstream measuring stations. The thermocouple junctions were randomly placed with respect to the roughness elements with each thermocouple consisting of separately placed Alumel-nickel and nickel-Chromel junctions. The observed variations among the C_{Hx} values are taken to be representative of the deviation of the C_{Hx} value determined by any single thermocouple from the ideal C_H which would be obtained with a uniform temperature surface. For all tubes it was noted that the pattern of C_{Hx} versus circumferential and axial thermocouple location remained nearly fixed for the three tests with fixed Re and Pr and varying $\dot{q}_o$, and also the C_{Hx} pattern was observed to evolve in a continuous manner as Re and Pr were varied. These observations indicate that the C_{Hx} variations were due primarily to systematic effects such as those previously discussed. In establish-ing the effects caused exclusively by roughness, a reduction in the observed C_{Hx} perturbations was made to eliminate the secondary contribution of the random e.m.f. reading errors. The estimated uncertainties in the circumferentially averaged C_H values due to local roughness effects and other uncorrected local disturbances are desig-nated $\% \delta R.E.$ and are evaluated as follows:

$\% \delta R. E. (E-3) = \pm 1.4$

$\% \delta R. E. (D-3) = \pm 0.0 \text{ to } 15.0$

$\% \delta R. E. (C-9) = \pm 1.4$ (116)

$\% \delta R. E. (A-4) = \pm 4.0$

The large spread in C_{Hx} values which was observed at high Reynolds numbers for tube D-3 is associated almost entirely with a systematic variation in the gross roughness characteristics with circumferential location; at low Re the spread is negligible. This important source of C_H error on this particular tube will be discussed more thoroughly in Section IV-C.

The existence of local variations in C_{Hx} for the smooth tube (E-3) implies the presence of local variations in wall thickness and/or in heat transfer film conductance (h). Variations in wall thickness have the primary effect of perturbing the local $\dot{q}_o$ from the mean value and the secondary effect of perturbing the local ΔT_w from the mean. Local thickness variations, large enough to account for ob- served C_{Hx} distribution for the smooth tube, could exist within the resolution of the thickness measurements which were taken from the enlarged cross-section pictures discussed in Appendix II-C. The observed spread in C_{Hx} values depends to some extent on Rey- nolds number. Since the magnitude of this Reynolds number depen- dence cannot be completely explained by variations in local ΔT_w induced by thickness irregularities, it must be assumed that some Reynolds-number-dependent perturbations in "h" were also present in the smooth tube.

Plots of C_{Hx} versus thermocouple position for tubes E-3 and D-3 revealed, in addition to the circumferential variations just

discussed, a consistent decrease in the circumferentially averaged C_H values between the middle thermocouple station, at approximately 26 diameters from the start of heating, and the last thermocouple station at approximately 40 diameters. As with the circumferential variations, this $\overline{C}_H$ fall-off, which tended to increase percentage-wise with increasing Re, could not be completely explained in terms of random local thickness variations. Further, the percentage fall-off was shown to be nearly independent of heat flux level after the $\overline{C}_H$ values at the two thermocouple stations were adjusted to correspond to the same mixed fluid temperature. Hartnett's data for the thermal entrance region of smooth pipes operated at Prandtl number equals 7 and Reynolds number equals 2.3 to 8.6×10^4 were presented by Allen (Ref. 11, p. 84). These data indicate that the heat transfer coefficient, adjusted to correspond to a fixed reference temperature of the fluid, has not quite attained an asymptotic value at 26 diameters from the onset of heating but that it has very nearly done so at 40 diameters. The longitudinal variation in $\overline{C}_H$ observed in the present experiments is in qualitative agreement with the data for the corresponding test conditions presented in Allen's plots. This agreement may be an indication that the $\overline{C}_{H7}$ values, given as the final results of the present experiments, do represent very nearly fully established conditions; however, at higher bulk temperatures, i.e. lower Pr, the percentage change in $\overline{C}_H$ between the two down-stream stations increases, and the assumption that the 40 diameter station represents completely established conditions has less cer-tainty. For this reason, a third source of C_H error, not evident from the data reduction formula, is assigned to the E-3 and D-3

results. This error is evaluated by the assumption that the fully established C_H value is contained in the interval between the $\overline{C}_{H7}$ value and this value minus one-half of the difference $(\overline{C}_{H4}-\overline{C}_{H7})$. This possible error in $\overline{C}_{H7}$ due to insufficient entrance length will be designated $\%\,\delta E.L.$, and it has the following values for limiting cases of fluid temperature (T_L) and mass flow rate $(\dot{w})$:

Tube	T_L (^{O}F)	$\dot{w}$ (lb/sec)	$\%\,\delta E.L.$
E-3	80	.35	+1.0 -0.0
E-3	80	1.75	+1.5 -0.0
E-3	290	.35	+1.5 -0.0
E-3	290	1.75	+3.0 -0.0
D-3	80	.20	+0.0 -0.0
D-3	80	1.75	+2.0 -0.0
D-3	290	.20	+1.0 -0.0
D-3	290	1.75	+2.0 -0.0

$$(117)$$

There were some indications of a similar entrance length effect in the two rougher tubes, but they were less pronounced and less consistent than the effects observed with the smoother tubes. The small longitudinal variations in $\overline{C}_H$ observed in some rough tube tests are assumed to be accounted for in the $\%\,\delta R.E.$ error presented and discussed previously.

In determining the confidence limits for the final C_H results, most of the errors discussed herein are treated as being continuously

distributed in a near-normal manner. Combining such errors to
yield the same confidence coefficient for the composite as existed
for the individual contributors is accomplished by taking the square
root of the sum of the squares of the individual percentage errors.
The exceptions to this rule are the potentiometer calibration error
(% δ P. C.), the error due to the calorimetric power discrepancy
(% δ H. L.) and the uncertainty in the degree of full establishment
of the heat transfer conditions (% δ E. L.). These error elements
are assumed to exist necessarily as either one or the other of the
error limits given, i.e. , they have a double delta function type
of probability distribution. The combination of these delta-function-
distributed errors with the other normally distributed errors is
accomplished here by simply adding the given values of the delta
function errors to the two-standard-deviation limits of the com-
bined, normally distributed errors. This procedure is slightly
conservative in that it yields final accumulated C_H confidence
limits with a confidence coefficient slightly increased over the
95 percent confidence coefficient associated with the limits for
the individual error contributors. With reference to the crude
estimates used for the individual errors, a more precise combi-
national procedure is unwarranted.

The final C_H values, which constitute the results of these
experiments, are the consequence of averaging the three C_{Hx}
values at the downstream thermocouple station in each test and
of extrapolating the results of three tests at differing heat flux
to isothermal conditions. Each of these two operations is an
averaging process, and they serve to reduce the random errors

associated with the individual terms contributing to the respective averages. Making use of the C_H errors discussed in this section and referring to the immediately preceding discussion, the composite confidence limits on the reported C_H values can be written as

$$
\%\delta C_H = \left[\!\!\left[\frac{1}{3} \left[\!\!\left[\left[\frac{1}{2}\%\delta\Delta P_v \right]^2 + \frac{1}{3}\left[(1+\zeta)\left(\frac{\Delta_x E_{11T}}{\Delta_x E_{11}}\right)\%\delta(\Delta_x E_{11T}) \right]^2 \right.\right.\right.
$$

$$
\left.\left. + \frac{1}{3}\left[(1+\zeta)\%\delta G.F. \right]^2 + \left[(1+\zeta)\%\delta W_P \right]^2 \right]\!\!\right]
$$

$$
+ \left[\frac{1}{2}\%\delta K \right]^2 + \left[(1-\zeta)\%\delta D \right]^2
$$

$$
+ \frac{1}{3}\left[(1+\zeta)\left(\frac{\delta_x E_{11}}{\Delta_x E_{11}}\right)\%\delta(\delta_x E_{11}) \right]^2 + \left[(1+\zeta)\%\delta e \right]^2
$$

$$
\left. + \left[\zeta\%\delta t \right]^2 + \left[\zeta\%\delta k \right]^2 + \left[\%\delta R.E. \right]^2 \right]^{1/2}
$$

$$
+ (1+\zeta)\%\delta P.C. + \%\delta H.L. + \%\delta E.L. \tag{118}
$$

where the coefficient ζ is defined by equation 100. The multipliers involving ζ are obtained from the listing given as equation 99. The terms in the order of their occurrence on the right hand side of equation 118 are evaluated respectively either in Section III-E-2 or in equations of this section as given by the following: Cf. Sec. III-E-2, 101, 103, 106, Cf. Sec. III-E-2, Cf. Sec. III-E-2, 102, 105, 108 and 109, 110, 116, 104, 114 and 115, 117. The 1/3 factor in front of the double brackets in equation 118 accounts for the averaging of the three tests at different heat flux while the 1/3 factor that appears in front of three different single-brackets terms accounts for the averaging of the results from the three circumferential locations

on the tube.

Table 2 presents the C_H confidence limits computed from equation 118 for the extremes of flow rate and bulk temperature used in the tests on each tube. The meaning of the $\% \delta C_H$ values presented in Table 2 is implied by the following statistical statement:

$$C_{Hm} \left(1 - \frac{\% \delta C_{H1}}{100}\right) \leqslant C_{Hc} \leqslant C_{Hm} \left(1 - \frac{\% \delta C_{H2}}{100}\right) \qquad (119)$$

is true 95 percent* of the time. In this statement, the subscripts "c" and "m" refer to the correct and the measured values respectively, and the subscripts 1 and 2 refer respectively to the upper and the lower values of $\% \delta C_H$ given in Table 2. Also included in Table 2 is a separate evaluation of

$$(\% \delta C_H)_{read.} = \frac{1}{\sqrt{3}} \left[\left[\frac{1}{2} \% \delta \Delta P_v \right]^2 + \frac{1}{3}(1+\zeta)\left(\frac{\Delta_x E_{11T}}{\Delta_x E_{11}}\right) \% \delta (\Delta_x E_{11T}) \right]^2 \right.$$
$$\left. + \frac{1}{3}[(1+\zeta) \% \delta G.F.]^2 + [(1+\zeta) \% \delta W_P]^2 \right]^{1/2} \qquad (120)$$

which represents the composite of the reading errors adjusted for the averaging. It is seen that the instrument reading errors, which are less than plus or minus 1.5 percent in all cases, make only a minor contribution to the over-all C_H uncertainty.

From the $\% \delta C_H$ values given in Table 2, it is seen that in general the over-all C_H uncertainty is somewhat larger for the high temperature tests than for the low temperature tests. The greatest uncertainty in the smooth tube results, +5.8%, occurs for the test at 290^OF (Pr = 1.20) and 1.75 pounds per second flow rate. Excluding

*Refer to the introductory discussion for Section III-E.

the values for the D-3 tube, the greatest uncertainty for the rough

tube C_H values, -7.2%, occurs for the roughest tube (A-4) at $290^\circ F$

and 0.20 pounds per second flow rate. The large uncertainty occur-

ring at high flow rate in the tube D-3 results is attributed to circum-

ferential variations in the tube roughness. A detailed discussion

of the source of this imperfection in the D-3 tube construction and

its implications will appear in Section IV-C.

F. Discussion of Methods

In this section a general appraisal of the techniques employed in the present experiments will be given. Along with this, recommendations will be made for improving the techniques for future experiments of this type.

The tubes used in the experiments will be considered first. These tubes represent a very satisfactory solution to the difficult problem of producing a prescribed roughness in a tube which has dimensions and material properties sufficiently well controlled to be useful in heat transfer experiments. However, several improvements can be suggested for the manufacture of tubes by the electroforming process for future experiments. It should be possible to electroform tubes with wall thickness as small as 0.005 inch which will be leak-tight and still conform to almost any desired roughness pattern. This could be accomplished by designing the copper electrodes to be fitted to the mandrel and shaped in such a way that, after the plating process is complete but before the mandrel is dissolved, a frame can be attached between the electrodes so that no bending loads will be sustained by the finished tube. The tube will have been electroplated to the electrodes in this process, and thus the need for brazing fittings to the tube after the tube has been produced will have been eliminated. The higher resistance of a very-thin-walled tube will permit the use of considerably lower current for the same heat flux and, hence, the size of the electrodes can be reduced, thereby minimizing electrode conduction as cause of spurious heat loss. Further, the corrections for wall temperature drop will be reduced in proportion to the thickness, thus reducing

another source of error in the ΔT_f determination. For roughness element size of the same order as (or greater than) the wall thickness, the specific placement of thermocouples in the peaks and cavities can provide some meaningful indication of local variations in the heat transfer film conductance (h).

The rough tubes in these experiments have a short (approximately 2 diameters long) smooth region following the unheated entrance length. This was formed in order to facilitate the static pressure measurement. It was felt that the momentary change in wall shear stress, experienced by the flow as it passed this region, would not change the velocity profile appreciably and that the established profile would be re-formed a few diameters downstream from this region. This reasoning is supported by the results of channel flow measurements performed by W. Jacobs (Cf. Ref. 18, p. 482). The C_{Hx} results on the C-9 tube showed clear evidence of a non-axially symmetric disturbance at the first thermocouple station, approximately five diameters downstream from the pressure tap region. This disturbance was no longer evident at the succeeding thermocouple stations. This effect is attributed to a known slight difference between the diameters of the smooth pressure-tap section and the rest of the tube and also to a possible slight nonconcentricity at the juncture. A good match between a smooth and a rough region is difficult to attain, and the velocity profile is apparently very sensitive to small disturbances in tubes with small roughness ratio. Hence it is suggested, for future experiments with low tube roughness ratio (say ϵ/D less than 0.01), that the smooth region be eliminated and that the pressure-tap holes be drilled directly into the

rough wall. Auxiliary measurements were performed on the D-3 tube ($\epsilon/D \cong 0.002$) wherein the upstream static pressure measurement was taken from holes drilled into the rough region near the downstream end of the entrance section. The C_F values computed from these measurements were in good agreement with the measurements taken from the standard tap. Additional tests are necessary to demonstrate the validity of this procedure at larger ϵ/D values. Certainly the procedure would not be satisfactory for tubes with very large roughness ratio, but in such cases the smooth section method used in these experiments appears to be acceptable.

Aside from the pressure-tap area disturbance, the wide uncertainty limits allowed for the tube D-3 results were attributed to spatial variations in the surface roughness. This indicates that greater care in manufacturing the tube mandrels, particularly when very small roughness elements are being used, would result in higher quality experimental results. Also there was evidence in these experiments that somewhat longer thermal entrance lengths may be required to provide fully established conditions. The use of more wall thermocouples located at intermediate stations would help to demonstrate the existence of fully established conditions.

It is felt that the machine methods developed for reducing the thermocouple data and computing the final dimensionless parameters were essential to the test program, not only in diminishing the formidable task of reducing the large amounts of data, but in minimizing the chances for error associated with the repetitive operations. A considerable amount of preliminary data analysis was performed by hand in the procedures used in these

experiments; this could also be done by machine if the initial data-taking procedures were modified.

The single-pass flow system used in these tests provides a simple means of obtaining a steady inlet water temperature at a steady flow rate. There is the problem of attaining steady thermal conditions throughout the system and of making the required measurements within the time interval established by the volume of the reservoir tank and the fluid flow rate. If the electrode regions and the mixing flange had not been brought up to operating temperature by preheaters prior to tests at high fluid temperatures, a large portion of the run time would have been required to establish equilibrium by means of heat losses from the test fluid. Auxiliary tests, performed at the highest fluid temperature (290°F) have demonstrated that less than 10 percent of the total fluid is required to bring the system to thermal equilibrium if the preheaters are used. The portion of the fluid required to reach equilibrium is nearly independent of the mass flow rate ($\dot{w}$). This is understood by noting that the heat transfer film conductance (h) is, to a first order, proportional to $\dot{w}$ so that the integrated amount of heat added to, and hence the temperature of, the surrounding metal is approximately proportional to the integrated amount of passing fluid.

In many of the high power tests, heat generated in the connecting cables was conducted to the tube electrodes thus raising their temperature above the operating point. Although a first order correction was made for this effect on the basis of the calibration tests, the electrode heat exchange does represent a

possible source of error. This situation could be improved if the electrodes and part of the lead-in conductors were made with hollow passages allowing a through-flow of water maintained at the correct temperature. If the mixing flange were designed in a similar manner the need for the electrical heating tapes and controls would be eliminated.

As shown in Table 2 the effects of instrument reading errors on the C_H determination were kept relatively small through the use of considerable redundancy and repetition in the measurements. The principal contribution to the C_H uncertainty comes from the various systematic effects. The systematic errors introduced by the calorimetric power discrepancy and by the apparent residual entrance effects could possibly be reduced or eliminated by improved techniques including those suggested in this section. It is difficult to see how the errors due to the so-called roughness effects could be appreciably reduced if electrical heating of the tube is to be used. The error analysis has also indicated that the conditions of the present experiments were sufficiently well controlled to permit the use of the results as tests of theories and of correlations among the primary parameters. Much of the previously existing experimental work on rough tube heat transfer is not usable for this purpose principally because conditions of the experiments such as entrance length, roughness characteristics, fluid property variations in the heat-transfer region, and surface fouling are either poorly controlled or incompletely described.

IV DISCUSSION AND ANALYSIS OF EXPERIMENTAL RESULTS

A. Presentation of Results

In this section the principal results of the experiments together with certain general observations will be presented. A more detailed discussion will be deferred to the subsequent sections.

The friction factors (C_F) as functions of Reynolds number for each of the four experimental tubes are tabulated in Table 3 and are displayed in Figure 12. In the figure, the data points are given symbols to designate the nominal fluid temperature used for each measurement. The C_F results presented were derived exclusively from the isothermal calibration tests; these isothermal results were confirmed by the C_F measurements obtained from the heat transfer tests at the lowest heat flux within the accuracies of the experiments. In general, the effect of the radial fluid property variations on C_F was so small for the low values of heat flux employed in these ex- periments that only qualitative remarks can be made concerning this effect. The smooth tube and the D-3 tube operating in the low Reynolds number region showed a decrease in C_F with increasing wall-to-mixed-fluid temperature difference (ΔT_f) similar to that ob- served in other experiments with smooth tubes (Cf., e.g., Ref. 11, p. 56). The rough tubes, operating in the so-called fully rough Rey- nolds number region wherein C_F is independent of Re, showed little if any C_F dependence on ΔT_f. This might have been expected; if the isothermal C_F is independent of Re, i.e. of the fluid properties, then the radial variation of the fluid properties should have no effect.

The solid lines drawn in Figure 12 represent the best esti- mate for a correlation of the C_F data of the present experiments.

The value of the hydraulic equivalent sand-grain diameter (ϵ_s) shown for each of the rough tubes was selected on the basis of Nikuradse's (Ref. 10) experimental results in which he evaluated the similarity parameter, $A\{\epsilon*\}$, appearing in the friction similarity law (Cf. Eq. 26, Sec. II). For $\epsilon* > 67$, Nikuradse found that A becomes constant at 8.48. Thus for this so-called fully rough condition, corresponding to the region shown to the right of the light diagonal line in Figure 12, the friction similarity law for sand grain roughness can be written

$$\frac{1}{\sqrt{C_{FF.R.}/2}} + 2.5 \, \ell n(2\epsilon_s/D) + 3.75 = 8.48 \tag{121}$$

where $C_{FF.R.}$ is the friction factor in the fully rough region. Values of $C_{FF.R.}$ chosen for each tube on the basis of the plots in Figure 12 were then used in equation 121 to yield the equivalent sand-grain roughness ratio (ϵ_s/D). Then the complete

$$A\{\epsilon*\} \equiv A\{(\epsilon_s/D) \, Re \, \sqrt{C_F/2}\}$$

function for Nikuradse's sand-grain roughness together with the ϵ_s/D values determined for each of the present experimental tubes was used in equation 26 to generate the dashed $C_F\{Re\}$ curves shown in Figure 12. These dashed curves thus display the $C_F\{Re\}$ functions that should be obtained with true sand-grain roughened tubes having the same $C_{FF.R.}$ as the respective tubes investigated in the present work. Also in Figure 12, the smooth tube (E-3) friction results are compared directly to the Prandtl relation (Ref. 18, p. 413) which in turn is confirmed by Nikuradse's smooth pipe experiments.

As a general observation, the C_F curves for the rough tubes, compared in Figure 12, are seen to have a Reynolds number dependence similar to those of Nikuradse's sand surfaced pipes. The presence of a minimum between the Reynolds number regions of smooth-type behavior and fully rough behavior is seen in the D-3 tube results and is suggested by the shape of the low Re characteristics of the C-9 tube. This C_F {Re} characteristic is taken as evidence that a definite scale of roughness exists in these tubes. As a contrast to this C_F {Re} characteristic, Colebrook (Ref. 27) discusses the case of a more random type of roughness such as that observed in naturally rough pipes. With random roughness, the C_F {Re} function monotonically decreases with increasing Re until the fully rough condition is asymptotically approached. The small differences in the shape of the C_F {Re} curves for the tubes used in these experiments from the shape of the C_F {Re} curves for tubes with true sand-grain roughness show that the geometry of the latter is closely approached but probably not quite attained in the present tube construction. A comparison of the directly measured roughness ratios (ϵ/D) for each of the tubes with the corresponding computed ϵ_s/D values will appear in the discussions of the individual tube results in the succeeding sections.

The heat transfer results are presented next. Tables 4 through 7 present the experimental Stanton numbers as a function of Reynolds number and Prandtl number for each of the tubes. These C_H values represent the averages of the measurements at the three thermocouples located at the downstream station (approximately 38 diameters from the start of heating); these averages have been normalized to the conditions of the nominal local mixed fluid temperature and combined with other measurements at differing heat flux values to obtain the

equivalent isothermal Stanton numbers (Cf. Sec. III-D-3). These results are shown plotted as $C_H\{Re;Pr\}$ for each tube in Figures 13 through 16 respectively. For reference, the respective mean curve for $(C_F/2)\{Re\}$ taken from Figure 12 is reproduced on each of the C_H plots. The smooth tube $(C_F/2)\{Re\}$ is also included on each plot for reference. The heavy lines in Figures 13 through 16 were drawn to best interpolate the data points shown.

Cross comparisons of the results from the various tubes are presented in the $(2C_H/C_F)\{Re;\epsilon_s/D\}$ curves shown in Figures 17 through 20 respectively for each of the four nominal Prandtl numbers investigated. The points plotted in these figures are based on the C_H data listed in Tables 4 through 7, and the C_F values for the corresponding Reynolds numbers are taken from the mean $C_F\{Re\}$ curves (Fig. 12). These interpolated C_F values together with the computed $2C_H/C_F$ values are also tabulated in Tables 4 through 7.

The final item in the final data presentation is Figure 21 showing the Prandtl number dependence of $2C_H/C_F$ for each tube at a Reynolds number of 1.5×10^5. At this Re value, tubes C-9 and A-4 are in the fully rough regime while tube D-3 is still in the transition region between smooth-type and fully-rough-type behavior. The points shown in Figure 21 are taken from the smoothed curves in Figures 17 through 20; the extrapolations shown in Figure 20 were used for the points at Pr equals 5.94. The solid lines drawn in Figure 21 represent an estimated interpolation of the data points while, for the case of the smooth tube, the dashed line corresponds to a theory derived by Rannie* (Ref. 14).

---

*Rannie's Theory is used without the correction term, Cf. footnote p. 28, Sec. II.

B. <u>Discussion of Results for Tube E-3 (Smooth)</u>

The smooth tube experiments were conducted in part to provide a check on the experimental techniques for a case where direct comparisons can be made against experimental information existing in the literature and in part to provide a direct comparative basis for the rough tube results. The provision of a smooth-tube basis for the present work is necessary since, as will be shown, some disagreement persists in the published results of experiments in which the idealized conditions being investigated were approached. To serve the purposes just described, the comparisons of the tube E-3 results with other smooth tube experimental results will be included in this section. This procedure will not be followed in the comparisons for the rough tube results. In that case the comparisons will be treated separately in Section VI rather than in the discussions of the individual tube results (Sections IV-C, D and E).

The smooth tube friction measurements are seen in Figure 12 to be well correlated by the Prandtl theory (Ref. 18, p. 413) except at the highest Reynolds number tested. This theory is the friction similarity law for smooth pipes (Cf. Eq. 27 in Sec. II) with the constants being evaluated from Nikuradse's smooth pipe results. Since all of Nikuradse's data points also fall very close to the C_F {Re} curve derived from the Prandtl theory, it may be stated that the tube E-3 measurements are in essential agreement with Nikuradse's experimental results at all but the highest Reynolds number tested herein.

The small deviation of the C_F {Re} curve for tube E-3 from the Nikuradse curve at high Re was to be expected on the basis of

the finite roughness exhibited by the finished tube. It is noted here that the single experimental point representing this condition is substantiated by the measurements in the hot tests at low heat flux, and hence the point is not merely due to experimental scatter. This C_F deviation at high Re corresponds to the effect expected for an approximate equivalent-sand-grain roughness ratio (ϵ_s/D) of 3×10^{-4}. The maximum peak-to-valley variations measured by use of the Brush Surface Analyzer (Cf. Fig. 4) correspond to ϵ/D values of 5×10^{-4} for the longitudinal profile and 10×10^{-4} for the circumferential profile, these being of the same order or magnitude as the computed ϵ_s/D. This observed roughness was anticipated for this tube since the soft aluminum mandrel used in the construction showed scratches of this scale both from longitudinal die marks and from random scratches due to the cleaning process. Nevertheless, for the range of Reynolds number employed in these experiments, the designation "smooth tube" appears to remain appropriate.

The complete set of heat transfer results for the E-3 tube is presented in Figure 13 and is tabulated in Table 4. It is interesting to note that, at Pr of 1.20, the $C_H\{Re\}$ curve follows the deviation of the $C_F\{Re\}$ curve at the high Re point. This behavior ought to be expected if the underlying effect is finite surface roughness as has been hypothesized.

In Figure 22 an example is presented of the tube E-3 plots of the local C_{Hx} values computed for each thermocouple station as a function of tube length from the start of heating. The conditions for the particular test represented in this figure are Re = 4.22×10^4, Pr = 5.88 and ΔT_f = 22.6°F. A measure of the thermal entrance

effects in the E-3 tube is afforded by a comparison of the slope of the line joining the circumferential mean of the C_{Hx} values at each station with the slope of the reference line. The slope of this reference line shows the $C_H\{x/D\}$ variation expected for hydrodynamically and thermally fully established conditions. This slope is determined by the dependence of C_H on the local Re and Pr values which in turn depend on the longitudinal rise in mixed fluid temperature due to heating. The $C_H\{Re;Pr\}$ dependence used for computing the reference line slope is taken from the results in Figure 13. The reference line is drawn to pass through the mean C_H value at the 40 diameter point. Using the same scheme as that employed in Figure 22, Allen (Ref. 11, p. 84) presented Hartnett's (Ref. 28) heat transfer measurements. These measurements were obtained with conditions similar to those of the test used for Figure 22 but a longer tube was employed. The reference line drawn by Allen was matched to the C_H results in the region of 60 to 70 diameters after the start of heating. The smoothed curve for Hartnett's data gives local C_H values approximately 6.0 percent above the reference line at 5.8 diameters after the start of heating, 2.5 percent at 27 diameters and 1.0 percent at 40 diameters. The $C_H\{x/D\}$ variations shown in Figure 22 are typical of the results obtained in the present experiments, and they are seen to be in close agreement with Hartnett's measurements taken with longer tubes. This agreement implies that very nearly fully established conditions prevail at the last thermocouple station (x/D = 40) for the E-3 tube. A small allowance for the possibility that the thermal entrance effects are not entirely negligible at this station is made

in the error analysis, Cf. Sec. III-E-2. Since it was not the intention in the present work to study entrance effects and since the number of measuring stations are inadequate to shed much light on this subject, only the data taken at the final thermocouple station are presented. The foregoing discussion is included only to indicate how closely the desired, fully established conditions are represented by the E-3 tube results.

An example of the extrapolations used to obtain isothermal C_H values for tube E-3 is presented in Figure 23 wherein C_H is plotted against the wall-to-mixed-fluid temperature difference (ΔT_f) for a Prandtl number of 5.94 (80°F) and Reynolds numbers of 2.44, 4.18, 6.94 and 12.18 x 10^4 respectively. Allen (Ref. 11, p. 57) observed that, for water flowing at 60°F bulk temperature in a smooth tube, the percentage-wise dependence of C_H on ΔT_f is a rather strongly increasing function of Reynolds number. This observation is in dis-agreement with older relationships employing either the $(\mu\{T_L\} / \mu\{T_w\})^{0.14}$ factor or an evaluation of the fluid properties at the "film temperature" $[(T_L + T_w)/2]$ to account for the effects of radial, fluid-property variations. (Cf., e.g., Ref. 29, p. 219). The slopes passed through the experimental points in Figure 23 are taken from Allen's results, and they are seen to correlate the present data within the accuracy of these data. The inadequacy of the $(\mu\{T_L\}/\mu\{T_w\})^{0.14}$ factor for correlating the results is evident from the corresponding slope shown in Figure 23. Also the slope, based on evaluation of properties at the "film temperature" is seen to be an even poorer approximation to the observed slope. In the present experiments, the slope $dC_H/d(\Delta T_f)$ was observed to decrease with increasing bulk fluid temperatures, becoming nearly zero at 290°F. Since the intention

of these experiments is to establish the isothermal condition, the tests were conducted at relatively low ΔT_f values. For this reason and because of the fact that, at most, three points are available for any one Re-Pr combination, the usefulness of the present results as an independent source of experimental information on the influence radial, fluid-property variations on C_H is restricted. Consequently the results presented on this subject are limited to the qualitative remarks of this paragraph.

In Figure 24 and 25 comparisons are made among the C_H results for tube E-3 and the results of other experiments wherein attempts have been made to obtain fully established, isothermal conditions for heat transfer measurements with water flowing in smooth tubes. Figure 24 is carried over from a figure appearing in Allen's thesis (Ref. 11, p. 64) with the addition of the present results which have been extrapolated to Pr = 8.0 to provide a direct comparison with Allen's extensive investigations at this Prandtl number. In this plot the heat transfer coefficient is referred directly to the Dittus-Boelter (Cf., e.g., Ref. 29, P. 219) expression,

$$C_{H_{D-B}} = 0.023 \, Re^{-0.2} \, Pr^{-0.6}$$

The current results are seen to agree with Allen's curve both in magnitude and in Re dependence within the confidence limits prescribed for high Prandtl number conditions in Table 2; to be rigorous, these confidence limits should be broadened somewhat to account for the uncertainty in the above mentioned Prandtl number extrapolation. The current results also agree in magnitude with the results of earlier experiments by Eagle and Ferguson (Ref. 30);

however, a somewhat different Re dependence is apparent. It is noted

that the Eagle and Ferguson results shown in Figure 24 have been ad-

justed to be consistent with the Prandtl number-temperature dependence

which is used for the current experiments and which is essentially

the same as that used by Allen. This adjustment will be discussed

again in the succeeding paragraph. The difference of 5 to 10 percent,

seen in Figure 24, between the present smooth tube results and those

of Hartnett (Ref. 28) and of Hastrup (Ref. 31) is not explained in terms

of assumed uncertainties in the E-3 tube measurements. Considering

the general difficulty in making heat transfer measurements and the

many sources of systematic error such as those itemized in Section

III-E-2, it would be difficult to trace out specific causes for the

small, but nonetheless apparent, discrepancies among these results.

As a final item in Figure 24 it is seen that the Dittus and Boelter equa-

tion, which has great utility because of its simplicity, becomes an

increasingly poor approximation for the present experimental results

as Reynolds number increases.

In Figure 25 the comparisons of smooth tube results are

carried to the Prandtl number dependence. Along with the experi-

mental results of the present investigation and those of Hastrup

(Ref. 31), Eagle and Ferguson (Ref. 30), Allen (Ref. 11) and Nunner

(Ref. 5), the theories of Rannie (Ref. 14) and von Kármán (Ref. 21)

are compared for a fixed Reynolds number of 1.5×10^5. For purposes

of discussion, the C_H results presented in Figure 25 have been divided

by $C_F/2$ for the same Reynolds number. The C_F values determined

in each of the referenced investigations were used in deriving the

respective $2C_H/C_F$ ratios. The C_F values (at Re $= 1.5 \times 10^5$) so

determined are approximately 3.0 percent lower for the Hastrup,

Nunner, and Eagle and Ferguson results than for the Allen results
and the results of the present experiments. The Eagle and Ferguson
results were tabulated in Reference 30 in the form of Reynolds-
number-dependent coefficients for a truncated power series in (Pr-1)
with the stipulation that the resulting expression matched the original
data to $\pm 1/3$ percent. Thus the expression

$$\frac{2C_H}{C_F} = \frac{1}{1.065 + 0.302 \, (Pr-1) - 0.0031 \, (Pr-1)^2}$$

for $Re = 1.5 \times 10^5$ is used to represent their experimental results in
the region of Prandtl number from 3 to 10 over which their measure-
ments were made. As was done for Figure 24, the Eagle and Fergu-
son results presented in Figure 25 have been slightly shifted in the
direction of the Pr axis in order to provide a direct comparison with
the present results. The Prandtl number-temperature function for
water used by Eagle and Ferguson gave somewhat lower values of
Pr at the low temperatures (approximately 4 percent at $T_L = 77^{\circ}F$)
than the function published in Reference 12, p. 498, which is used
to correlate the results of the present experiments.

It is seen in Figure 25 that the Prandtl number dependence
of the adjusted Eagle and Ferguson measurements is very nearly
the same as that observed in the present experiments for the Pr re-
gion between 3.0 and 6.0. The point representing Allen's measure-
ments, which also agrees with the Eagle and Ferguson results, was
obtained by extrapolating the Allen curve in Figure 24 to $Re = 1.5 \times 10^5$.
In Figure 25 as in Figure 24, it is seen that Hastrup's smooth tube
C_H results are consistently lower than the E-3 tube data, the former
being considerably outside of the confidence limits prescribed for

the present results. Hastrup's measurement methods were nearly the same as those used in the present experiments, except that he employed stainless steel tubes. He mentioned that some uncertainty existed in the value of the tube wall thermal conductivity used in his data reduction. An error in assumed conductivity could have induced a systematic error into the computed wall temperature drop and hence into the C_H determination.

The smooth tube theories of Rannie* (Ref. 14) and of von Kármán (Ref. 21), which have been discussed in Section II, are displayed in Figure 25. Both of these theories make use of the assumptions leading to the heat transfer similarity law for smooth tubes, equation 57. For the region of Pr values being investigated, the two theories provide nearly the same predictions, and these predictions are in very close agreement with the results from the E-3 tube. As shown in Figure 25, the experimental point at Prandtl number of 1.20 for the E-3 tube and the point for Nunner's (Ref. 5) measurement with a smooth tube and with air as the working fluid both tend to verify the prediction of the simplified theory based on Reynolds analogy:

$$2C_H/C_F = 1.0 \quad \text{at Pr} = 1.0$$

The discussion presented in Section II would indicate that this good agreement between the simple theories and the experimental measurements is in part due to self-cancellation of the errors introduced with the simplifying assumptions in the theories. If an attempt is made to correct for any one of the assumptions at the exclusion

*See footnote on p. 28 in Section II.

of corrections for the others, the resulting "corrected" theory may exhibit poorer agreement with experimental results.

The final item presented in Figure 25 is the slope on the log-log plot given by

$$2C_H/C_F = Pr^{-2/3}$$

This expression, which is seen to yield very poor correlation with experimental results in the Pr region between 1.0 and 10.0, is often used in connection with heat transfer in smooth tubes. An equally simple power law which closely approximates the experimental results and the theories of Rannie and of von Kármán in this Prandtl number region is

$$2C_H/C_F = Pr^{-0.48} \tag{122}$$

The discussion of the smooth tube results is concluded with the following observations. First, close agreement was observed between E-3 tube results and the results of the more extensive measurements made by Allen at a single Prandtl number. This agreement was established in terms of the dependence of C_H on Re, ΔT_f and x/D. Secondly, the dependence of C_H on Prandtl number for the E-3 tube was found to agree with that observed in the carefully controlled experiments of Eagle and Ferguson. These comparisons with Allen's and Eagle and Ferguson's results are taken as evidence that the experimental methods used in the present work have successfully produced accurate determinations of heat transfer coefficients corresponding to the idealized conditions of isothermal, fully developed flow. Finally, the results of the E-3 tube measurements have

provided additional experimental corroboration of the theoretical expressions derived by Rannie and by von Kármán. The observed dependence of C_H on Prandtl number near a Prandtl number of unity is of particular interest since this was not covered by Eagle and Ferguson's experiments. The agreement of the present results with the theories in this region has direct bearing on the assumptions used in the heat transfer similarity law. This was discussed in Section II.

C. Discussion of Results for Tube D-3

The relatively small roughness height of the D-3 tube was se-
lected primarily to study the heat transfer coefficient in the Reynolds
number region where the transition from smooth-tube-type behavior
to fully rough behavior was observed by Nikuradse. The plot of
C_F{Re} for the D-3 tube in Figure 12 shows that the curve is charac-
teristically similar to the corresponding curve for Nikuradse's sand-
grain roughness having Reynolds number regions of smooth, transition
and fully rough behavior. In the ''smooth'' region, however, the C_F for
tube D-3 remains approximately 8 percent higher than the C_F for
sand-grain pipe.

Colebrook and White (Ref. 32) observed a C_F{Re} profile
quite similar to that of tube D-3 in an artificially roughened pipe.
On the inside surface of their pipe, sand of a uniform size was close-
packed and a uniform dispersion of larger grains was superposed,
the large grains covering only a few percent of the total surface. By
variations of this type of roughness distribution they were able to show
that the dispersed large grains were solely responsible for the increased
C_F in the ''smooth'' region while both the small grains and the large
grains contributed to the C_F level obtained in the fully rough region.
Since the absolute roughness height required for the D-3 tube was
only of the order of one-thousandth of an inch, great care and effort
was required to even approach the attainment of a uniform surface
roughness. It seems quite possible that the existence of dispersed
elements of anomalously large roughness height might have caused
the small observed increase in the C_F level in the ''smooth'' region.

The mean diameter ($d_{sg} = 0.0032$ inch) of the sand used in

making the mandrel for the D-3 tube is given in Table 1 along with

the computed hydraulic equivalent sand-grain roughness ($\epsilon_s = 0.00092$

inch). It had been expected that the roughness height would correspond

to about one-half of the mandrel sand-grain size since the grain inter-

stices on the mandrel were half-filled with lacquer as nearly as could

be judged. This should have given a roughness height, peak-to-valley,

of 0.0016 inch. Brush Surface Analyzer records of samples of the

finished tube, of which Figure 4 is an example, show the roughness

elements obtained to be of the order of 0.0005 to 0.0016 inches. This

implies that the mandrel grains were filled somewhat more than was

expected so that, on the average, a reduced roughness was obtained

in the finished tube. The surface analyzer records are rather im-

perfect measures of the true roughness height both because they

display a straight-line trace of the surface which only occasionally

passes directly over the maximum contour of a roughness element

and because the instrument measures the difference in height between

the position of a rider and the measuring stylus. For the latter rea-

son, often an excessive peak-to-valley measurement and/or an

incorrect profile shape are registered for surfaces having the rough-

ness magnitude of the D-3 tube. The agreement between the computed

ϵ_s value and the coarse measurements by the surface analyzer is

satisfactory; however, no accurate independent check on Nikuradse's

experiments is afforded thereby. Additional information on the D-3

tube roughness was obtained by a close microscopic examination of

the tube-sample surface which showed longitudinal strips of a circum-

ferential width on the order of 30 to 90 degrees of arc where the

roughness height appeared to be less than the average height. This

indicated that the amount of lacquer filling of the sanded mandrel was not perfectly uniform. This observation will be referred to again in the discussion of the C_H measurements.

The composite of the D-3 tube heat transfer results in terms of the circumferential mean C_H is presented in Figure 14 and in Table 5. In order to illustrate the relatively large circumferential variations in C_H that are peculiar to this tube, Figures 26 through 29, given respectively for each of the nominal Pr values, are also presented. In these latter figures the C_H values obtained from two different circumferential locations at the last thermocouple station are plotted. These individual C_{Hx} values, which are also tabulated in Table 5, were derived using the same method of extrapolation-to-isothermal-conditions used in obtaining the mean C_H values. The mean C_H values, plotted in Figure 14, are replotted in Figures 26 through 29. The C_H results from the third circumferential location are not shown since they are nearly the same as the mean values. For purposes of comparison and discussion, the mean $(C_F/2)\{Re\}$ functions for both the D-3 tube and the smooth tube, along with the smooth tube $C_H\{Re\}$ function for the corresponding Prandtl number, are also presented in these figures. Inspection of the plots in Figures 26 through 29 reveals several important features: 1) At low Reynolds number, the C_H values for the D-3 tube are very nearly those of the smooth tube for the same respective Pr values. 2) At low Re values, the C_H values at the three circumferential positions converge to the mean value. 3) As the transition region is approached, the heat transfer coefficient as well as the friction coefficient begins to increase with respect to the corresponding smooth tube coefficients, and

concurrently the local C_H values at the three circumferential positions begin to separate from each other. 4) This trend continues as Re increases until the fully rough condition is approached. And 5), shortly before the fully rough Reynolds number is reached, the separation of the individual C_H values acquires a fixed pattern independent of Reynolds number and of Prandtl number with the C_H values at the number 7 position being approximately 14 percent above and the values at the number 8 position being approximately 14 percent below the mean C_H value.

Considering the low Re region, one sees that, for Re less than about 3.0×10^4, the heat transfer characteristics as well as the momentum transfer characteristic (C_F) are very similar to the respective characteristics of the smooth tube. The detail of this similarity appears also in plots for tube D-3 (not shown herein) of C_H as a function of tube station and the plots of C_H as a function of ΔT_f; both of these plots are nearly identical in all respects to the respective plots for the smooth tube shown in Figures 22 and 23.

The variation in the measured C_H values with circumferential location in the high Reynolds number region persists, with the same circumferential orientation, throughout the length of the heated test section. This fact is illustrated in Figure 30 which shows C_H values computed for each of the nine thermocouple locations for a selected test in the fully rough region. Also seen in Figure 30, a comparison of the mean $C_H\{x/D\}$ line with the bulk temperature reference line* indicates that the thermal entrance effects may not have completely disappeared at the last measurement station. This is typical of the

*The generation of the bulk temperature reference line is discussed in Section IV-B in connection with Figure 22.

E-3 and the D-3 tubes and has been accounted for in the error analysis.

The most probable explanation for the observed circumferential variation in C_H values for the D-3 tube is that slight anomalies in the surface roughness exist which are sufficient to cause non-uniform shear stress and heat transfer film conductance. The conclusion that deviations of this magnitude are not due to individual thermocouple errors or to local variations in the tube wall composition or thickness is implied by the error analysis of Section III-E-2. This conclusion is further substantiated by the facts that the C_H spread is observed to be independent of heat flux and that, at the low Reynolds numbers, the spread is nonexistent. The possibility was considered that the small non-concentricity between the smooth center-pressure-tap area* and the rough test section could cause a distortion in the fluid velocity profile leading to the observed effects. However, it seems doubtful that such a locally induced distortion would propagate undiminished for 40 diameters down the tube and that this would hold true over a large range of Reynolds numbers. Following the main series of tests, a check for the possibility that a ridge might have been formed into the tube at the exit end of the smooth pressure-tap area was made by passing an expandable reamer through the entrance section and into the pressure-tap region. No evidence of a ridge was found, and following the reaming operation, several of the heat transfer tests were repeated with no significant changes from the previous tests being observed.

Under the hypothesis that circumferential variations in roughness are responsible for the observed differences in local C_H values,

---

*See Appendix I for details on the tube construction.

an estimate of the roughness variation necessary to produce these results can be made. First it is noted that, for the Reynolds number range of interest, the radial gradients of velocity and temperature are concentrated in a region very close to the wall. Thus it is assumed that there exists little interaction between circumferentially adjacent parts of the wall exhibiting small differences in shear stress. Further, it is assumed that, for each circumferential region of wall with a particular roughness, the velocity outside of the wall region corresponds to the velocity that would be attained in a tube of the same diameter having this particular roughness over its entire surface. This reasoning is essentially similar to that used in ascertaining the turbulent friction coefficients in non-circular ducts from circular tube data by use of the so-called hydraulic diameter.

On the basis of this model, the Stanton number (C_{Hi}) measured in a particular roughness region, is that which would be obtained in a tube having this same roughness throughout and operating at fully established conditions with the same discharge velocity (u_m). Using the cross correlation, to be developed in Section IV-F, for C_H as a function of ϵ/D at given Re and Pr, it is possible to estimate the circumferential variations in roughness height necessary to produce the C_{Hi} variations of ± 14 percent observed for tube D-3. The result is that a percentage variation in the roughness height of approximately three times the percentage variation in C_{Hi}, i.e. ± 42 percent, is required to explain the observations. Based on the mean equivalent sand-grain roughness of 0.00092 inch, this implies that the roughness height varied from 0.0005 to 0.0013 inch in the

circumferential direction. As discussed previously in this section, roughness variations of this order were observed and could have come about due to inaccurate distribution of the lacquer used to fill the grain interstices on the tube mandrel. The lacquer was sprayed in longitudinal traverses which may explain the fact that the same circumferential pattern in C_{Hi} values extends throughout the test section.

One of the purposes of the present investigation is to provide a comparison between the heat transfer and momentum transfer coefficients at various ϵ/D, Re and Pr values. For use in the cross comparisons among the results of the three rough tubes, the D-3 tube is identified with the ϵ_s/D value determined from the measured friction factor at high Reynolds number. There is no way to clearly determine which of the three measured local C_{Hi} values most closely corresponds to the surface-averaged C_F determined from the tube pressure drop, since the portion of the tube surface area represented by any of the measured C_{Hi} values is unknown. Thus the three C_{Hi} values are treated as random samples from a distribution of surface roughness conditions, and the mean value of the three C_{Hi} values is taken as a measure of the Stanton number corresponding to the measured C_F. From the various inspections and measurements of the samples taken from the finished tube and from the preceding discussion on the sensitivity of the variations in C_{Hi} to variations in roughness, it is concluded that the observed circumferential variations in C_{Hi} represent nearly the maximum variations in roughness occurring in the D-3 tube. Thus it is assumed that the observed spread in the

C_{Hi} values represents the maximum uncertainty in the $\overline{C}_{Hi}$ point average as a measure of the desired, area-averaged Stanton number. Thus $\pm$ 14 percent is used in Section III-E-2 as the "roughness error" ($\% \delta$ R.E.) for the D-3 tube operating at high Reynolds numbers. Thus, for the cross comparisons, a relatively large over-all uncertainty of as high as $\pm$ 17 percent (at high Re; low Pr) is allowed for the heat transfer results of the D-3 tube.

It is important to note that the relatively large uncertainties ascribed to the D-3 tube results do not apply directly to the "form" of the measured $(C_H/C_F)\{Re;Pr\}$ dependence. Within the assumptions of non-interaction between adjacent wall regions as used in the preceding discussion, each arc of wall having a particular roughness characteristic gives the same $C_H \{Re, Pr\}$ function as would be obtained if the wall had this particular roughness throughout. Thus the $C_{Hi}\{Re, Pr\}$ measured at any of the thermocouple locations gives a meaningful functional form; the uncertainty exists only as to what local roughness is represented by C_{Hi} and what local C_{Fi} corresponds to the C_{Hi}. Thus the effective, area-averaged $C_H\{Re, Pr\}$ function, that corresponds to the measured mean $C_F\{Re\}$ and the ϵ_s/D deduced from the mean C_F, is expected to run consistently between some pair of the measured $C_{Hi}\{Re, Pr\}$ functions. That is, in the case of the Re dependence shown in Figures 26 through 29, this effective, area-averaged $C_H\{Re\}$ for a given Pr is expected to run more or less parallel to the average $\overline{C}_{Hi}$ curve shown, and the area-averaged curve is expected to lie somewhere between the extreme $C_{Hi}\{Re\}$ curves. Thus even though the level of the effective curve is given a large uncertainty, the curve is not expected to change

its relative position between the uncertainty limits as Re is changed.

The same arguments hold for the cross plots of Figures 26 through

29 at fixed Re values. From comparisons among these figures it

can be seen that the relative percentage spread between the individual

C_{Hi} curves at a fixed Re is nearly independent of Pr such that the

cross plots on log-log paper will show a series of nearly parallel

lines. The shape of the desired area-averaged $C_H\{Pr\}$ curve is

thus closely represented by the average of the three measured

$C_{Hi}\{Pr\}$ curves.

The discussion is now returned to the general D-3 tube results

and to the relationships of heat and momentum transfer in the transi-

tion region which are given by these results. First it is noticed that

the sensitivity of the heat transfer coefficient to wall roughness

appears to increase with Prandtl number in the transition region.

The shift in the $C_F\{Re\}$ curve away from the smooth type behavior

(Cf. Figures 26 through 29 and Figure 14) appears to be anticipated

at a lower Reynolds number by the $C_H\{Re\}$ curves for high Pr values.

In connection with this observation, there is a region in the curves

for Prandtl number equals 5.94 and 4.38 respectively where C_H is

increasing with increasing Re while C_F is still decreasing.

A second interesting relationship is apparent from a com-

parison of the E-3 and D-3 curves for $(2C_H/C_F)\{Pr;Re\}$ in Figure

21 and the curves for $(2C_H/C_F)\{Re;Pr\}$ in Figures 17 through 20.

In Figure 21 it is seen that the values of $2C_H/C_F$ increase with re-

spect to those for the smooth tube as Prandtl number is increased,

and at the high Pr values, the roughness of tube D-3 has a greater

effect on C_H than on C_F such that the ratio $2C_H/C_F$ exceeds that of

the smooth tube. This enhancement of C_H relative to C_F is peculiar

to operation in the transition region. The dependence of $2C_H/C_F$ on

Re shown in Figures 17 through 20 displays the general tendency of

these values for tube D-3 to rise faster with increasing Re near the

beginning of the transition region than the $2C_H/C_F$ values for the

smooth tube. Then as transition nears completion the tube D-3 curves

fall away from the respective smooth tube curves. The latter behav-

ior, which is typical of the results from the other rough tubes, can

only be seen for tube D-3 at a Prandtl number of 1.20 whereat Rey-

nolds numbers in the fully rough conditions are attained.

The discussion of the D-3 tube results is summarized as

follows. The heat transfer measurements on this tube are of some-

what poorer quality than those of the other tubes. This is primarily

due to the difficulties involved in producing a uniform roughness of

the small scale required for measurements in the transition region

with the tube diameter used for these experiments. A definite transi-

tion region was observed for the D-3 tube with a $C_F\{Re\}$ character-

istic not too unlike that obtained by Nikuradse for sand-grained sur-

faces, and several important features of the heat transfer charac-

teristics for this region were also noted. It was found that, in the

region of smooth-type friction, the heat transfer coefficient is simi-

lar to that of a smooth tube. Then, as the Reynolds number is

increased and the friction coefficient rises above the smooth tube

curve, the heat transfer coefficient also rises, this effect being

more pronounced at high Prandtl number. Finally, as the transition

to fully rough behavior nears completion the heat transfer coefficient

forms a maximum and again starts to decrease with increasing Rey-

nolds number. In the D-3 tube results, this formation of a maximum

is only weakly implied by making comparisons of $C_H\{Re\}$ curves at different Pr values; however, the existence of such a maximum is substantiated in the comparisons with the other rough tube results in Section IV-F. One of the most interesting observations from the D-3 tube results is the presence of maxima in the $(2C_H/C_F)\{Re\}$ curves which occur in the transition region. For high Pr values, the $2C_H/C_F$ values in the region of these maxima even exceed the respective smooth tube values.

D. Discussion of Results for Tube C-9

The intermediate roughness of the C-9 tube provides information on the heat transfer characteristics near the high Reynolds number portion of the transition region and over an appreciable segment of the fully rough region. The friction factor versus Reynolds number curve (Cf. Figure 12) for the C-9 tube closely resembles the Nikuradse function for an equivalent sand-grain roughness ratio (ϵ_s/D) of 0.0138. The presence of a distinct rise in C_F with Reynolds number at low Re values implies that a definite scale of roughness height exists in the C-9 tube. As was mentioned in Section IV-A, Colebrook showed that, in natural pipe surfaces where many scales of roughness coexist, C_F decreases monotonically with Reynolds number in such a way that the fully rough condition is approached asymptotically. The small rise of approximately 6 percent in the C_F {Re} curve which occurs for Re greater than about 2×10^5 may be indicative of a roughness shape in the C-9 tube which is somewhat different from that of Nikuradse's pipes.

As shown in Table 1, the mean sand grain size used to make the mandrel for tube C-9 was approximately 0.0075 inch; whereas the hydraulic equivalent sand-grain size for the finished tube is 0.00542 inch. This could be taken to imply that the grains on the mandrel were filled with lacquer to approximately one-third of the height of the grains, an implication which is not unreasonable. However, another possibility exists. Friction experiments were performed by Schlichting (Ref. 18, p. 424) using a wide rectangular duct with various regular arrays of roughness elements distributed on one of the long side-walls. In these experiments velocity profiles were

measured to establish the height of Nikuradse's sand roughness which would produce the same logarithmic velocity profile. For one case investigated by Schlichting, spherical segments with height equal to 0.65 of the spherical radius were placed close-packed on the wall with the result that the hydraulic equivalent sand-grain size was 1.40 times the height of the segments. This illustrates that roughness shapes differing only slightly from sand grains can give appreciably different friction for the same roughness height. Since the roughness used in the present work is definitely of different shape than sand grain roughness, it could well be that the relatively large hydraulic equivalent sand roughness of the C-9 tube is due to the shape and not to the height of the roughness. Measurements of the maximum peak-to-valley excursions on cross sections of the C-9 tube such as are shown in Figure 3 give support to this reasoning.

A typical example of the local variation of the heat transfer coefficient for the C-9 tube is shown in Figure 31. The relatively wide circumferential dispersion at the first thermocouple station is most probably due to an asymmetrical disturbance in the main flow generated by a slight non-concentricity of the upstream pressure-tap region. At the two downstream stations, this disturbance is seen to have damped out. A comparison of the average C_H line to the bulk temperature reference slope shows that fully established flow conditions are nearly attained at 26 diameters downstream from the start of heating.

The $C_H\{Re; Pr\}$ plots of Figure 15 will be discussed next. A rise in C_H with increasing Re is clearly evident in the transition

region where C_F is also rising; this is commensurate with the behavior of the D-3 tube. As transition is completed and the $C_F\{Re\}$ function assumes a nearly constant value, the $C_H\{Re\}$ function attains a maximum and begins to decrease as Reynolds number increases. This deviation of the $C_H\{Re\}$ dependence from that of the $C_F\{Re\}$ in the fully rough regime is shown more directly in the $(2C_H/C_F)\{Re\}$ plots of Figures 17 through 20. In the figures, as in the D-3 tube results, the $2C_H/C_F$ values for the rough tube exceed those of the smooth tube in the transition region at the higher Prandtl numbers; whereas the rough tube value progressively falls away from the smooth tube results as Re is increased into the fully rough region.

The cross plot of these $2C_H/C_F\{Re;Pr\}$ curves is shown in Figure 21. The Reynolds number (1.5×10^5) for this cross plot is well into the fully rough region for tube C-9. As Prandtl number increases, the $2C_H/C_F$ ratio for the C-9 tube increases with respect to the same ratio for the smooth tube. This effect is not as pronounced as in the case of the D-3 tube which is operating in the transition region at Reynolds number of 1.5×10^5.

It is clearly evident from the tube C-9 results that the heat transfer coefficient is still strongly dependent on Reynolds number and Prandtl number in the fully rough region. Thus, C_H is still dependent on the molecular transport properties even though the friction factor (C_F) is independent of the molecular shear stress coefficient (viscosity). This will be discussed further in Section V.

E. Discussion of Results for Tube A-4

The A-4 tube was produced and tested to determine the heat transfer characteristics in the fully rough regime over a wide range of Reynolds numbers. The friction factor obtained for this tube (Cf. Fig. 12) is somewhat greater than that of the roughest pipe tested by Nikuradse. The fully rough condition extends throughout the most of the Reynolds number range tested. The slight drop in the $C_F\{Re\}$ function at low Reynolds number occurs close to the point predicted for the equivalent sand-grain roughness. A slight rise in the $C_F\{Re\}$ function, similar to that observed for the C-9 tube, occurs at the high Reynolds number end of the curve.

The equivalent sand grain size for the A-4 tube (0.0195 inch-diameter) is larger than the mean grain size (0.015 inch-diameter) used in producing the tube mandrel. It is estimated that the grain interstices on the mandrel were filled with lacquer to 10 to 20 percent of the grain diameter so that the roughness height in the A-4 tube is approximately 0.013 inch. Thus the A-4 tube roughness has about the same hydrodynamic effect as a sand grain surface of 50 percent larger roughness height. As proposed in the discussion of the C-9 tube (Sec. IV-D), this is most probably due to the non-similarity between the shape of Nikuradse's sand grains and shape of the roughness elements obtained in the tubes of these experiments.

An example of the local C_{Hx} distributions for the A-4 tube is shown in Figure 32. The relatively wide dispersion of the local measurements for this tube is attributed primarily to variations of heat transfer coefficient measured at random locations on the

roughness elements. This effect, which is discussed in Section
III-E-2, is responsible for the larger uncertainty allowed in Table
2 for the A-4 tube results as compared to that of the C-9 tube. The
distribution of the individual C_{Hx} values shown in Figure 32 varies
to some extent with the Reynolds and Prandtl numbers of the other
tests, but in all tests the line joining the mean $\overline{C_{Hx}}$ values at each
longitudinal station indicates that fully established conditions are
prevalent throughout the heated test section.

Several observations can be made concerning the isothermal,
fully established C_H values presented for the A-4 tube. The plot
of $C_H\{Re;Pr\}$ in Figure 16 shows that the fall off of C_H with increas-
ing Reynolds number observed in the tube C-9 results is continued
farther into the fully rough regime. Figure 20 shows that, even
for this very rough tube, the $(2C_H/C_F)\{Re\}$ values for Prandtl num-
ber of 5.94 exceed those of the smooth tube near the transition
region which is being approached at the low Reynolds numbers. In
Figure 17 one sees that this high C_H/C_F performance of the very
rough tube relative to the smooth tube is no longer evident at low
Prandtl number (1.20). Even if the $(2C_H/C_F)\{Re\}$ curve is extrapo-
lated back to the transition region, it does not appear that the
$2C_H/C_F$ values will exceed those of the smooth tube. In Figure 21,
the $(2C_H/C_F)\{Pr\}$ dependence for the A-4 tube is seen to be very
similar to that of the C-9 tube. This might have been expected since,
at Reynolds number of 1.5×10^5 used as the basis for this plot, both
tubes are operating in the fully rough regime.

F. Collective Comparisons of Results

In Section II it was shown by means of a similarity analysis and certain simplifying approximations that the general experimental task of finding the four-variable dependence $C_H\{Re, Pr, \epsilon/D\}$ can be reduced to finding a three-variable dependence,

$$\frac{(C_F/2\,C_H)-1}{\sqrt{C_F/2}} = g\,\{\epsilon^*, Pr\} - A \tag{54}$$

insofar as geometrically similar roughness shapes are being considered. The assumptions used to generate equation 54 are closely related to assumptions successfully used in certain smooth pipe theories for Prandtl number greater than 0.6. These smooth pipe theories contain the expression

$$\frac{(C_F/2C_H)-1}{\sqrt{C_F/2}} = F\{Pr\} \tag{57}$$

Thus, as similarity parameter ϵ^* approaches low values where the rough tubes of the type being investigated give the same heat transfer and friction characteristics as a smooth tube, the quantity $(g\,\{\epsilon^*, Pr\} - A)$ should approach $F\{Pr\}$ thus becoming independent of ϵ^*.

From this deduction and to the extent that the roughness elements in the three pipes of these experiments are geometrically similar, it should be possible to plot the group

$$(\frac{C_F}{2C_H} - 1)\,/\sqrt{C_F/2}$$

for all of the rough tubes as a function of

$$\epsilon^* \equiv (Re\,\sqrt{C_F/2}\,\,\epsilon/D)$$

resulting in a single valued function for each fixed Prandtl number.

Before presenting such a plot, consideration must be given to the observation that the mandrels used for making the three rough tubes apparently contained successively smaller percentages of lacquer filling as the roughness scale increased. This fact is deduced from the comparison in Table 1 of the mean sand-grain size (d_{sg}) used to make the mandrels with equivalent sand-grain roughness for the finished tubes (ϵ_s) as determined by the friction measurements. This variation in the amount of lacquer filling on the mandrels was in part intentional in order to obtain as small a resulting roughness as possible commensurate with the smallest mandrel grains that could be readily produced. To a certain extent, however, the increased filling of the smaller grains was unavoidable with the lacquer spraying techniques employed and with the necessity of having some lacquer in all of the interstices. Thus it is seen that the roughness shapes in the three tubes are not exactly geometrically similar even though the mandrel sand grains were statistically similar. This defect in the finished tubes is partially overcome, for purposes of the cross comparisons of the heat transfer coefficients, by assigning the equivalent sand grain roughness to each tube.

As given by the friction similarity law (Eq. 26) discussed for any set of tubes with geometrically similar roughness elements,

$$B \, \ell n(2\epsilon/D) = A\{\epsilon *\} \; -\beta \; - \frac{1}{\sqrt{C_F/2}} \tag{123}$$

where B and β are constants and where $A\{\epsilon *\}$ is constant in the fully rough regime. Thus the ratio of the ϵ/D values for two different tubes with similar roughness shape must bear a definite

relation to the fully rough friction factors ($C_{F\,F.R.}$) regardless of the particular type of roughness being considered. Thus from equation 123 one can write

$$\ln \frac{(\epsilon/D)_a}{(\epsilon/D)_b} = \frac{1}{B}\left[\frac{1}{\sqrt{(C_{FF.R.})_b/2}} - \frac{1}{\sqrt{(C_{FF.R.})_a/2}}\right] \qquad (124)$$

where the subscripts "a" and "b" refer to any two tubes respectively. This must be true, independently of the function $A\{\epsilon*\}$ which characterizes the particular "shape" of the roughness elements under study. The Nikuradse sand-grain surfaces were found to obey the relationship in equation 123 and hence equation 124. Therefore, by associating the Nikuradse equivalent sand-grain size (ϵ_s) with each of the tubes of these experiments, equation 124 is forced to apply to the present results, and thus the satisfaction of the similarity requirements for the friction behavior is assured before attempting to show that the similarity requirement for heat transfer is valid. Having established ϵ_s/D from the $C_{F\,F.R.}$ value of any tube, the remaining $C_F\{Re\}$ function for Nikuradse's sand-grain roughness is generated by using his $A\{\epsilon*\}$ function in equation 123. The degree to which these $C_F\{Re\}$ functions for the sand-grain type of roughness also describe the transition-region behavior of the present tubes is shown by good agreement between the solid and the dashed lines in Figure 12.

Using the equivalent sand-grain roughness, the results from all of the tubes of this experiment are then presented in Figure 33 in which

$$\frac{(C_F/2C_H)-1}{\sqrt{C_F/2}} + 8.48 \equiv g\{\epsilon*;Pr\} \qquad (125)$$

is plotted for the four Prandtl numbers investigated and where $\epsilon*$ is defined

$$\epsilon^* \equiv \text{Re}\sqrt{C_F/2}\,(\epsilon_s/D) \tag{126}$$

The constant 8.48, which is the value of Nikuradse's $A\{\epsilon^*\}$ for the fully rough condition, is included in the definition of $g\{\epsilon^*;Pr\}$ for convenience in comparing the results with the theoretical reasoning to be presented in Section V. The "g" values for the smooth tube can be represented by Rannie's theory (Ref. 14) which was shown by Figure 25 to correlate the results of the E-3 tube. Thus for the smooth tube

$$g = F\{Pr\} + 8.48$$

where $F\{Pr\}$ is the function developed by Rannie. Since this is independent of ϵ^*, the result is represented by short horizontal lines at the low ϵ^* end of the curves in Figure 33. These lines then represent the asymptotes of the rough tubes results insofar as the heat transfer and friction coefficients approach the smooth tube behavior at low Reynolds number.

The fact that the curves generated in Figure 33 by the data points of the three tubes of differing roughness are nearly continuous is regarded as a significant substantiation of the similarity rule, $g\{\epsilon^*;Pr\}$, developed in Section II. At Prandtl number of 1.20, the match between the results of the different tubes is excellent, while at the highest Prandtl number some discrepancy between the tube C-9 and the tube A-4 points is apparent in the region of overlap. To ascertain the significance of this discrepancy, it is first noted that, at Prandtl number of 5.94, a one percent variation in "g" implies 0.75 to 0.90 percent variation in C_H, and at Prandtl number of 1.20,

a one percent variation in "g" implies 0.44 to 0.88 percent variation

in C_H. Thus the maximum spread of approximately 10 percent in the

"g" values for the C-9 and A-4 tubes at Prandtl number of 5.94 in

the region of overlap corresponds to approximately 9 percent C_H dis-

crepancy. As seen in Table 2, the uncertainty in the tube A-4 results

at the low Reynolds number is approximately $\pm$ 5 percent and the un-

certainty for the C-9 tube at high Re values is approximately $\pm$ 3

percent. Thus some of the 9 percent discrepancy could be attributed

to systematic errors in the measurements. The remaining discrep-

ancy could be a result of the slight lack of similarity between the

roughness shapes of these two tubes. The fact that the D-3 tube data

points blend so well with the extensions of the C-9 and A-4 tube re-

sults shows that the identification of a roughness scale selected to

meet the friction similarity requirements with tubes having slightly

dissimilar roughness shapes leads to a successful correlation of the

heat transfer results. This will be shown again in the discussion of

Nunner's results in Section VI.

The ϵ^* abscissa in Figure 33 is the same parameter with

which the various regimes of the friction behavior of rough tubes

is described. For ϵ^* less than about 3.5, Nikuradse (Ref. 10) found

sand-grained tubes to have nearly the same friction characteristics

as smooth tubes. Between ϵ^* values of 3.5 and 67 he found a tran-

sition region, and for ϵ^* greater than 67 he observed the fully rough

condition. Figure 33 shows that these regions also have significance

for the $g\{\epsilon^*; Pr\}$ functions. For the low ϵ^* values, the D-3 tube

points are seen to approach the respective smooth tube lines, ap-

pearing slightly above the latter for all four nominal Pr values.

The transition region for the higher Pr values is characterized by the formation of a minimum near the high $\epsilon*$ end of the region. At Prandtl number of 1.20, the $g\{\epsilon*\}$ function rises monotonically in the transition region. In the fully rough region the $g\{\epsilon*\}$ curves for the various Prandtl number values become parallel on the log-log plot and tend toward a fixed positive slope.

By the use of the empirically established $g\{\epsilon*;Pr\}$ functions of Figure 33, it is now possible to predict the desired $C_H\{Re,\epsilon/D;Pr\}$ functions for this general type of roughness over a much wider range of Reynolds number than was investigated for any particular tube. Further it is possible to interpolate the $C_H\{Re;\epsilon/D;Pr\}$ functions for ϵ/D values other than those for the three rough tubes investigated. Inverting the definition of "g" (Eq. 125) there is obtained

$$C_H\{Re,\epsilon/D;Pr\} = \frac{C_F\{Re,\epsilon/D\}/2}{[\,C_F\{Re,\epsilon/D\}/2\,]^{1/2}[\,g\{\epsilon*;Pr\}-8.48\,]} \tag{127}$$

where

$$\epsilon* \equiv (\epsilon/D)\,Re\,[C_F\{Re,\epsilon/D\}/2]^{1/2} \tag{128}$$

Thus a knowledge of the $C_F\{Re,\epsilon/D\}$ function and the $g\{\epsilon*;Pr\}$ function is sufficient to determine C_H for a given type of roughness. Further, the $C_F\{Re,\epsilon/D\}$ is given by the friction similarity law (Eq. 26) once the $A\{\epsilon*\}$ function for the given roughness type has been established. The plots of $C_H\{Re;\epsilon/D\}$ shown in Figures 34 and 35, for Prandtl numbers of 1.20 and 5.94 respectively, were generated from the smoothed $g(\epsilon*;Pr)$ curves of Figure 33 and the $A\{\epsilon*\}$ function for Nikuradse's sand-grain roughness. Additional discussion of these extensions of the results will appear in Section VII.

The C_H values predicted from the $g\{\epsilon*;Pr\}$ functions for Reynolds numbers below about 2300 are of course meaningless since, as Nikuradse showed, completely laminar flow occurs in this region for all roughness ratios, and hence the analysis used in generating the "g" function becomes inapplicable.

In the fully rough region, the $g\{\epsilon*;Pr\}$ function can be represented by a simple exponential relationship. This is clearly indicated in Figure 36 wherein the $g\{\epsilon*;Pr\}$ experimental points from Figure 33 have been multiplied by the respective values of $(Pr)^{-0.44}$. The congruence of the points shows that the exponential form quite adequately describes the Prandtl number dependence not only in the fully rough region but also in part of the transition region for the higher levels of Prandtl number. For the fully rough region, the $g(Pr)^{-0.44}\{\epsilon*\}$ function is closely approximated by the straight line of slope 0.20 shown in Figure 36 so that a simple analytical function can be written:

$$g_{F.R.} = 5.19 \, (\epsilon*)^{0.20} \, (Pr)^{0.44} \tag{129}$$

Entering this in equation 127 gives a complete analytical relation between the heat transfer and friction coefficients for tubes having the roughness type investigated herein and operating in the fully rough regime:

$$C_{HF.R.} = \frac{C_{FF.R.}/2}{1 + \sqrt{\frac{C_{FF.R.}}{2}} \left[5.19 \left(Re \sqrt{\frac{C_{FF.R.}}{2}} \frac{\epsilon_s}{D} \right)^{0.20} (Pr)^{0.44} - 8.48 \right]} \tag{130}$$

where

$$\epsilon_s/D = \exp\left\{(3.0 - \frac{1}{\sqrt{C_{FF.R.}/2}})/2.5\right\} \qquad (131)$$

Equation 131 is an inversion of the friction similarity law (Eq. 26) for the equivalent sand-grain roughness ratio.

Discussion of the collective comparisons of the experimental results as culminated in Figure 36 will be continued in the next section, "Interpretation of Results."

V INTERPRETATION OF RESULTS

Several analytical forms for predicting the relationships of heat transfer from rough surfaces have been suggested. Some of these are based on certain auxiliary experimental observations while others are the result of deduction supplemented by considerable conjecture. None of these theories considered herein adequately prescribe all aspects of the results from the present experiments. In this section an attempt will first be made to explain the similarity parameter for heat transfer in terms of the results of these experiments. Secondly, several of the previously existing theories for rough tube heat transfer will be discussed within the context of the heat transfer similarity law and the experimental results.

A. <u>Physical Interpretation of the Similarity Parameter for Heat Transfer</u>

The similarity arguments presented in Section II lead to the reduction of the general four-variable relationship for heat transfer in pipes having geometrically similar roughness elements, $C_H\{Re, \epsilon/D, Pr\}$, to the three-variable relationship, $g\{\epsilon*, Pr\}$. This simplification, which is supported by the results of the present experiments, greatly reduces the problem of empirically determining the heat transfer coefficient for a range of the variables Re, ϵ/D and Pr. In the same manner this simplified relationship is most useful for interpreting the experimental observations. Thus it will be convenient to discuss the experimental results in terms of the functions $g\{\epsilon*; Pr\}$ or $g(Pr)^{-0.44}\{\epsilon*; Pr\}$ shown in Figures 33 and 36 respectively.

For the low $\epsilon*$ region, it was expected that the rough tube would show heat transfer characteristics nearly equal to those of a smooth tube for the same reasons that Nikuradse found the friction characteristics to be independent of roughness in this region. It is assumed that for low $\epsilon*$ the nearly laminar flow zone next to the wall is so thick compared to the height of the roughness elements that the fluid velocity near the elements is very low. Thus the flow disturbance caused by the presence of the elements is negligible. Further, under conditions of heat transfer, the temperature drop in the immediate neighborhood of the roughness elements is expected to be negligible compared to the temperature drop across the laminar zone. Thus the rough tube is expected to exhibit all of the smooth tube characteristics as $\epsilon*$ becomes small. In terms of the heat transfer similarity parameter this implies, as shown in equation 57, Section II, that

$$g\{\epsilon*, Pr\} = F\{Pr\} + 8.48$$

as $\epsilon *$ approaches zero. The function $F\{Pr\}$ is the smooth tube integral given by equation 48. The D-3 tube results have confirmed this expectation as shown by the close approach of the $g\{\epsilon *; Pr\}$ curves to the respective $(F\{Pr\}+8.48)$ values at low $\epsilon *$. The value of the function $(F\{Pr\}+8.48)$ is indicated by the dashed lines on the left hand sides of Figures 33 and 36. The failure of the curves to match the $F\{Pr\}$ values exactly can be attributed to the observed deviation of the $C_F\{Re\}$ curve for tube D-3 from that of the smooth tube in the low Reynolds number region where smooth-type behavior should have been in evidence (Cf. Fig. 12). This was explained in Section IV-C as possibly being due to surface imperfections in the D-3 tube.

Because of the complex nature of the flow which occurs for $\epsilon *$ values in the transition region, it is difficult to carry any interpretations of the $g\{\epsilon *, Pr\}$ function for this region much farther than to say that a continuous evolution from the smooth-type behavior to the fully-rough-type behavior should occur. That such a continuous conversion of the "g" factor dependence on Pr and $\epsilon *$ does characterize the transition region is clearly evident in the $g(Pr)^{-0.44}\{\epsilon *; Pr\}$ plots of Figure 36. In the transition region, the dependence of "g" on $\epsilon *$ changes from essentially no dependence in the "smooth" region to $\epsilon *^{0.20}$ in the fully rough region for all Prandtl numbers. Also in the transition region, the Pr dependence changes from $(F\{Pr\}+8.48)$ for the "smooth" region to $(Pr)^{-0.44}$ for the fully rough region.

The following heuristic description of the flow in the transition region provides a qualitative explanation for the observed C_F and C_H behavior. As Reynolds number, and hence also $\epsilon *$, is increased beyond the "smooth" region, the wall layer, in which the

molecular momentum transport is paramount, becomes progressively
thinner. Concurrently, the mean fluid velocity in the vicinity of the
tips of the roughness elements becomes greater until the flow begins
to separate from the highest of the elements. This instigates a sec-
ondary flow, perhaps intermittent, in the neighboring roughness
cavities and also sheds vortices into the stream, thus introducing
disturbances into the laminar wall layer. The improved momentum
exchange due to this added turbulence brings the mean wall shear,
and hence C_F, to a larger value than would be attained in a smooth
tube at the same Reynolds number. As Re is further increased, sepa-
ration occurs at all elements, the laminar layer is disintegrated and
the turbulent momentum-exchange-coefficient becomes dominant
right to the tips of the elements. The increased turbulence also de-
creases the thermal resistance of the laminar region leading to an
increase in the rough tube C_H over that of a smooth tube. At higher
Prandtl numbers, a greater percentage of the total radial tempera-
ture change occurs in the layer close to the wall; hence at high Pr
values the heat transfer coefficient is more sensitive to the amount
of turbulence in the so-called laminar layer. The supplementary
disturbance in this layer induced by the roughness then has relatively
more effect on C_H for a high Pr condition than for low Pr. This
Prandtl number sensitivity was observed for the rough tubes of this
experiment operating in the transition region.

An attempt to explain the transition region $g\{\epsilon^*, Pr\}$ function
in terms of the functions appearing on the right hand side of equation
55 of Section II does not look promising. In the transition region,
some laminar flow external to the roughness persists. However, the
amount and distribution of eddy viscosity in this part of the flow is

changed from that of a smooth tube because of the turbulence being shed at some of the roughness elements from which separation is beginning to occur. This is further complicated by the interaction of the rough under-surface with the turbulence being generated near the outer edge of the laminar layer. From this discussion it appears difficult if not impossible to establish, other than by direct measurement, the way in which the mean axial velocity distribution changes from the log profile in the fully turbulent, outer flow to the velocity, u_g, at the tips of the roughness elements. Thus the $F\{Pr, \epsilon^*\}$, and $(u_g/u_\tau)\{\epsilon^*\}$ functions in equation 55 cannot be predicted, and without (u_g/u_τ), the boundary condition needed for determining the cavity Stanton number (C_{H_c}) is not established.

Turning to the fully rough region, one finds the problem of quantitatively interpreting the results to be a little less formidable. Here the complete $g\{\epsilon^*, Pr\}$ dependence is experimentally found (Cf. Sec. IV-F, Eq. 129) to be well represented by the simple exponential variation

$$g_{F.R.}\{\epsilon^*, Pr\} = 5.19 \, (\epsilon^*)^{0.20} \, (Pr)^{0.44} \qquad (129)$$

Also, by the development presented in Section II, the complex of terms on the right hand side of the theoretical equation 55 simplifies in the fully rough region to yield

$$g_{F.R.}\{\epsilon^*, Pr\} = \frac{1}{8.48 \, C_{H_c}\{8.48\epsilon^*, Pr\}} \qquad (56)$$

Hence the problem of theoretically interpreting the experimental $g\{\epsilon^*, Pr\}$ results for fully rough conditions is reduced to that of finding a theoretical expression for the roughness-cavity Stanton number

that corresponds to the expression in equation 129.

In Appendix VII, a model for the flow conditions in the roughness cavities called the turbulent vortex hypothesis is presented. The assumptions for this model are developed as follows. In the fully rough region the so-called laminar boundary layer is completely disrupted and the realm of sensible, molecular momentum and heat transport is relegated to a very thin layer at the surfaces of the cavities formed by the roughness elements. The flow becomes separated from the elements producing a drag due to surface pressure distribution which far exceeds the effects of shear in the local cavity boundary layers. Roshko (Ref. 33) has confirmed this picture by direct measurements of the pressure distribution and shear stresses inside of a two-dimensional, rectangular cutout on a flat plate. Then, since the pressure distribution on the cavity walls and hence the friction factor (C_F) is dependent on the geometry of the flow in the cavity and since C_F is independent of Reynolds number in the fully rough region, it is concluded that the time averaged flow pattern in the cavities is independent of Reynolds number. Thus for a given type of roughness, a particular pattern of standing vortices are thought to exist between the roughness elements, and further, this mean flow pattern is assumed to contain considerable turbulence. Arguments are presented in Appendix VII to show that the principal thermal resistance of the cavities is concentrated in the thin boundary layers formed on the cavity walls.

The complete prediction of the cavity Stanton number, and hence of the $g_{F.R.} \{\epsilon^*, Pr\}$ function is dependent on a knowledge of the boundary layer characteristics, viz., the dependence of heat transfer coefficient on Prandtl and Reynolds numbers for boundary

layers formed near the stagnation points on bodies immersed in highly turbulent streams. Such information is not presently available. However, as shown in Appendix VII, reasonable guesses as to the behavior of these boundary layers lead to predicted values of $g_{F.R.}\{\epsilon^*, Pr\}$ which are of the same order-of-magnitude as the observed values given in equation 129. This crude check is used as evidence that the concepts of a turbulent vortex model may have some validity.

An interesting feature of the $g_{F.R.}\{\epsilon^*, Pr\}$ function is predicted by the turbulent vortex hypothesis if the additional assumption is made that the Reynolds number and Prandtl number dependence of the heat transfer coefficient for the cavity boundary layer can be expressed by a power law. It follows from this assumption that the dependence of $g_{F.R.}$ on ϵ^* and Pr will remain the same as the roughness type is changed. Thus in equation 129 it is predicted that only the coefficient 5.19 will change in the $g_{F.R.}\{\epsilon^*, Pr\}$ functions for pipes with roughness type differing from that of the present experiments. This extension of the present results to other types of roughness by means of the turbulent vortex hypothesis will be discussed in Section VII. Also a test of the validity of this prediction will be discussed in Section VI in connection with Nunner's heat transfer measurements on ring-type roughness elements.

B. Comparisons with Existing Theories

First, a theory by Nunner (Ref. 5) will be discussed. He developed an analytical expression for heat transfer in rough pipes derived from the results of his experiments with air flow in pipes having eight different geometries of two-dimensional roughness elements (rings). He observed that a correlation existed between the friction factor ratio of rough-to-smooth pipe (C_F/C_{FS}) and the Nusselt number obtained at any given Reynolds number. This relation approximated the results regardless of the actual pipe roughness geometry. Nunner then imagined a schematic geometry to represent the effect of roughness on C_F and C_H. In this scheme a row of detached obstructions are thought of as existing at the outer edge of the laminar sublayer that would exist if the tube were smooth. These obstructions produce the form drag required to account for the observed increase in the C_F of the rough tube over that of the smooth tube, but the obstructions benefit the heat transfer only insofar as the turbulence level in the core flow is increased. The resulting theory becomes,

$$C_H = \frac{C_F/2}{1 + 1.5 \, Re^{-1/8} \, Pr^{-1/6}[\, Pr(C_F/C_{FS})\text{-}1]}$$ (132)

Nunner measured, in addition to C_H and C_F, the velocity and temperature profiles in his pipes, and he found that for the rough pipes the radial temperature profile was flatter with respect to the velocity profile than was the case for a smooth pipe under the same operating conditions. He noted that this same effect is produced by increasing Prandtl number in smooth tubes. Equation 132 shows that the effect of roughness appears in the C_F/C_{FS} term and that

variations in this term have nearly the same effect on C_H as changes in Prandtl number. Thus Nunner interpreted his temperature-velocity profile measurements as supporting his theory. With regard to these profile measurements, it is noted that the similarity arguments in Section II, which result in the establishment of the $g\{\epsilon*, Pr\}$ function, imply that the shape of the velocity and temperature profiles in the central region, away from the immediate neighborhood of the wall, should remain similar to each other for all Prandtl numbers and roughness ratios (compare equations 36 and 57). In order to show that this implication is compatible with Nunner's observations, a temperature profile for a particular rough tube was computed by an analysis (not included herein) whereby it was assumed that the profiles of velocity and temperature remain similar in the central region. Also, account was taken for the fact that the separated flow at the rough walls is less effective in locally improving the heat transfer than in improving the momentum transfer. The resulting temperature profile for rough surfaces was normalized to the temperature difference between the wall and the pipe center, as was done by Nunner. It was then found that the temperature profile so computed continues to look very nearly like that for a smooth tube even though the velocity profile of the rough tube is considerably more peaked than that of the smooth tube. This is just what Nunner observed. From this discussion, it is pointed out that Nunner's profile measurements do not abrogate any of the arguments leading to the use of the $g\{\epsilon*, Pr\}$ function.

Nunner's hypothesis (Eq. 132) expressed in terms of the "g" factor becomes

$$g \equiv \frac{(C_F/2C_H)-1}{\sqrt{C_F/2}} + 8.48$$

$$= \frac{1.5\left[Pr\left(C_F/C_{FS}\right)-1\right]}{\sqrt{C_F/2}\,Re^{1/8}\,Pr^{1/6}} + 8.48 \tag{133}$$

The friction similarity law (Eq. 26) may be used to convert both C_F and C_{FS} in this equation to functions of ϵ/D and $\epsilon*$, but even so, the right side of equation 133 cannot be brought into a function of $\epsilon*$ and Pr only. Thus Nunner's equation does not satisfy the similarity law for heat transfer developed in Section II.

In Figure 37, the results of plotting Nunner's equation (Eq. 132) in the $g(Pr)^{-0.44}$ and $\epsilon*$ coordinates with ϵ_s/D and Pr as parameters are shown. The hydraulic equivalent roughness ratios (ϵ_s/D) are used as a basis for all of the information presented in Figure 37, so that direct comparisons between the various theories and the experimental data points are meaningful. The correct relationships between the separate variables C_F, C_H, Re, Pr, and ϵ_s/D are obtained if the coordinates of this figure are converted back through the definitions of ''g'' and $\epsilon*$ and through the friction similarity law (Eq. 26) using Nikuradse's $A\{\epsilon*\}$ function. For the fully rough region all of the results of the present experiments are summarized by the single heavy curve which is taken from Figure 36. Presumably the Prandtl number dependence of the present results would still be valid at a Pr value of 0.72, so that this same heavy curve is assumed to also represent the extrapolation of the present results to that Prandtl number. Curve number 5 in Figure 37 shows that Nunner's theory is inadequate for predicting the results of the present experiments. This curve is computed for a Prandtl number

of 5.94 and ϵ_s/D of 0.015 which are conditions met in some of the tube C-9 tests. It is seen that the predictions are as much as a factor of two away from the observed "g" factor. This corresponds to a slightly smaller percentage discrepancy for $2 C_H/C_F$ at these conditions. The Nunner prediction (not shown) for Pr = 1.20 is much closer to the experimental results, the discrepancy in "g" ranging from 10 to 15 percent for the C-9 tube and from 10 to 25 percent for the A-4 tube. The comparison of Nunner's theory with his own experimental results is deferred to Section VI.

A comparison of the reasoning leading to Nunner's theory with that of the turbulent vortex hypothesis (Cf. Appendix VII) shows that the same ingredients are involved in each. Both theories use assumptions that flow separation produces a high drag which is independent of fluid viscosity and that a viscosity dependent boundary flow over a locally smooth surface establishes the thermal resistance of the wall region. The differences in the resulting theories stem from the difference in the methods by which the parameters for the boundary flow are obtained.

Next an expression will be discussed which was suggested by Martinelli (Ref. 34) and which has been used to correlate certain experimental results. This expression comes directly from a relationship between C_H and C_F for smooth tubes. Martinelli developed an expression for smooth pipe heat transfer using the same eddy viscosity distribution in the wall layers as that used by von Kármán, but he did not make von Kármán's assumption that the mean velocity and the mixed mean temperature are attained at the same radius. The resulting form of Martinelli's equation is somewhat different from von Kármán's, but the computed values for C_H are almost

identical in the Prandtl number region from 0.7 to 10. In applications
of his theory, Martinelli also assumed that the eddy diffusivities of
heat and momentum were equal so that his smooth tube theory is
written

$$\frac{2C_H}{C_F} \cong \frac{(\frac{T_w - T_c}{T_w - T_L})\{Re, Pr\}}{5\sqrt{C_F/2}[Pr + \ell n(1 - 5Pr) + \frac{1}{2}\ell n(\sqrt{C_F/2}Re/60)]} \tag{134}$$

where $(T_w - T_c)/(T_w - T_L)$ is the ratio of the maximum temperature
difference to the wall-to-mixed fluid temperature difference. This
is given in tabulated form and varies from about 0.82 to 1.0 in the
Pr and Re range of interest here. Martinelli suggested that this equa-
tion, altered only by dropping the temperature term in the numerator,
could also be applied to rough tubes, the effect of the roughness being
expressed by the C_F terms. By making use of the friction similarity
law (Eq. 26) in equation 134 and then putting equation 134 into the
form of the ''g'' factor, there is obtained

$$g\{\epsilon*, Pr\} = 5[(Pr-1) + \ell n(1+5Pr) + \frac{1}{2}\ell n \epsilon*]$$

$$+ 8.71 - A\{\epsilon*\} \tag{135}$$

Thus, in contrast to Nunner's theory, Martinelli's equation satisfies
the heat transfer similarity law, i.e. ''g'' is a function of $\epsilon*$ and Pr
only. It is interesting to note that some $\epsilon*$ dependence still exists
in Martinelli's equation for fully rough conditions where $A\{\epsilon*\}$ is
constant. Rearranging von Kármán's equation for smooth tubes in
the same manner leads to an equation for ''g'' that is independent
of $\epsilon*$ so that the induced rough tube function would be horizontal-line
extensions of the smooth-tube lines indicated at the left end of Figure
37.

Martinelli's theory in the form of equation 135 is plotted as curves number 7 and 6 in Figure 37 for Pr values of 0.72 and 5.94 respectively. Colebrook's (Ref. 27) form for the $A\{\epsilon*\}$ function was used for the 0.72 curve while Nikuradse's (Ref. 10) form was used for the 5.94 curve. For the fully rough region ($\epsilon* > 70$) both of these $A\{\epsilon*\}$ functions become the same constant (8.48). Also the differences in "g" values obtained by using the different $A\{\epsilon*\}$ functions in the transition region are small. It is seen in Figure 37 that Martinelli's equation is in disagreement with the results of the present experiments by factors of 1.5 to 2.0, and the functional dependence of "g" on both $\epsilon*$ and Pr is different from the observed dependence. Like Nunner's theory, the predictions are particularly poor for large Prandtl number. Retaining the $(T_w-T_c)/(T_w-T_L)$ term, which Nunner's profile measurements showed to be nearly the same for rough as for smooth pipes, failed to improve the applicability of the Martinelli equation to the present experimental results.

As a third comparison, the results of an analysis by Mattioli (Ref. 35) will be considered. This analysis led to the following theoretical expression which was expected to apply to the fully rough region:

$$\left(\frac{2C_H}{C_F}\right)_{F.R.} = \frac{1}{1 + \sqrt{C_F/2}\,[\Delta_r(\epsilon*Pr)^n - \Delta]} \tag{136}$$

where Δ is a constant between 7.9 and 8.06, and n and Δ_r are constants to be determined by experiments. The restraint is suggested that $1/2 < n < 1$. Equation 136 can be rewritten

$$g_{F.R.}\{\epsilon*, Pr\} = \Delta_r(\epsilon*, Pr)^n + (8.48 - \Delta) \tag{137}$$

which is seen to satisfy the heat transfer similarity rule. Since the suggested value for Δ is close to 8.48, the last term in equation 137 is small compared to the value of $g_{F.R.}$, and it can be dropped, leaving a form,

$$g_{F.R.}\{\epsilon*, Pr\} \cong \Delta_r (\epsilon*, Pr)^n \tag{138}$$

This can be compared with the results of the present experiments,

$$g_{F.R.}\{\epsilon*, Pr\} = 5.19 \, \epsilon*^{0.20} \, Pr^{0.44} \tag{129}$$

It is seen that the use of the unified variable $(\epsilon*Pr)$ is not successful. This can also be seen in terms of the original $C_H\{Re, Pr, \epsilon/D\}$ functions by considering a given tube operating in the fully rough (constant C_F) region. For this situation, $(\epsilon*Pr)$ is proportional to $(RePr)$. Thus the Pr dependence in a chart for $C_H\{Re; Pr\}$ should reduce to a single curve if $C_H\{(Re)(Pr)\}$ is plotted instead. That this procedure fails for the present results is demonstrated by referring to the log-log plots of $C_H\{Re; Pr\}$ in Figure 16 and shifting each of the curves along the abscissa by a factor equal to its respective, associated Prandtl number.

As a final comparison with existing theories, a theoretical expression developed by Lancet (Ref. 36) will be discussed briefly. Lancet treated the problem of heat transfer over rough surfaces at fully rough conditions by starting from a highly schematic representation of the flow between the roughness elements. He assumed a region of purely laminar flow to exist at the bottom of the roughness cavities, a fully turbulent flow at the tips of the roughness elements, and a flow with varying amounts of eddy viscosity between

the roughness tips and the laminar region. The eddy-viscosity is supposed to decay with tube radius by a power law in the latter region. The resulting theory has the form

$$C_{H F.R.} = \sqrt{C_F/2} \; f_1 \{\epsilon * Pr\} \tag{139}$$

with several unspecified parameters being allowed to influence the function (f_1). Some of these parameters are used to describe the roughness shape; one parameter, the eddy-viscosity decay exponent, is to be determined empirically; and one of the parameters still appears to depend on the variables of the problem ($\epsilon *$ and Pr). In applying this model to a correlation of experimental results for air flow through a rough channel, Lancet made this latter parameter a function of the product ($\epsilon * Pr$) also, so that the theory then indeed has the form shown in equation 139. As discussed in connection with Mattioli's theory, the use of the combined variable ($\epsilon * Pr$) is not consistent with the results of the present experiments.

From the preceding discussion of several of the previously existing theoretical models for rough tube heat transfer, it is seen that none is sufficient to describe all aspects of the present experimental results. The most conspicuous failing is in predicting the Prandtl number dependence. This might have been expected since all previous verifications of the theories were based on experiments at one Prandtl number only. Hence, the Prandtl number dependence predicted by these theories has remained untested up until the present time.

VI COMPARISONS WITH OTHER EXPERIMENTAL RESULTS

This section contains comparisons of the present experimental results for heat transfer from rough surfaces with the results of other researches. Similar comparisons for the smooth tube were presented separately in Section IV-B. The heat transfer similarity group (g) will be used to compare the present results with the results of two other experimental investigations wherein the idealized conditions of fully developed, isothermal pipe flow were approached. Much of the literature on rough surface heat transfer reports experiments in which these conditions are not met; however, several of these investigations afford special interest and will be compared herein by means of relating the performance of each surface to that of a smooth surface under the same operating conditions.

Experiments by W. Nunner:

Nunner's (Ref. 5) experiments were performed with air flowing through rough tubes heated by condensing steam and preceded by an entrance section. An approximation to isothermal results was obtained by evaluating the fluid properties at the "film temperature," $(T_w + T_L)/2$. Rings were placed in the test pipe at regular intervals to form the roughness. The geometry was varied by using rings of different cross sectional forms and by varying the ring spacing. These tubes displayed the fully rough friction characteristic immediately upon transition from laminar to turbulent flow. In two cases a rather sharp rise in the $C_F\{Re\}$ curve was observed at the high Reynolds number end of the curve. This indicates, according to the arguments of Appendix VII, that a change in the pattern of the separated flow around the roughness elements occurs as Re

increases.

The points shown in Figure 37, which is a graph of the function $g(Pr)^{-0.44}\{\epsilon*, Pr\}$, are taken from the smoothed curves of Nunner's results. Only those Reynolds number regions where the friction factor was relatively independent of Reynolds number are presented here. The equivalent sand-grain roughness ratio with the A constant equal to 8.48 was used in computing "g" and $\epsilon*$ for these results. Hence the points representing Nunner's results may be compared directly with the heavy line representing the present results. As mentioned in Section V, this line for the fully rough region represents the present results at all Prandtl numbers tested; hence, the same line indicates the extrapolation to Prandtl number of 0.72.

Nunner's tubes B-20 and D-20 were both made with rings of semicircular cross section and with spacing equal to 20 times the ring thickness. However the D rings have twice the ring-thickness-to-pipe-diameter ratio of the B rings. Thus these two tubes have different ϵ/D values, but their roughness geometry is similar. Hence the results from the B-20 and D-20 tubes are expected, by the heat transfer similarity law (Eq. 54, Sec. II), to form a continuous curve on this plot. Further, the deduction from the turbulent vortex hypothesis discussed in Appendix VII indicates that the curves on the $g\{\epsilon*\}$ plot for roughness types other than that tested in the present experiments should be parallel to the curve representing the present results. The line drawn through Nunner's results in Figure 37 is evidence that both of these expectations are fulfilled.

Nunner's tube A-20 is identical to B-20 in all respects except that the A-20 rings have a square cross section. The D-5 and D-2

tubes have rings with the same cross section as tube D-20 but the ring spacing is changed to a ratio of spacing-to-height of 5:1 for the D-5 tube and to a close-pack for the D-2 tube. Remarkably, the results from these tubes fall nearly on the same line used to correlate the results from the first tubes considered. The turbulent vortex hypothesis would predict only that the curves for these different roughness geometries should be parallel. The observed uniqueness of the correlating curve is attributed to the use of a common roughness scale based on the friction similarity law. If the ring-height-to-pipe diameter ratio (0.043 for tubes B-20 and A-20 and 0.086 for D-20, D-5 and D-2) were used for generating the ϵ^* abscissa, the lines for the respective non-similar tubes would be shifted away from each other in the horizontal direction. The magnitude of this shift is indicated by comparing tubes D-5 and D-2 which have the same ring-height-to-pipe-diameter ratio but have hydraulic equivalent sand-grain roughness ratios of 0.335 and 0.0555 respectively. Thus the technique of assigning a hydraulic equivalent roughness ratio to each pipe appears to lead to a very simple correlation of the $g\{\epsilon^*\}$ results for pipes having widely differing roughness shapes. This must be regarded as an entirely empirical observation at this point. The turbulent vortex model predicts this result only for geometrically similar roughnesses having supposedly geometrically similar vortex patterns between the roughness elements.

The comparison of Nunner's results for various two-dimensional types of roughness with the curve representing the results of the present experiments with three-dimensional roughness indicates that a larger coefficient in the equation

$$g = K_f \, (\epsilon*)^{0.20} \, (Pr)^{0.44} \tag{140}$$

must be incorporated for Nunner's results. This is true even though the hydraulic equivalent roughness formulation was used for both cases. Thus, for entirely different roughness forms, the empirical relation discussed in the preceding paragraph may not be valid.

The exponents of equation 140 were evaluated from the data of the present experiments. It was then observed that Nunner's data can be represented by means of the same exponent on $\epsilon*$. This fact is in agreement with the prediction from the turbulent vortex hypothesis that both exponents should be independent of roughness type. The applicability of the exponent for Prandtl number could not be checked by Nunner's experiments, but it is now conjectured that this exponent is also given by equation 140. Then evaluating the K_f factor in equation 140 by the line through Nunner's data in Figure 37, a complete theory for the relation between C_H and C_F is obtained. This theory, which should be applicable to pipes with a wide variety of two-dimensional types of roughness, can be expressed by

$$C_{HF.R.} = \frac{C_F/2}{1+\sqrt{C_F/2}\,[\,6.37(\epsilon*)^{0.20}(Pr)^{0.44}-8.48]} \tag{141}$$

where

$$\epsilon* \equiv Re\,\sqrt{C_F/2}\ \exp\{\frac{3.0\,-1/\sqrt{C_F/2}}{2.5}\} \tag{142}$$

The exponential term in equation 142 is the hydraulic equivalent roughness ratio (ϵ_s/D) established by the friction similarity law for fully rough conditions (Eq. 26).

A reproduction of Nunner's theory, discussed in Section V, is also placed on Figure 37. The curve number 3 for Pr of 0.72 and

ϵ_s/D of 0.133 corresponds to the conditions for his B-20 tube, while curve number 4 for Pr of 0.72 and ϵ_s/D of 0.332 corresponds to the conditions for his D-20 tube. Nunner's theoretical correlation is fairly good for the B-20 tube at low $\epsilon*$, i.e. low Re, but the results from the D-20 tube are seen to deviate by as much as 16 percent from the predicted curve. A given percentage deviation in ''g'' is nearly equivalent to the percentage deviation in C_H for the cases at hand. A close examination of the correlating plot appearing in Nunner's report (Ref. 5) shows this same discrepancy.

In a report by Kemeny and Cyphers (Ref. 37), a correlation plot for Martinelli's theory and Nunner's data was presented in which close agreement was shown. A plot of the Martinelli equation for Pr of 0.72, line number 6 in Figure 37, shows that the equation compares closely with Nunner's <u>theory</u> for the D-20 tube (line number 4), but it deviates markedly from Nunner's data, particularly at low $\epsilon*$ values. The good agreement shown by Kemeny and Cyphers does not bring out this discrepancy.

The present proposed equation for Nunner's data, expressed in equation 141 and shown by curve number 2 in Figure 37, appears to agree with the data at Pr of 0.72 much better than either Nunner's or Martinelli's theory. Further, the turbulent vortex hypothesis will predict greatly different results than either Nunner's or Martinelli's theory at higher Pr values. Thus a critical test of the relative applicability of these theories could be provided by the results of experiments on two-dimensional types of roughness at Prandtl numbers higher than 0.72.

Experiments by J. W. Smith and N. Epstein:

Heat transfer measurements on several naturally rough pipes with air through-flow were performed by Smith and Epstein (Ref. 9) and by Nunner (Ref. 5). The techniques used by Smith and Epstein were similar to those described for Nunner's work. The results for Nunner's cast iron pipe and for Smith and Epstein's "Karbate" pipe and three sizes of galvanized pipe are displayed in Figure 37. In all cases the data falls in the transition region. The shapes of the C_F {Re} curves (not included herein) are closely approximated by the use of the hydraulic equivalent sand-grain roughness ratio, together with the Colebrook (Ref. 27) function, in the friction simi- larity law (Eq. 26). The Colebrook function can be written

$$A\{\epsilon *\} = 8.48 - 2.46 \ln (1 + 3.3/\epsilon *) \tag{143}$$

An extrapolation of the present D-3 tube results to a Prandtl number of 0.72 is shown for comparison as line number 1-c in Figure 37.

The results from the three galvanized pipes are seen to gen- erate a nearly continuous curve in this plot implying that, in a sta- tistical sense, geometrically similar roughness distribution exists among these pipes. This would be expected if the surfaces were created by the same manufacturing process in such a way that as pipe diameter is changed the shape of the surface is fixed, again in a statistical sense.

A meaningful comparison among pipes with differing types of roughness is achieved by determining which roughness type yields the highest C_H/C_F performance at given Re and C_F levels. This method of comparison, which will be discussed at greater length subsequently in this section, is used for the following discussion.

In the transition region, the percentage variation in C_H/C_F lies between 1.0 and 0.3 times the magnitude of the percentage variation in the ''g'' factor; an increase in ''g'' corresponds to a decrease in C_H/C_F. Thus, from Figure 37, it is estimated that the galvanized pipes give on the order of 10 to 20 percent lower C_H/C_F performance than the ''Karbate'' pipe. It is noted that fixing Re and C_F for these pipes which have the same $A\{\epsilon*\}$ functions is equivalent to fixing $\epsilon*$ (Cf. Eqs. 25 and 26). By the same arguments, Nunner's cast iron pipe appears to give only approximately 10 percent higher C_H/C_F performance than the ''Karbate'' pipe. This latter difference may even be within the combined uncertainty limits of the respective experiments.

Comparisons of the present D-3 tube data with the data from the random roughness pipes on the plot of Figure 37 are less straightforward. The D-3 tube, having a definite scale of roughness size, has a different $A\{\epsilon*\}$ function in the transition region. By using the differing $A\{\epsilon*\}$ functions with equations 25 and 26 of Section II, it can be shown that, for comparisons at a fixed Re and C_F, the ''g'' factor for the D-3 tube should be read at a lower $\epsilon*$ value than that of the random roughness tubes. Thus the predicted C_H/C_F performance of the D-3 tube, in relation to the random roughness pipes, is somewhat better than is indicated from a comparison at fixed $\epsilon*$ in Figure 37. A separate calculation was made which indicates that the C_H/C_F performance for the D-3 tube is from 10 to 30 percent better than either the ''Karbate'' pipe or the cast iron pipe for operation in the transition region.

The "Karbate" pipe is described by Smith and Epstein as having a pyramid-shaped roughness. This is probably not too different from the surface expected in a cast iron pipe. The galvanized pipes would be expected to have a relatively larger radius of curvature in the roughness elements, i.e. less sharpness, than either the cast iron or "Karbate" pipes. The experimental results for naturally rough pipes show that at least in the transition region the technique of relating the roughness to the friction equivalent of sand grains does not bring all results into a single $g\{\epsilon *\}$ function. Thus each general type of natural roughness should probably be treated separately. In passing, it is noted that, for the particular case of the galvanized pipe measurements, the Martinelli equation, represented in Figure 37 with the Colebrook-type friction factor relation, provides a good correlation for these particular data taken at Prandtl number of 0.7. This was previously noted by Smith and Epstein.

Introduction to the Comparisons Based on the Ratio of Heat Transfer Coefficient to Friction Coefficient:

The remaining comparisons of experimental results are presented in Figure 38. This figure displays some results from five different investigations on rough surface heat transfer including, for comparison, those of Nunner and of the present experiments. The coordinates in this figure show the relation between the C_H/C_F ratio for the various rough surfaces and the same ratio for a smooth surface. This is plotted against the effective increase in friction due to roughness. The Reynolds number, Prandtl number and roughness geometry must all appear as parameters on such a plot. In many of the experiments, either no attempt was made to maintain fully

developed, isothermal conditions, or a full description of the experimental conditions could not be obtained from the respective reports. Also, in some instances the results reported for the smooth surfaces in the various investigations show anomalous characteristics. It is felt that, under the above mentioned circumstances, relating the rough surface results directly to those of the smooth surface in the same experiments will tend to cancel out secondary effects and allow a reasonable comparison with the present results. In Figure 38, the value C_{FS} in C_F/C_{FS} refers to the friction factor for a smooth surface operating at the same Reynolds number as the rough surface having the friction factor C_F. Similarly, the value C_{HS} in C_{HS}/C_H refers to the smooth surface heat transfer coefficient for the same Reynolds number and Prandtl number at which the rough surface has the coefficient C_H. The increase in C_H for any rough surface with respect to C_{HS} can be obtained from this plot by multiplying the ordinate of a given point by its abscissa.

The theoretical significance of the C_H/C_F value lies in a deduction from the Reynolds analogy which states that this ratio should be 0.5 for smooth surfaces at Prandtl number of 1.0. This deduction derives from the expected similarity of the temperature and velocity distributions for these conditions (Cf. Eq. 60, Sec. II). For rough surfaces operating at Pr of 1.0, the velocity and temperature profiles external from the roughness element are still expected to be similar, even in the transition region for which a vestige of the laminar boundary layer external to the roughness still remains. Inside of the roughness cavities, however, any amount of separation of the flow will produce a pressure drag such that the

shear on the cavity surfaces will constitute only a part of the total wall drag. The Reynolds analogy again suggests that the thermal conductance of the boundary layers in the cavities will depend directly on the shear stress and not on the pressure drag at the wall. Thus it is expected that the C_F value for the pipe will increase by a greater amount than the C_H value as wall roughness effects become finite. Hence, for Prandtl number near 1.0, it is expected that $(C_H/C_F)/(C_{HS}/C_{FS})$ will always be less than 1.0 as C_F is increased due to roughness. The situation at higher Prandtl number with operation in the transition region is somewhat different as was suggested in Section V. For this case the radial temperature gradient in the residual laminar flow near the wall is greater than the velocity gradient. This offers the possibility that the added disturbances caused by a rough wall will preferentially improve the heat transfer over the momentum transfer in the region external to the roughness. Under these circumstances, the C_H/C_F ratio can be increased with respect to the corresponding smooth tube ratio if the drag due to flow separation at the roughness elements has not become too great.

The significance of the C_H/C_F ratio for heat exchanger design will be discussed in Section VII.

In Figure 38, the curves (items 9, 10 and 11) from the present experiments at a Pr value of 1.2 and the curves (items 3, 4 and 5) for three of Nunner's tubes at a Pr value of 0.7, all with Re as the auxiliary variable, show a general fall-off in the C_H/C_F performance relative to that of smooth surfaces as friction increases due to roughness. The curves 6, 7 and 8, representing results at Prandtl number of 6.0 for each of the rough tubes of the present investigations, show segments where $(C_H/C_F)/(C_{HS}/C_{FS})$ values are greater than 1.0.

Wherever this occurs, the segments correspond to Re values in the transition region. This result can be understood on the basis of the preceding discussion. It is interesting to note, in this connection, that Nunner's theory, given herein by equation 132, predicts that the ratio $(C_H/C_F)/(C_{HS}/C_{FS})$ will decrease with increasing Prandtl number for a given C_F/C_{FS} value. This is opposite to the results obtained with the tubes of the present experiments as is clearly shown by comparing the curves for Prandtl numbers of 6.0 and 1.2 in Figure 38.

Experiments of P. Fortesque and W. B. Hall:

Fortesque and Hall (Ref. 2) made measurements of heat transfer to various gases (Pr = 0.7) in an annular passage with transverse aluminum fins mounted on a heated inner core. These investigations, which were carried out in support of the Calder Hall gas-cooled-reactor design, used an electrically heated core to simulate the heat load from a fissioning fuel element. The results were presented in the form of C_H/C_{HS} and C_F/C_{FS} as functions of the fin geometries employed. The heat transfer surface used in the definition of C_H is the cylinder generated by the tips of the fins, and the base velocity used for the definition of C_H is the volumetric discharge divided by the cross-sectional area between the fin tips and the outer wall. The C_F definition is based on this same discharge velocity and on the pressure gradient along the passage. The relating smooth surface coefficients are defined on the basis of a similar annulus formed by substituting a solid rod, of diameter equal to that of the fin tips, for the finned surface. Item 1 in Figure 38 represents the geometry

having the highest relative C_H/C_F performance of those studied.
This geometry consists of a fin pitch of 3/16 inch with the fin-tip-
to-fin-root diameter ratio varying from 1.3 to 1.9. This tip-to-root
diameter ratio is the variable forming the trace for item 1 in Figure
38. There was evidence presented to indicate that the "fin effect"
was appreciable so that the performance of an isothermal finned
surface would be higher than that shown. Even without a correction
for the "fin effect," the particularly good performance of the 3/16
inch-pitch fin configuration with respect to the smooth surface would
appear to refute the theoretical considerations just presented.
That these considerations are not so refuted comes from the fact
that, with the annular configuration, the entire surface participating
in the friction is not involved in transferring heat. The following
discussion is presented to show, semi-quantitatively, how the heat
transfer coefficients in pipe flow and annular passage flow are re-
lated.

In discussing the Fortesque and Hall results, Sheriff (Ref.
38) showed that the ratio C_{Fi}/C_{FiS}, where subscript "i" refers to
the inner surface of the annulus, is considerably larger than the
(C_F/C_{FS}) used in the Fortesque and Hall correlations. In doing this,
however, Sheriff made an assumption that tended to overestimate
the computed C_{Fi}/C_{FiS} value. As a more nearly correct approach,
the following is proposed: From the preceding definition for C_F
in annular passages and from a force balance on the surfaces de-
scribed,

$$\frac{C_F}{2} \equiv \frac{(dP/dx)(D_o - D_i)}{4\rho\,u_m^2} = \frac{\tau_o\,D_o + \tau_i\,D_i}{\rho\,u_m^2(D_o + D_i)} \tag{144}$$

where subscript ''i'' refers to the inner surface of the annulus or the fin tips, and subscript ''o'' refers to the outer wall of the annulus. Comparing a smooth annulus and a finned annulus with the same discharge velocity (u_m), the same outer wall diameter (D_o), and the same inner wall (or fin tip) diameter (D_i); the following relation can be derived

$$\frac{C_F}{C_{FS}} = \frac{\tau_i}{\tau_{iS}} \left[\frac{(\tau_o/\tau_i)D_o + D_i}{(\tau_{oS}/\tau_{iS})D_o + D_i} \right] \tag{145}$$

From here on, only that fin geometry which Fortesque and Hall showed to give the best relative performance will be considered. From measurements on velocity profiles in smooth annuli by Knudsen and Katz (Ref. 39, p. 186), it can be shown that τ_{oS}/τ_{iS} is nearly 1.0 for the diameter ratio of interest. Equation 145 can thus be simplified and rearranged to give

$$\frac{C_{Fi}}{C_{FiS}} = \frac{(C_F/C_{FS})(D_o + D_i) - (\tau_o/\tau_{oS})D_o}{D_i} \tag{146}$$

where C_{Fi} is defined

$$C_{Fi} \equiv \frac{2\tau_i}{\rho u_m^2} \tag{147}$$

Sheriff made the assumption that the shear stress on the outer surface would be the same with and without fins on the inner surface. With this assumption, equation 146 and the geometry being considered lead directly to

$$\frac{C_{Fi}}{C_{FiS}} = 1.87 \frac{C_F}{C_{FS}} \tag{148}$$

Knudsen (Ref. 39, p. 194) presents velocity profile measurements

for finned-annuli configurations not too different from the one of interest here. From these it can be deduced that τ_o/τ_{oS} for the case at hand should be approximately 2.5 rather than 1.0 as implied by Sheriff. This is because, for a given bulk velocity, the increased turbulent momentum exchange, established at the inner wall due to the introduction of fins, forces the velocity profile to reach its maximum closer to the outer wall. The increased total shear force is thus partially shared with the outer wall. Introducing a τ_o/τ_{oS} value of 2.5 into equation 146 yields

$$\frac{C_{Fi}}{C_{FiS}} = 1.52 \frac{C_F}{C_{FS}} \tag{149}$$

where (C_F/C_{FS}) is based on the pressure drop along the passage as discussed previously.

Applying equation 149 to the peak value of $(C_H/C_F)/(C_{HS}/C_{FS})$ equal to 1.34 shown in Figure 38 and noting that in these experiments

$$C_H \equiv C_{Hi}$$

one obtains for the finned inner surface of the annulus

$$\frac{C_{Hi}/C_{Fi}}{C_{HiS}/C_{FiS}} = 0.88; \quad \frac{C_{Fi}}{C_{FiS}} \cong 5.0 \tag{150}$$

The ratio $(C_{Hi}/C_{Fi})/(C_{HiS}/C_{FiS})$ for annuli should be nearly comparable to the corresponding quantity measured in pipes. It is seen by equation 150 that, for the best configuration investigated by Fortesque and Hall, the ratio conforms to the expectation that it should be less than 1.0.

It is pointed out that, even if the rough estimates leading to equation 150 are correct, the use of the mean discharge velocity (u_m)

in defining the C_{Fi} and C_{Hi} does not quite satisfy the requirements of a reference velocity for the inner surface. For a given u_m, the shift in the velocity profile with the introduction of fins is influenced by the location of the outer wall. Thus a correct reference velocity for the inner surface should be some complicated function of the discharge velocity and the width of the annular gap.

From the preceding discussion, it is seen that heat transfer results such as those of Fortesque and Hall demonstrate great improvements in performance due to roughness for flow passages with inert surfaces. However, it is very difficult to use these in obtaining momentum and heat transfer coefficients applicable to pipes and to free boundary layers.

If it can be assumed that the point computed in equation 150 is representative of values attainable in pipes having rectangular wells for roughness elements, it is seen by item 1' in Figure 38 that this would offer considerable advantage over the other surface geometries compared at Prandtl numbers near 1.0. The fin-pitch-to-depth ratios showing the good performances in annuli were between 0.5 and 1.0. Velocity measurements and flow visualizations of single cavities (Refs. 2; 33; 40; and 39, p. 195) indicate the presence of a single standing vortex for the square well and of double, oppositely-rotating vortices for the deeper one. Such simple cavity flow configurations may thus be particularly effective in yielding high C_H/C_F performance.

Experiments by R. Hastrup:

Hastrup (Ref. 31) carried out heat transfer measurements by methods similar to those used in the present work. He also used

water flowing at various temperatures to obtain the effects of vary-
ing Prandtl number. His thin-walled tube was formed by hard-
knurling of the outside surface to produce pyramid shaped pockets
with slightly rounded edges as the inside heat transfer surface. The
$C_F\{Re\}$ curve obtained for this tube was nearly parallel to the smooth
curve throughout the range of Reynolds number tested (4×10^4 to 5.6×10^5).
This is characteristic of a "wavy" surface and indicates that com-
plete flow separation from the roughness elements does not occur.
The C_H dependence on Reynolds number was also quite similar to
that of the smooth tube. Since the ratios C_H/C_{HS} and C_F/C_{FS} were
nearly constant with Re, each of the points (items 12 and 13) shown in
Figure 38, for Pr of 1.2 and 6.0 respectively, represent most of the
range of Reynolds numbers tested.

The point at Pr of 1.2 coincides with the result for the D-3
tube of the present work; whereas, at Pr of 6.0, Hastrup's tube
shows 10 to 15 percent lower C_H/C_F ratio than the tubes of the pres-
ent experiment. Thus the preferential improvement of C_H with re-
spect to C_F, occurring at high Pr in the transition region of a "sharp"
roughness surface, is not in evidence for the "wavy" surface which
does not display a transition.

Another interesting point in connection with Hastrup's tube
is that, even for a "wavy" type roughness, the increases in C_H and
C_F due to roughness are not simply explained by the increased sur-
face area. For this tube the surface area was increased approximately
10 percent by roughening, while the C_H and C_F were observed to in-
crease by approximately 50 and 60 percent respectively.

Experiments of G. Grass:

Grass (Ref. 3) carried out heat transfer measurements on three
small (0.3 inch diameter) aluminum tubes with water through-flow.
The tubes had respectively longitudinal grooves, cross grooves, and a
combination of these two cut into their inner surface. The cross-
groove roughness showed the highest C_H/C_F performance with respect
to a smooth tube which was also tested. The cross grooves were
about 0.0016 inch deep with a pitch of approximately 0.05 inch. The
reported information on the test conditions is insufficient to determine
whether or not an entrance section was provided or if the heat flux val-
ues were such that appreciable radial variations in fluid properties
were avoided. Assuming, however, that the conditions were similar
for the smooth and the rough tubes, the point, item 14 in Figure 38,
computed from Grass' report should allow a comparison with the pres-
ent results. The Prandtl modulus for the Grass experiments is
assumed to be approximately 6.0 although the bulk water temperature
was not reported. The high performance ratio, $(C_H/C_F)/(C_{HS}/C_{FS})$
of 1.09, is similar to that obtained from the present results at this
Pr value for operation in the transition region. Although the informa-
tion presented in Reference 3 does not permit direct computation of
C_F, it can be shown from the information that is available that the
C_F characteristic is increasing with Reynolds number near Re of
3.7×10^4. This is the Re value used in Figure 38; hence, it is prob-
able that the observed high performance was attained in the transition
region.

Experiments of E.C. Brouillette, T. R. Mifflin, and J. E. Myers:

Brouillette, Mifflin, and Myers (Ref. 41) produced roughness

elements by cutting circumferential, 60-degree "V" grooves into the internal surface of one-inch-diameter copper pipes. A small flash was formed on either side of each groove creating two "fins" for each groove. Heat supplied by condensing steam on the outer surface of the tubes was conducted to a water through-flow. The temperature difference between the inside tube surface and the condensing steam was deduced by an extrapolation technique using various water flow rates and an assumed dependence of the heat transfer film conductance on flow rate. Since this dependence was the object of the investigation, an iteration was required to improve the accuracy of the final results. A smooth tube entrance section was used which means that a readjustment of the radial velocity distribution occurred in the rough test section. Thus some entrance effects are included in the reported heat transfer coefficients. The rough test section was 24 diameters long. The results are also assumed to be influenced by radial fluid property variations since no mention is made of corrections for this effect.

The friction coefficients obtained by these observers for their "plain" copper tube was nearly independent of Reynolds number and was from 40 to 100 percent higher than the results for smooth tubes obtained in the present work as well as in the experiments by Nikuradse and others. The heat transfer coefficient for the "plain" tube was shown to be not too different from the equation of Dittus and Boelter,

$$C_H \approx 0.023 \, (Re)^{-0.2} \, (Pr)^{-0.6}$$

which in turn was shown by Allen and by the present work to underestimate the C_H for water flow by 10 to 15 percent (Cf. Fig. 24).

In accordance with the method adopted for the presentations in Figure 38, the smooth surface results from Reference 41 are used in forming the C_F/C_{FS} and C_H/C_{HS} ratios even though these results appear to be anomalous.

Three of the five grooved tubes tested had nearly the same pitch-to-depth ratio for the grooves (approximately 2.5). Results from these three tubes are presented as item 15 in Figure 38. The ratio of the roughness height (distance from the bottom of the groove to the lip on either side) to the pipe diameter was 0.017, 0.027 and 0.050 for the respective tubes. The Reynolds number selected for presentation in Figure 38 was 10^5; however, since the observed $C_H\{Re\}$ and $C_F\{Re\}$ curves were nearly parallel to the respective "plain" pipe curves when drawn on log-log plots, the values shown are nearly independent of Reynolds number. The Prandtl number is assumed to be approximately 6.0 although bulk temperature of the water was not reported. The C_H/C_F performance with respect to the smooth surface for these tubes is seen in Figure 38 to be from 20 to 40 percent lower than the results obtained with the tubes used in the present work and those of Hastrup and of Grass. Some of this difference is explained by the fact that the highest performance from the present results was attained in the transition region; whereas the results presented in Reference 41 were from the fully rough region.

Experiments by E. W. Sams:

Sams (Ref. 42) experimented with air flowing through 1/2-inch-diameter Inconel tubes which were heated by the passage of

electrical current through the tube walls. The heated test section
was 48 diameters long and was preceded by a 12 diameter smooth
entrance section. It was found that evaluation of the air properties
at the wall surface temperature provided good agreement among
the data at differing wall-to-fluid temperature ratios. This implies
that the data presented in this way will yield the equivalent isothermal
results. The rough surfaces were produced by machining square
threads into the inside surface of the test pipes. Tube A had an
element-height-to-tube-diameter ratio (h/D) of 0.0125 with the
thread width and space both being 0.725 times the height. Tube B
had an h/D ratio of 0.0185 with a thread-width-to-height ratio of
0.896 and a space-to-height ratio of 1.05. Tube C had an h/D ratio
of 0.008 with thread width and space both 1.12 times the height.

As can be seen from the thread shape ratios, the roughness
elements of tubes C and B were not far from being geometrically
similar. However the resulting $C_F\{Re\}$ curves showed that the
requirements of the friction similarity law were not met. This
law can be written (Cf. Eq. 26, Sec. II) for the fully rough condi-
tions as

$$\frac{\epsilon_1}{\epsilon_2} = \exp\{\frac{\sqrt{2/C_{F2}} - \sqrt{2/C_{F1}}}{2.5}\} \tag{151}$$

where the subscripts 1 and 2 refer to two different pipes with dif-
fering roughness height but with geometrically similar roughness
shapes. Using the measured C_F values for tubes B and C in equa-
tion 151 gives $\epsilon_1/\epsilon_2 = 6.3$; whereas the measured ratio of the element
heights between the B and C tubes was 2.3. This apparent failure
of the friction similarity law might have been due to small imper-
fections in the very fine roughness of the C tube. The C tube

gave only approximately 50 percent rise in C_F over that of the smooth tube at the highest Reynolds number tested (approximately 1.5×10^5), and practically no increase in C_H was observed. The B and A tubes gave nearly the same fully rough friction factor with the tube A value being higher by approximately 12 percent. However, in the transition region defined by the equivalent sand-grain behavior, the $C_F\{Re\}$ function for the A tube decreased with decreasing Re while the B tube showed a rise such that the characteristics crossed. The C_H behavior of these two tubes was nearly identical within the resolution of the experiments.

The $(C_H/C_F)/(C_{HS}/C_{FS})$ ratio for tube A, operated at Re values between 0.5 and 1.0×10^5, is shown as item 2 in Figure 38. The $(C_H/C_F)/(C_{HS}/C_{FS})$ values are seen to lie very close to those of Nunner's tube D-2 which contained the close-packed semicircular rings. Also, if the results of tube C-9 from the present experiments (item 10 in Fig. 38) are extrapolated from Prandtl number of 1.2 to 0.7, the shifted curve falls close to the results of Sams and of Nunner.

If the smoothed data* for the fully rough region from Sams' tubes A and B are processed like the other data presented in the $g(Pr)^{-0.44}\{\epsilon *\}$ plot of Figure 37, the points fall between the data from Nunner's experiments and the curve representing the present results. The slope generated by Sams' data in these coordinates is in the neighborhood of 0.10 to 0.15 which is in fair agreement with

---

*An adjustment was made in equation 10 of Reference 42. Changing the coefficient from 0.0070 to 0.0065 makes the equation more consistent with equation 11 and the results shown in Figure 6b, also of Reference 42.

the slope of 0.2 observed for Nunner's results and the results of the present experiments. The limited extension of the threaded tube data into the fully rough region, however, makes this only a weak confirmation of the hypothesis that these slopes should remain independent of the roughness configuration.

Summarizing Remarks:

Several general observations can be made with reference to the results of the various investigations on rough surface heat transfer which have been compared in this section. 1) The previously existing theories for rough surface heat transfer are inadequate to predict the C_H response to all of the pertinent parameters. 2) The use of the $g\{\epsilon^*, Pr\}$ plot correlates results from geometrically similar roughness patterns. 3) In the case of the two-dimensional roughnesses investigated by Nunner, associating a friction-equivalent roughness height with each pipe provided a correlation for non-similar roughness patterns. 4) This latter technique was unsuccessful in the case of natural roughness in the transition region. 5) Most observers record significant increases in C_H by the use of roughened surfaces. 6) These C_H increases are usually accompanied by even greater increases in C_F. Thus, as C_F/C_{FS} is increased by either changes in Reynolds number or changes in roughness geometry, $(C_H/C_{HS})/(C_F/C_{FS})$ decreases. 7) An exception to this general tendency occurs for Pr greater than 1.0 in the transition region. Under these conditions the smooth pipe C_H/C_F performance can be matched or even slightly exceeded for C_F/C_{FS} ratios as high as 2.7. 8) There are indications that,

with fixed values of C_F, Re and Pr*, C_H may still be changed by altering roughness shape. The results from measurements in annular passages reported by Fortesque and Hall, although not directly comparable to pipe flow results, suggest that close-packed, two-dimensional, rectangular wells may offer significant C_H/C_F performance advantages over other roughness shapes. However, the results of Sams' experiments appear not to support this suggestion. 9) In general the results obtained in the present work with a close-packed, granular, roughness shape show C_H/C_F performance as good or better than the other types of roughness compared in Figures 37 and 38.

---

*Note that fixing Re and Pr also fixes C_{FS} and C_{HS}.

VII APPLICATIONS OF RESULTS

A knowledge of the relationships among the basic parameters influencing heat transfer in rough tubes is a prerequisite to arriving at optimum designs for heat exchangers employing such tubes as elements. A limited range of the independent parameters affecting the heat transfer coefficients in long straight pipes with a close-packed, granular type of roughness are experimentally investigated in this thesis. The pertinent independent variables are completely represented by the dimensionless groups, Re, Pr and ϵ_s/D.

By means of the similarity rule for heat transfer in rough tubes it is possible to consolidate this information into a function of only two variables, $g\{\epsilon*, Pr\}$, as was shown in Figure 33. Then by analyzing the "g" function it is possible to regenerate the required design charts of $C_H\{Re; \epsilon_s/D; Pr\}$ which may now cover a much wider range of the parameters than was provided by the original data. This has been done in Figures 34 and 35 for Pr values of 1.20 and 5.94 respectively. The ϵ_s/D ratios selected for presentation correspond to those of the tubes tested in the experiments; however, curves for any ϵ_s/D values can be generated just as easily. Hence the complete Reynolds number-roughness ratio field could be described. This procedure clearly involves more than a graphical extrapolation of the experimentally obtained curves, since each point in Figures 34 and 35 is based on experimental data as presented in terms of the variables of the heat transfer similarity law. The complicated form of the curves shown would indeed have been difficult to generate purely analytically from the original data curves

in Figures 12 through 16. For Reynolds numbers in the fully rough
region shown to the right of the dashed lines ($\epsilon^* \cong 70$) in Figures 34
and 35, the curves for constant ϵ_s/D are closely represented by
the formulas presented in equations 130 and 131 of Section IV-F.

Because of the simple dependence of the "g" function on ϵ^*
and Pr depicted in the $\{g(Pr)^{-0.44}\}$ plots of Figure 36, it is assumed
that the observed ϵ^* and Pr dependence can also be extrapolated
somewhat beyond the present data limits in order to cover, say,
Prandtl numbers from 0.7 to 10 and ϵ^* values out to 5000. Such
extrapolations would seem to offer the best source of design infor-
mation for the extended regions, assuming that additional experi-
mental information is unavailable.

The information obtained in the present experiments should
strictly apply only to the particular close-packed, granular rough-
ness type which was studied. It is assumed however that, in the
absence of more directly applicable experimental data, the $g\{\epsilon^*;Pr\}$
functions from present results could be applied to other close-
packed, three-dimensional roughness types if the hydraulic equiva-
lent sand-grain scale is used to define the roughness. As seen in
Figure 37, the $g\{\epsilon^*;Pr\}$ curve from the present work closely
matches the data for certain naturally rough surfaces operated in
the transition region, but for other types of natural roughness the
agreement is poor. Charts for $C_H\{Re, \epsilon_s/D\}$ can be generated di-
rectly from the results shown for the naturally rough pipes, but
the Prandtl number dependence for such surfaces should be a sub-
ject for more experimentation. Results obtained by Nunner for
various two-dimensional (ring type) roughness patterns are well

represented in Figure 37 by a single line. This is expressed in equation 141 in Section VI and is recommended for use with this general type of roughness for operation in the fully rough regime.

Having available the relationships among the basic parameters affecting heat transfer in rough tubes, it is of interest to investigate those combinations of the parameters for which rough surfaces can be employed most advantageously. This must, in general, be defined in terms of the restraints of a particular application; however as will be shown by an example given in this section, high values of the ratio C_H/C_F are almost always desirable. In this connection, an interesting characteristic, which is likely to be common to all roughness types, is evident from the extension of the present results shown in Figure 35.

In this figure it is seen that as Reynolds number increases far into the fully rough regime, C_H becomes nearly independent of ϵ_s/D. An analysis of the generating formulas for these curves reveals that, for very large Reynolds numbers, a region of operation can be found wherein the C_H will actually decrease slightly with increasing ϵ_s/D for fixed Re and Pr values.

A plausibility argument for this behavior is presented as follows: The defining equation for "g", for the fully rough region, can be rearranged to give

$$C_F/2C_H = (1-8.48\sqrt{C_F/2}) + \sqrt{C_F/2}\ g_{F.R.}\{\epsilon^*, Pr\} \qquad (152)$$

As ϵ_s/D increases for fixed Re $\sqrt{C_F/2}$ and ϵ^* and thus "g" all increase monotonically. For very large ϵ_s/D, the last term on the right hand side of equation 152 becomes large compared to the

terms in parenthesis, so that,

$$C_H = \sqrt{C_F/2}/g_{F.R.} \quad , \quad \epsilon_s/D \to \infty \tag{153}$$

Following the discussion in Section II leading to equation 56, this can be written

$$C_H = \sqrt{C_F/2} \ 8.48 \ C_{Hc}\{8.48 \ \epsilon^*; \ Pr\} \ , \quad \epsilon_s/D \to \infty \tag{154}$$

where C_{Hc} is the cavity Stanton number discussed in connection with the turbulent vortex hypothesis (Cf. Appendix VII), and $8.48\epsilon^*$ is the pertinent cavity Reynolds number. Using this hypothesis with Prandtl number fixed and evaluating the exponent for ϵ^* from the present experimental results, there is obtained

$$C_{Hc} = K_1 \ (\epsilon^*)^{-0.2} \tag{155}$$

The K's in this discussion are constants. Using the definition

$$\epsilon^* \equiv Re \ \sqrt{C_F/2} \ \epsilon_s/D$$

equation 155 can be written for fixed Re and Pr as

$$C_{Hc} = K_2 \ (\epsilon_s/D)^{-0.2} \ (C_F)^{-0.1} \tag{156}$$

Then substituting equation 156 into equation 154 one obtains

$$C_H = K_3 \ \frac{(C_F)^{0.4}}{(\epsilon_s/D)^{0.2}} \quad , \quad \epsilon_s/D \to \infty \tag{157}$$

From an analysis of the $C_{F \, F.R.}\{\epsilon_s/D\}$ relation given by the friction similarity law (Eq. 26, Sec. II), it can be shown that $(C_F)^{0.4}\{\epsilon_s/D\}$ in equation 157 has a weaker dependence on ϵ_s/D than has $(\epsilon_s/D)^{0.2}$ for the region of interest in this discussion. Thus C_H will decrease

with increasing ϵ_s/D as ϵ_s/D becomes large.

The physical meaning of this result is that the Stanton number of a fully rough pipe flow is determined by the Stanton number of the cavity boundary layers (C_{Hc}). The pertinent Reynolds number for these boundary layers (Re_c) is proportional to ϵ_s/D, and the results of the present experiments were interpreted to mean that the $C_{Hc}\{Re_c\}$ function decreases with an increase of its argument. Thus under certain operating conditions, the cavity boundary layer effect becomes strong enough, with respect to other factors influencing the pipe Stanton number, to make C_H decrease with increasing ϵ_s/D.

This "folding-over" of the curves in the $C_H\{Re;\epsilon_s/D\}$ plots for this type of roughness establishes a maximum for the C_H increase which is attainable by surface roughening. This appears from Figures 34 and 35 to be on the order of a factor of 2.5 times the C_H for a smooth tube. This maximum improvement factor depends to some extent on Reynolds number and Prandtl number conditions. It can be shown analytically that for ϵ_s/D higher than about 0.1 the C_H again starts to slowly increase with ϵ_s/D at large ϵ^*; however, for these cases the roughness height is getting to be such a large portion of the tube radius that the analytical extension of the present results may no longer apply.

The fact that the heat transfer coefficient becomes insensitive to increases in roughness as the roughness ratio becomes large has an important bearing on the degree of roughening that can be used effectively for heat exchanger surfaces. The friction factor will continue to increase markedly with roughness ratio even as the maximum

C_H is being approached. Hence the greatest C_H/C_F performance for a rough tube with respect to a smooth tube will be obtained if the roughness ratio for a given Reynolds number is chosen so that the tube will be operating near the high Reynolds number end of the transition region. This can be seen by again referring to the $C_H\{Re; \epsilon_s/D\}$ curves of Figures 34 and 35. If roughness ratio is selected to be larger than the one described by the above criterion, the improvement in C_H will be small in comparison to the increase in C_F since the maximum C_H condition is being approached.

The discussion presented thus far in this section has concerned the relationships among the various dimensionless groups pertinent to heat transfer in rough tubes. These relations provide the basic information needed for heat exchanger designs; however, only qualitative statements concerning the optimum design can be made in terms of the dimensionless groups. A description of an optimum heat exchanger design must refer to the interactions with other parts of a system in terms of the components of the dimensionless groups. The decision of whether or not to employ roughened surfaces for specific heat exchanger designs will depend on the considerations such as installation and operating cost, space and weight limitations, pumping power availability, and temperature limitations of materials. Sheriff (Ref. 38) has considered several sets of design restraints for tube-type heat exchangers under which rough surfaces may be used advantageously. The general problem is to transfer heat $(\dot{Q})$ with a small temperature difference (ΔT), a low amount of pumping power (W) and often with small volume or low weight per heat exchanger element.

As an example, the conditions which could occur in a hypothetical heat exchanger design are considered. The coolant, the heat flux and the geometry, in particular the length and diameter of the cooling tube, are assumed to be established. The mean temperature drop between the wall and the coolant is assumed fixed. The flow rate however is allowed to vary and thus the temperature rise of the coolant is also variable. It is desired then to minimize the coolant pumping-power requirement by the selection of the optimum flow rate and roughness combination. Applying these conditions and using the definitions of C_F and C_H, it is readily shown that

$$W = K_1 C_F \{u_m\} / [C_H\{u_m\}]^3$$

where K_1 is a dimensional constant containing various fixed parameters in the problem and u_m is the discharge velocity of the tube. An auxiliary condition also appears,

$$u_m = K_2 / C_H \{u_m\}$$

with K_2 as another dimensional constant. The comparison of a rough (R) and smooth (S) surface can then be written

$$\frac{W_R}{W_S} = \frac{(C_{HS}/C_{FS})\{u_{mS}\}}{(C_{HR}/C_{FR})\{u_{mR}\}} \left[\frac{C_{HS}\{u_{mS}\}}{C_{HR}\{u_{mR}\}} \right]^2$$

with the auxiliary condition

$$\frac{u_{mR}}{u_{mS}} = \frac{C_{HS}\{u_{mS}\}}{C_{HR}\{u_{mR}\}}$$

In general the solution for W_R/W_S must be treated graphically using the experimentally determined $C_H\{Re; \epsilon_s/D\}$ and $C_F\{Re; \epsilon_s/D\}$ functions. For purposes of this simple illustration, a conservative assumption, in terms of the predicted power savings for rough surfaces,

is that the different C_H and C_F terms are evaluated at the same u_m, i.e. at the same Reynolds number. From Figures 34 and 35 it is seen that a rough tube may be selected for any Reynolds number that will give

$$C_{HR}/C_{HS} \geqslant 2.0$$

Then from Figure 38 it can be ascertained that, for C_{HR}/C_{HS} equal to 2.0, C_{FR}/C_{FS} would be on the order of 3.0, assuming for this illustration that a gas with Prandtl number of 0.7 is the coolant. Thus a reasonable selection of roughness scale would yield

$$\frac{C_{HS}/C_{FS}}{C_{HR}/C_{FS}} \simeq \frac{3}{2}$$

Then the power ratio becomes

$$\frac{W_R}{W_S} \simeq \frac{3}{2} \frac{1}{2^2} \simeq 0.375$$

This illustrates that a considerable reduction in power consumption can be afforded by the use of rough surfaces for the particular case analyzed. It should be emphasized again, however, that the possible power reduction depends on the constraints of the design, and the usefulness of the application of rough surfaces can only be judged by considering the entire system.

Despite the fact that advantageous use of rough surfaces can be demonstrated even when (C_H/C_F) falls below the smooth surface value, the best heat exchanger performance is always obtained when C_H/C_F is the maximum attainable for a given increase in C_H.

Consequently, the selection of an optimum roughness ratio for a given operating condition is necessary in order to realize the full advantages of rough surfaces. It may be appropriate to emphasize here that in view of the above discussion it is seen that rough surfaces can be more efficient than smooth surfaces for heat exchangers. This fact has not always been recognized by experimenters, and it does, of course, depend on the basis of comparison.

Several methods, other than surface roughening, have been investigated for inducing secondary flow and thereby for increasing heat transfer coefficients (Cf. Refs. 6, 7 and 43). Gambill, Bundy and Wausbrough (Ref. 6) studied the use of twisted tapes for inducing a swirl component to the flow. These tapes which have a width equal to the pipe diameter were extended through the full length of the pipes. For tubes having certain ratios of tape-pitch-to-pipe-diameter, they observed (C_H/C_F) values that exceeded computed values for smooth tubes with axial flow. This condition occurred for water flowing at $86^{\circ}F$ with pipe Reynolds numbers in the range of 2×10^4 to 3×10^5. This observation is weakened but not nullified by the fact that the smooth pipe law assumed for their comparison was

$$C_{HS} = (C_{FS}/2) (Pr)^{-2/3}$$

This gives C_{HS} values from 20 to 30 percent too low for the conditions presented.

The C_F values observed for the twisted tapes were independent of Reynolds number. This fact was attributed, by the authors, to a slight roughness of the pipe surface. It is interesting to note

that, in two cases considered, the rough tubes from the present

experiments, with roughness ratio selected to produce the same

$C_{FF.R.}$, yield nearly the same (C_H/C_F) performance as that at-

tained with swirl flow. This suggests that these two methods

offer competitive means for improving heat exchanger efficiency.

VIII SUMMARY

A process has been developed for producing tubes with rough surfaces from electroplated nickel. A wide variety of roughness forms can be reproduced by this method and the resulting tubes have thin, uniform walls suitable for use in heat transfer experiments. Four such tubes were built; one has a smooth surface and three others have varying degrees of a close-packed, granular type of roughness formed as the casts of mandrels coated with closely graded sand.

Heat transfer and pressure drop measurements were obtained with water flowing at various bulk temperatures through the tubes which were heated by the passage of electric current through the tube walls. A range of Reynolds numbers from 1.5×10^4 to 5×10^5 and Prandtl numbers from 1.2 to 6.0 were investigated with each tube. The idealized conditions of fully established, isothermal flow were approximated respectively by the use of long entrance sections of the surface structure under test and by an extrapolation of the data from three different heat flux values.

The estimated confidence limits for the reproduceability of the heat transfer measurements ranged from plus or minus 4 percent to plus or minus 7 percent for all tubes except the smoothest of the rough tubes for which the limits are set as high as plus or minus 17.5 percent. The latter tube, containing roughness elements with heights of approximately 0.001 inch, evidenced small circumferential variations in roughness.

The smooth tube heat transfer and friction results were found to confirm the predictions from the theories of Rannie and of von Kármán and to agree with the experimental measurements of

Eagle and Ferguson and of Allen.

Although the roughness elements in the three rough tubes are not thought to be exactly geometrically similar, it was found that the $C_F\{Re\}$ dependence for each tube follows closely to that observed by Nikuradse for geometrically similar, sand-grain surfaces. In particular, the tube with smallest roughness ratio exhibited smooth, transition, and fully rough Reynolds number regions.

A similarity rule for heat transfer in rough pipes with geometrically similar roughness elements has been proposed. By this rule the general problem of determining the four-variable dependence of C_H, Re, Pr, and ϵ/D is reduced to a three-variable system. This is analogous to a related development by von Kármán and Nikuradse by which the three-variable (C_F, Re and ϵ/D) relationship for friction in rough pipes was reduced to a two-variable system. The results of the present work as well as those from other experiments were shown to support the heat transfer similarity rule. In establishing this support, the roughness ratios for each tube were evaluated in such a way that conformity with the requirements of the friction similarity rule was assured. By means of the heat transfer similarity rule it is possible to expand the experimental results for a given roughness type to provide a description of the $C_H\{Re, Pr, \epsilon/D\}$ dependence over wider ranges of Re and ϵ/D than were contained in the original data.

A simple analytical form was found which closely describes the complete $C_H\{Re, Pr, \epsilon/D\}$ dependence of the present results for the fully rough regime. A hypothesis was proposed which explains this analytical form in terms of the characteristics of thin

boundary layers formed in the cavities of the roughness elements. A prediction from the hypothesis states that this analytical form should be the same for surfaces with other roughness shapes and that it should be necessary to change only one empirical constant to account for each particular roughness type. This prediction was fulfilled by Nunner's results for heat transfer in tubes having rings inserted as roughness elements.

Increases in heat transfer coefficient of up to 2.7 times the smooth tube value were observed for the rough tubes of the present experiments. The C_H increase is in general accompanied by a larger increase in C_F; however, for Pr values from 4 to 6 and for operation in the transition region, the C_H/C_F performance of the rough tubes slightly exceeds the smooth tube performance. Extensions of the present results by means of the similarity rule indicate that a limit exists beyond which increases in roughness will continue to raise the friction coefficient but will cease to improve the heat transfer coefficient.

The Reynolds number region near the juncture of the transition and fully rough regimes was shown to yield the highest C_H/C_F performance for a given roughness ratio. Also the highest values of the heat transfer coefficient for rough tubes with respect to smooth tubes were obtained in this region.

In general, greater improvements in heat transfer coefficient due to roughness were observed at higher Prandtl numbers.

The granular surfaces studied in the present work were shown to provide C_H/C_F performance as high or higher than that of the other roughness patterns compared. Hence, the present

results should be representative of the advantages to be gained by artificially roughening heat exchanger surfaces. A simple example of a case where the use of a roughened surface would offer considerable advantages over smooth surfaces was presented. It was also indicated that, if care is used in selecting a roughness ratio, roughened surfaces should offer strong competition to other means, such as the introduction of swirl generators, for efficiently increasing heat transfer coefficients in tubes.

SYMBOLS AND ABBREVIATIONS

A	Friction similarity function, defined by equation 26
B	Empirical constant from equations 9 and 10
B_x	Dimensionless parameter, defined by equation 76
C_F	Friction coefficient for tubes, defined in equation 20
C_H	Heat transfer coefficient (Stanton number) for tubes, defined in equation 29
C_{Hc}	Roughness-cavity Stanton number, defined by equation 51
c_p	Specific heat at constant pressure
D	Tube inside diameter, defined for rough tubes by equation 69
e	Thermoelectric power, $e \equiv dE/dT$
E	Thermocouple e.m.f. with water-ice temperature as reference
E_{TS}	Potential-drop in the test section
f	General function
F	Function, defined by equation 48
g	Heat transfer similarity function, defined by equation 54
h	Heat transfer film conductance, $h \equiv \dot{q}_o/(T_w - T_L)$
I	Current
k	Thermal conductivity
K	Dimensional discharge coefficient for the metering venturi, defined in Figure 11
L	Length of the heated test section
L_R	Length of the rough tube between the test section pressure taps
Pr	Prandtl number, $Pr \equiv c_p\mu/k$
$\dot{q}_o$	Mean heat flux normal to the tube wall

r	Radius coordinate
R	Tube radius, $R \equiv D/2$
R_e	Electrical resistance of the tube
Re	Reynolds number for tubes, defined in equation 24
Re_c	Roughness cavity Reynolds number, defined by equation 50
t	Tube wall thickness, defined for rough tubes by equation 70
T	Temperature
T_{abs}	Temperature on an absolute scale
T_L	Mixed-mean fluid temperature, defined by equation 30
T_w	Tube wall temperature
u	Mean axial velocity, a function of ''y'' only
u_m	Tube discharge velocity, defined in equation 18
u_τ	Friction velocity, defined in equation 12
$\dot{w}$	Mass flow rate
W_P	Tube heating power, measured electrically at probes on the test tube
W_{TS}	Tube heating power, measured electrically at the test section electrodes
W_{TSC}	Tube heating power, measured calorimetrically
x	Axial distance coordinate, originates at the start of heating
y	Distance from the wall coordinate
y*	Dimensionless distance from the wall, defined in equation 12

Greek letters:

β	Constant, defined by equation 19
$\delta_x E_{11}$	Isothermal difference in e.m.f. between the thermocouples at locations x and 11
$\Delta_x E_{11}$	Difference in e.m.f. between the thermocouples at locations x and 11

$\Delta_x E_{11T}$ — The term $\Delta_x E_{11}$ compensated for effects not due to electrical heating (Cf. App. IV-A)

ΔP_v — Pressure-drop in the metering venturi

ΔP_{TS} — Pressure-drop in the test section

ΔT_c — Temperature-rise of the fluid passing through the test section, $\Delta T_c \equiv T_{11} - T_o$

ΔT_f — Temperature difference between the wall and the local mixed-mean fluid, $\Delta T_f \equiv T_w - T_L$

ΔT_w — Temperature-drop across the tube wall

$\Delta_x T_{11}$ — Difference in temperature of the mixed-mean fluid at locations x and 11

ΔV — Incremental volume of a section of the tube

ϵ — Roughness height

ϵ_M — Turbulent diffusion coefficient for momentum transfer

ϵ_H — Turbulent diffusion coefficient for heat transfer

ϵ_s — Sand-grain roughness height for equivalent friction coefficient at fully rough conditions

ϵ^* — Dimensionless roughness height, defined by equation 13

ζ — Dimensionless parameter, defined by equation 100

μ — Absolute viscosity

ν — Kinematic viscosity

ρ — Density

ρ_e — Electrical resistivity

τ — Mean shear stress, a function of ''y'' only

τ_o — Mean shear stress at the tube wall

Subscripts:

av — Longitudinal average

CL — Tube center line

F.R. — Fully rough

g	Average value on that surface described by the tips of the roughness elements
S	Smooth
x	Refers to any of the thermocouple locations: inlet fluid, x = 0; first longitudinal station on the tube wall, x = 1, 2 or 3; second station, x = 4, 5 or 6; third station, x = 7, 8 or 9; and outlet fluid, x = 11

Abbreviations:

amp	Amperes
AC	Alternating current
DC	Direct current
e.m.f.	Electromotive force
gpm	Gallons per minute
HP	Horse power
kva	Kilovolt-amperes
mv	Millivolts
psia	Pounds per square inch absolute
psid	Pounds per square inch differential
psig	Pounds per square inch gage
r.m.s.	Root mean square
v	Volts
μv	Microvolts
%δ	An operator read, "percentage variation"
{ }	Braces are used exclusively as a functional form, e.g., f{Re;Pr} is read, "the variable f, a function of Re with Pr as a parameter."

REFERENCES

1. Stanton, T. E., Friction, London (1923).

2. Fortescue, P. and Hall, W. B., "Heat Transfer Experiments on the Fuel Elements," Jour. of British Nuclear Energy Conf., Vol. 2, #2 (April, 1957), p. 83.

3. Grass, G., "The Improvement of Heat Transfer to Water Derivable from the Artificial Roughening of Surfaces in Reactors or in Heat Exchangers," Atomkernenergie, Vol. 3 (1958), pp. 328-331; AEC Translation No. 3641 by G. Dessauer.

4. Sheriff, N., "The Effectiveness of Roughened Surfaces in Heat Transfer," M.S. Thesis, Victoria Univ. of Manchester (Oct., 1957).

5. Nunner, W., "Heat Transfer and Pressure Drop in Rough Tubes," VDI-Forschungsheft 455, Series B, Vol. 22 (1956), pp. 5-39; A.E.R.E. Lib./Trans. 786 (1958) by F. Hudswell.

6. Gambill, W. R., Bundy, R. D. and Wansbrough, R. W., "Heat Transfer, Burnout, and Pressure Drop for Water in Swirl Flow through Tubes with Internal Twisted Tapes," Oak Ridge Nat. Lab., No. 2911, (March, 1960).

7. Koch, R., "Pressure Loss and Heat Transfer in Turbulent Flow," VDI-Forschungsheft 469, Series B, Vol. 24 (1958), pp. 1-44.

8. Cope, W. F., "The Friction and Heat Transmission Coefficients of Rough Pipes," Proc. Inst. Mech. Engrs.,Vol. 145 (1941), pp. 99-105.

9. Smith, J. W. and Epstein, N., "Effect of Wall Roughness on Convective Heat Transfer in Commercial Pipes," Jour. AIChE, Vol. 3 (June, 1957), pp. 242-248.

10. Nikuradse, J., "Laws for Flow in Rough Pipes," VDI-Forschungsheft 361, Series B, Vol. 4 (1933); Translation, Brielmaier, A. A., NACA TM 1292 (1950).

11. Allen, R. W., "Measurements of Friction and Local Heat Transfer for Turbulent Flow of a Variable Property Fluid (Water) in a Uniformly Heated Tube," Ph.D. Thesis, Univ. of Minnesota (September, 1959).

12. Eckert, E. R. G. and Drake, R. M. Jr., Heat and Mass Transfer, Second Edition, McGraw-Hill, New York (1959).

13. Hama, F. R., "Boundary Layer Characteristics for Smooth and Rough Surfaces," Trans. Soc. of Naval Architecture and Marine Engineering, Vol. 62 (1954), pp. 333-358.

14. Rannie, W. D., "Heat Transfer in Turbulent Shear Flow," Ph.D. Thesis, California Institute of Technology (1951); also, Jour. Aero. Sci., Vol. 23 (May, 1956), pp. 485-489.

15. Townsend, A. A., The Structure of Turbulent Shear Flow, University Press, Cambridge (1956).

16. Laufer, J., "The Structure of Turbulence in Fully Developed Pipe Flow," NACA Report 1174 (1954).

17. Millikan, C. B., "A Critical Discussion of the Turbulent Flows in Channels and Circular Tubes," Proc. of the 5th International Congress of Applied Mech., Cambridge, Mass. (1938), pp. 386-392.

18. Schlichting, H., Boundary Layer Theory, McGraw-Hill, New York (1955).

19. Bakhmeteff, B., The Mechanics of Turbulent Flow, Princeton University Press (1936).

20. Jakob, M., Heat Transfer, Vol. 1, John Wiley and Sons, New York (1949).

21. von Kármán, T., "The Analogy between Fluid Friction and Heat Transfer," Trans. ASME, Vol. 61 (1939), pp. 705-710.

22. Reichardt, H., "The Principles of Turbulent Heat Transfer," Archiv. f. die gesamte Wärmetechnik, No. 6/7 (1951); Translation, Reiss, S., NACA TM 1408 (1957).

23. Deissler, R. G., "Analysis of Turbulent Heat Transfer, Mass Transfer, and Friction in Smooth Tubes at High Prandtl and Schmidt Numbers," NACA Report 1210 (1955).

24. Wise, E. M. and Schaefer, R. H., "The Properties of Pure Nickel," Metals and Alloys (Sept., Nov. and Dec., 1942), pp. 424-428, 891-893, 1067-1071.

25. Smith, C. S. and Palmer, E. W., "Thermal and Electrical Conductivities of Copper Alloys," Am. Inst. of Mining and Metallurgical Engin., Vol. 2, No. 6 (Sept., 1935); Tech. Pub. No. 648.

26. McElroy, D. L., "Progress Report No. 1, Thermocouple Research," Oak Ridge Nat. Lab., No. 2467 (Nov., 1956 - Oct. 1957).

27. Colebrook, C. F., "Turbulent Flow in Pipes with Particular Reference to Transition Between Smooth and Rough Laws," Jour. Inst. Civil Engrs., Vol. 11, London (1938-39), pp. 133-156.

28. Hartnett, J. P., "Experimental Determination of the Thermal Entrance Length for the Flow of Water and of Oil in Circular Pipes," Ph.D. Thesis, U. of Calif. (1954); also Trans. ASME, Vol. 77 (1955), pp. 1211-1220.

29. McAdams, W. H., Heat Transmission, 3rd Ed., McGraw-Hill, New York (1954).

30. Eagle, A. and Ferguson, R. M., "On the Coefficient of Heat Transfer From the Internal Surface of Tube Walls," Proc. Roy. Soc., Vol. 127 (June, 1930), pp. 540-566.

31. Hastrup, R. C., "Heat Transfer and Pressure Drop in an Artificially Roughened Tube at Various Prandtl Numbers," Thesis for the degree of Mechanical Engineer, Calif. Inst. of Tech. (1958); also Jet Propulsion, Vol. 28 (April, 1958), pp. 259-263.

32. Colebrook, C. F. and White, "Experiments with Fluid Friction in Roughened Pipes," Proc. Roy. Soc., Vol. 161 (1937), p. 369.

33. Roshko, A., "Some Measurements of Flow in a Rectangular Cutout," NACA TN 3488, (Aug., 1955).

34. Martinelli, R. C., "Heat Transfer to Molten Metals," Trans. ASME, Vol. 69 (1947), p. 947.

35. Mattioli, G. D., "Theory of Heat Transfer in Smooth and Rough Pipes," Forschung auf dem Gebiete des Ingenieurwesens, Vol. 11, No. 4 (July-Aug., 1940); Translation, Boelter, L. M. K., NACA TM 1037 (1942).

36. Lancet, R. T., "The Effect of Surface Roughness on the Convection Heat Transfer Coefficient For Fully Developed Turbulent Flow in Ducts," MS Thesis, Univ. of Cincinnati (1957).

37. Kemeny, G. A. and Cyphers, J. A., "Heat Transfer and Pressure Drop in an Annular Gap with Surface Spoilers," ASME Paper No. 60-HT-15 (May, 1960).

38. Sheriff, N., "The Effectiveness of Roughened Surfaces in Heat Transfer," MS Thesis, Victoria Univ. of Manchester (Oct., 1957).

39. Knudsen, J. G. and Katz, D. L., <u>Fluid Dynamics and Heat Transfer</u>, McGraw-Hill, New York (1958).

40. Wieghardt, K., "Erhöhung des turbulenten Reibungswiderstandes durch Oberflächenstörungen (Increase of the Turbulent Frictional Resistance Caused by Surface Irregularities)," Forschungsbericht 1563, ZWB, (March, 1942); also, <u>Jahrb., deutchen Luftfhartfor-schung</u> (1943), pp. 1-17.

41. Brouillette, E. C., Mifflin, T. R. and Myers, J. E., "Heat Transfer and Pressure-Drop Characteristics of Internal Finned Tubes," ASME Paper No. 57-A-47 (1957).

42. Sams, E. W., "Experimental Investigation of Average Heat-Transfer and Friction Coefficients for Air Flowing in Circular Tubes Having Square-Thread-Type Roughness," <u>NACA RM E52D17</u> (June, 1952).

43. Kreith, F. and Margolis, D., "Heat Transfer and Friction in Turbulent Vortex Flow," <u>Appl. Sci. Res.</u>, Vol. 8, Section A, (1959), pp. 457-473.

44. Rupe, J. H., "A Semi-Automatic, Size Differentiating Droplet Counter," Jet Propulsion Laboratory, Prog. Rept. No. 20-162 (Feb., 1952).

45. Lees, C. H., "Thermal and Electrical Conductivity of Metals and Alloys at Low Temperatures," <u>Phil. Trans. Roy. Soc.</u>, Vol. 208 A (1908), p. 426.

46. Schofield, F. H., "Thermal Conductivities of Some Pure Metals," <u>Proc. Roy. Soc.</u>, Series A, Vol. 107 (Jan.-April, 1925), p. 206.

47. Kreith, F. and Summerfield, M., "Investigation of Heat Transfer at High Heat-Flux Densities: Experimental Study with Water of Friction Drop and Forced Convection With and Without Surface

Boiling in Tubes," Jet Propulsion Laboratory, Prog. Rept. No. 4-68 (April, 1948).

48. McAdams, W. H., Addoms, J. N. and Kennel, W. E., "Heat Transfer at High Rates to Water with Surface Boiling," Argonne National Laboratory 4268 (Dec. 1948); reissued as U. S. Atomic Energy Comm. AECU-200.

49. Schlichting, H., "Experimental Investigation on the Roughness Problem," Ing.-Arch., Vol. 7 (1936), pp. 1-34; Translation, NACA TM 823 (1937).

TABLE I. TUBE DIMENSIONS
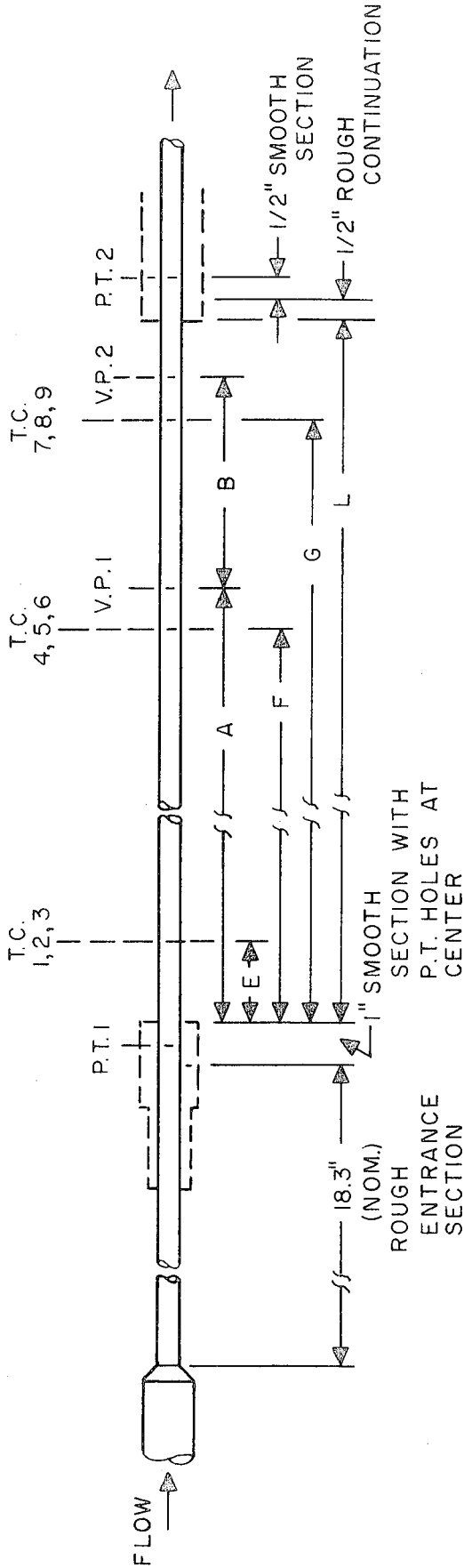
TUBE	D	L	t_7	d_{sg}	ϵ_s	ϵ_s/D	A	B	E	F	G
				ALL DIMENSIONS IN INCHES							
E-3	0.377	17.40	0.0201	—	—	—	12.38	3.65	2.18	10.17	15.14
D-3	0.384	17.39	0.0226	0.0032	0.00092	0.0024	11.04	5.02	2.13	10.15	15.12
C-9	0.393	17.39	0.0176	0.0075	0.0054	0.0138	10.99	5.03	2.18	10.17	15.14
A-4	0.399	17.41	0.0187	0.0150	0.0195	0.0488	11.09	5.01	2.14	10.12	15.12

NOTES

P.T. PRESSURE TAP
V.P. VOLTAGE PROBE
T.C. THERMOCOUPLE
d_{sg} DIAMETER OF MANDREL SAND GRAINS

t_7 WALL THICKNESS AT T.C. STATION 7

E,F,G, STATION OF T.C. 2,5,8, RESPECTIVELY
OTHERS ~ ± 0.15-in. FROM THESE LOCATIONS

TABLE 2

Confidence Limits* for Experimental Heat Transfer Coefficients

Tube	T_L ($^\circ$F)	$\dot{w}$ (lb/sec)	$\% \delta C_H$ (Reading error only)	$\% \delta C_H$**
E-3	80	0.35	± 1.1	+3.4 -3.1
	80	1.75	± 1.1	+4.0 -3.0
	290	0.35	± 1.2	+4.0 -3.7
	290	1.75	± 1.3	+5.8 -3.8
D-3	80	0.20	± 1.1	+2.1 -2.4
	80	1.75	± 1.2	+14.6 -13.2
	290	0.20	± 1.2	+6.7 -6.0
	290	1.75	± 1.4	+17.8 -17.0
C-9	80	0.35	± 1.2	+2.5 -3.3
	80	1.75	± 1.2	+2.7 -3.5
	290	0.35	± 1.2	+2.7 -4.2
	290	1.75	± 1.3	+3.1 -4.3
A-4	80	0.20	± 1.2	+4.9 -6.3
	80	1.75	± 1.2	+4.9 -5.9
	290	0.20	± 1.2	+5.0 -7.2
	290	1.75	± 1.4	+5.2 -6.6

*Confidence coefficient equals approximately 95 percent.
**Refer to expression 119 of the text for an interpretation of $\% \delta C_H$.

TABLE 3-a

Isothermal Friction Factor Results

Tube E-3				Tube D-3			
D = 0.377 in., smooth				D = 0.384 in., ϵ_s/D = 0.0024			
T_L	$\dot{w}$	Re	C_F	T_L	$\dot{w}$	Re	C_F
(^oF)	(lb/sec)	$\times 10^{-4}$	$\times 10^3$	(^oF)	(lb/sec)	$\times 10^{-4}$	$\times 10^3$
80	0.352	2.45	5.97	81	0.202	1.40	7.83
80	0.591	4.12	5.62	81	0.352	2.43	6.89
80	0.998	6.96	4.76	81	0.600	4.15	6.07
81	1.75,0	12.3,0	4.23	81	0.935	6.48	5.82
				81	0.996	6.90	5.74
105	0.352	3.28	5.56	80	1.74,2	11.9,5	5.77
105	0.599	5.58	5.05				
105	0.997	9.29	4.61	104	0.202	1.82	7.42
106	1.74,8	16.4,7	4.06	105	0.363	3.22	6.52
				104	0.601	5.44	5.95
151	0.348	4.88	5.11	104	0.930	8.52	5.92
152	0.598	8.45	4.56	104	1.73,9	15.7,2	5.81
152	0.997	14.1,0	4.16				
152	1.72,8	24.4	3.75	153	0.197	2.77	6.57
				153	0.352	4.94	6.08
291	0.982	30.6	3.61	153	0.598	8.41	5.80
290	1.65,3	51.5	3.47	153	0.949	13.3,5	5.61
				155	1.71,8	24.5	5.89
				287	0.202	6.04	5.57
				288	0.344	10.4,0	5.63
				287	0.581	17.4,0	5.79
				289	0.959	28.9	5.94
				290	1.11,9	34.0	5.95
				291	1.50,3	46.1	5.98
				291	1.68,1	51.5	6.08

TABLE 3-b

Isothermal Friction Factor Results

Tube C-9

$D = 0.393$ in., $\epsilon_s/D = 0.0138$

T_L ($^\circ$F)	$\dot{w}$ (lb/sec)	Re $\times 10^{-4}$	C_F $\times 10^3$
67	0.347	1.97	9.42
74	0.364	2.25	9.06
78	0.356	2.31	8.96
82	0.353	2.42	9.43
74	0.626	3.87	10.0,8
82	0.600	4.12	10.3,5
88	0.596	4.33	10.2,9
74	0.816	5.04	10.3,8
74	1.00,0	6.18	9.99
79	0.99,9	6.59	10.2,9
74	1.37,3	8.49	10.4,3
74	1.78,0	11.0,0	10.7,1
82	1.75,0	12.0,0	10.7,2
82	1.78,0	12.2,0	10.7,1
104	0.350	3.10	9.82
104	0.596	5.28	10.3,6
103	1.00,2	8.81	10.2,7
103	1.74,0	15.3,2	10.9,2
151	0.342	4.62	9.92
151	0.596	8.05	10.5,9
150	0.997	13.4,0	10.6,7
151	1.72,0	23.2,3	11.2,0
290	0.979	28.1	11.4,8
290	1.68,3	50.0	11.4,8
289	1.68,9	50.1	11.4,5

Tube A-4

$D = 0.399$ in., $\epsilon_s/D = 0.0488$

T_L ($^\circ$F)	$\dot{w}$ (lb/sec)	Re $\times 10^{-4}$	C_F $\times 10^3$
81	0.204	1.36	17.2
81	0.347	2.31	17.8
79	0.597	3.88	18.0
81	0.996	6.64	18.0
81	1.74,0	11.6,0	17.7
104	0.201	1.76	17.8
104	0.356	3.11	17.5
104	0.599	5.24	18.1
102	0.998	8.51	18.1
104	1.74,0	15.2,0	17.8
152	0.205	2.74	18.1
153	0.351	4.75	17.8
152	0.601	8.05	18.2
152	0.992	13.3,0	18.2
153	1.72,0	23.2,5	18.4
290	0.197	5.77	17.5
288	0.351	10.2,0	17.5
294	0.588	17.3,5	18.5
290	0.941	27.5	18.5
291	1.67,0	49.2	18.9

TABLE 4

Heat Transfer Results for Tube E-3

D = 0.377 in.   Smooth

T_L ($^\circ$F)	$\dot{w}$ (lb/sec)	Pr	Re x10^{-4}	C_H x10^3	C_F x10^3	$2C_H/C_F$
80	0.350	5.94	2.44	1.14,7	6.19	0.370
80	0.599	5.94	4.18	1.05,5	5.46	0.386
80	0.995	5.94	6.94	0.982	4.88	0.402
80	1.74,6	5.94	12.1,8	0.892	4.31	0.414
103	0.351	4.38	3.22	1.32,4	5.80	0.456
103	0.599	4.38	5.49	1.20,1	5.11	0.470
103	0.997	4.38	9.14	1.10,0	4.59	0.479
103	1.74,0	4.38	15.9,4	1.02,5	4.10	0.500
149	0.350	2.79	4.86	1.52,9	5.04	0.606
149	0.598	2.79	8.30	1.43,8	4.70	0.611
149	0.995	2.79	13.8,0	1.29,2	4.22	0.612
149	1.72,2	2.79	23.9	1.20,4	3.79	0.635
290	0.348	1.20	10.7,5	2.07,7	4.43	0.935
290	0.590	1.20	18.2,1	1.88,6	3.99	0.945
290	0.978	1.20	30.2	1.71,4	3.66	0.936
290	1.68,8	1.20	52.2	1.62,7	3.47	0.937

TABLE 5

Heat Transfer Results for Tube D-3

$D = 0.384$ in. $\quad\quad\quad\quad\quad\quad\quad\quad\quad\quad\quad\quad\quad\quad\quad \epsilon_s/D = 0.0024$

T_L (°F)	$\dot{w}$ (lb/sec)	Pr	Re x10^{-4}	C_{H_7}* x10^3	C_{H_8}* x10^3	C_H x10^3	C_F x10^3	$2\,C_H/C_F$
80	0.205	5.94	1.40	1.28,5	1.28,5	1.28,5	7.85	0.327
80	0.352	5.94	2.41	1.23,0	1.23,6	1.21,6	6.88	0.358
80	0.598	5.94	4.10	1.21,5	1.23,5	1.17,5	6.14	0.396
80	0.995	5.94	6.82	1.21,2	1.30,2	1.12,2	5.72	0.423
80	1.74,6	5.94	11.9,6	1.31,2	1.49,2	1.14,2	5.61	0.468
103	0.205	4.38	1.85	1.46,2	1.46,1	1.46,0	7.37	0.396
103	0.351	4.38	3.16	1.41,5	1.42,3	1.39,6	6.45	0.439
103	0.599	4.38	5.40	1.39,6	1.44,6	1.32,6	5.90	0.473
103	0.997	4.38	8.98	1.43,7	1.57,7	1.30,7	5.63	0.510
103	1.74,1	4.38	15.7,0	1.50,6	1.71,6	1.31,6	5.77	0.521
149	0.203	2.79	2.76	1.78,0	1.77,7	1.77,3	6.66	0.534
149	0.350	2.79	4.77	1.69,5	1.72,5	1.63,5	6.00	0.564
149	0.598	2.79	8.15	1.69,5	1.80,5	1.57,5	5.68	0.596
149	1.001	2.79	13.6,5	1.71,2	1.92,2	1.51,2	5.69	0.602
149	1.72,3	2.79	23.5	1.78,0	2.04,0	1.56,0	5.90	0.603
290	0.199	1.20	6.05	2.52,7	2.62,7	2.40,7	5.80	0.872
290	0.348	1.20	10.60	2.47,6	2.65,6	2.28,6	5.60	0.884
290	0.588	1.20	17.8,9	2.45,0	2.73,0	2.18,0	5.81	0.844
290	0.979	1.20	29.8	2.42,0	2.77,0	2.10,0	5.96	0.821
290	1.68,9	1.20	51.4	2.37,0	2.73,0	2.07,0	6.00	0.791

*These columns represent isothermal C_H values for two different circumferential locations at the final thermocouple station.

TABLE 6

Heat Transfer Results for Tube C-9

$D = 0.393$ in. $\qquad\qquad \epsilon_s/D = 0.0138$

T_L	$\dot{w}$	Pr	Re	C_H	C_F	$2\,C_H/C_F$
(^{O}F)	(lb/sec)		x10^{-4}	x10^3	x10^3	
80	0.354	5.94	2.37	2.00,0	9.50	0.421
80	0.599	5.94	4.01	2.15,0	10.00	0.430
80	0.998	5.94	6.68	2.09,5	10.5	0.399
80	1.74,6	5.94	11.6,9	1.94,2	10.7	0.364
103	0.352	4.38	3.10	2.43,0	9.75	0.498
103	0.595	4.38	5.23	2.47,0	10.3	0.480
103	1.000	4.38	8.80	2.34,2	10.7	0.438
103	1.74,0	4.38	15.3,1	2.17,8	10.8	0.403
149	0.352	2.79	4.68	3.87	10.2	0.562
149	0.595	2.79	7.92	2.91	10.6	0.549
149	0.999	2.79	13.3,0	2.74	10.7	0.512
149	1.72,0	2.79	22.9	2.50	11.2	0.447
290	0.346	1.20	10.2,9	3.82	10.7	0.713
290	0.583	1.20	17.3,2	3.61	11.0	0.656
290	0.982	1.20	29.2	3.42	11.3	0.605
290	1.68,8	1.20	50.1	3.13	11.4	0.549

TABLE 7

Heat Transfer Results for Tube A-4

$D = 0.399$ in. $\qquad\qquad \epsilon_s/D = 0.0488$

T_L	$\dot{w}$	Pr	Re	C_H	C_F	$2\,C_H/C_F$
(°F)	(lb/sec)		$\times 10^{-4}$	$\times 10^3$	$\times 10^3$	
80	0.205	5.94	1.35	3.10	17.2	0.360
80	0.352	5.94	2.32	3.03	18.0	0.337
80	0.598	5.94	3.94	2.87	18.0	0.319
80	0.995	5.94	6.56	2.60	18.0	0.288
80	1.75,0	5.94	11.5,3	2.25	18.0	0.250
103	0.205	4.38	1.78	3.54	17.8	0.398
103	0.352	4.38	3.05	3.43	18.0	0.380
103	0.599	4.38	5.19	3.17	18.0	0.352
103	0.997	4.38	8.64	2.83	18.0	0.314
103	1.74,1	4.38	15.1,0	2.50	18.1	0.276
149	0.204	2.79	2.68	4.14	18.0	0.460
149	0.350	2.79	4.59	3.95	18.0	0.439
149	0.599	2.79	7.85	3.58	18.0	0.397
149	0.996	2.79	13.0,7	3.16	18.0	0.350
149	1.72,4	2.79	22.6	2.82	18.3	0.308
290	0.200	1.20	5.85	5.03	18.0	0.559
290	0.346	1.20	10.1,2	4.64	18.0	0.515
290	0.590	1.20	17.2,6	4.21	18.2	0.463
290	0.979	1.20	28.6	3.89	18.5	0.421
290	1.68,9	1.20	49.3	3.41	18.8	0.362

E-3

D-3

0   1   2

C-9

A-4
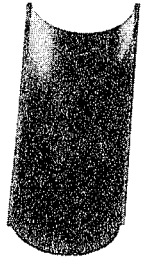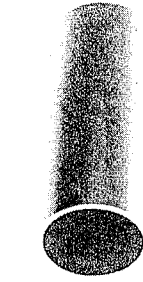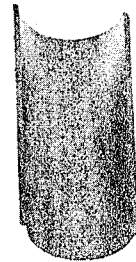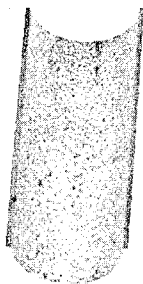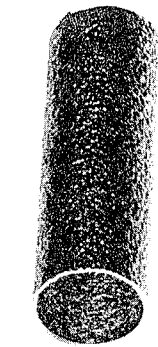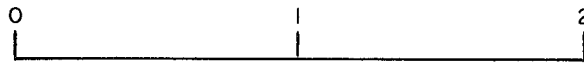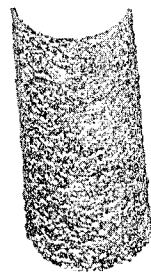
FIG. I. TUBE SAMPLES
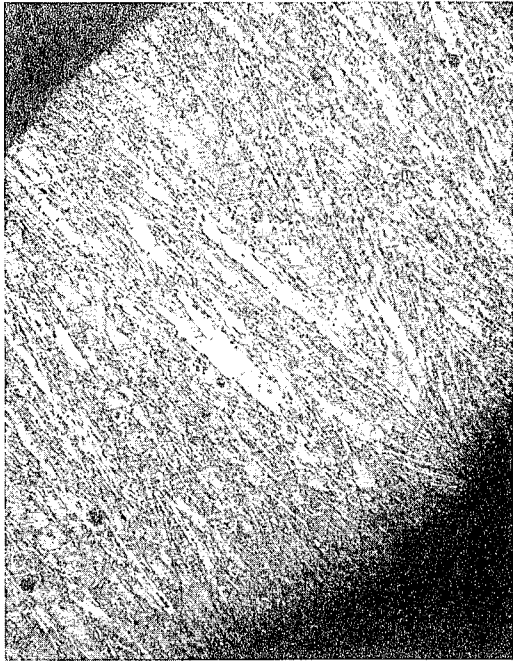
TUBE D-3
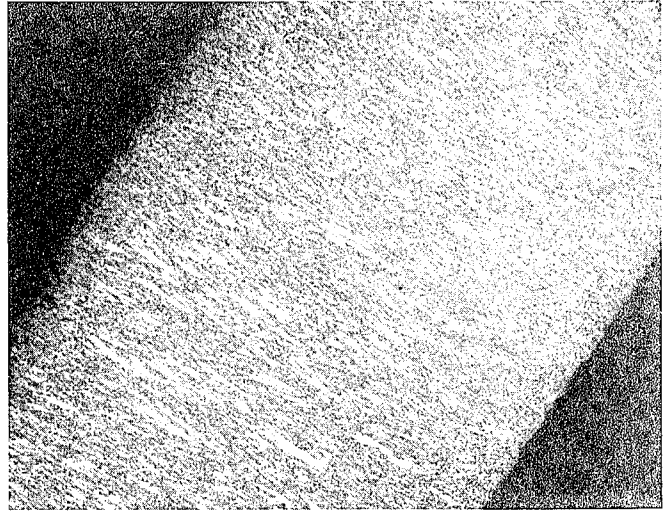
TUBE E-3
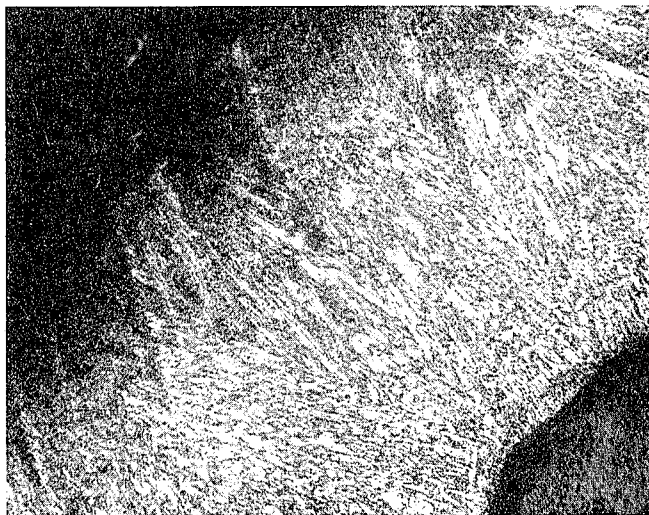
TUBE C-9

TUBE A-4

INSIDE TUBE SURFACE TO LOWER RIGHT IN ALL PHOTOS

FIG. 2 PHOTOMICROGRAPHS OF ETCHED TUBE SAMPLES 130×
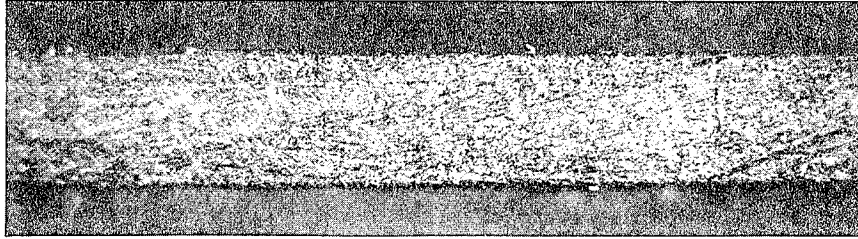
TUBE E-3 (SMOOTH) LONGITUDINAL
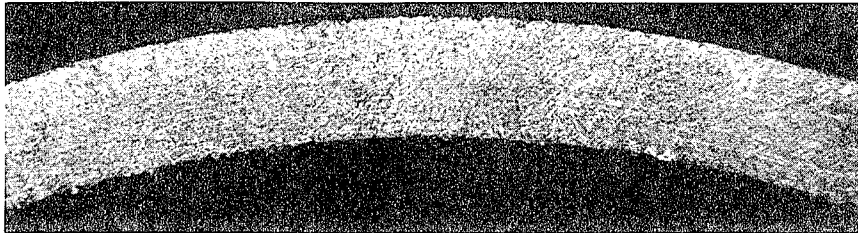
TUBE E-3 (SMOOTH) CIRCUMFERENTIAL
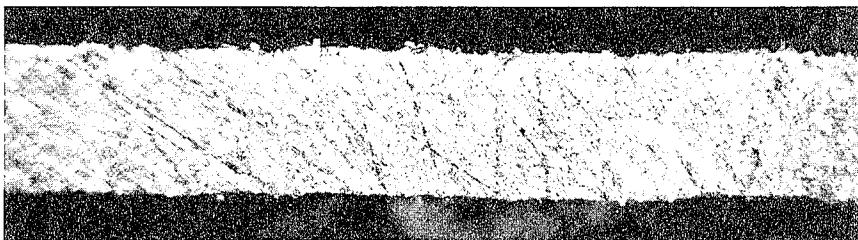
TUBE D-3   LONGITUDINAL
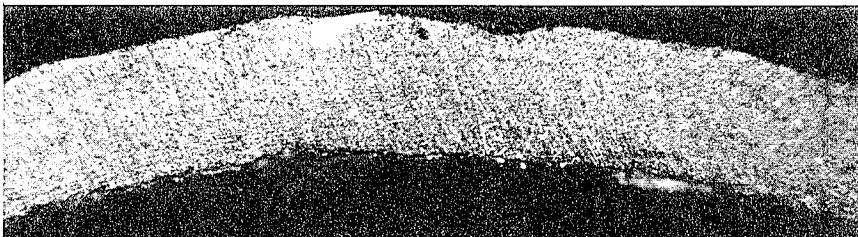
TUBE D-3 CIRCUMFERENTIAL

INSIDE TUBE SURFACE IS SHOWN ON LOWER SIDE IN ALL PHOTOS

FIG. 3-a. TUBE CROSS-SECTION PHOTOMICROGRAPHS 25 to 35X
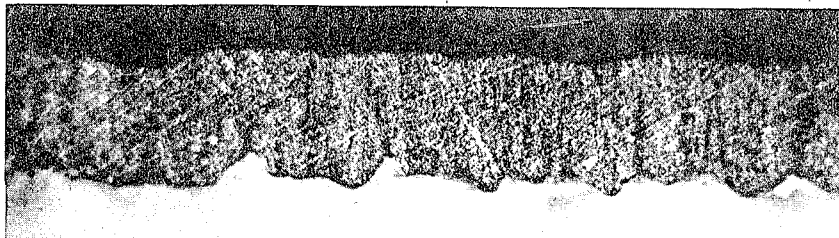
TUBE C-9   LONGITUDINAL
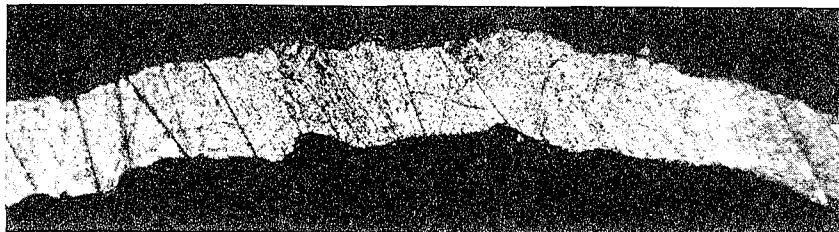
TUBE C-9   CIRCUMFERENTIAL

TUBE A-4 LONGITUDINAL
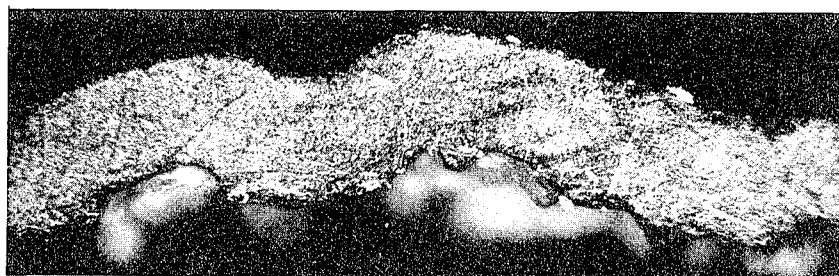
TUBE A-4 CIRCUMFERENTIAL

INSIDE TUBE SURFACE IS SHOWN ON LOWER SIDE IN ALL PHOTOS

FIG. 3-b. TUBE CROSS-SECTION PHOTOMICROGRAPHS 25 to 35X
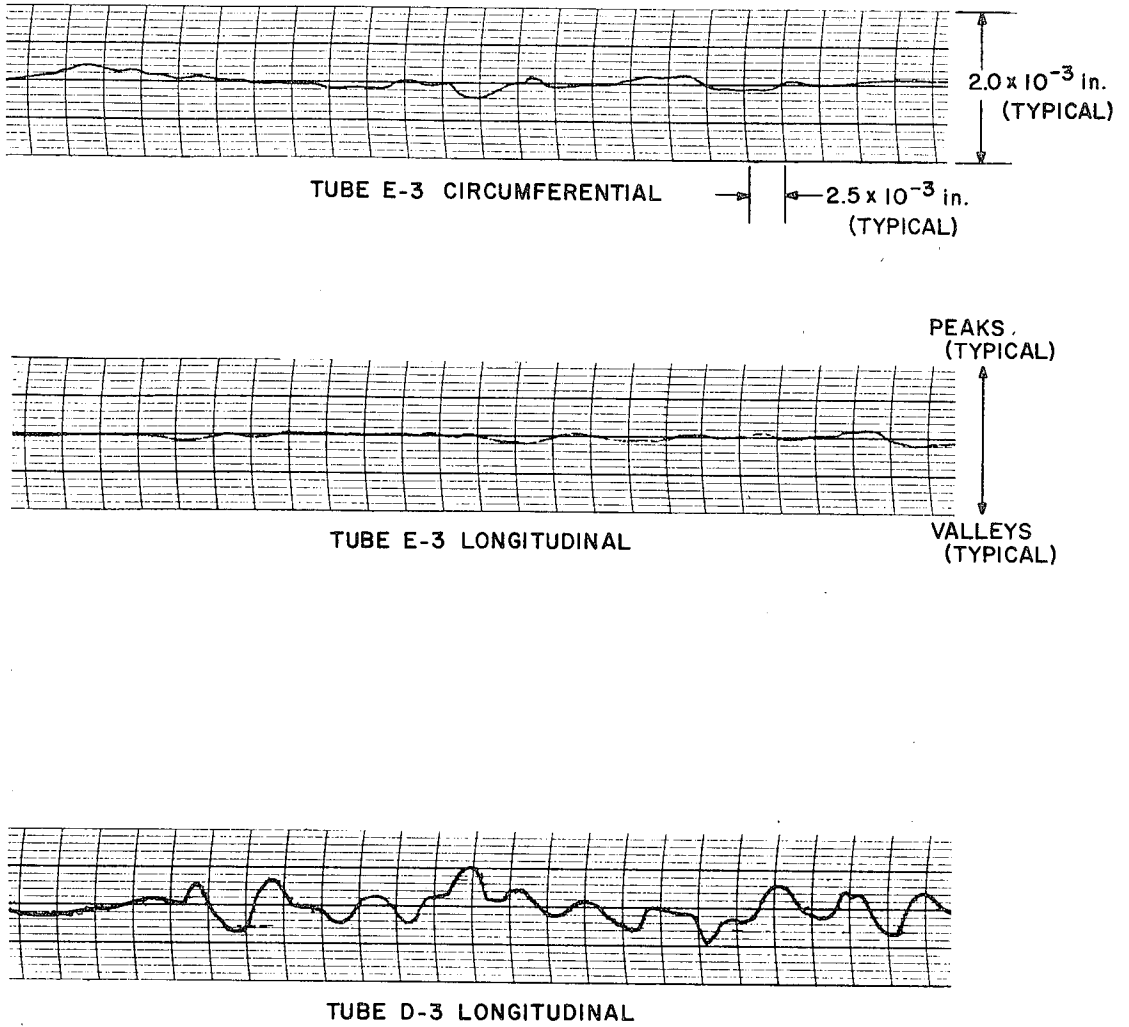
FIG. 4. SURFACE ANALYZER SAMPLE TRACES FOR TUBES E-3 AND D-3

FIG. 5   TEST SECTION
ASSEMBLY
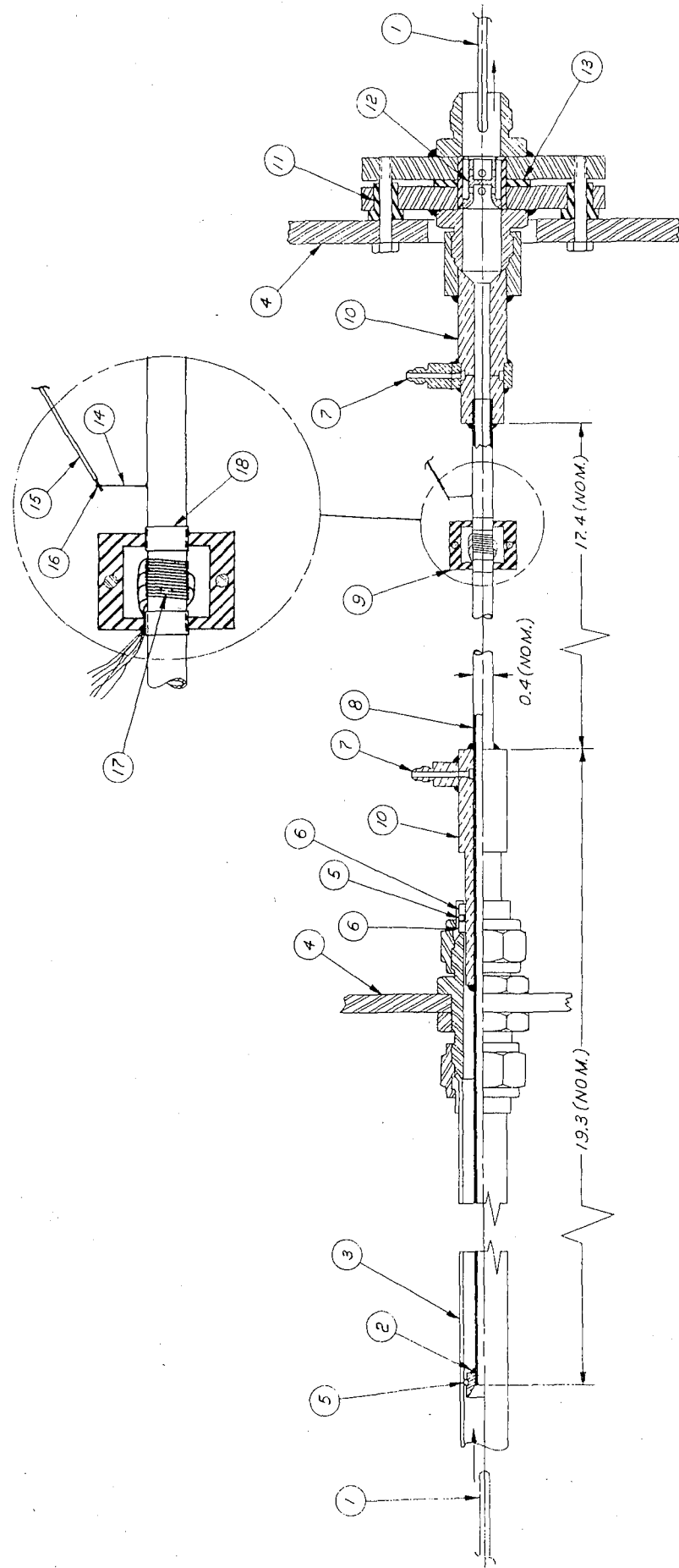
1. THERMOCOUPLE GLASS CELL
2. ALL JOINTS SILVER BRAZED.
3. STAINLESS STEEL GUIDE TUBE
4. MOUNTING PLATE
5. SILICONE O-RING
6. TEFLON SPACER
7. PRESSURE TAP
8. NICKEL TUBE TEST SECTION
9. THERMOCOUPLE SHIELD
10. COPPER ELECTRODE
11. FIBER INSULATING GROMMET

12. BRASS THERMAL EQUALIZER
13. TEFLON INSULATION
14. VOLTAGE PROBE, ½" CONSTANTAN WIRE 30 GAGE
    WELDED TO NICKEL TUBE SURFACE.
15. COPPER LEAD WIRE 22 GAGE
16. SOFT SOLDER
17. THERMOCOUPLE MADE FROM 6' LENGTH OF
    36 GAGE CHROMEL-ALUMEL WIRE WITH
    DOUBLE GLASS FILAMENT INSULATION.
    BARED WIRE ENDS DISCHARGE WELDED TO
    TUBE WALL WITH NOMINAL .020 GAP. (CONT.)

3 JUNCTION PAIRS SPACED 120°
AROUND TUBE WITH 3-4 TURNS OF
EACH INSULATED WIRE WRAPPED
TIGHTLY AGAINST TUBE
18. GLASS CLOTH TAPE
19. 2 ADDITIONAL THERMOCOUPLE
    STATIONS AND 1 ADDITIONAL VOLTAGE
    PROBE ARE NOT SHOWN.
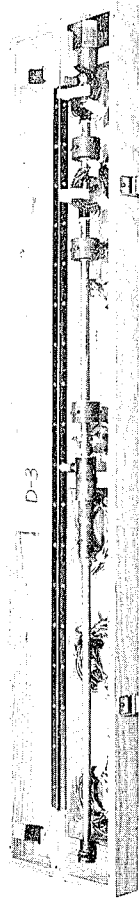
FIG. 6. VIEW OF TUBE PRIOR
TO INSTALLATION
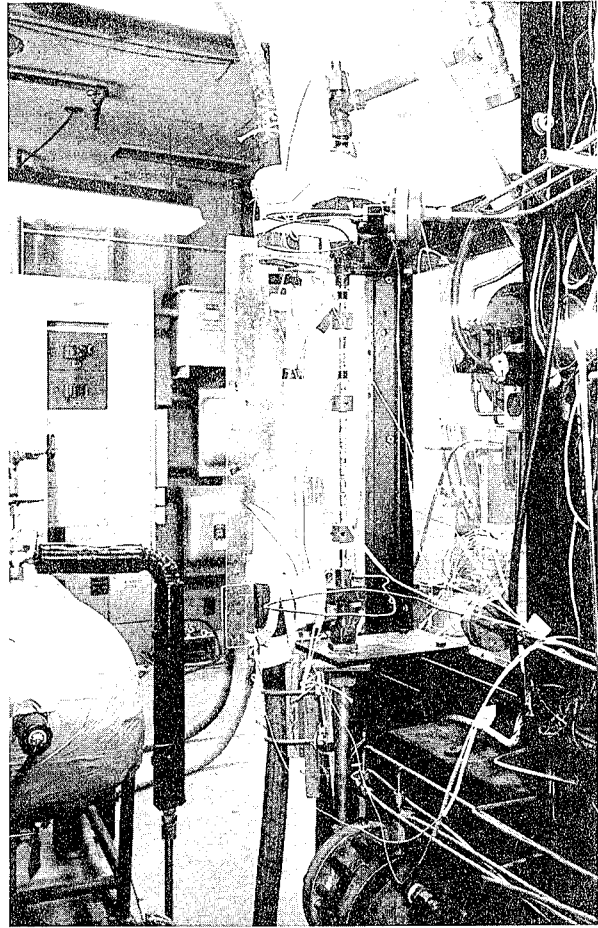
FIG. 7. VIEW BEHIND GAGE PANEL SHOWING
TUBE INSTALLED
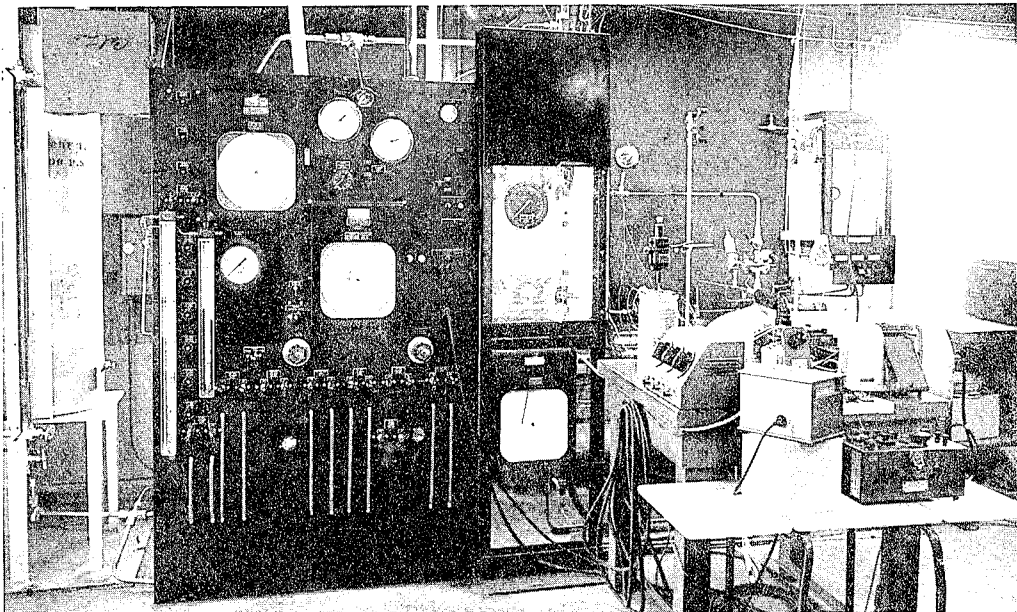
FIG. 8. GENERAL VIEW OF TEST FACILITY
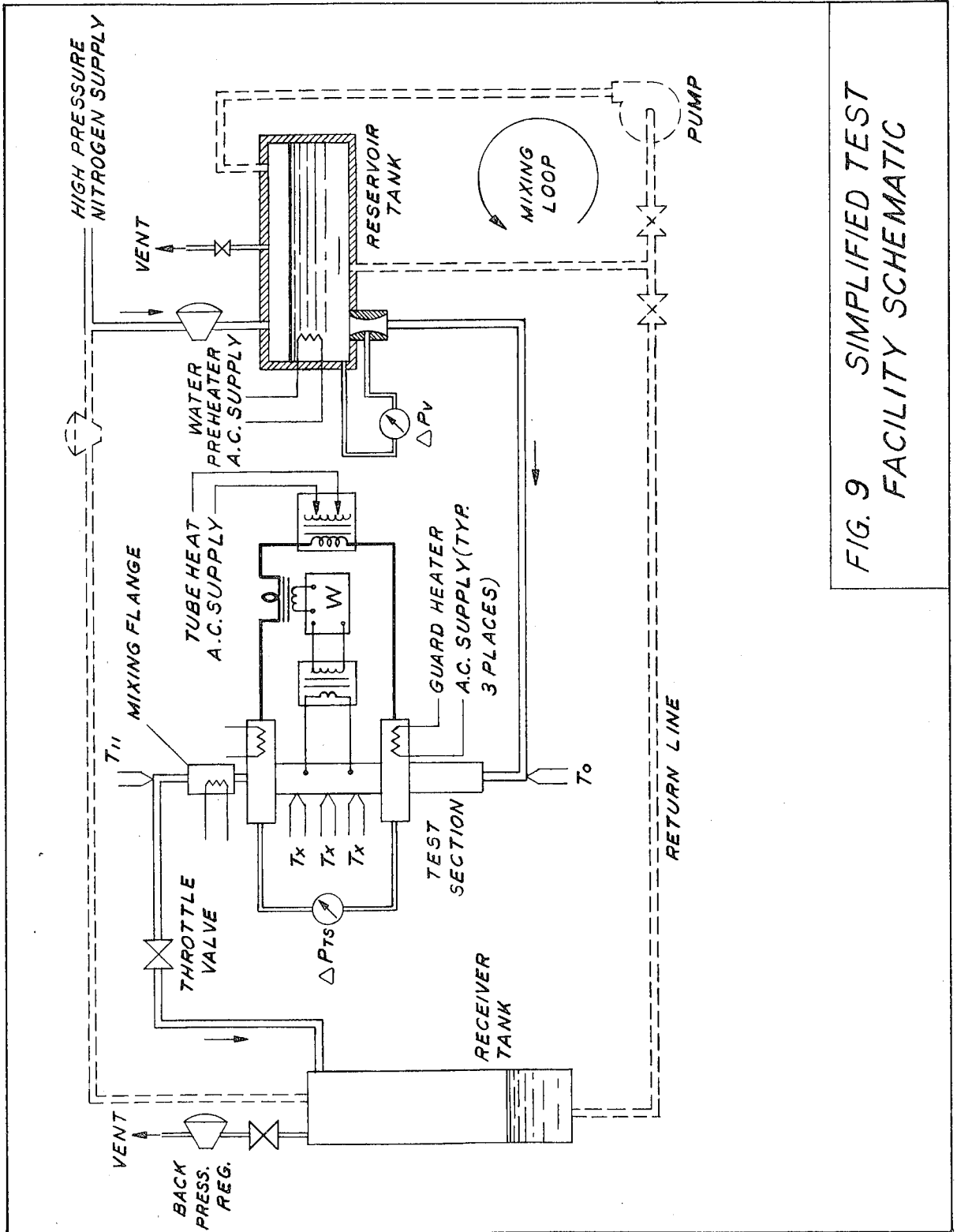
FIG. 9   SIMPLIFIED TEST FACILITY SCHEMATIC

FIG. 10   IMMERSION
THERMOCOUPLE
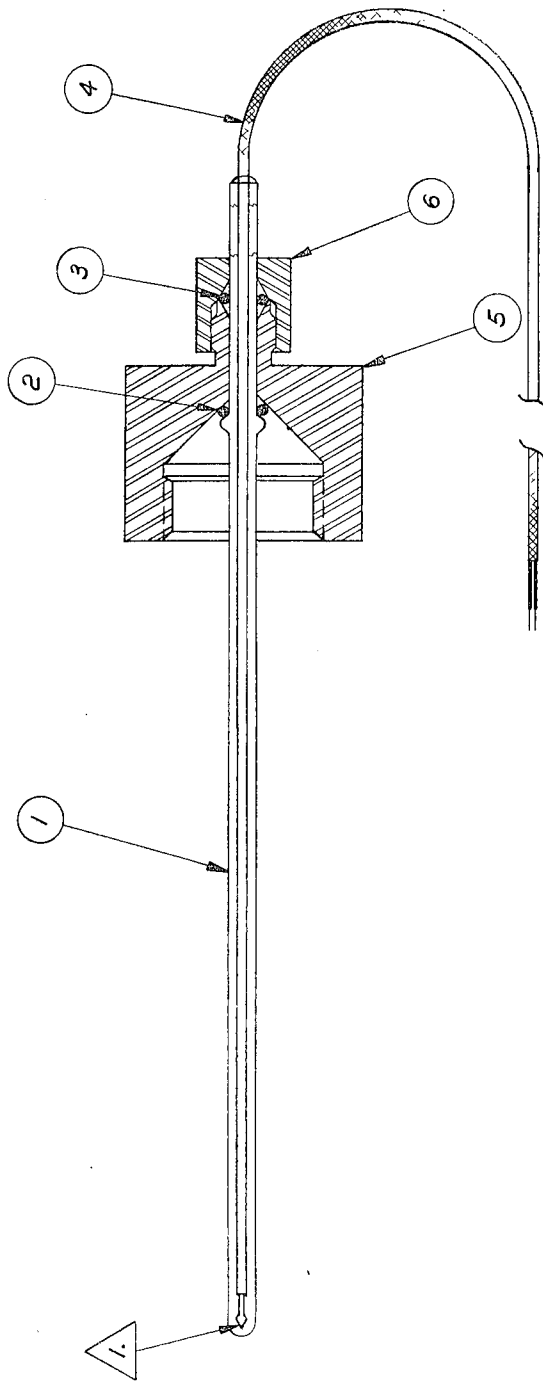
1. ⅛" PYREX TUBE APPROX. 6 INCHES LONG
2. TEFLON O-RING
3. NEOPRENE O-RING
4. 30 GAGE CHROMEL-ALUMEL DOUBLE WOUND GLASS INSULATION
5. MODIFIED AN 894 EXPANDER
6. MODIFIED AN 817 NUT

△ 1. THERMOCOUPLE JUNCTION WELDED THEN
     FUSED IN GLASS.
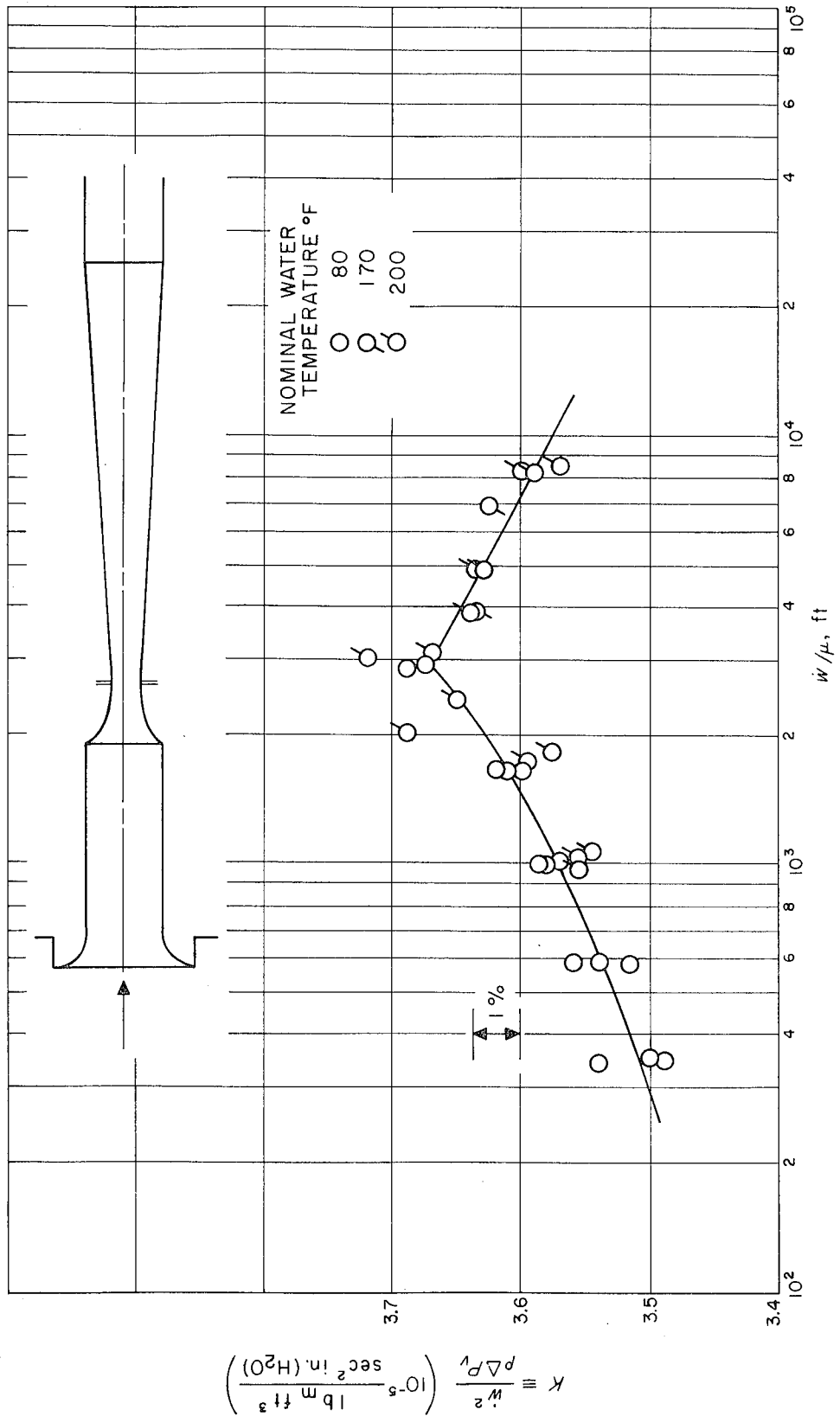
FIG. II. METERING VENTURI CALIBRATION

NOMINAL WATER
TEMPERATURE °F

○ 80
◐ 170
◑ 200

$\dot{w}/\mu$, ft

1%

$$K \equiv \frac{\dot{w}^2}{\rho \Delta P_v} \left(10^{-5} \frac{lb_m \ ft^3}{sec^2 \ in.(H_2O)} \right)$$
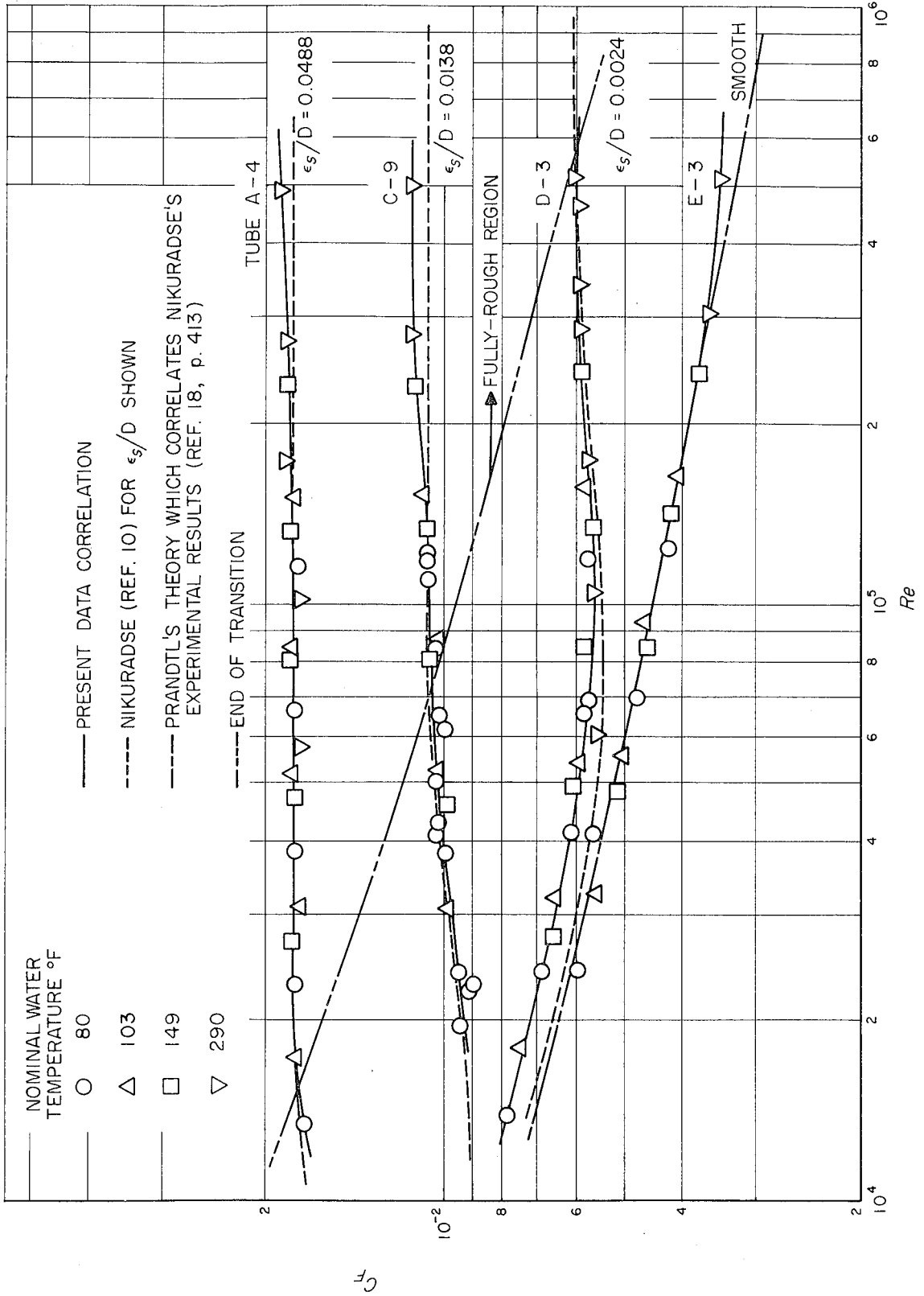
FIG. 12. FRICTION COEFFICIENT vs REYNOLDS NUMBER FOR TUBES E-3, D-3, C-9 AND A-4
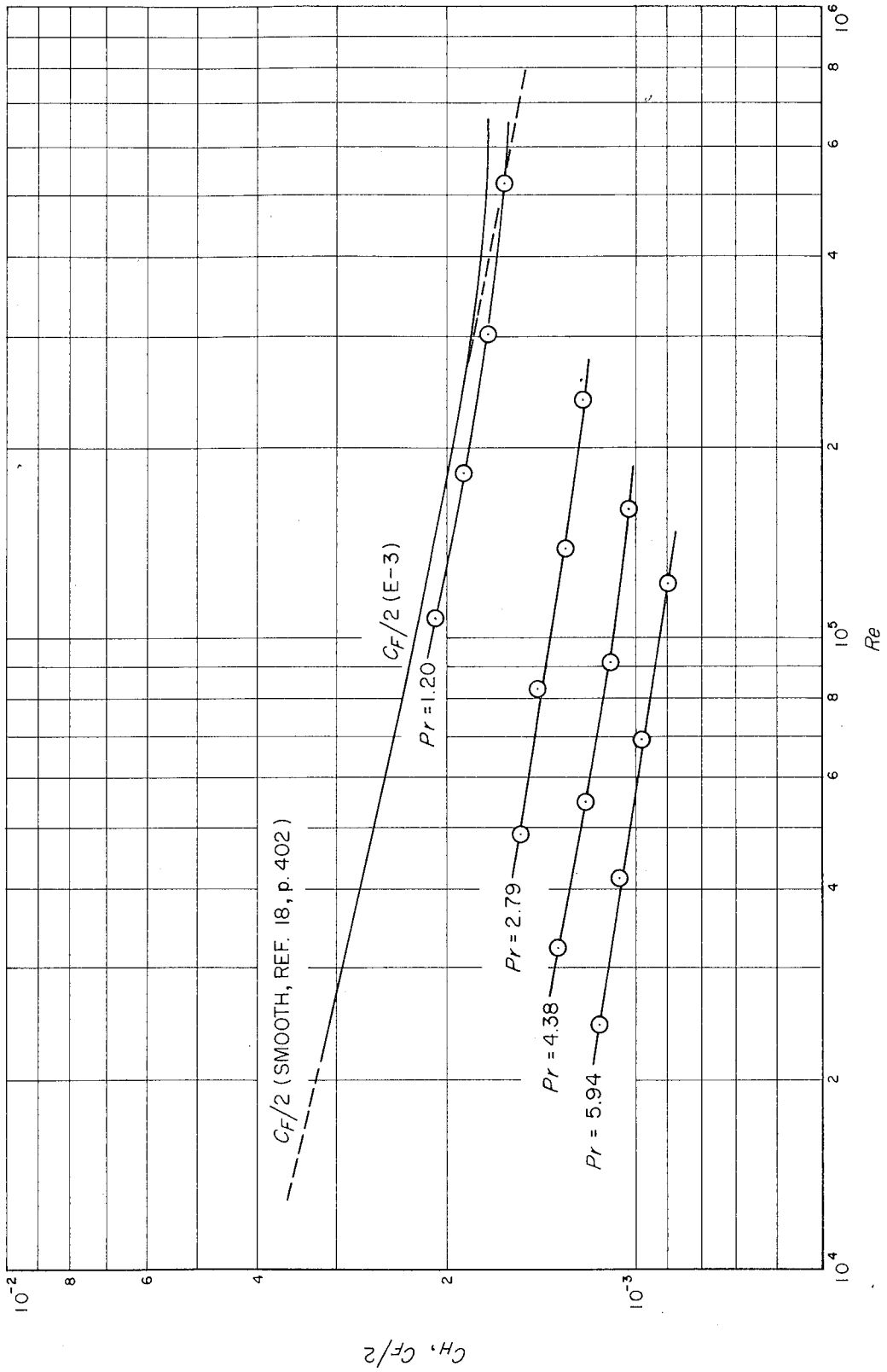
FIG. I3. HEAT-TRANSFER COEFFICIENT vs REYNOLDS NUMBER FOR TUBE E-3 (SMOOTH) AT PRANDTL
NUMBERS OF I.20, 2.79, 4.38 AND 5.94
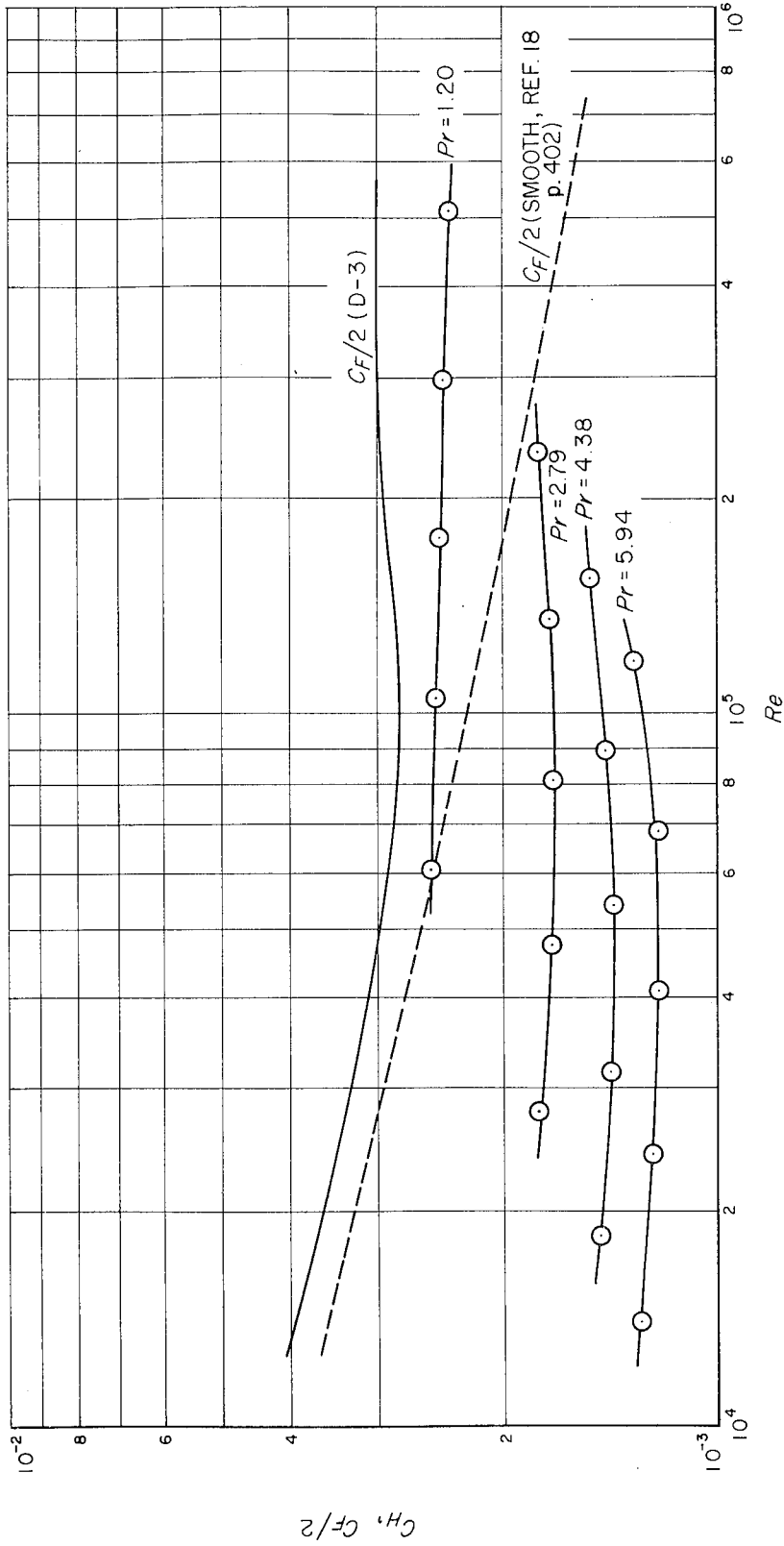
FIG. 14. HEAT-TRANSFER COEFFICIENT vs REYNOLDS NUMBER FOR TUBE D-3 ($\epsilon_S/D = 0.0024$)

AT PRANDTL NUMBERS 1.20, 2.79, 4.38 AND 5.94
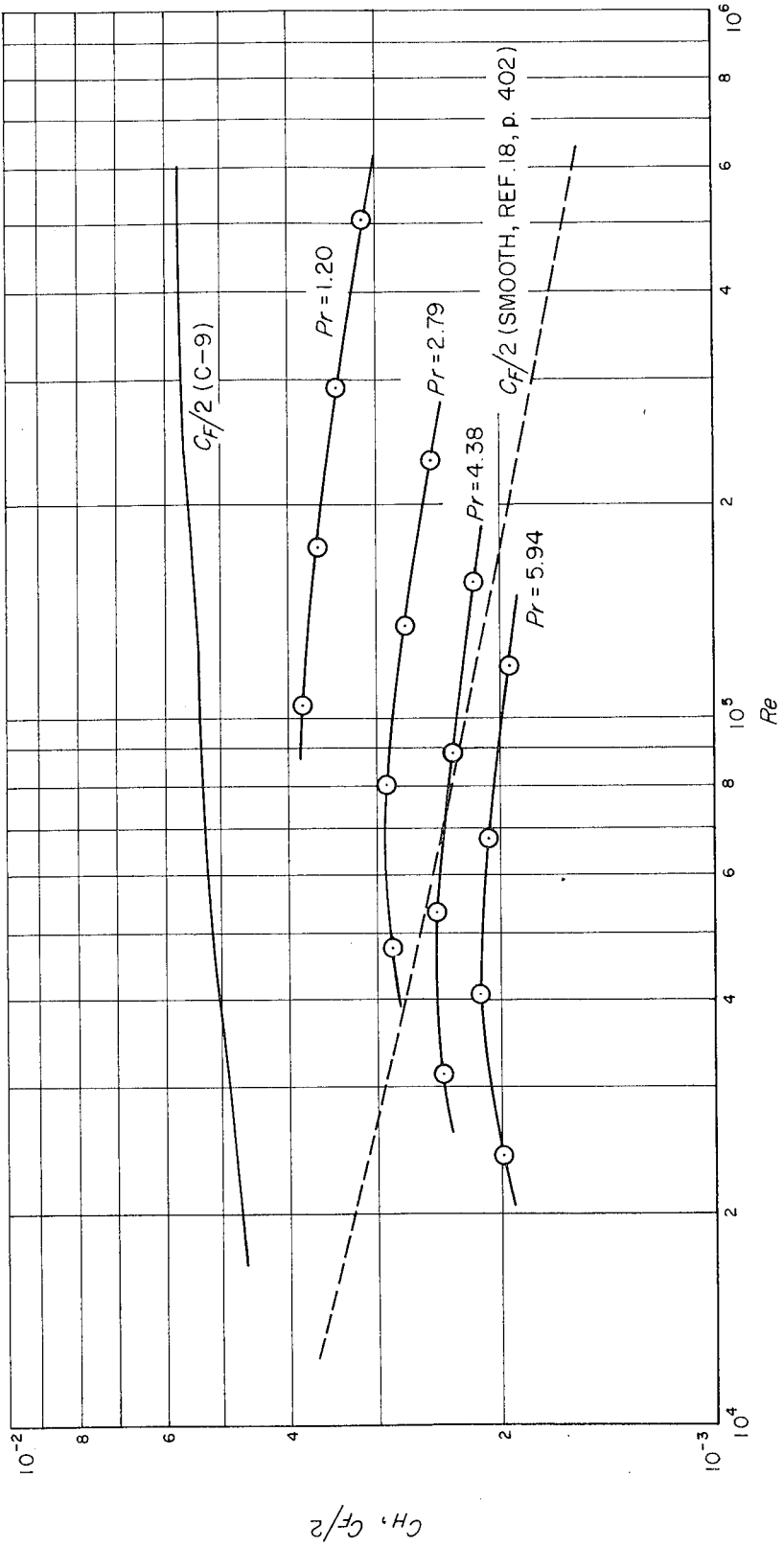
FIG. 15. HEAT-TRANSFER COEFFICIENT vs REYNOLDS NUMBER FOR TUBE C-9 ($\epsilon_s/D = 0.0138$) AT PRANDTL NUMBERS 1.20, 2.79, 4.38 AND 5.94
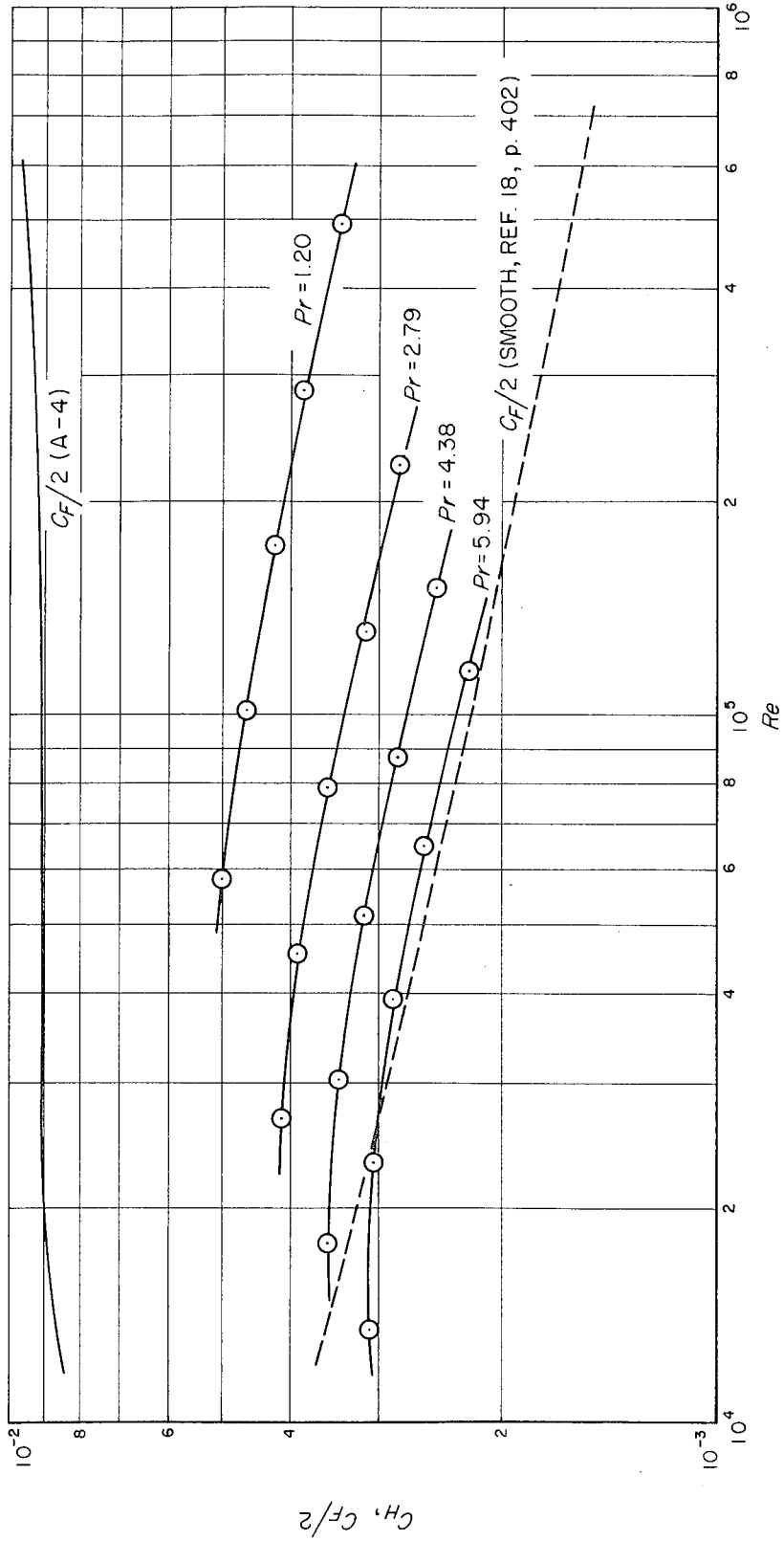
FIG. 16. HEAT-TRANSFER COEFFICIENT vs REYNOLDS NUMBER FOR TUBE A-4 ($\epsilon_S/D = 0.0488$)

AT PRANDTL NUMBERS 1.20, 2.79, 4.38 AND 5.94
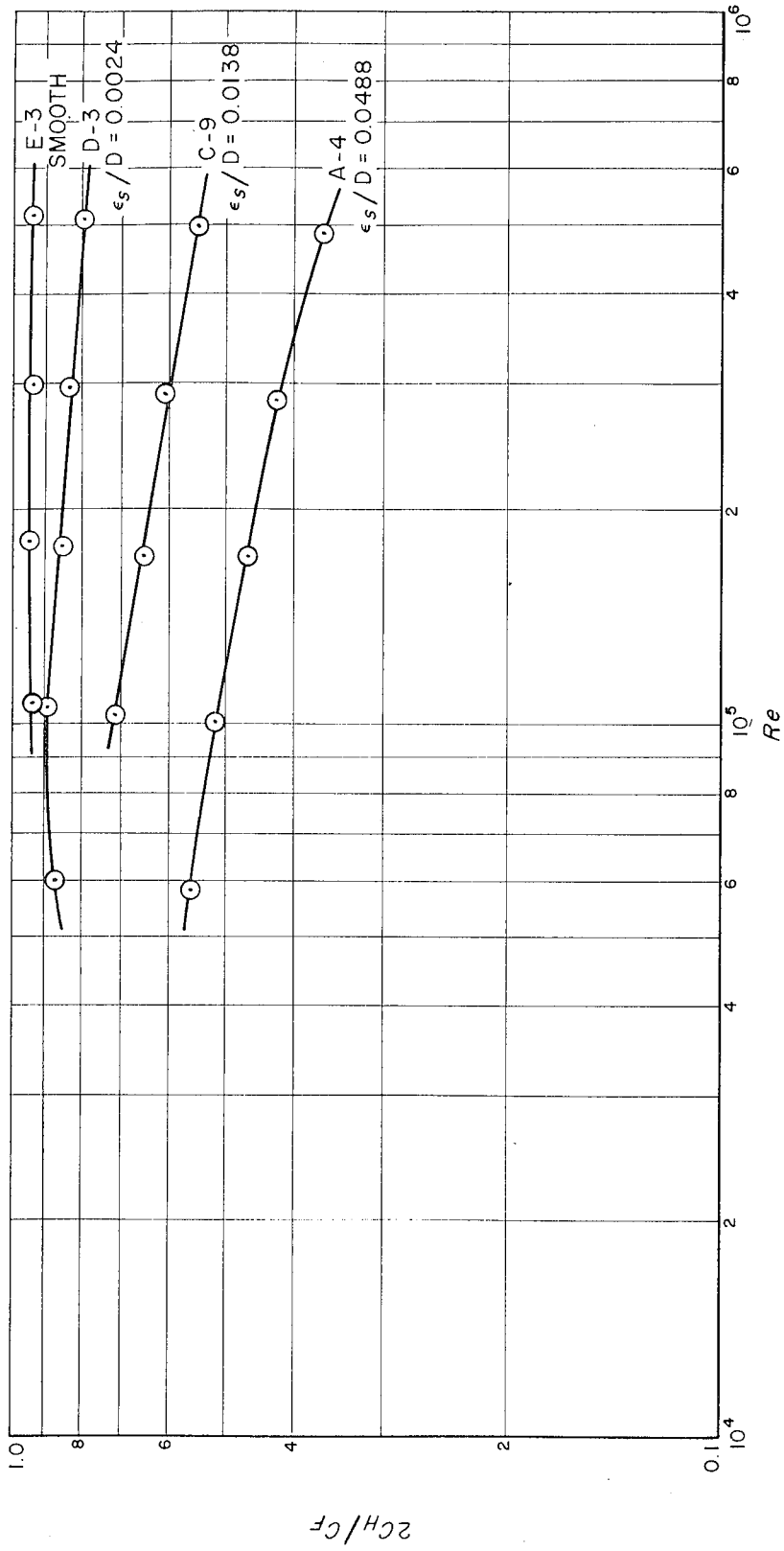
FIG. 17. COMPARISONS OF HEAT-TRANSFER AND FRICTION COEFFICIENTS vs REYNOLDS NUMBER FOR $Pr = 1.20$
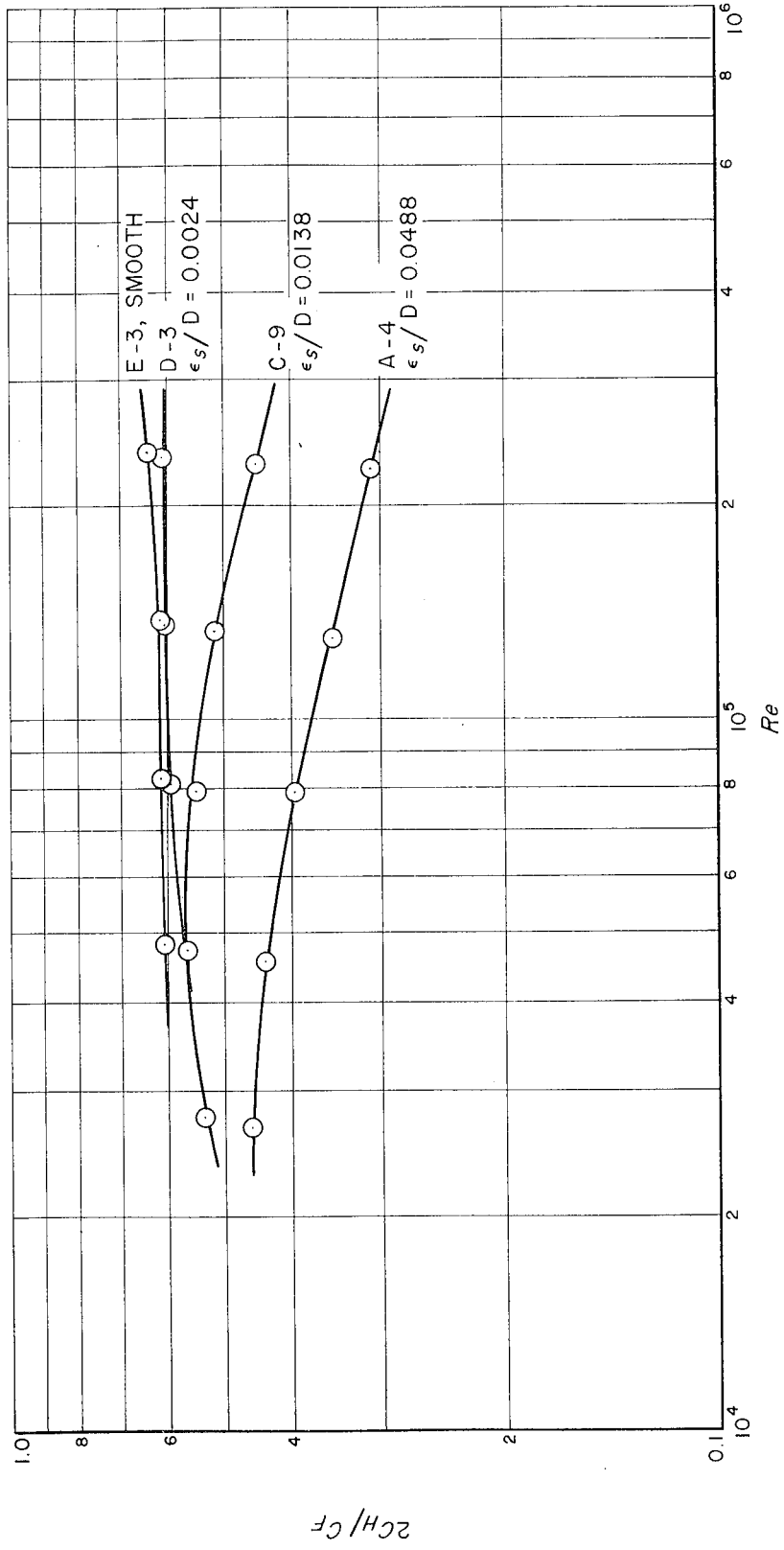
FIG. 18. COMPARISONS OF HEAT-TRANSFER AND FRICTION COEFFICIENTS vs REYNOLDS NUMBER FOR $Pr = 2.79$

D-3
$\epsilon_s/D = 0.0024$

E-3
SMOOTH

C-9
$\epsilon_s/D = 0.0138$

A-4
$\epsilon_s/D = 0.0488$

$2C_H/C_F$

Re
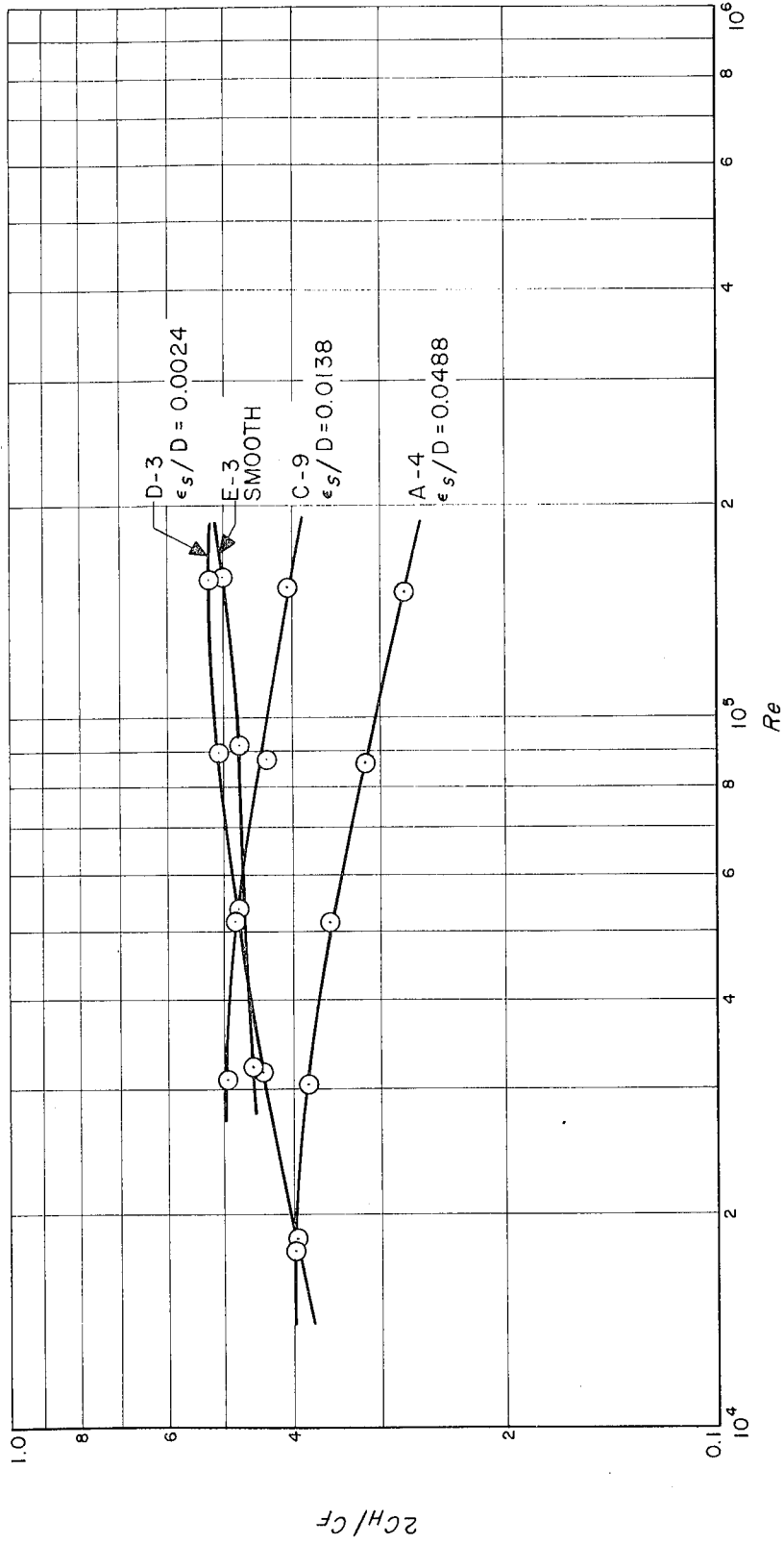
FIG. 19. COMPARISONS OF HEAT-TRANSFER AND FRICTION COEFFICIENTS vs REYNOLDS NUMBER FOR $Pr = 4.38$
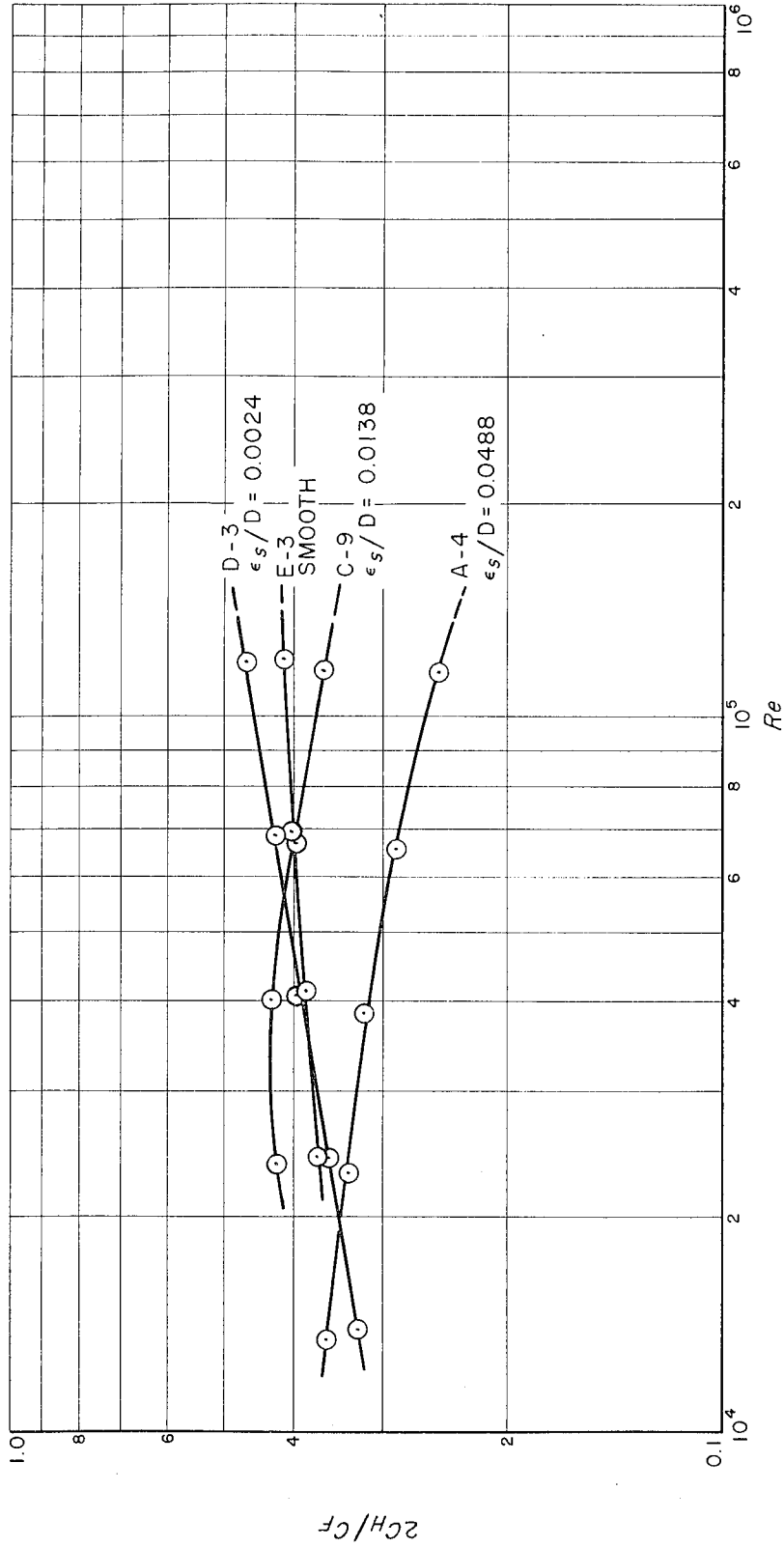
FIG. 20. COMPARISONS OF HEAT-TRANSFER AND FRICTION COEFFICIENTS vs REYNOLDS NUMBER FOR $Pr = 5.94$
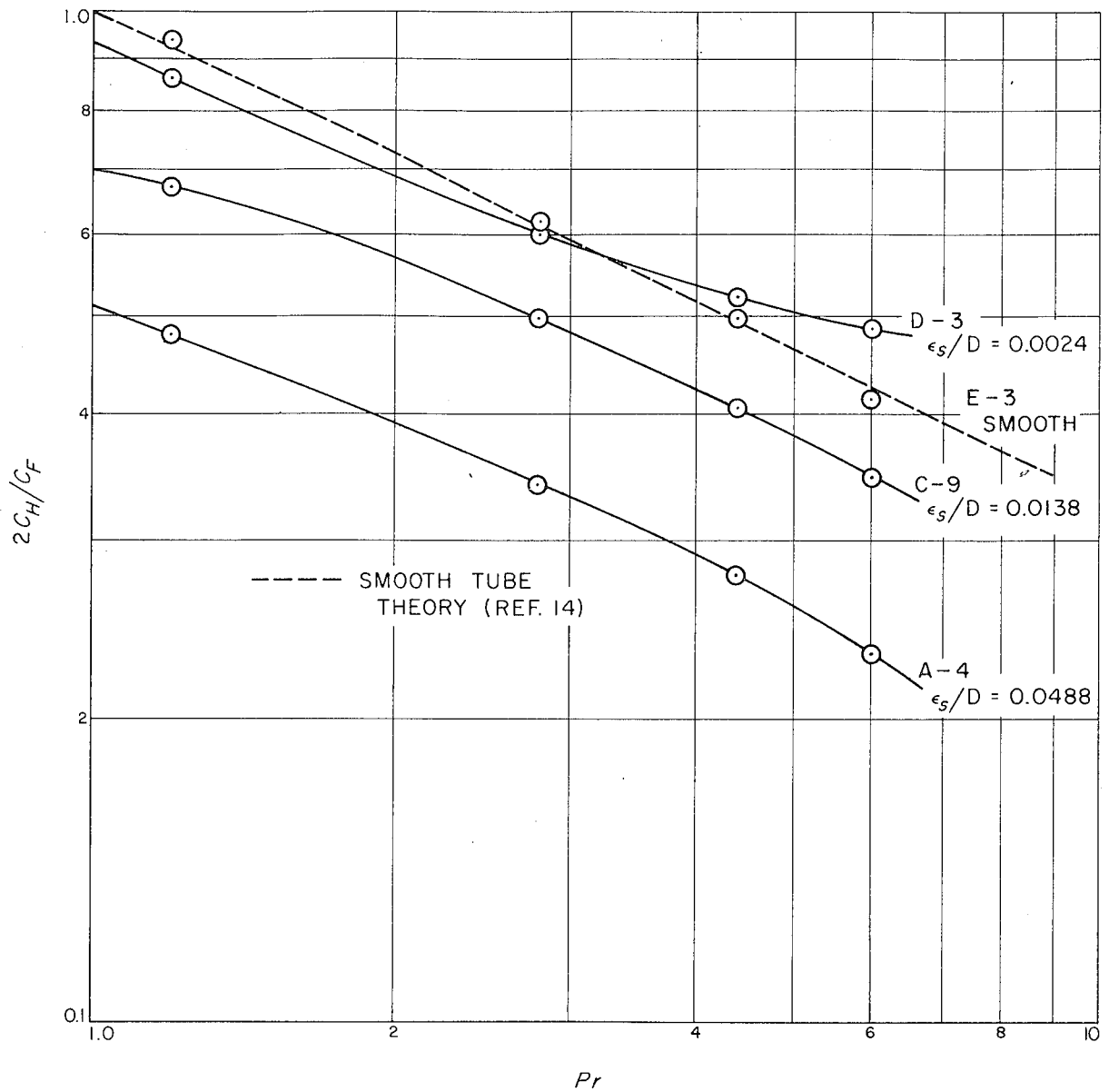
FIG. 2I. COMPARISONS OF HEAT-TRANSFER AND FRICTION COEFFICIENTS
vs PRANDTL NUMBER FOR REYNOLDS NUMBER OF 1.5×10^5
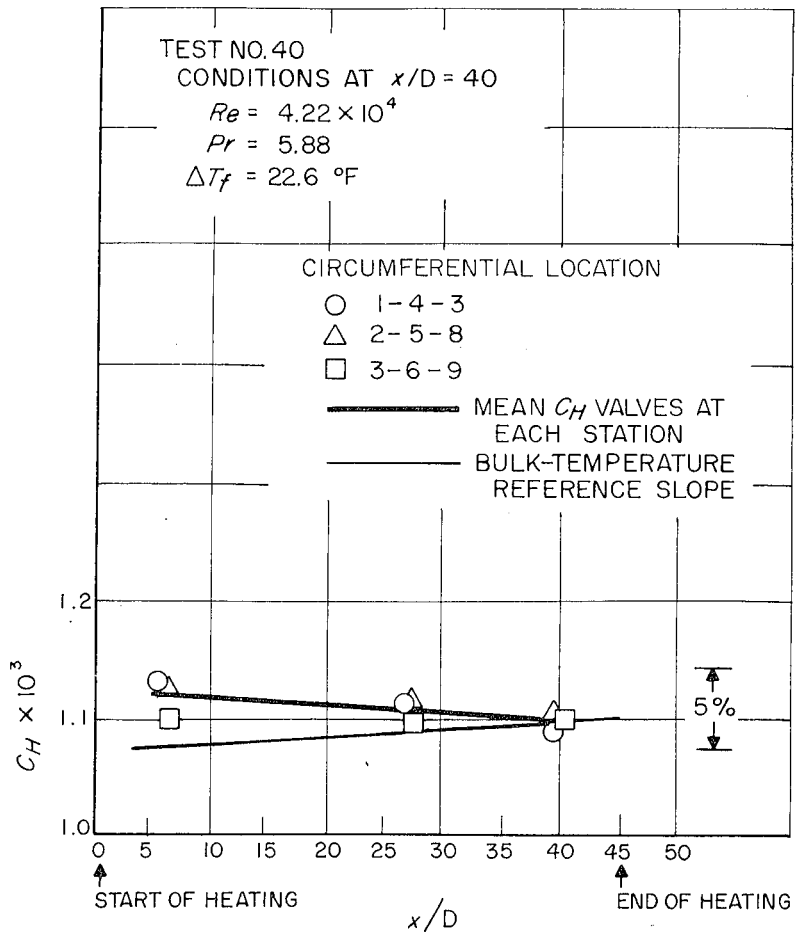
FIG. 22. HEAT−TRANSFER COEFFICIENT vs
LONGITUDINAL STATION FOR A
SELECTED TEST ON TUBE E-3
(SMOOTH)
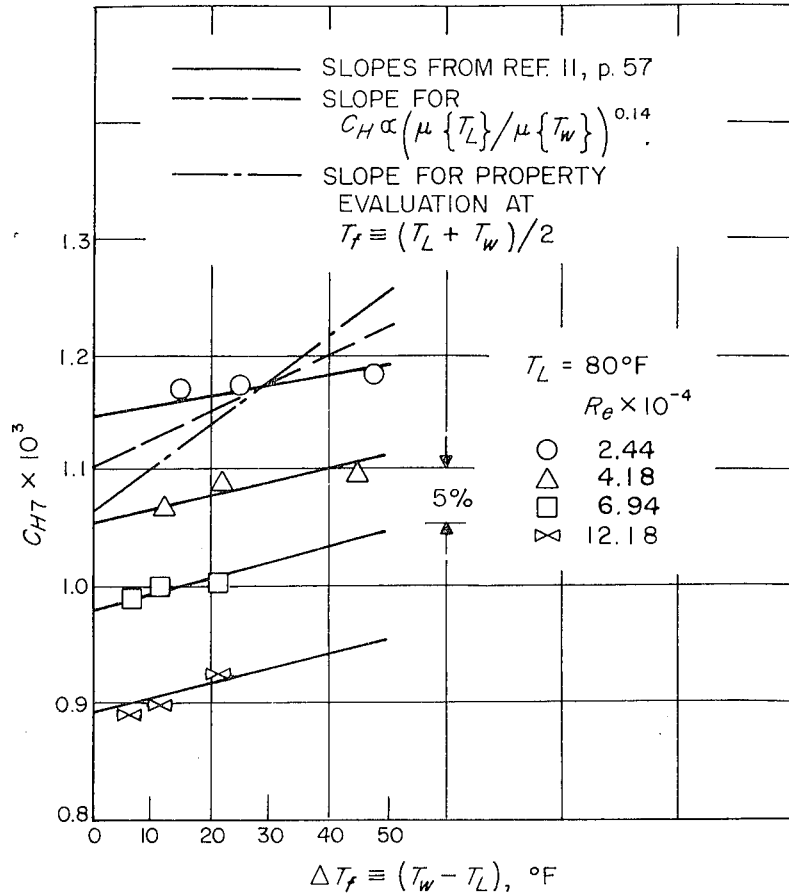
FIG. 23. VARIATION OF HEAT-TRANSFER
COEFFICIENT WITH WALL-TO-FLUID
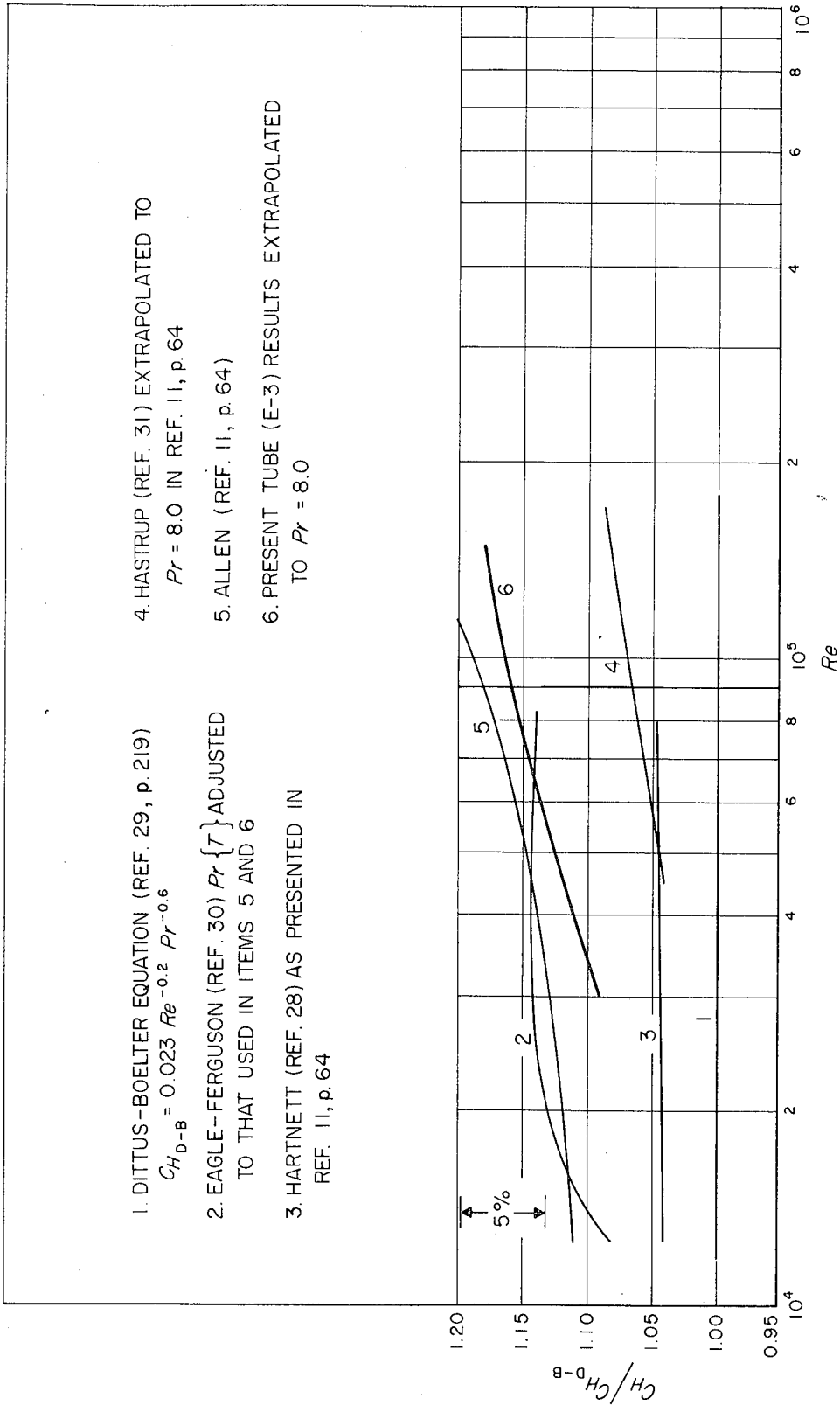TEMPERATURE DIFFERENCE FOR
TUBE E-3 (SMOOTH)
P_r = 5.94

FIG. 24. COMPARISONS—EXPERIMENTAL HEAT-TRANSFER RESULTS FOR SMOOTH TUBES AT $Pr = 8.0$
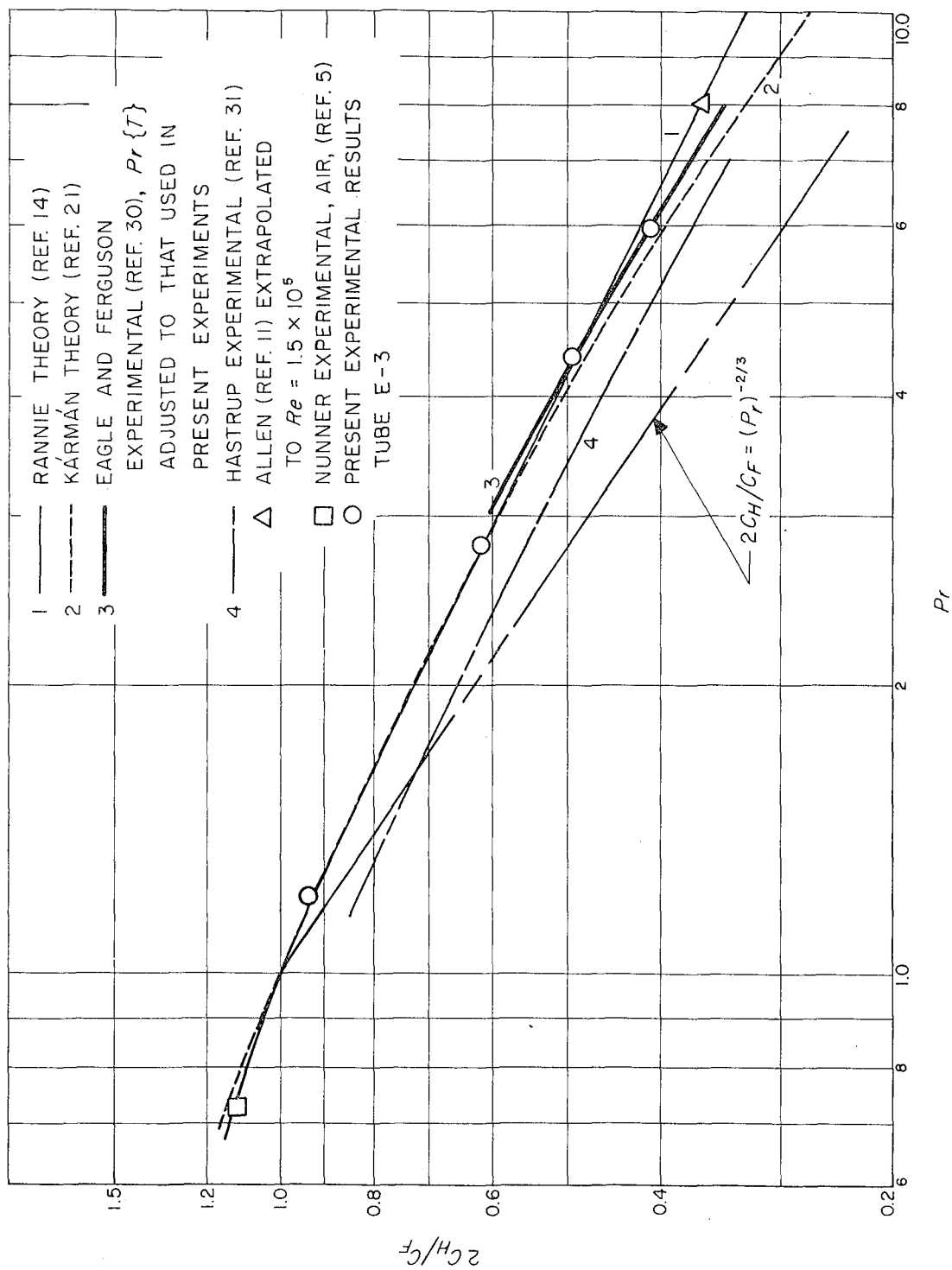
1. DITTUS–BOELTER EQUATION (REF. 29, p. 219)
   $C_{H_{D-B}} = 0.023 \, Re^{-0.2} \, Pr^{-0.6}$

2. EAGLE–FERGUSON (REF. 30) $Pr\{T\}$ ADJUSTED TO THAT USED IN ITEMS 5 AND 6

3. HARTNETT (REF. 28) AS PRESENTED IN REF. 11, p. 64

4. HASTRUP (REF. 31) EXTRAPOLATED TO $Pr = 8.0$ IN REF. 11, p. 64

5. ALLEN (REF. 11, p. 64)

6. PRESENT TUBE (E-3) RESULTS EXTRAPOLATED TO $Pr = 8.0$

FIG. 25. COMPARISONS—PRANDTL NUMBER INFLUENCE ON HEAT–TRANSFER COEFFICIENTS IN SMOOTH TUBES AT $Re = 1.5 \times 10^5$
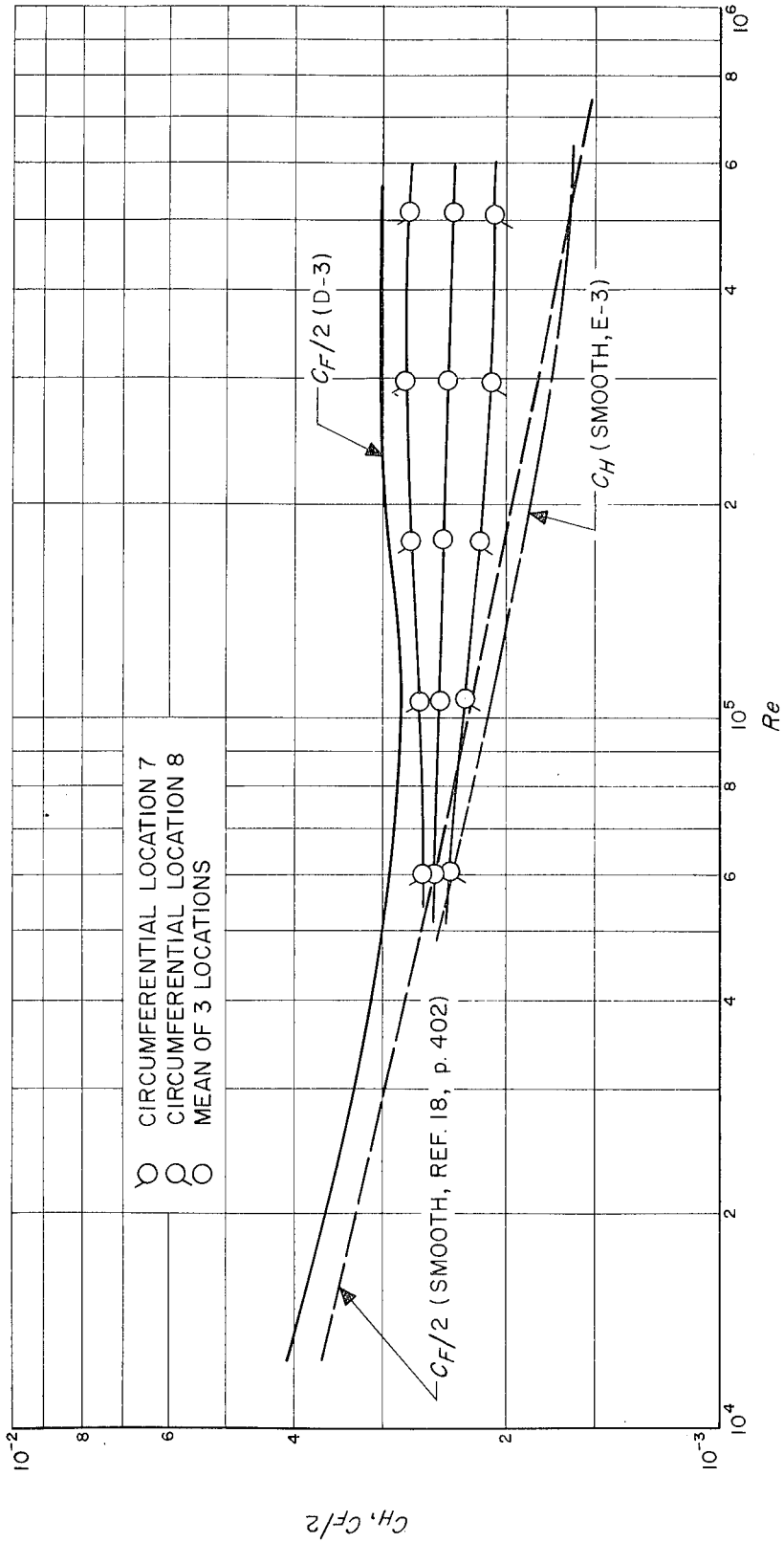
FIG. 26. TUBE D-3 CIRCUMFERENTIAL DISTRIBUTION OF HEAT-TRANSFER COEFFICIENTS AT $Pr = 1.20$
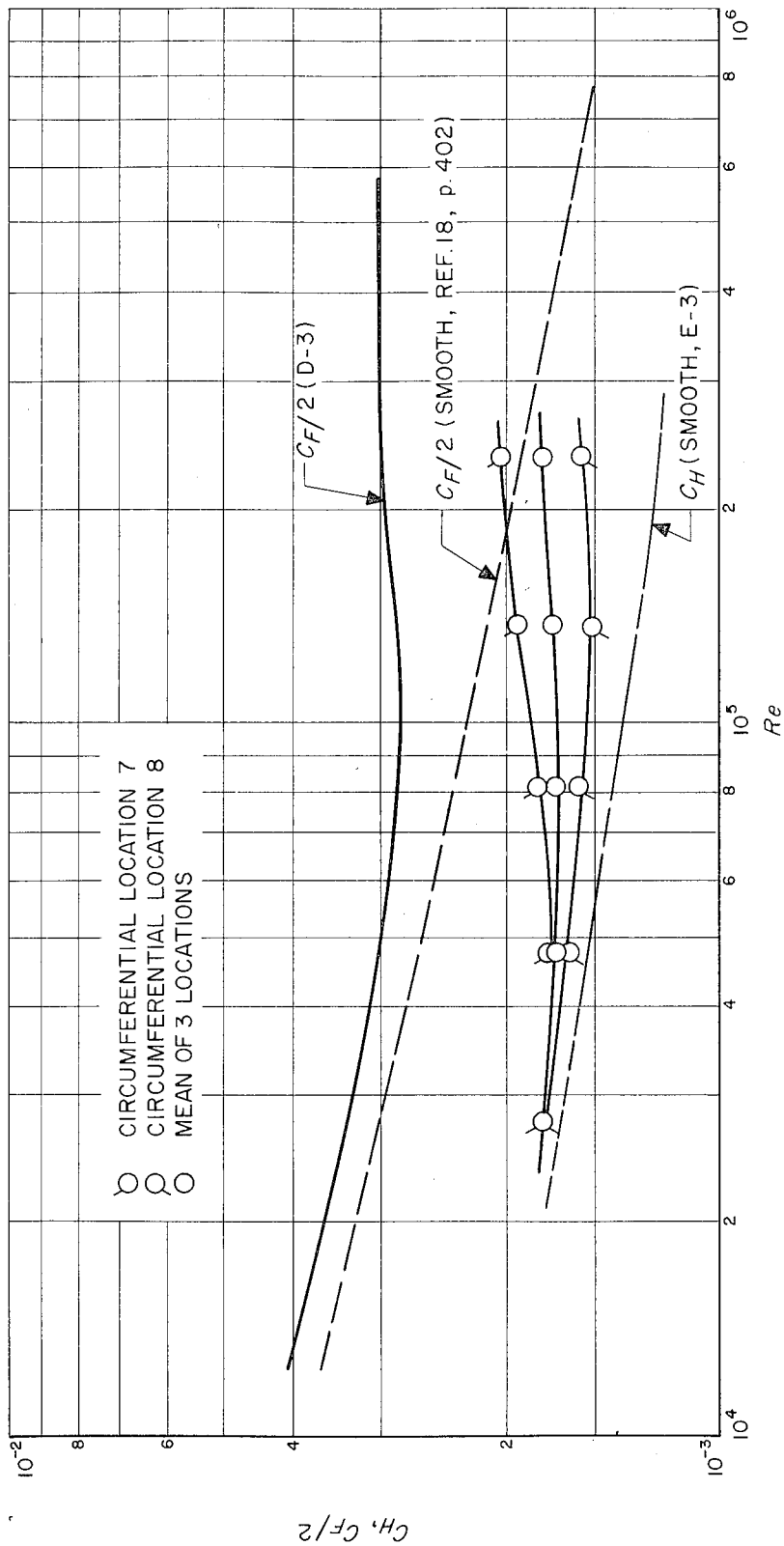
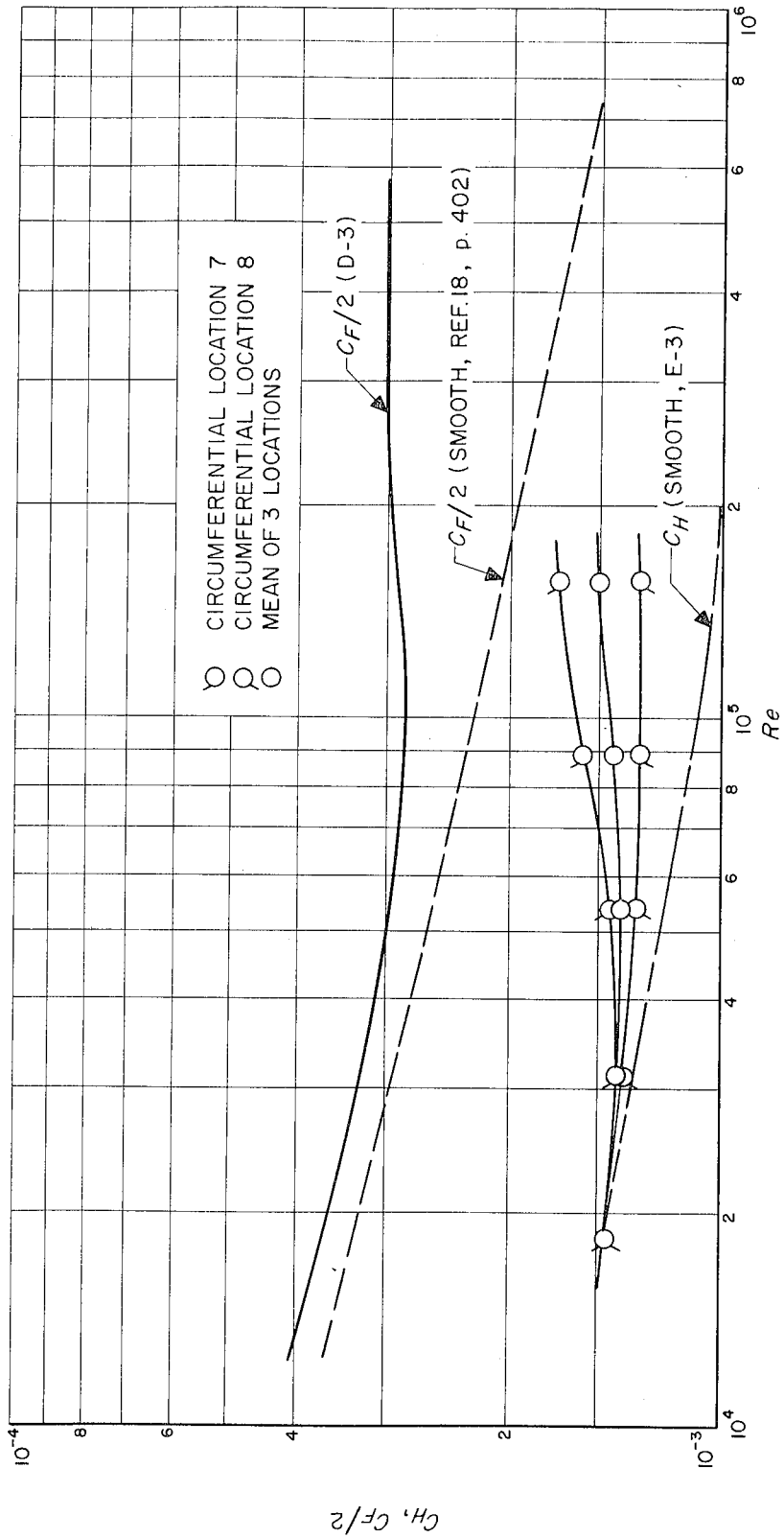FIG. 27. TUBE D-3 CIRCUMFERENTIAL DISTRIBUTION OF HEAT-TRANSFER COEFFICIENTS AT $Pr = 2.79$

FIG. 28. TUBE D-3 CIRCUMFERENTIAL DISTRIBUTION OF HEAT-TRANSFER COEFFICIENTS AT $Pr = 4.38$
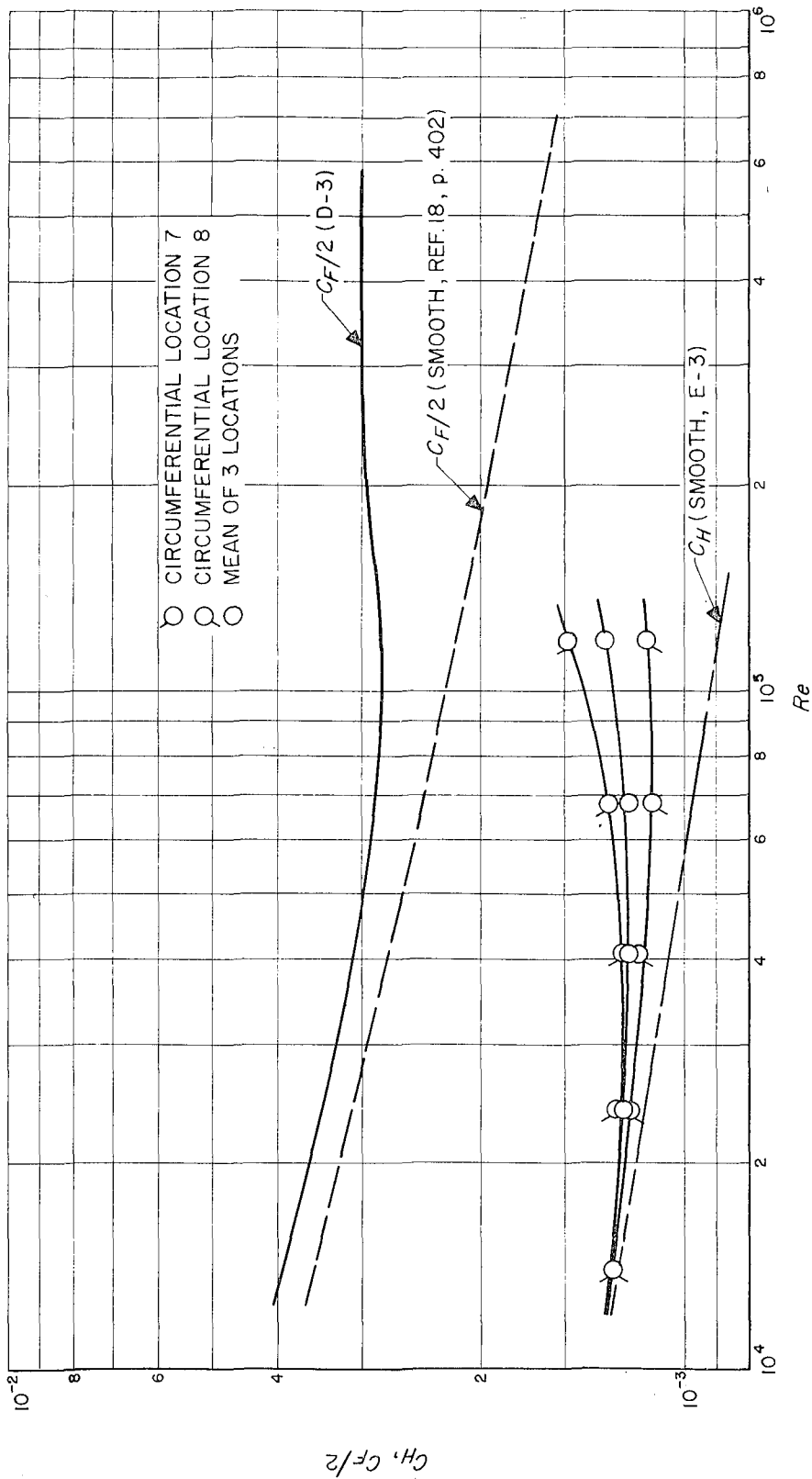
FIG. 29. TUBE D-3 CIRCUMFERENTIAL DISTRIBUTION OF HEAT-TRANSFER COEFFICIENTS AT $Pr = 5.94$
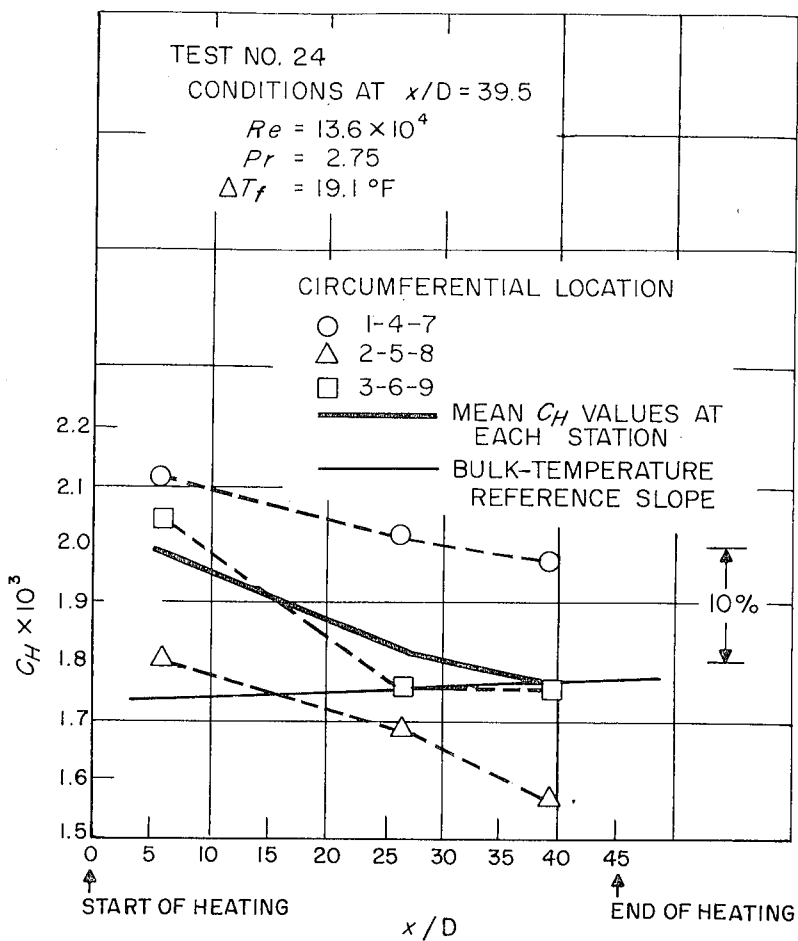
FIG. 30. HEAT-TRANSFER COEFFICIENT vs
LONGITUDINAL STATION FOR A
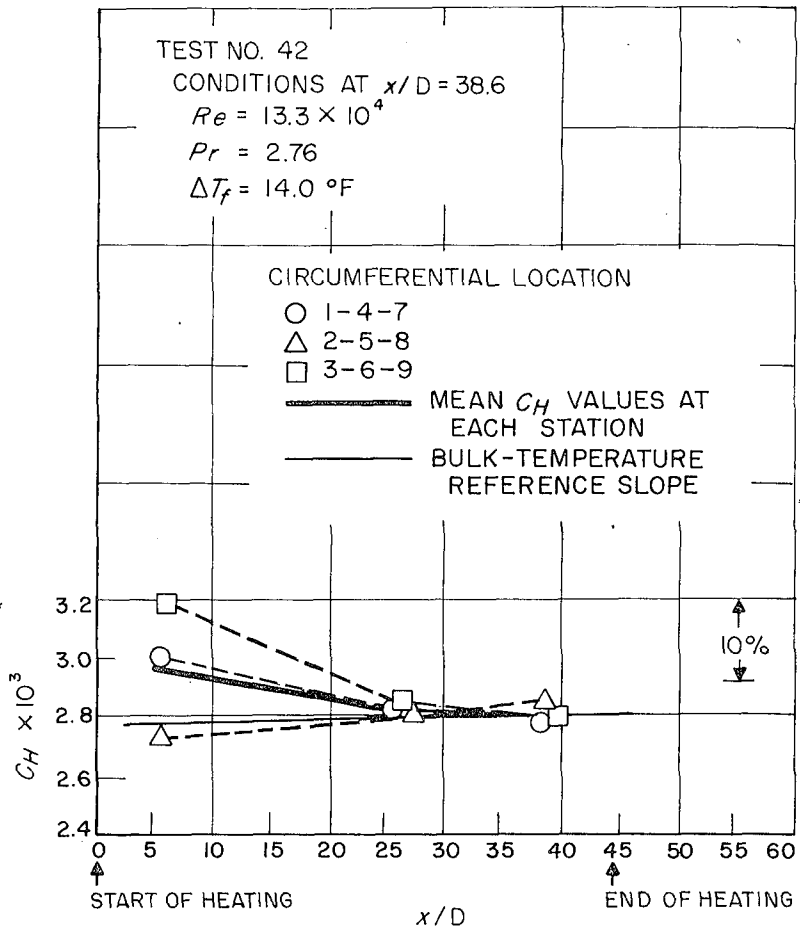SELECTED TEST ON TUBE D-3

FIG. 3I. HEAT-TRANSFER COEFFICIENT vs
LONGITUDINAL STATION FOR A
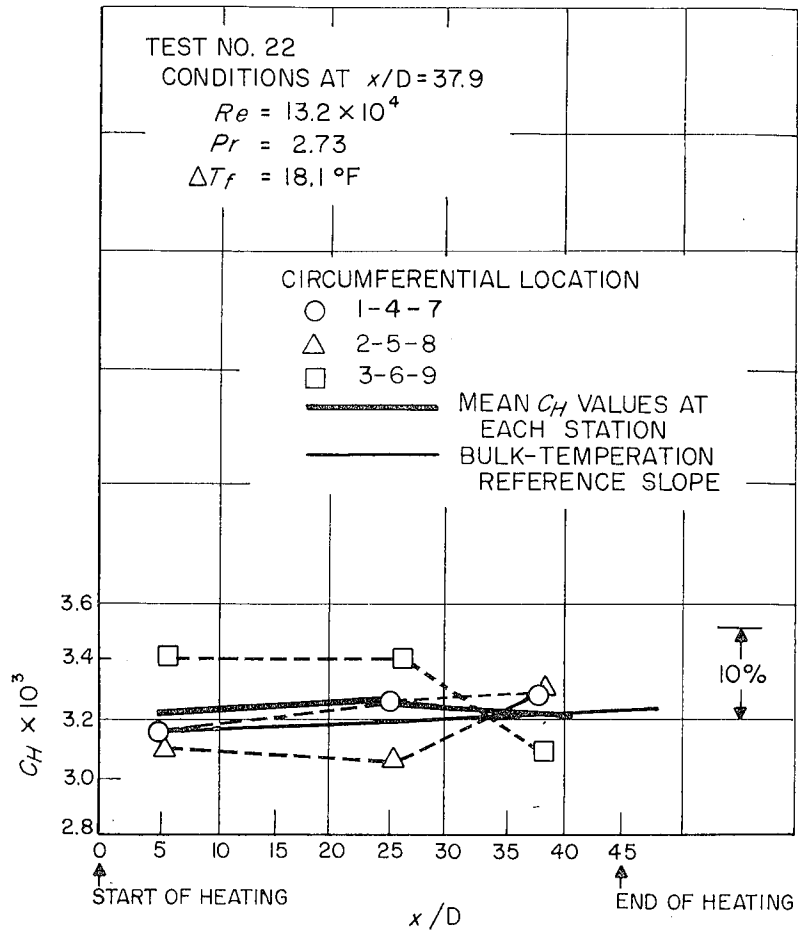SELECTED TEST ON TUBE C-9

FIG. 32. HEAT-TRANSFER COEFFICIENT vs
LONGITUDINAL STATION FOR A
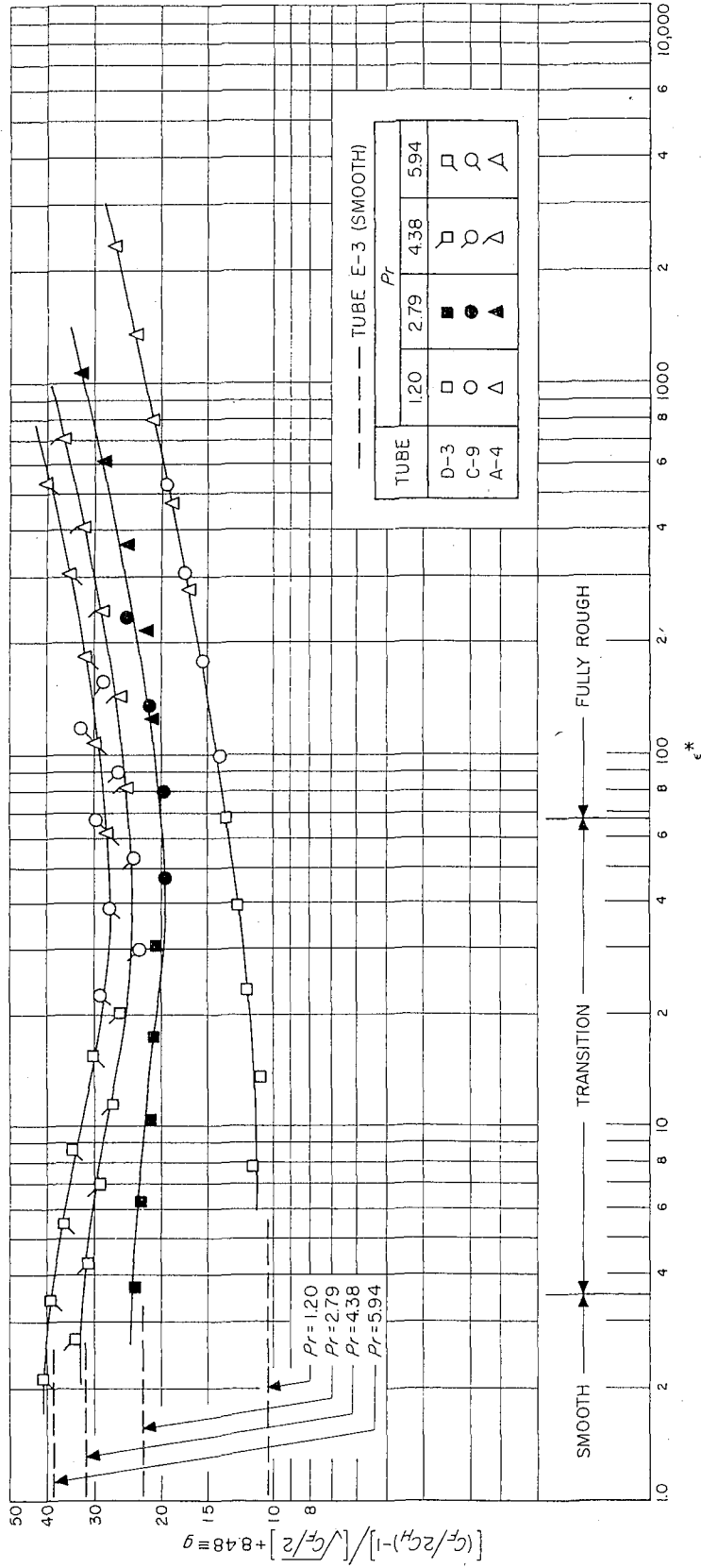SELECTED TEST ON TUBE A-4

FIG. 33. CORRELATION OF EXPERIMENTAL RESULTS, USING THE HEAT-TRANSFER SIMILARITY LAW
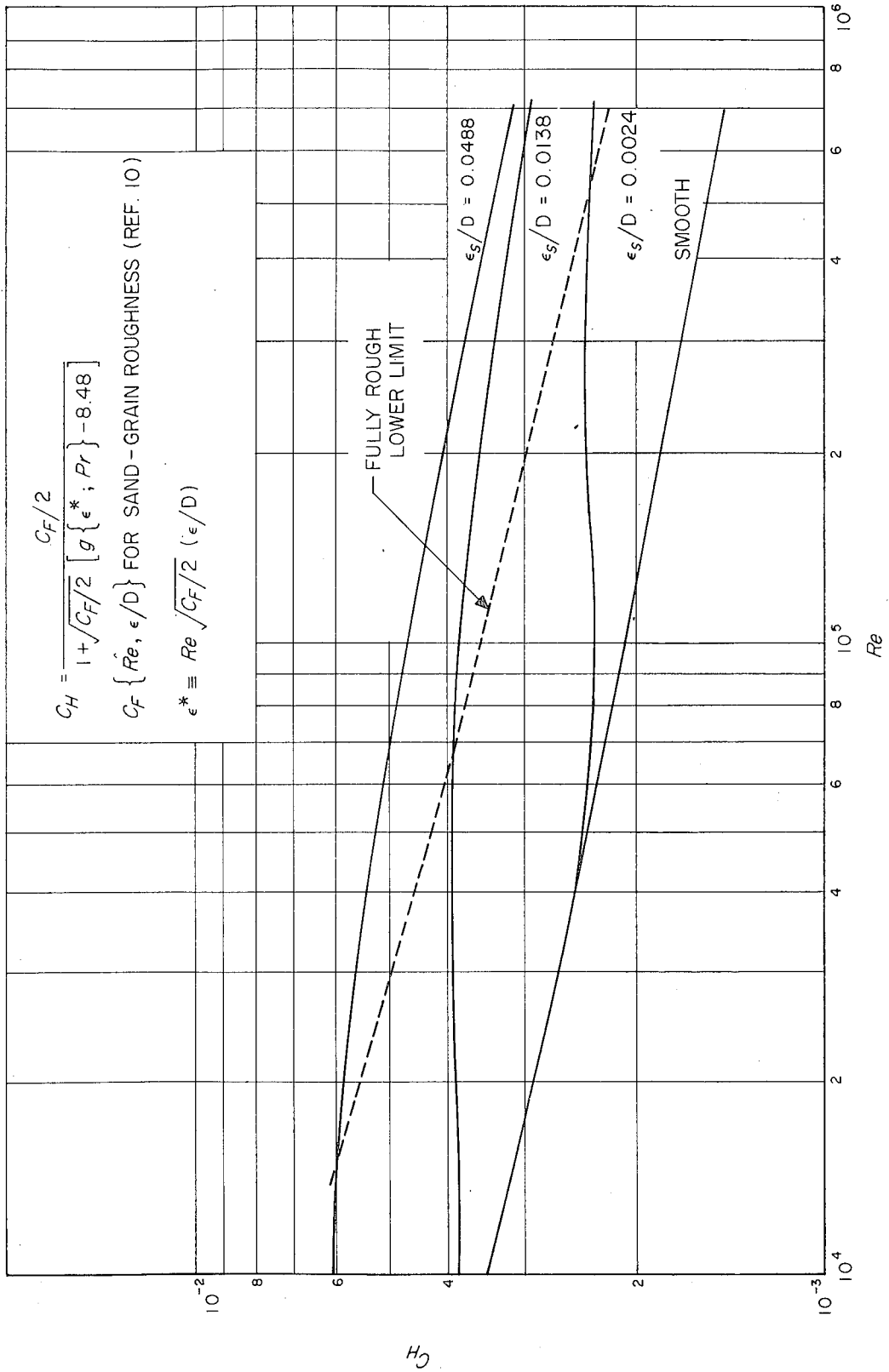
FIG. 34. EXTENSIONS OF EXPERIMENTAL RESULTS USING THE HEAT TRANSFER SIMILARITY LAW, $Pr = 1.20$
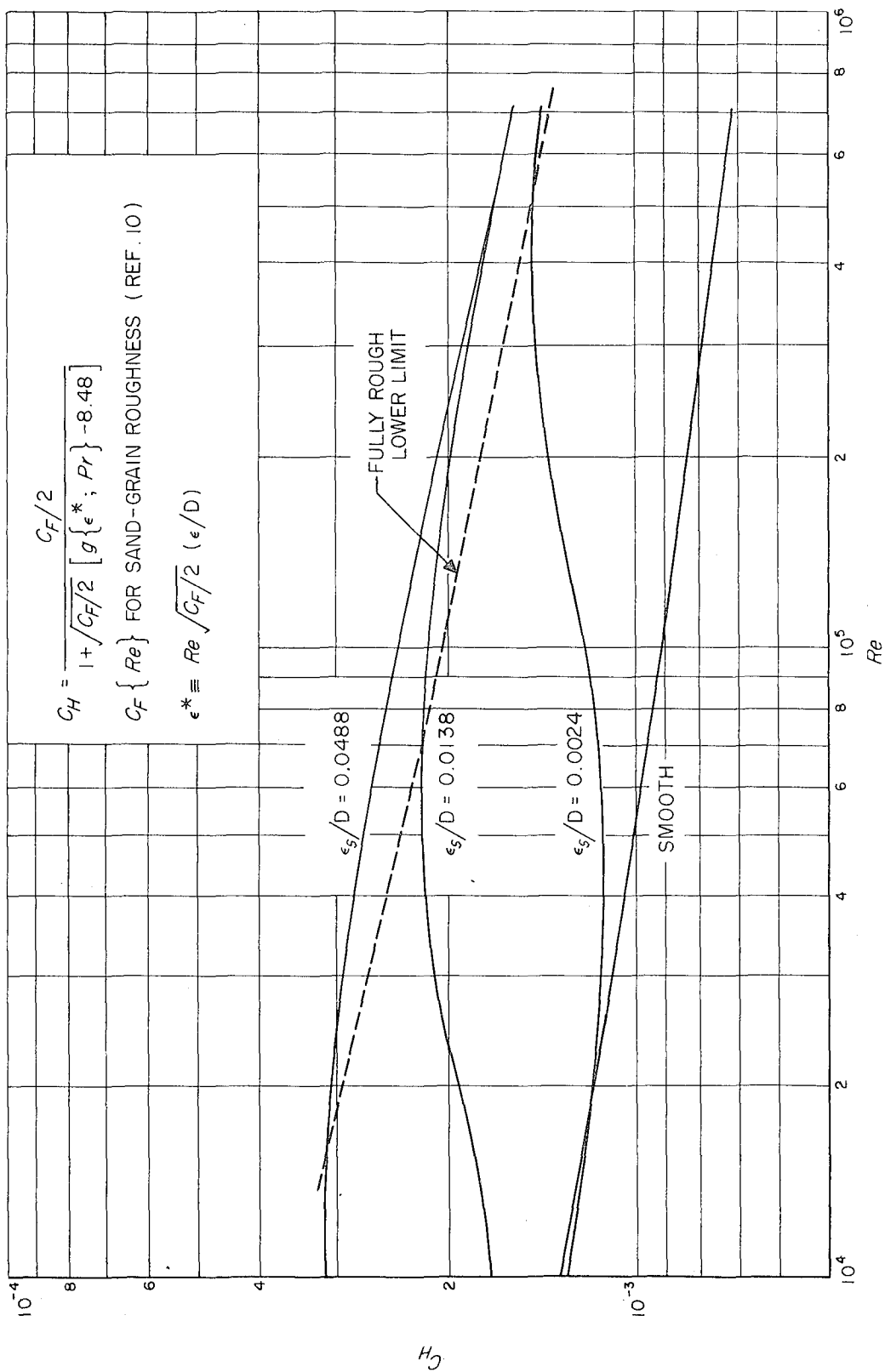
FIG. 35. EXTENSIONS OF EXPERIMENTAL RESULTS USING THE HEAT-TRANSFER SIMILARITY LAW, $Pr = 5.94$

$$C_H = \frac{C_F/2}{1 + \sqrt{C_F/2}\,\left[\,g\{\epsilon^*\,;\,Pr\}\,-8.48\,\right]}$$

$C_F\{Re\}$ FOR SAND-GRAIN ROUGHNESS (REF. 10)

$$\epsilon^* \equiv Re\,\sqrt{C_F/2}\,(\epsilon/D)$$

FULLY ROUGH
LOWER LIMIT

$\epsilon_s/D = 0.0488$

$\epsilon_s/D = 0.0138$

$\epsilon_s/D = 0.0024$

SMOOTH

C_H

Re

FIG. 36. CORRELATION OF EXPERIMENTAL RESULTS USING THE HEAT-TRANSFER
SIMILARITY LAW AND A POWER LAW FOR PRANDTL NUMBER

SMOOTH TUBE
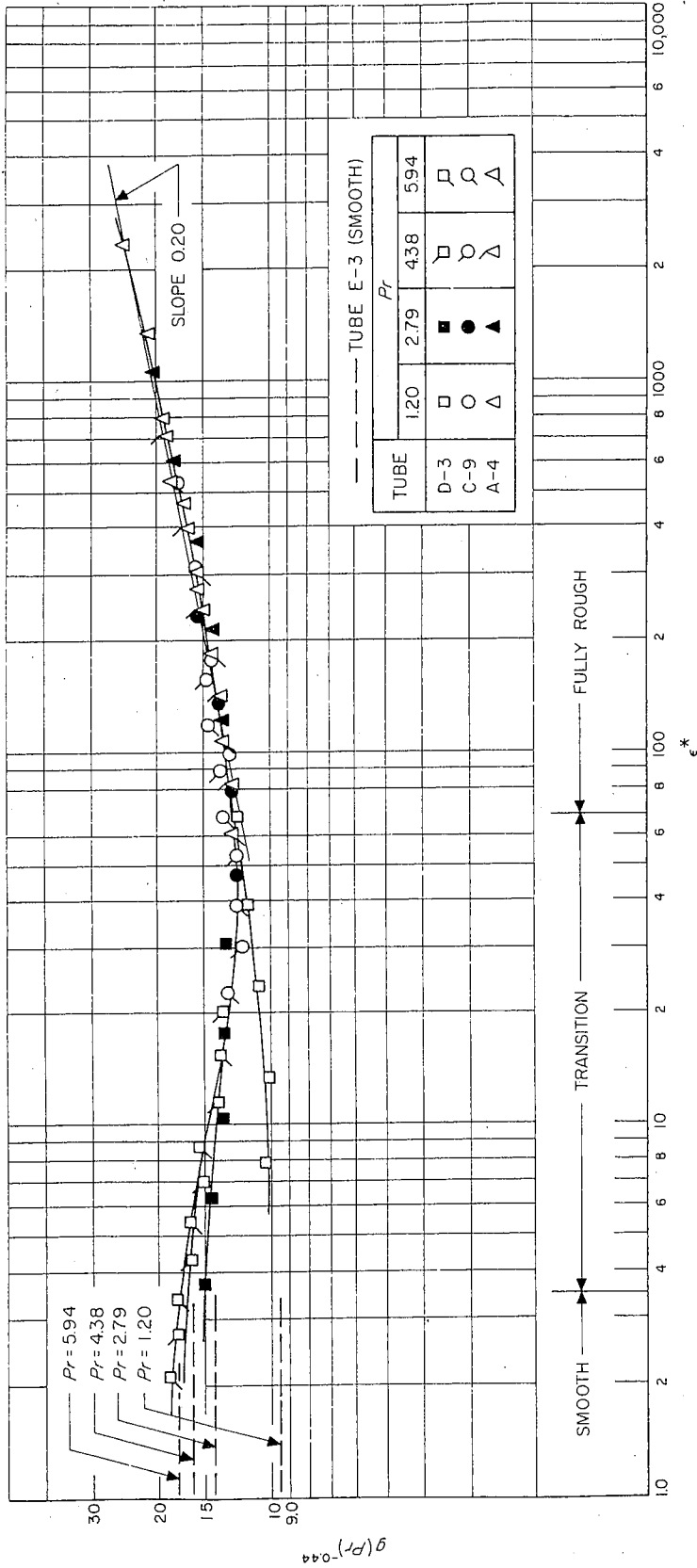
$Pr = 5.94$
$Pr = 1.20$
$Pr = 0.72$

NUNNER (REF. 5)
EXPERIMENTAL, $Pr = 0.72$

	PIPE	ϵ_s/D
△	B-20	0.133
▽	D-20	0.332
◁	D-5	0.335
▽	D-2	0.0555
□	A-20	0.194
-X-	CAST IRON	0.0038

SMITH AND EPSTEIN (REF. 9)
EXPERIMENTAL, $Pr = 0.72$

	PIPE	ϵ_s/D
○	1/8-in. GALVANIZED	0.0158
◐	1/4-in. GALVANIZED	0.0089
◑	3/8-in. GALVANIZED	0.0047
-+-	1/2-in. "KARBATE"	0.0053

SMOOTH ← → TRANSITION ← → FULLY ROUGH

PRESENT EXPERIMENTS

1-a $Pr = 5.94$
1-b $Pr = 1.20$
1-c $Pr = 0.72$ (EXTRAPOLATED)

2   NUNNER (REF. 5), EXPERIMENTAL, $Pr = 0.72$
     NUNNER (REF. 5), THEORY
3    $Pr = 0.72$, $\epsilon_s/D = 0.133$ (PIPE B-20)
4    $Pr = 0.72$, $\epsilon_s/D = 0.332$ (PIPE D-20)
5    $Pr = 5.94$, $\epsilon_s/D = 0.015$

     MARTINELLI (REF. 34), THEORY
6    $Pr = 0.72$, COLEBROOK'S A $\{\epsilon^*\}$
7    $Pr = 5.94$ NIKURADSE'S A $\{\epsilon^*\}$
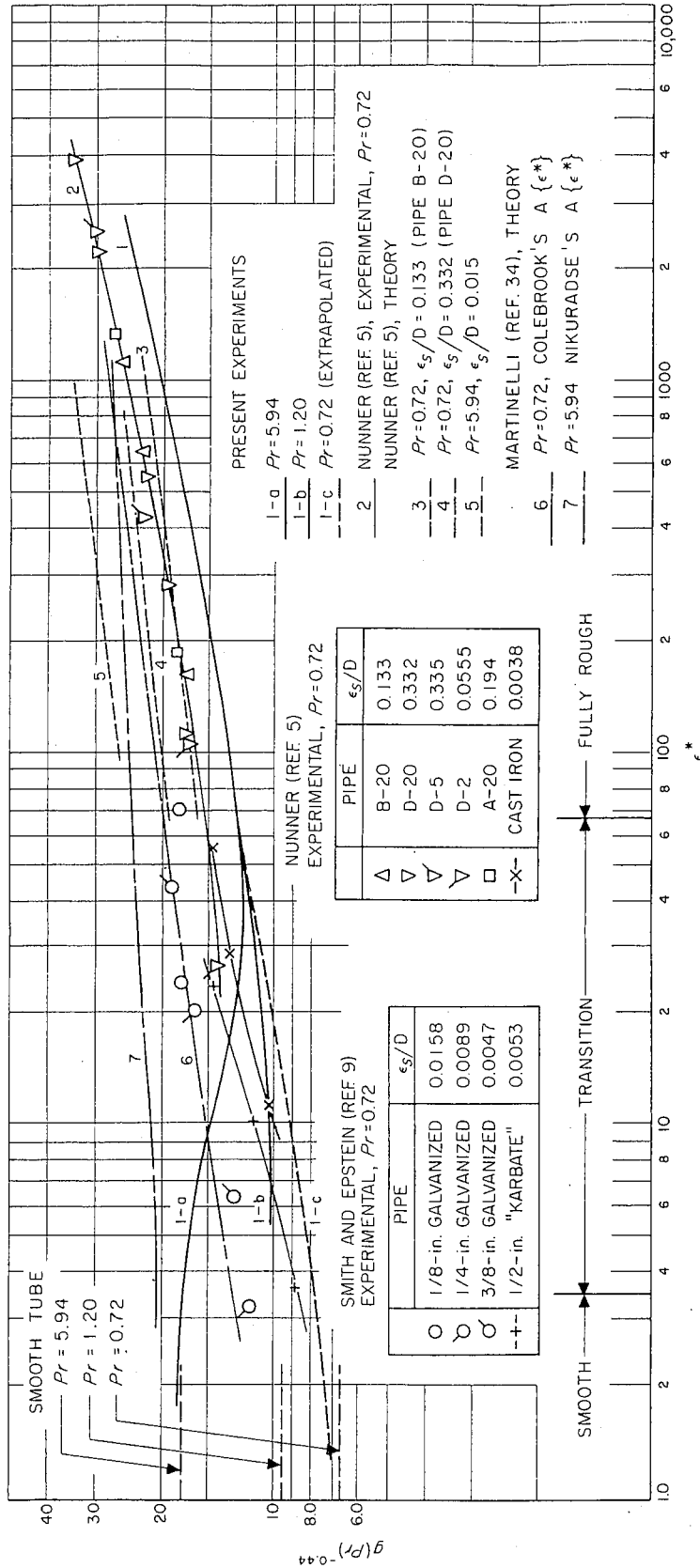
ϵ^*

$g(Pr)^{-0.44}$

FIG. 37. COMPARISONS—ROUGH TUBE HEAT-TRANSFER EXPERIMENTAL RESULTS AND THEORIES
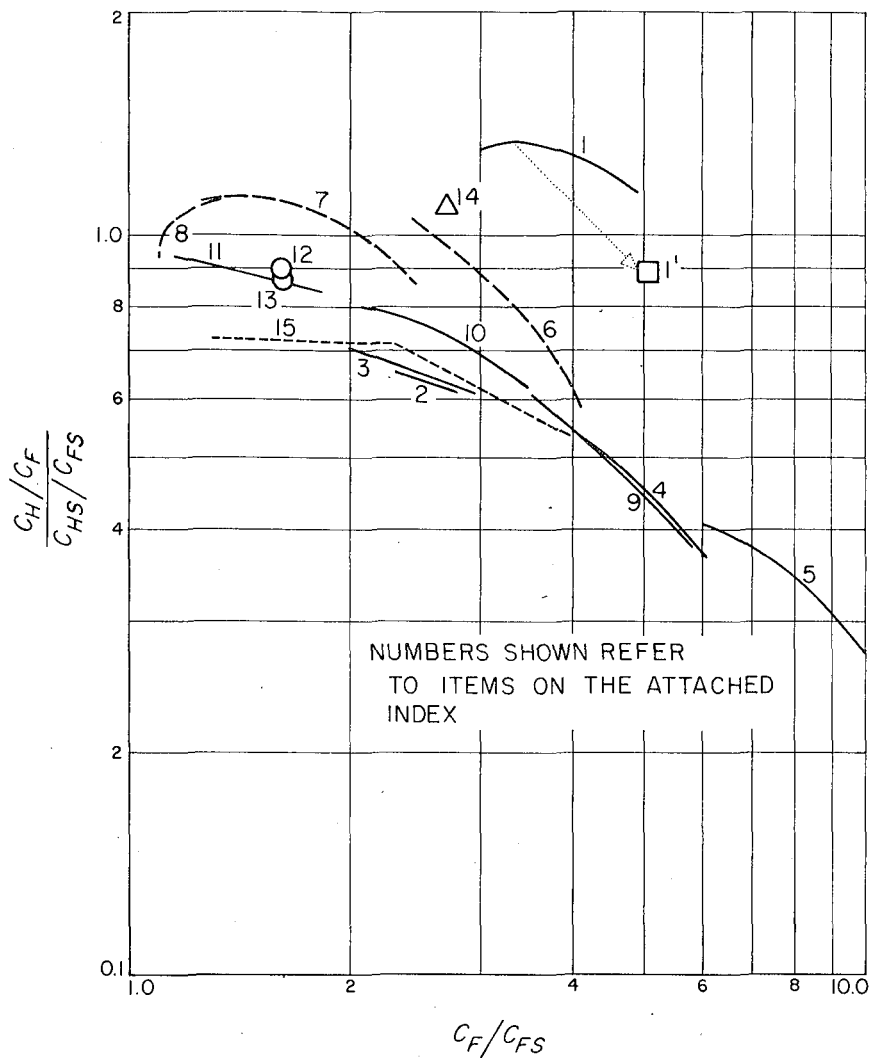
FIG. 38. COMPARISONS OF EXPERIMENTAL HEAT-
TRANSFER RESULTS FOR ROUGH SURFACES IN
RELATION TO SMOOTH SURFACES

INDEX TO FIGURE 38

Item	Investigator	Roughness Geometry	Reynolds Number	Prandtl Number	Remarks
1	Fortesque and Hall (Ref. 2)	Transverse fins on inner wall of an annulus, Fin Root Dia. $\cong$ 1.4 in. Channel Dia. $\cong$ 4.0 in. Fin Pitch $\approx$ 3/16 in. Tip-to-Root-Dia. ratio of fins 1.3 to 1.9	Not Given	~0.7	Combination of outer and inner wall effects in C_F terms
1'	Same	Same		~0.7	C_F terms computed on the basis of the inner, heat-transfer-ring surface only.
2	Sams (Ref. 42)	Square threads in pipe, Tube A Thread ht./Dia. $\cong$ 0.013	$5-10 \times 10^4$	~0.7	
3	Nunner (Ref. 5)	Ring elements of semicircular cross section in pipe, pipe D-2 Ring ht./Dia. $(h/D) \cong 0.08$ Pitch/height $(\ell/h) \approx 2.0$	$0.5-2 \times 10^4$	~0.7	
4	Same	Pipe B-20, $h/D \cong 0.04$, $\ell/h \approx 20$	$1-7 \times 10^4$	~0.7	
5	Same	Pipe D-20, $h/D \cong 0.08$, $\ell/h \approx 20$	$0.5-4 \times 10^4$	~0.7	

INDEX TO FIGURE 38 (Cont'd)

Item	Investigator	Roughness Geometry	Reynolds Number	Prandtl Number	Remarks
6	Present Investigation	Close-packed, granular roughness in pipe Tube A-4, $\epsilon_s/D = 0.049$	$1.4\text{--}11.5 \times 10^4$	6.0	
7	Same	Tube C-9, $\epsilon_s/D = 0.014$	$1.4\text{--}11.5 \times 10^4$	6.0	
8	Same	Tube D-3, $\epsilon_s/D = 0.0024$	$1.4\text{--}11.5 \times 10^4$	6.0	
9	Same	Tube A-4, $\epsilon_s/D = 0.049$	$5.8\text{--}51.0 \times 10^4$	1.2	
10	Same	Tube C-9, $\epsilon_s/D = 0.014$	$5.8\text{--}51.0 \times 10^4$	1.2	
11	Same	Tube D-3, $\epsilon_s/D = 0.0024$	$5.8\text{--}51.0 \times 10^4$	1.2	
12	Hastrup (Ref. 31)	Inverse knurl in pipe Height/Dia. = 0.021	10^5	~6.0	Nearly independent of Re value
13	Same	Same	10^5	~1.2	Nearly independent of Re value
14	Grass (Ref. 3)	Cross-grooved pipe Groove depth/Dia. = 0.005	3.7×10^4	~6.0 Assumed for water	
15	Brouillette, Mifflin and Myers (Ref. 41)	"V"-shaped, cross-grooves in pipe $\ell/h \cong 2.5$ Groove Depth/Dia. = 0.017 to 0.050	10^5	~6.0 Assumed for water	Nearly independent of Re value

APPENDIX I

Electroplated Nickel Tube Construction

The tubes used in the experiments were constructed by electroplating nickel onto a sand-covered mandrel and subsequently dissolving the mandrel.

The sand used for the three rough tubes was selected from stocks having nearly symmetrical shapes and having a mean size in the region of interest. The sand was then separated with pairs of standard Tyler-series screens to obtain the desired size range. The screens used for the three different sands had 200 to 270, 80 to 100, and 42 to 48 meshes per inch respectively. In all cases, a ROTAP separating machine was used to agitate the screens for approximately five minutes per one fluid ounce batch. In the case of the finest sand, 200 to 270 mesh, the sand was screened with a large, continuous process, SWECO separating machine prior to final separation with the ROTAP machine.

Statistical samples were selected from the processed sand, and photomicrographs displaying the grain profiles were made of each sample. The statistical distribution of the profile sizes was then measured both by direct scaling of the photographs and by the use of an automatic counting machine.* The size attributed to each grain corresponded to a diameter somewhere between that of the minimum circumscribed circle and the maximum inscribed circle. The sample sizes were of the order of 200 grains; hence, the actual distribution obtained is not too meaningful. However, the mean

---

* This machine, which was designed to measure distribution of circular images, is described in Reference 44—this reference number refers to the list accompanying the text.

value obtained was taken to be significant. The size distribution in each of the three sand sizes was found to be centered around the hole size of the screen with the larger openings; only a few grains smaller than the openings of the smaller screen were in evidence. This observation implies that the separation process was sufficient to clean out all of the grains smaller than the openings of the finer mesh screen, and, in fact, the process was so complete that a significant number of slightly elongated grains with mean size larger than the maximum screen opening were found in the samples. In Figure A-I-1, an example of the photomicrographs of each grain size shows both the good uniformity of the grains and the tendency to slight elongation.

A mandrel was prepared as follows: First a thin coating of thermosetting polyester plastic* was applied to a 4-1/2 foot length of 3/8 inch-diameter, drawn aluminum tubing. The coated tubing was then placed inside of a length of one-inch-diameter pipe which was provided with centering fixtures and was capped at one end. The large pipe was placed, capped-end down, in a vertical position, and the graded sand was poured into the annular region via a funnel arrangement which directed the sand down along the inner periphery of the large pipe. After the plastic had set, the sand was poured out leaving a single layer of grains adhered to the outer surface of the aluminum tube. A stiff brush was used to remove any grains that had been caught between the adhering grains. A one-inch long section at the center of the tube, which had been masked during the sanding operation, was then wrapped with an integral number of

*Pittsburgh Selection #5119

turns of a special plastic tape.* This formed a one-inch smooth section on the mandrel with a diameter slightly greater than that of the sanded portion. The entire mandrel was then sprayed with successive light coats of acrylic lacquer. The lacquer was made opaque, and hence more visible, by the addition of white pigment. The spraying process was continued until a microscopic examination of the surface revealed slight menisci formed in the interstices of the grains. Finally, an extremely thin coating of silver was chemically deposited on the mandrel surface rendering it electrically conductive. The mandrel for the smooth tube (E-3) was also made from 3/8-inch-diameter, drawn aluminum tubing which was cleaned with detergent and silver coated.

The completed mandrel was hung vertically in a Watts-type nickel-sulphate and nickel-chloride electroplating bath with the cathode attached to the upper end of the mandrel. Nickel deposition, at a rate of the order of 0.001 inch-per-hour, was continued until a thickness of between 0.015 and 0.025 inch was attained.** Figure A-I-2 shows a sketch of the plated mandrel. Following the plating operation, the plated mandrel was soaked successively in solutions of potassium hydroxide and hydrofluoric acid to remove first the aluminum tube and then the sand and plastics. The remaining nickel shell, which served as the test section, was mounted in a lathe head which was rotated slowly as a stiff fiber brush was drawn back and forth through the tube. The brushing was followed by a water flush,

* 3M Scotch Brand #470 Electroplating Tape.
** The electroplating was performed by Electroforms, Inc., Gardena, California.

and the procedure was repeated until all traces of plastic ash were removed from the roughness pockets.

At this stage, temporary fittings were brazed to the ends of the completed tubes, and the assembly was leak tested and pressure tested to 350 psig—one rough tube sample was pressurized to 1900 psig before bursting. In early attempts at producing these tubes, leak tests revealed very many microscopic holes (less than 0.0001 inch in diameter) passing through the tube wall. This problem was eliminated by using great care in preparing the mandrels such that all of the voids between the grains had well formed menisci of the acrylic plastic. It is hypothesized that, if a void exists on the original mandrel surface, the nickel grows from the sides of the cavity and meets to form a ''cold joint'' or ''pipe'' which propagates through the wall as the nickel is deposited. On the other hand, if the surface cavity has a depth of the same order as its width, the growth will proceed from all surfaces. Figure 2 (Tube A-4) of the text shows a cavity region which is properly formed.

Another source of imperfections in electroplated tubes is the interruption of the plating process prior to completion. Photomicrographs of a cross-section of a sample tube, not used in the experiments, revealed the presence of a very dark ring located midway between the inner and outer walls of the tube. This was interpreted to be a layer of oxide which was formed while the tube had been removed from the bath for inspection before completion of the plating process. Such an imperfection would be unacceptable for an experimental heat transfer tube where the material properties must be uniform and well understood.
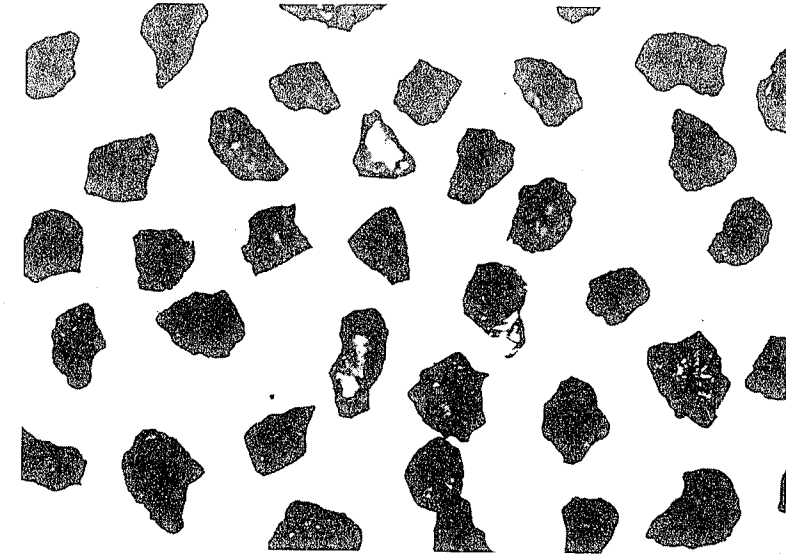
FOR TUBE A-4
22.3X
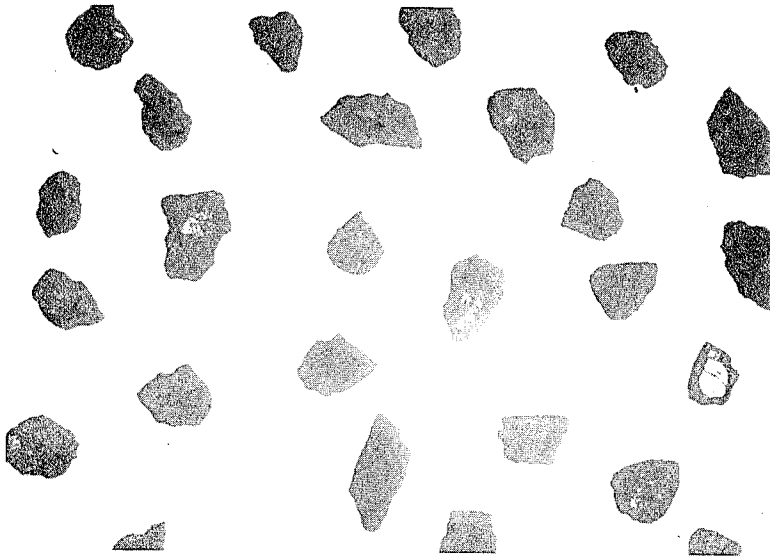
FOR TUBE C-9
40.1X
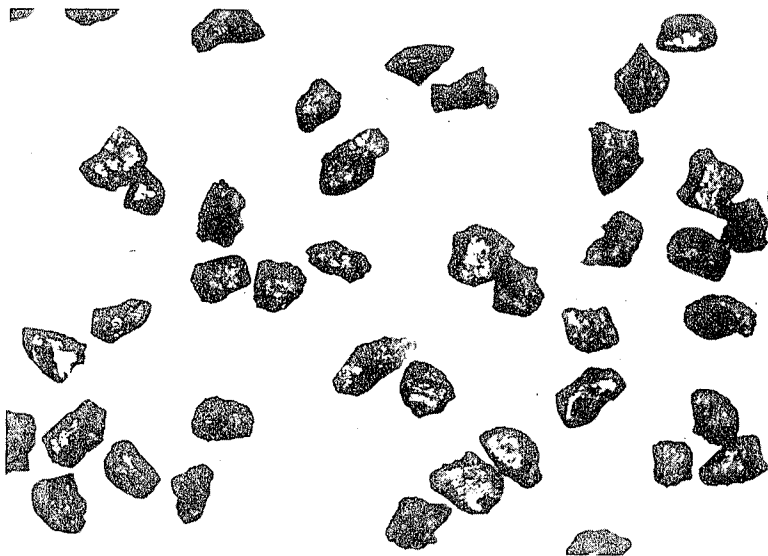
FOR TUBE D-3
86.9X

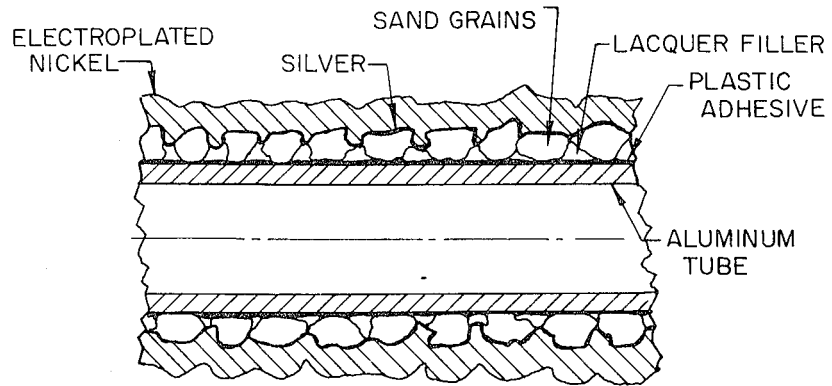FIG. A-I-I. SAMPLE PHOTOMICROGRAPHS OF TUBE-MANDREL SAND GRAINS

FIG. A-I-2. SKETCH OF NICKEL-PLATED
TUBE MANDREL

APPENDIX II

Deductions from Direct-Current Measurements of Tube Resistance

A. Electrical Resistivity

The electrical resistance-per-unit-length of each tube was determined by passing a measured direct-current through the tube wall and measuring, by potentiometer, the voltage drop between a pair of probes in contact with the tube at two different longitudinal stations. The wall was maintained at selected temperatures between 72° and 290°F by the passage of heated water through the tube. Heat generated by the small electric current (70 amperes) and the heat exchanged to the surrounding air were insufficient to produce significant thermal gradients within the tube wall; hence, the tube wall could be assumed to be maintained at the measured water temperature throughout its length. Repeating the resistance measurement at many stations along the tube provided plots of resistance-per-unit-length as a function of station and of temperature. The ends, trimmed from each tube, provided samples for measurement of tube wall cross sectional area at both ends of the test section. These samples were ground and polished to provide a true cross section perpendicular to the axis of the tube. This area was then measured by casting a magnified (10X) image of the section on the screen of a Kodak Comparator onto which a piece of photographic print paper was affixed. The resulting photographic image was planimetered along with the superimposed image of the Comparator reticule, the latter providing a direct calibration of the stretch of the photographic paper during development. In computing the resistivity of the various tubes, a first order, geometrical correction

factor was applied in order to account for the effect of undulations in the walls of the rough tubes. From the information thus obtained, the resistivity was computed for each of the samples taken from each end of the four tubes by

$$\rho\{T\} = \frac{A_{cs}}{G} \frac{dR}{dx} \{T\} \quad * \tag{II-1}$$

where A_{cs} is the measured cross sectional area, $(dR/dx)\{T\}$ is the measured resistance-per-unit-length at temperature (T) and G is the geometrical correction computed to be approximately 1.08 for the roughest tube and 1.00 for the smooth tube. The resistivity values obtained for the rough tubes agreed to within plus 9 percent to minus 1 percent with the average of the two values obtained for the smooth tube ($\rho = 2.95 \times 10^{-6}$ ohm-in. at 72°F); this agreement was taken as evidence that the wall material was essentially the same from tube to tube and from end to end on each tube, within the resolution of the measurements.

Because of the uncertainty involved in establishing the geometrical correction (G) in equation II-1 for the rough tubes, a second method was employed to check the resistivity of these tubes in comparison to the smooth tube for which the G factor is unity. This method is based on measurements of the thermal coefficient of resistivity $(d\rho/dT)$. Wise and Schaefer (Ref. 24, p. 1071)[**] have shown that $(d\rho/dT)$ is essentially independent of either the amount (up to several percent) or the type of impurities or alloying

---

[*] The nomenclature of the main text will be followed in this appendix, except that the subscript e will be dropped from ρ_e and R refers to electrical resistance instead of pipe radius.
[**]The reference numbers in this appendix refer to the reference list accompanying the text.

elements present in nickel. This observation is confirmed also by the results of other experimenters; note the existence of nearly parallel lines in Figure A-II-1 formed by the $\rho\{T\}$ measurements of Lees (Ref. 45), Jäger and Diesselhorst (Ref. 45), Shofield (Ref. 46) and those reported by Wise and Schaefer (Ref. 24, p. 427). The fixed $(d\rho/dT)$ rule may be expressed for restricted temperature ranges as,

$$\rho_a\{T\} = \rho_a\{T_0\} + K(T-T_0) \tag{II-2}$$

where the subscript "a" refers to a particular nickel alloy, T_0 is a fixed base temperature and K is a constant independent of the nickel composition. Considering two different compositions, "a" and "b", one can write equation II-2 for composition "b" and multiply through by the resistivity quotient at the base temperature to obtain

$$\rho'_b\{T\} \equiv \rho_b\{T\} \frac{\rho_a\{T_0\}}{\rho_b\{T_0\}} = \rho_a\{T_0\} + \frac{\rho_a\{T_0\}}{\rho_b\{T_0\}} K(T-T_0) \tag{II-3}$$

In the measurements of $\rho\{T\}$ via equation II-1, the accuracy obtained for the smooth tube is considerably better than that obtained for the rough tubes since the cross sectional area is easier to measure and no geometrical correction is required. Consequently, for the comparisons to be made by use of equation II-3, the subscript "a" will be taken to refer to the smooth tube. Then, by using equation II-1, the value of $\rho'_b\{T\}$ for any one of the rough tubes is independent of the cross sectional area of the rough tube:

$$\rho'_b\{T\} = \frac{(dR/dx)_b\{T\}}{(dR/dx)_b\{T_0\}} \rho_{(E-3)}\{T_0\} \tag{II-4}$$

This quantity, determined from the DC resistance measurements, has been plotted for each of the tubes in Figure A-II-1, with T_0 taken as $72^O F$. As can be seen, the $\rho_b'\{T\}$ values for all of the tubes fall essentially right on the $\rho_{(E-3)}\{T\}$ curve for all temperatures tested. Comparing equations II-2 and II-3, it is seen that the coincidence of these curves, at temperatures other than $T = T_0$, can occur if, and only if,

$$\rho_b\{T_o\} = \rho_a\{T_o\} \equiv \rho_{(E-3)}\{T_o\}$$

where ''b'' refers to any of the rough tubes. It was further observed for each tube that the ratio

$$\frac{(dR/dx)\{T_1\}}{(dR/dx)\{T_2\}}$$

formed for any two temperatures (T_1 and T_2) is the same for any station along the tube. By the arguments used with equation II-4, this observation confirms the supposition that the resistivity is uniform throughout the length of each tube and is uniform from tube to tube. It is also noted that the validity of the $\rho\{T\}$ function for the smooth tube is attested by the close parallel it forms with the pure nickel curve given by Reference 24, Cf. Figure A-II-1. Had there been error in the cross sectional area measurement of the smooth tube, by say 10 percent, a sensible disagreement in the slopes should have been evident.

From the preceding analysis and consideration of the various measurement errors, it is concluded that the $\rho\{T\}$ function shown in Figure A-II-1 represents the resistivity of all of the test tubes at all stations to $\pm$ 3 percent. Considering the extreme sensitivity of resistivity to small amounts of impurity, the comparison of this

curve with the results presented for very high purity, electrolytic nickel indicates that high purity and freedom from inclusions was attained in the production of these tubes. This conclusion is supported by chemical analyses of electroplated nickel samples which were produced in the same equipment used for making the test tubes. It should be noted that it cannot be assumed, a priori, that electroplated tubes will have high purity material. One of the early attempts at electroforming tubes for the present experiments resulted in a material with resistivity nearly equal to that of the 99.2 percentpure nickel investigated by Schofield (Cf. Fig. A-II-1).

B. Thermal Conductivity

Since the resistivity measurements showed the nickel in the tubes to be very nearly pure, it is implied that other properties, namely thermal conductivity (k), will be very nearly the same as published values for the pure substance. The Wiedemann-Franz-Lorentz equation (Cf. Ref. 20, p. 112),

$$L \equiv \frac{k \ \rho}{T_{abs}} = \text{dimensional constant} \tag{II-5}$$

where L is the so-called Lorentz number and T_{abs} is the absolute temperature, has been found to hold true for many pure metals including nickel. A modification of this expression was suggested by Smith and Palmer (Ref. 25) for use with groups of alloys having the same principal constituent,

$$L = L_a + a \ (\rho/T_{abs}) \tag{II-6}$$

where L_a and ''a'' are constants independent of the particular alloy composition.

Smith and Palmer's investigations gave values of the two coefficients in equation II-6 for copper alloys, and Powell found the coefficients for iron alloys, aluminum alloys and magnesium alloys (Cf. Ref. 20, p. 117). Using the definition of L in equation II-5, one can rewrite the Smith-Palmer equation as

$$k = L_a (T_{abs}/\rho) + a \qquad \qquad (II-7)$$

The data given by Shofield, Lees, Jäger and Diesselhorst, and Wise and Schaefer (Cf. Refs. 46, 45 and 24) for nickel with various purities were plotted by the present writer as "k" versus (T_{abs}/ρ). The "k" values were shown to agree within approximately 8 percent in the regions of overlap. This is remarkable agreement considering that variations of as much as 100 percent exist among the "k" values and among the ρ values for the various compositions at a given temperature. The observed agreement is taken as verification of the Smith-Palmer relation for nickel alloys. Since the resistivity of the nickel tubes used in these tests is very close to that of the high purity nickel, only the high purity $\rho\{T\}$ and $k\{T\}$ functions (Refs. 12, p. 498; 24, p. 425-427) were used for determining the particular L_a and "a" values employed in computing the thermal conductivity of the test tubes from the electrical resistivity measurements. Using these, equation II-7, becomes

$$k(\frac{Btu}{Hr-Ft-{}^oF}) = 1.86 \times 10^{-7} \frac{T_{abs}({}^oR)}{\rho(ohm-in)} + 17.8 \qquad (II-8)$$

When equation II-8 is applied to the $\rho\{T\}$ values measured for the experimental tubes (Fig. A-II-1), the $(1/k)\{T\}$ relationship shown in Figure A-II-2 is obtained. Other measurements of nickel having

various impurity levels are shown for comparison in this figure.

The straight line approximation

$$\frac{1}{k} \left(\frac{Hr\text{-}Ft\text{-}^{\circ}F}{Btu}\right) = 0.0187 + 1.41 \times 10^{-5} \, T(^{\circ}F) \tag{II-9}$$

drawn in Figure A-II-2 was used for all calculations in this report. This expression is expected to give thermal conductivity values within ± 3.5 percent of the correct value, assuming that the error limits on the measurements reported in References 12, p. 498 and 24, p. 425 for very pure nickel are an order of magnitude less than this.

C. Tube Wall Thickness

For the smooth tube, the wall thickness at the ends of each of the test tubes was scaled directly from the Kodak Comparator pictures of the tube cross sections discussed in Part A of this appendix. In the case of the roughest tube, the height of the roughness elements are of the same order as the wall thickness, and the meaning of wall thickness is less clear; hence, it becomes necessary to define an effective wall thickness. This is done by means of an idealized geometrical model. The resistivity of a rough tube can be written

$$\rho = \frac{\Delta R \, A_{cs(eff)}}{\Delta L_{eff}} \tag{II-10}$$

where $A_{cs(eff)}$ is the area of a warped surface passing across the tube in such a way that it is everywhere normal to the current flux lines; ΔL_{eff} is the effective average length of all current flux paths passing between two longitudinal stations; and ΔR is the measured resistance between the two stations. A "warped mean surface" is

then imagined as that surface passing midway between the inner and outer walls of the tube. An effective wall thickness (t) is described as the average distance between the inner and outer tube walls in a direction normal to the "warped mean surface," and the ΔL_{eff} is assumed to be approximated by an average path length in the axial direction along the "warped mean surface." The diameter of a cylinder passing near the center of the wall can be taken as (D+t) where D is the volumetric internal diameter defined by equation 69 of the text. It is then assumed that, to a first order approximation, the same geometrical factor (G), which converts distance along the tube axis (Δx) to the average longitudinal path length along the "warped mean surface" (ΔL_{eff}), also converts the cylinder diameter (D+t) into an effective average circumferential path length along the "warped mean surface" and that the latter path length may be used with "t" to define $A_{cs(eff)}$. Thus if

$$\Delta L_{eff} = G \, \Delta x \tag{II-11}$$

then

$$A_{cs(eff)} = G \, \pi \, (D + t) \, t \tag{II-12}$$

Substituting equations II-11 and II-12 into II-10 and rearranging gives

$$t\{x\} = \frac{\rho}{\pi \, (dR/dx)\{x\} \, (D+t\{x\})} \tag{II-13}$$

Equation II-13 is taken as an operational definition of the wall thickness of the rough tubes as well as the smooth tube. Assuming that the resistivity (ρ) is determined from Part A of this appendix and that D is separately measured, then the $(dR/dx)\{x\}$ measurement

yields $t\{x\}$ as a solution of the implicit equation II-13. The thickness so defined is something like a thickness measured in the direction normal to the tube walls; it gives meaningful values for both limiting cases, wall-thickness-to-roughness-height ratio equals zero and infinity respectively. The latter case is that of the smooth tube. The thickness derived by equation II-13 gives good agreement with measurements taken from the cross-section photomicrographs of the rough tubes in those regions where it appears that the plane of the cross section passes through the center of a roughness element such that a thickness normal to the local wall surface is exposed.

Any attempt to further refine the thickness definition is considered meaningless. In the experiments wherein thickness is used in the estimation of the difference in temperature between the tube outside wall and the inside wall, the effect of locally non-uniformly distributed heating and the effects of locally non-uniform heat transfer film conductance of the fluid contribute uncertainties of the same order as the remaining uncertainty in the effective wall thickness.

Since the diameter of the tube and the resistivity of the tube material are observed to be uniform and since the tube diameter is large compared to the thickness, the ratio of the thickness at any station to the thickness at the ends of the tube is closely approximated from equation II-13 by

$$\frac{t\{x\}}{t\{L\}} = \frac{(dR/dx)\{L\}}{(dR/dx)\{x\}} \tag{II-14}$$

The resistance measurements used with equation II-14 revealed a linear variation in (dR/dx), and hence in thickness, of the order of

10 percent in the 17.5-inch-long heated test section for all tubes. This is accounted for in the data reduction. The tubes are thicker near the end where the cathode was attached in the plating operation, but, since this effect is not detrimental to the present use of these tubes, no attempt was made to correct it. The tube sample cross sections showed very uniform thickness in the circumferential direction in all tubes.
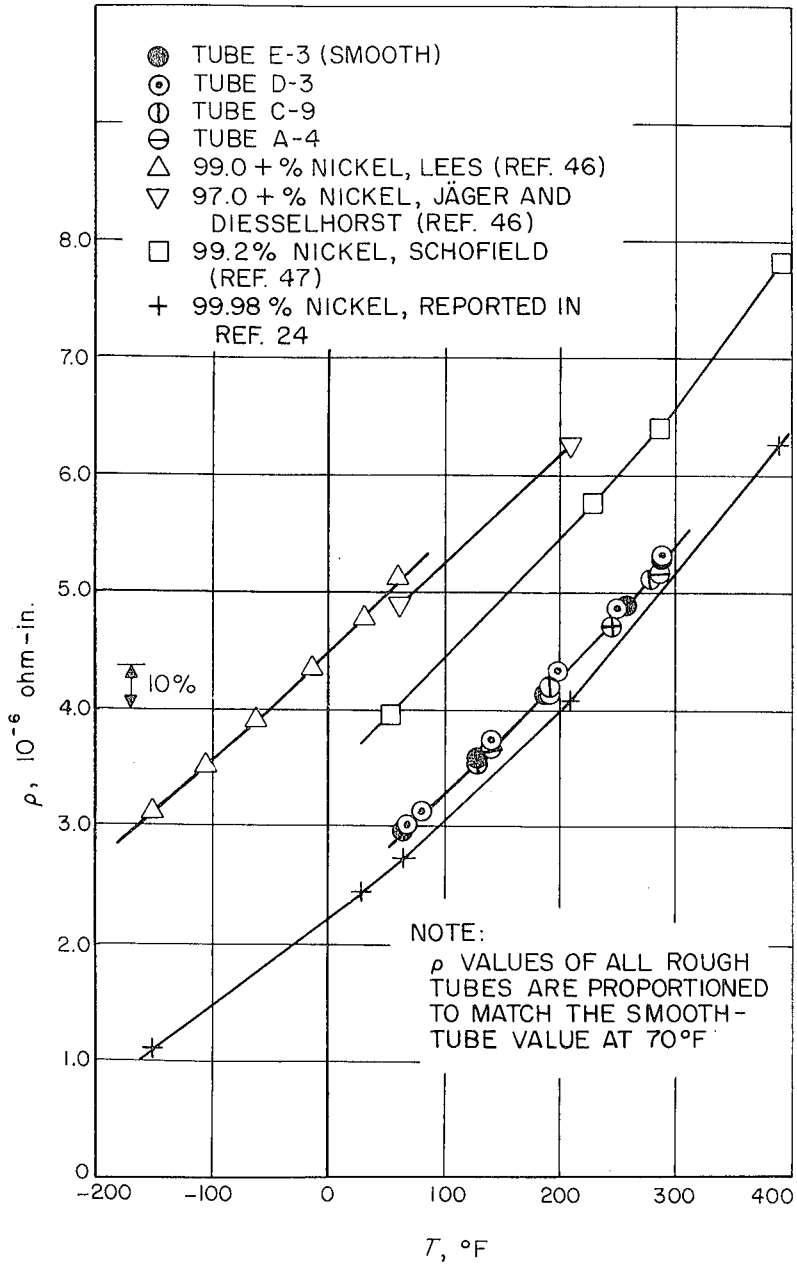
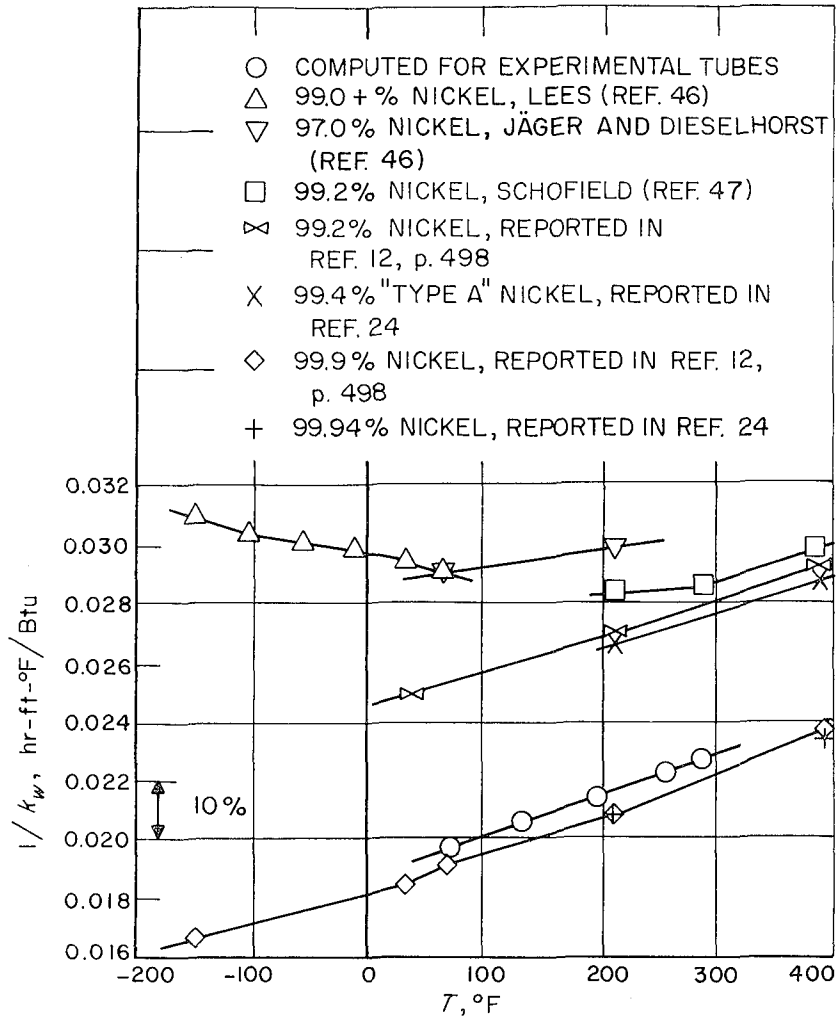FIG. A-II-I. ELECTRICAL RESISTIVITY OF NICKEL TUBES
WITH COMPARISONS

FIG. A-II-2. COMPUTED NICKEL TUBE THERMAL
CONDUCTIVITY WITH COMPARISONS

APPENDIX III

System Schematics and Equipment Lists

Figure A-III-1 shows the complete hydraulic system. The principal feature of the system, shown in this figure and not included in Figure 9 of the text, is the system of differential pressure meters. The valving is arranged to permit selection of a 0-25 psid gage, a 0-100 inch-water recorder or a 0-20 inch-water recorder for the tube pressure drop measurement and selection of a 0-50 psid gage, a 0-300 inch-water recorder or a 0-100 inch-water recorder for the venturi pressure drop measurement. A single 0-100 inch-water recorder is used in either circuit. Valving is also provided to allow complete bleeding of the air from the gage lines and the bellows chambers of each meter. Viewing tubes are provided (see the bottom of the gage panel in Figure 8 of the text) to indicate when bleeding is complete. Also shown in Figure A-III-1 is the gage calibration circuit consisting of manometers and a nitrogen regulator with interconnections to all of the gages. The plumbing is arranged to permit purging of all interconnecting lines and the bellows chambers prior to calibration so that no liquid heads remain and so that the atmosphere can be used as one leg of the calibration circuit.

The chilled water supply for the receiver tank cooler shown in Figure A-III-1 was used to lower the system water temperatures following the tests.

The items enumerated in Figure A-III-1 are described in the following equipment list. Specifications and/or manufacturer are included only for the principal items.

1. Reservoir tank, capacity 45 gallons, stainless steel, approximately 1-1/2 inch rock-wool-type insulation.

2. Tank exit venturi, special design, stainless steel.

3. Receiver tank, capacity 65 gallons, galvanized steel.

4. Sight glass.

5. Centrifugal pump, 15 gpm* at 150 foot head.

6. Pump motor, 5 HP.

7. Bearing-coolant heat exchanger for pump.

8. Solenoid operated, 4-way gas valve.

9. Mercury U-tube manometer, 30 inch.

10. Water U-tube manometer, 20 inch, used with Meriam Unit Oil — Spec. D-2969.

11. Water filter

12. Immersion-type dial thermometer, 50-500°F.

13. Immersion-type dial thermometer, 50-300°F, 2 required.

14. Electrical isolation flange joint and mixing chamber (Cf. Fig. 5 of text).

15. Electrical isolation flange joint, 2 required.

16. Pneumatically operated ball valve, stainless steel body, Teflon seats.

17. Solenoid valve.

18. Toggle switch, 2 required.

19. Gas filter.

20. Burst diaphragm, 265 psid.

21. Burst diaphragm, 585 psid.

---

*Abbreviations used in this appendix are defined in the list accompanying the text.

22. Dome controlled regulator, 5-1500 psi outlet, 3 required.

23. Dome loader regulator, 50-300 psi outlet, 2 required.

24. Back pressure regulator, 100-2000 psi.

25. Differential pressure gage, 0-50 psid, Barton, #C149-3.

26. Pressure gage, 0-300 psig, 3 required.

27. Pressure gage, 0-200 psig.

28. Differential pressure gage, 0-25 psid, Barton, #SC-181-1.

29. Differential pressure recorder, 0-300 inch-water, Barton,
    #202-656.

30. Ball valve, stainless steel body, Teflon seats, 3 required.

31. Throttling valve.

32. Pressure gage, 0-3000 psig.

33. Differential pressure recorder, 0-20 inch-water, Barton,
    #202-106.

34. Check valve.

35. Back pressure regulator, modified Grove power reactor,
    #RBX204-015.

36. Regulator, Watts model M-1.

37. Differential pressure recorder, 0-100 inch-water, Barton,
    #202-107.

38. Horizontal gage lines, 10' x 0.25'' x 0.035'', stainless steel.

Figure A-III-2 shows the complete electrical system. The
tube-heating power metering system provides for selection of tube
probes or electrode probes as the potential source for the watt-
meter. Separate current transformers are used for the wattmeter
current input and for the ammeter. Tube voltages lower than those
afforded by the variable-primary power transformer are attained

by the use of an auxiliary, tap-water-cooled tube as a resistance element in the high-current line. When the auxiliary tube is not required, the heavy cables are joined to bypass it. The power to the electrode and mixing flange guard heaters is controlled by variable auto-transformers, and the temperatures of the electrodes and the flange are monitored by a thermocouple-potentiometer system separate from the principal thermocouple system. All thermocouple wires are connected to copper wires in the ice bath, thus allowing all switch interconnections to be made with copper wire. The main thermocouple rotary switch provides for connection of the potentiometer with any of the tube-wall or the water-immersion thermocouples. In addition, by the use of switch position number 3 shown in Figure A-III-2, the electrical difference between the outlet-water-thermocouple e.m.f. and the e.m.f. of any of the other thermocouples selected by the rotary switch is read by the potentiometer. The method of calibration of the main potentiometer-galvanometer circuit is discussed in Section III-D-2 of the text; switches number 26 and 29 shown in Figure A-III-2 are used for this purpose. Supplementary resistances, also shown in the figure, provide an input impedance to the potentiometer of 320 ohms under all switch arrangements. This facilitates the potentiometer calibration and permits the use of the galvanometer as a deflection instrument.

The items enumerated in Figure A-III-2 are presented in the following equipment list.

1. Rotary, double pole thermocouple switch, 12 position, Leeds and Northrup.

2. Double pole double throw knife switch, 5 required.

3. Six-inch-diameter Dewar flask for the thermocouple-cold-junction ice bath; stirring motor; 28, separate, partially oil-filled, glass wells (approx. 6'' deep) used to accept wire junctions.

4. Electrical resistance heating tape insulated with glass fiber and with asbestos tape, 275 watt, 3 required.

5. Variable auto-transformer, 3 required.

6. Fuse, 3 required.

7. Immersion-type, Chromel-Alumel thermocouple (Cf. Fig. 10 of text), total lead resistance 40 ohms, 2 required.

8. Thermocouple, Chromel-Alumel, resistance welded to respective surfaces, 3 required.

9. Potential step-up transformer, General Radio, type 942-A.

10. Wattmeter, 0-50 watts, 0-2.5 amp, 0-5.0 amp, 0-50v, 0-100v, Weston Mod. No. 310.

11. Current transformer, 500:1 ratio, Weston Mod. No. 327, Type 2.

12. Tube-heating, step-down transformer, 100 kva, 5000 amp max. on secondary, 440 v max. on primary, variable tap primary yields 44 different ratios between 11:1 and 22:1.

13. Magnetic circuit breaker.

14. Push button, dead-man switch.

15. AC voltmeter, 0-5v, 0-10v, Weston Mod. No. 433.

16. AC voltmeter, 0-10v, 0-20v.

17. AC ammeter, 0-5 amp, 0-10 amp, Weston Mod. No. 433.

18. Current transformer, 240:1 ratio, Weston Mod. No. 327, Type 2.

19. Electrically insulating flange joint, 2 required.

20. Resistance tube, 9'' or 18'' x 0.375'' x 0.065'', type 347 stainless steel tubing, cooled with tap water.

21. Gate valve.

22. Pressure gage, 0-100 psig.

23. Hand balance potentiometer.

24. Light beam galvanometer, Rubicon Mod. No. 3404H.

25. Hand balance potentiometer, Rubicon Mod. No. 2702.

26. Single pole double throw, fast acting, switch.

27. Double pole single throw toggle switch, 3 required.

28. Resistor, 120 ohm, 3 required.

29. Single pole double throw knife switch.

30. Tube wall thermocouples, Chromel-Alumel (Cf. Fig. 5 of text), total lead resistance 160 ohms, 9 required.

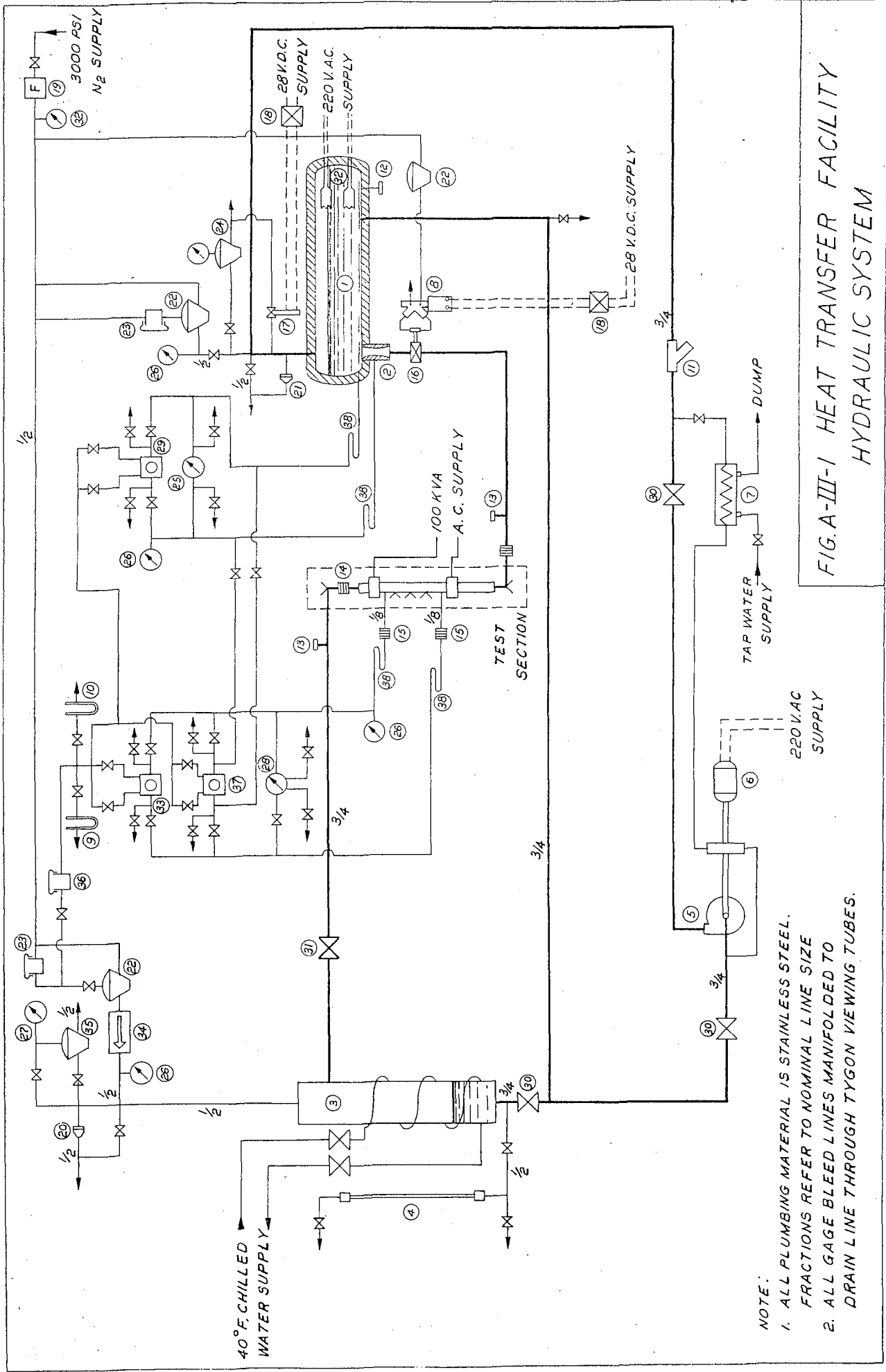31. Resistor, 320 ohm.

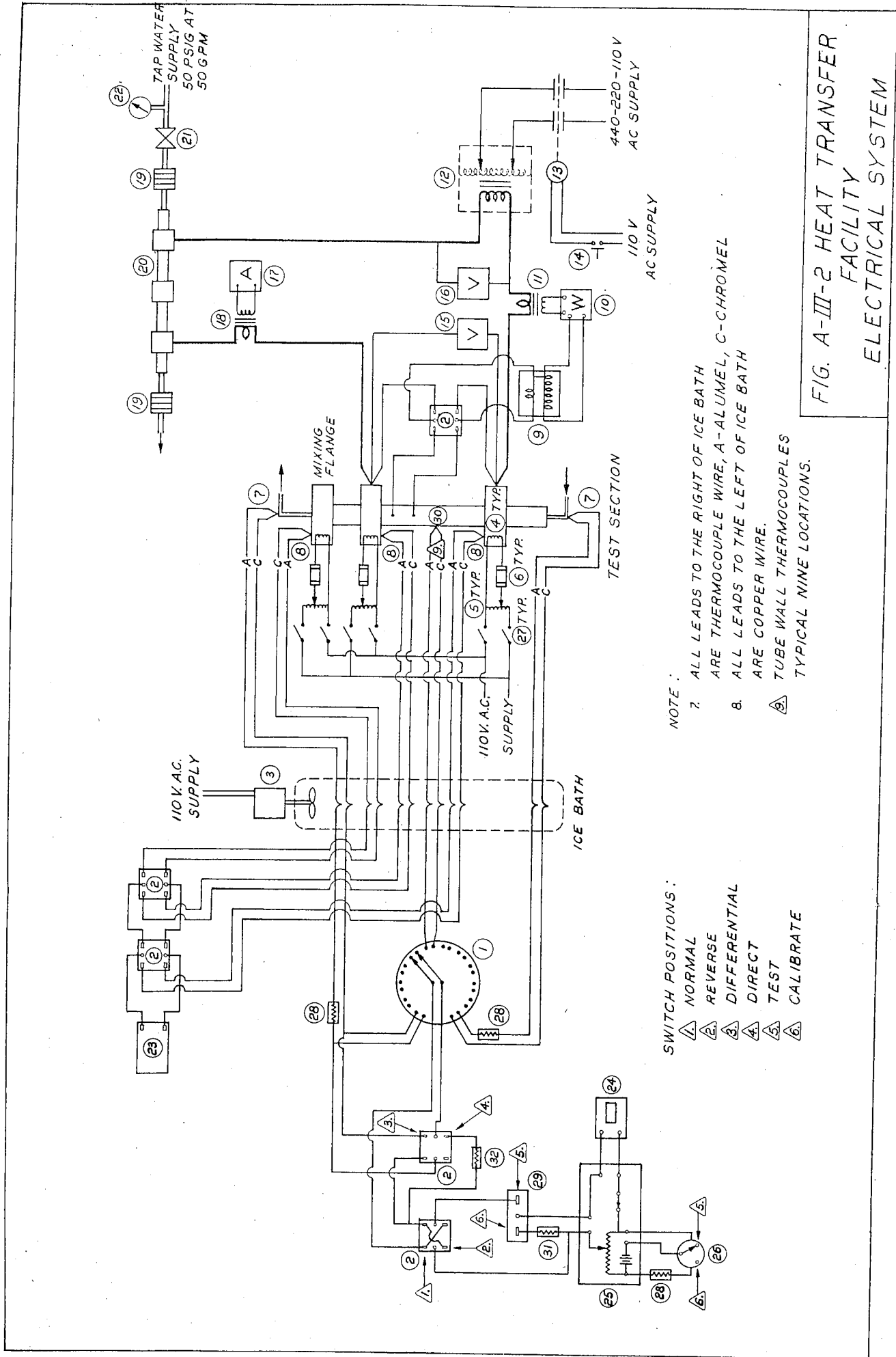32. Resistor, 160 ohm.

FIG. A-III-I HEAT TRANSFER FACILITY
HYDRAULIC SYSTEM

NOTE:
1. ALL PLUMBING MATERIAL IS STAINLESS STEEL.
   FRACTIONS REFER TO NOMINAL LINE SIZE
2. ALL GAGE BLEED LINES MANIFOLDED TO
   DRAIN LINE THROUGH TYGON VIEWING TUBES.

FIG. A-III-2 HEAT TRANSFER
FACILITY
ELECTRICAL SYSTEM

NOTE :

7. ALL LEADS TO THE RIGHT OF ICE BATH
   ARE THERMOCOUPLE WIRE, A-ALUMEL, C-CHROMEL

8. ALL LEADS TO THE LEFT OF ICE BATH
   ARE COPPER WIRE.

△9. TUBE WALL THERMOCOUPLES
    TYPICAL NINE LOCATIONS.

SWITCH POSITIONS :

△1. NORMAL
△2. REVERSE
△3. DIFFERENTIAL
△4. DIRECT
△5. TEST
△6. CALIBRATE

APPENDIX IV

Data Reduction Formulation

### A. Thermocouple Data Conversion

The purpose of this discussion is to deduce from the thermo-couple e.m.f. measurements the temperature differences, caused solely by electrical heating of the tube, between the outer tube wall and the outlet water and between the inlet water and outlet water.

The principal temperature-related data available from each hot test consist of the following: 1) E_o* and E_{11}, the e.m.f.'s of the inlet and outlet water thermocouples respectively, 2) $\Delta_o E_{11}$, the e.m.f. difference between these two thermocouples, 3) $\Delta_x E_{11}$, the e.m.f. difference between each of the wall thermocouples and the outlet-water thermocouple and 4) E_{CE}, E_{EE} and E_F, the thermo-couple e.m.f.'s from locations on the center electrode, the exit electrode and the mixing flange respectively. Applying conversions from standard thermocouple tables to E_o, E_{11}, E_{CE}, E_{EE} and E_F respectively, the temperature differences $(T_{CE}-T_o)$, $(T_{EE}-T_{11})$ and (T_F-T_{11}) can be determined with acceptable accuracy. From the results of the non-heating calibration tests with mismatched electrode temperatures, coefficients are evaluated which, when multiplied by the temperature differences $(T_{CE}-T_o)$, etc., yield the temperature rise in the flowing water due to heat addition or extraction at the respective electrode or flange locations. These coefficients are established for each of the nominal water flow rates. The results of the non-heating calibration tests with matched electrode temper-atures yield the frictional temperature rise of the water (occurring mostly in the mixing flange) as a function of water flow rate, and

*The nomenclature of this appendix follows that of the text except where otherwise noted.

they also yield values for the small temperature loss from the fluid due to a spurious heat loss. The latter was observed to exist only for water bulk temperature at $290°F$. This spurious heat loss also depends on flow rate. A knowledge of the flow rate, the bulk temperature level and the temperature differences $(T_{CE}-T_o)$, etc., for the hot tests then permits calculation of the secondary effects: electrode-heating, frictional-heating, and spurious cooling of the fluid. These effects are expressed in terms of e.m.f. and are subtracted from the respective measured differential e.m.f.'s to yield the e.m.f. differences, $\Delta_x E_{11T}$, which result solely from the electrical tube heating. The computation of $\Delta_x E_{11T}$ was accomplished in the preliminary data reduction operation.

The e.m.f. differences $(\Delta_x E_{11T})$ are converted to temperature differences by a technique which is particularly well suited to machine computation methods. The thermoelectric power, $dE/dT \equiv e$, of the exit-water thermocouple is given from the calibrations as a function of e.m.f. level. It is noted that the immersion thermocouples are not changed when tubes are changed; thus, this $e\{E_{11}\}$ information is applicable to all tubes. The thermoelectric power function for the exit thermocouple is shown in Figure A-IV-1. The isothermal e.m.f. differences between any of the other thermocouples and the outlet-water thermocouple $(\delta_x E_{11})$, as a function of e.m.f. level, is also available from the calibrations for each tube. An example of these functions for the D-3 tube is shown in Figure A-IV-2. The use of $e\{E_{11}\}$ and $\delta_x E_{11}\{E_x\}$ in converting the measured e.m.f. differences to temperature differences is illustrated by the following construction.
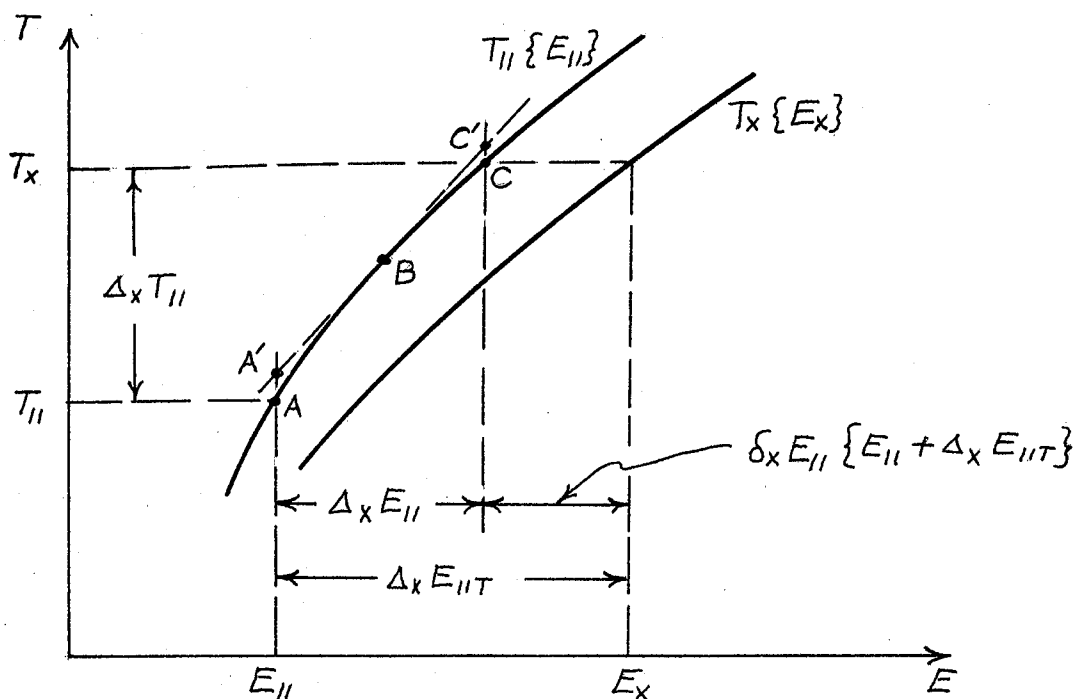
Segments of the respective calibration curves for the outlet-water thermocouple, $T_{11}\{E_{11}\}$, and for one of the other thermocouples, $T_x\{E_x\}$, are shown. The available information includes $\Delta_x E_{11T}$ and E_{11} from the tests and $\delta_x E_{11}\{E_x\}$ and $e\{E_{11}\}$ from the calibrations. The e.m.f. difference between the points A and C on the $T_{11}\{E_{11}\}$ curve is obtained by

$$\Delta_x E_{11} = \Delta_x E_{11T} - \delta_x E_{11}\{E_{11} + \Delta_x E_{11T}\} \qquad \text{(IV-1)}$$

The temperature difference between the points A' and C' is then given by dividing $\Delta_x E_{11}$ by the slope of the $T_{11}\{E_{11}\}$ curve evaluated at the point B midway between A and C. To a high accuracy this also gives the temperature difference, $\Delta_x T_{11}$, between points A and B. Thus the desired formulation for the temperature differences becomes

$$\Delta_x T_{11} = \frac{\Delta_x E_{11}}{e\{E_{11} + \Delta_x E_{11}/2\}} \qquad \text{(IV-2)}$$

where $\Delta_x E_{11}$ is given by equation IV-1.

Finally, the temperature level of the inlet fluid, required only for fluid property evaluations, is determined with sufficient accuracy by a straight line approximation of the $T_o\{E_o\}$ function. The best fit for the temperature range 70 to 300^oF is derived from the calibrations as

$$T_o(^oF) = 35 + \frac{E_o(mv)}{0.0232} \tag{IV-3}$$

Similarly a satisfactory approximation for any of the outer wall temperatures is obtained from

$$T_x(^oF) = 35 + \frac{E_x(mv)}{0.0228} \tag{IV-4}$$

B. Tube-Wall Temperature Drop

The temperature drop in the wall ΔT_w is computed from a knowledge of the local heat flux ($\dot{q}$), the thermal conductivity of the wall (k), and the wall thickness (t). A modification of an expression presented in Reference 47* is used to compute ΔT_w. This derivation applies strictly only to the case of smooth, cylindrical tubes having electric current passing axially through the walls and having all heat removal occurring at the inside surface. The original derivation allows for a linear temperature variation of both electrical resistivity (ρ_e) and thermal conductivity (k), and it retains lower order terms, modified herein to suit the present needs, in series expansions for t/R, $\alpha\Delta T'_{wp}$ and $\beta\Delta T'_{wp}$ where

$$\Delta T'_{wp} \equiv \frac{(dE/dx)^2 t^2}{2\,\rho_{eow}k_{ow}} \tag{IV-5}$$

*Reference numbers in this appendix refer to the reference list in the text.

where α and β are defined in

$$k\{T\} = k_{ow} [1 + \alpha (T-T_{ow})] \tag{IV-6}$$

and

$$\rho_e\{T\} = \rho_{eow}[1 + \beta (T-T_{ow})] \tag{IV-7}$$

and where (dE/dx) is the axial voltage gradient in the tube and the subscript "ow" refers to the temperature of the outer wall. Retaining only the first order correction terms and using the present re-defined terms, the relation from Reference 47 can be written

$$\Delta T_w = \Delta T'_{wp}[1 + \frac{1}{3}(t/R) + \dots$$

$$+ (\frac{\beta}{6} + \frac{\alpha}{2}) \Delta T'_{wp} + \dots] \tag{IV-8}$$

To convert equation IV-8 into the form desired for reducing data wherein voltage gradient does not appear explicitly, a substitute for $\Delta T'_{wp}$ was developed as follows: From an energy balance,

$$2\pi R \dot{q}_o = (dE/dx) I \tag{IV-9}$$

where $\dot{q}_o$ is the heat flux at the inner surface of the tube and I is the current. Using Ohm's law together with the fact that the applied voltage gradient is assumed to be independent of radius,

$$I = dE/dR_e = (dE/dx) \int_R^{R_{ow}} \frac{2\pi r dr}{\rho_e\{T\{r\}\}} \tag{IV-10}$$

where R_e is electrical resistance, R is the inner wall radius of the tube, R_{ow} is the outer wall radius, and "r" is the variable radius. Combining equations IV-9 and 10,

$$\Delta T'_{wp} = \frac{\dot{q}_o t}{2 k_{ow}} \left[\frac{R t}{\rho_{eow} \int_R^{R_{ow}} \frac{r \, dr}{\rho_e \{T\{r\}\}}} \right] \qquad (IV-11)$$

The term $\rho_e \{T\{r\}\}$ is evaluated by using equation IV-7 and the first order wall temperature variation,

$$T\{r\} = T_{ow} - \frac{\dot{q}_o t}{2 k_{ow}} \left(\frac{R_{ow} - r}{t}\right)^2 \qquad (IV-12)$$

Performing the integration in equation IV-11, expanding the result and retaining only first order corrective terms; there results

$$\Delta T'_{wp} = \Delta T_{wp} \left[1 - \frac{1}{2} (t/R) + \ldots - \frac{1}{3} \beta \Delta T_{wp} + \ldots \right] \qquad (IV-13)$$

where

$$\Delta T_{wp} \equiv \frac{\dot{q}_o t}{2 k_{ow}} \qquad (IV-14)$$

Finally, substituting equation IV-13 into equation IV-8, the desired result is obtained:

$$\Delta T_w = \Delta T_{wp} [1 - \frac{1}{6} (t/R) + \ldots$$

$$+ (\frac{\alpha}{2} - \frac{\beta}{6}) \Delta T_{wp} + \ldots] \qquad (IV-15)$$

where the primary term, ΔT_{wp}, depends on T_{ow} and $\dot{q}_o$ both of which are available from the data reduction in the present experiments.

The two correction terms for ΔT_w, displayed in equation IV-15, are small (each is on the order of 1 percent) for the conditions of the present tests. It is noted that a similar expression is developed in Reference 48 in which only the geometrical correction term,

$(1/6)(t/R)$, is included. While the correction terms may not signifi-
cantly affect the experimental heat transfer coefficients in many
cases, the inclusion of one of these terms at the exclusion of the
other is quite meaningless. At high heat flux values, such as in
nucleate boiling experiments, the second correction term, which ad-
justs for radial variations in the material properties, may become
of paramount importance.

C. Computer Program Formulation

   The machine computations were performed on a digital com-
puter* for which a standard program was prepared and used in
reducing the data from all tubes. The following data, available
from the preliminary reduction for each test, were read into the
machine:

1. ΔP_{TS} - measured test section pressure drop, gage
   uncorrected.

2. ΔP_v - metering venturi pressure drop, gage corrected.

3. W_P - power input at the tube probes; in cases where
   W_{TS} was measured, the measured value was
   converted to the equivalent W_P.

4. E_o - e.m.f. from inlet-water thermocouple.

5. E_{11} - e.m.f. from outlet-water thermocouple.

6. $\Delta_o E_{11T}$ - differential e.m.f. between inlet-water and
   outlet-water thermocouples, corrected for heat
   gains or losses not due to electrical heating.

7. $\Delta_x E_{11T}$, $x=1$ to 9 - differential e.m.f. between tube-wall
   and outlet-water thermocouples, corrected as
   in item 6.

8. E_{TS} - test section r.m.s. voltage drop.

9. I - test section r.m.s. current.

*Datatron 205

The machine's "memory" was provided with the following function tables from which interpolations were automatically computed:

1. $\dot{w}'\{\Delta P_v\}$ - initial rough estimate of flow rate for use in item 4.

2. $\mu\{T\}$ - fluid viscosity.

3. $\rho\{T\}$ - fluid density.

4. $K\{\dot{w}/\mu\}$ - dimensional, square of the venturi discharge coefficient (Cf. Fig. 11 of the text).

5. $\delta_x E_{11}\{E_x\}$, $x = 0$ to 9 - isothermal e.m.f. difference between the inlet-water thermocouple and the outlet-water thermocouple and between each of the tube-wall thermocouples and the outlet-water thermocouple.

6. $e\{E_{11}\}$ - thermoelectric power of the outlet-water thermocouple.

7. $c_p\{T\}$ - fluid specific heat.

8. $Pr\{T\}$ - fluid Prandtl number.

The tabulation of item 5 above for the tube-wall thermocouples was different for each tube; the other items formed a permanent part of the program.

The sequence of operations performed by the machine are given in the list appearing subsequent to the following explanatory notes. The intention here is to display only the functional forms employed; consequently, the various dimensional coefficients are represented only as K's. These K's were also stored in the machine's "memory" as part of the computer program. A numerical subscript on a given K implies that that coefficient is changed from tube to tube; whereas a numerical superscript implies that the coefficient to which it is attached is a permanent part of the program. The subscript "x" attending any of the computed quantities refers, for $x = 0$, to the inlet-water condition or, for $x > 0$, to one of the wall thermocouple

locations--

    1,2,3 at the first thermocouple station

    4,5,6 at the second thermocouple station and

    7,8,9 at the last thermocouple station.

The appearance of the ''x'' subscript means that that particular computation must be repeated for each value of the subscript. A similar meaning is ascribed to the subscript ''y'' except that in this case the computation need only be repeated for one of the thermocouple locations at each of the three, wall thermocouple stations. The subscript ''y'' takes the values 1 for the first thermocouple station, 4 for the second station and 7 for the final station. If one of the dimensional coefficients (K) is followed by a subscript ''x'' or ''y'', it means that there is a different value for that coefficient for each value of the subscript. The appearance of a functional expression, e.g., $\mu_o \{T_o\}$, in the machine operations list means that the operation is to determine the dependent variable, given the independent variable, using the appropriate stored tabulation. Further explanatory notes will be attached to the individual items. The sequence of machine operations is:

1. $T_o = K^{(1)} + K^{(2)} E_o$

See Eq. IV-3.

2. $\mu_o \{T_o\}$

3. $\dot{w}' \{\Delta P_v\}$

4. $K\{\dot{w}'/\mu\}$

See the definition of K in Figure 11 of the text.

5. $\rho_o\{T_o\}$

6. $\dot{w}^2 = 10^{-5} \rho_o \Delta P_v K$

7. $\dot{w} = (\dot{w}^2)^{1/2}$

8. $\delta_x E_{11} \{E_{11} + \Delta_x E_{11T}\}$

Refer to Appendix IV-A for a discussion of the thermocouple data reduction performed in items 8, 9, 10, 11 and 25 herein.

9. $\Delta_x E_{11} = \Delta_x E_{11T} - \delta_x E_{11}$

10. $e_x \{E_{11} + \Delta_x E_{11}/2\}$

11. $\Delta T_c = - \Delta_o E_{11}/e_o$

12. $T_{Lav} = T_o + \Delta T_c/2$

13. $\rho_{av} \{T_{Lav}\}$

14. $C_F = K_3 [\dfrac{\rho_{av} \Delta P_{TS}}{\dot{w}^2} - K_4]$

Refer to Sec. III-D-3 in the text. Computation 14 is also performed on data from the non-heating calibration tests to obtain isothermal C_F values.

15. $T_y = K^{(1)} + K^{(5)} [E_{11} + \Delta_y E_{11}]$

where T_y is the outside tube wall temperature at each of the three thermocouple stations. See Appendix IV-A.

16. $B_y = \Delta T_c /(K^{(6)} + T_y)$

This is an approximation for the dimensionless group defined by equation 76 in the text.

17. $W_{TS} = K_7 W_P (1 + K_8 B_7)$

The correction term $K_8 B_7$ accounts for the longitudinal temperature gradient in the tube wall as discussed in Sec. III-D-3 of the text.

18. $C_{pav} \{T_{Lav}\}$

19. $W_{TSC} = c_{pav} \Delta T_c \dot{w}$

where W_{TSC} is the calorimetrically measured rate of heat addition to the fluid.

20. $\% \delta W_{TSC} = 100 (W_{TSC} - W_{TS})/W_{TS}$

21. $W_{TSE} = K^{(9)} E_{TS} I$

where W_{TSE} is the heating power measured by ammeter and voltmeter.

22. $\%\delta\ W_{TSE} = 100\ (W_{TSE} - W_{TS})/W_{TS}$

23. $\dot{q}_{oy} = K_{10y}\ W_{TS}\ (1 + K_{11y}B_y)$

This expression is derived by evaluating the coefficients in equation 72 of the text.

24. $\Delta T_{wy} = K_{11}\ \dot{q}_{oy}t_y\ [1 + K^{(12)}T_y][1 - K^{(13)}\dot{q}_{oy}]$

This expression follows from the development in Appendix IV-B. The first bracketed term on the right accounts for the variation of thermal conductivity of the wall with temperature. The correction term $[1-(1/6)(t/R)]$ in equation IV-15 is absorbed here in K_{11} while $[1-K^{(13)}\dot{q}_{oy}]$ represents the other correction term in equation IV-15.

25. $\Delta T_{fx} = (\Delta_x E_{11}/e_x) + K_{14x}\ [1 - K_{15\,y}B_y + K_{16\,y}\ B_y^{\ 2}] - \Delta T_{wy}$

This expression follows from the discussion leading to equation 81 in Sec. III-D-3 of the text. The second term on the right of the above equation is the bulk temperature rise in the fluid between the tube-wall thermocouple station and the exit.

26. $T_{Ly} = T_o + K_{17\,y}\ \Delta T_c$

This is a first order approximation for the local bulk fluid temperature.

27. $c_{py}\ \{T_{Ly}\}$

28. $C_{Hx} = K_{18}\ \dot{q}_{oy}/\dot{w}\ c_{py}\ \Delta T_{fx}$

29. $\overline{C}_{Hy} = \dfrac{1}{3}\ \displaystyle\sum_{x \neq y}^{x=(y+2)}\ C_{Hx}$

This is the mean Stanton number for each thermocouple station.

30. $\mu_y\ \{T_{Ly}\}$

31. $Re_y = K_{19}\ \dot{w}/\mu_y$

32. $Pr_y\ \{T_{Ly}\}$

That part of the computer read-out which was used in the final phase of the data reduction consists of the following quantities:

$\dot{w}$, ΔT_c, $\%\delta W_{TSC}$, $\%\delta W_{TSE}$, ΔT_{w7}, T_{Ly}, ΔT_{fy}, C_{Hx}, $\overline{C}_{Hy}$, Re_y and Pr_y

where the subscripts x and y have the same meanings provided for

them in the preceding discussion.

As a check on the computer program, a complete and independent hand calculation was performed for one test on each of the four tubes.
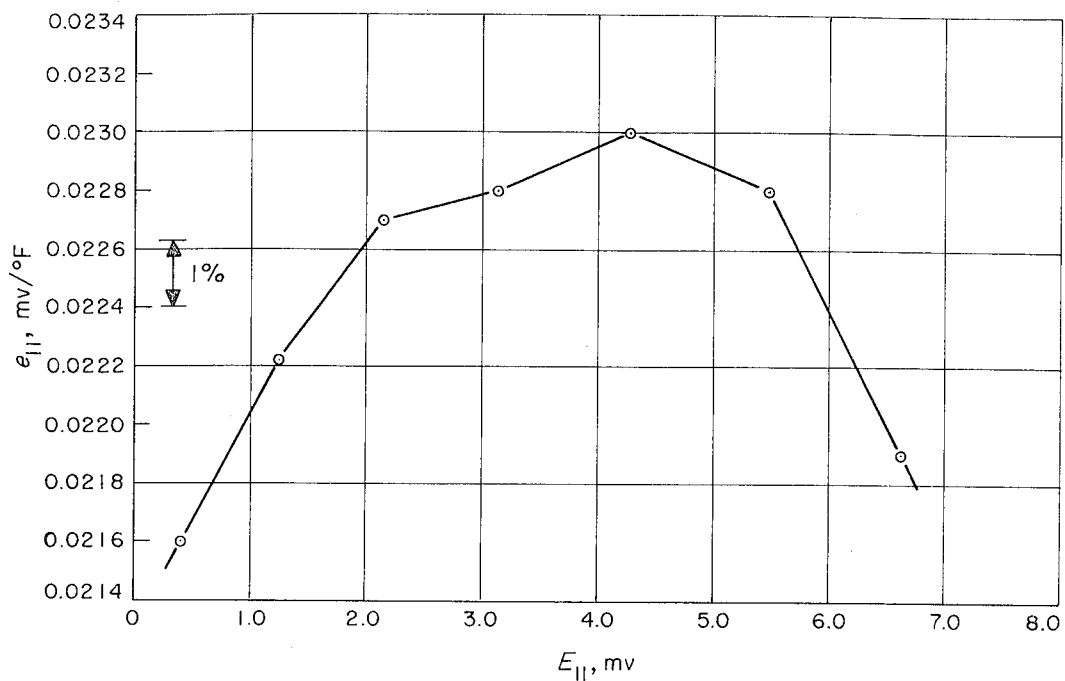
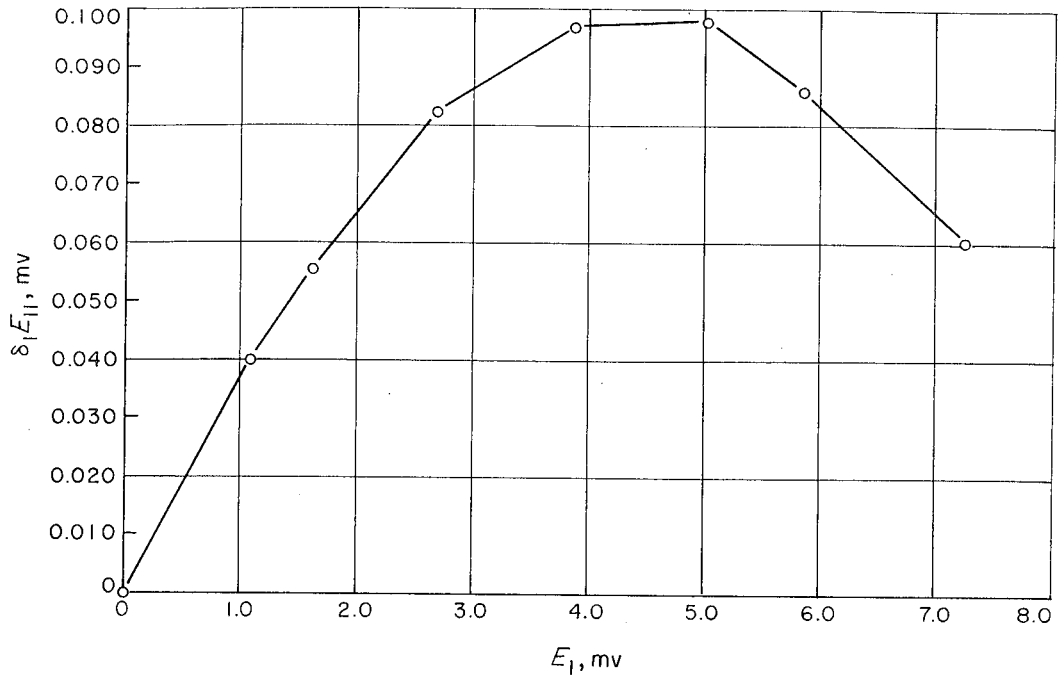FIG. A-IV-I. OUTLET-WATER THERMOCOUPLE
THERMOELECTRIC POWER

FIG. A-IV-2. ISOTHERMAL e.m.f. DIFFERENCE BETWEEN A
TUBE-WALL THERMOCOUPLE AND THE OUTLET-WATER
THERMOCOUPLE

APPENDIX V

End Conduction Effects for Experimental Tubes

In order to provide a simple model for determining the first order effects of thermal conduction along the tube wall, the following assumptions will be incorporated:

i) The copper electrode blocks at either end of the heated test section are maintained at a temperature equal to the fluid bulk temperature, T_L*. This condition was approximated in the experiments by means of controlled electrode heaters (Cf. Sec. III-C of the text and Appendix III).

ii) The fluid flow rate is considered to be high enough that the axial temperature gradient in the bulk fluid has a negligible effect on the problem at hand. Thus T_L is assumed constant.

iii) The heat transfer coefficient (C_H), and hence the heat transfer film conductance (h), is constant throughout the test section. This means that the thermal entrance effect near the upstream electrode is neglected.

iv) The slight increase in heat-generation-per-unit-length $(d\dot{Q}/dx)$ in the direction of flow due to increase in temperature, and hence in the resistivity of the tube, is neglected, i.e., $(d\dot{Q}/dx)$ is assumed constant.

A heat balance for a longitudinal segment of the tube is stated: Heat generated in the tube wall equals the net axial conduction plus the radial convection to the fluid, or symbolically,

---

*The nomenclature of the text is used in this appendix except where otherwise noted.

$$\frac{d\dot{Q}}{dx} \, \Delta x = \pi \, Dtk \left[\frac{dT}{dx} \, \{x\} - \frac{dT}{dx} \, \{x + \Delta x\} \right]$$

$$+ \, \pi D \Delta x h \left[\, T \left\{ x + \frac{\Delta x}{2} \right\} - T_L \right] \tag{V-1}$$

where $T\{x\}$ refers to the local inside wall temperature and T_L is the fluid bulk temperature. Writing equation V-1 in infinitesimal form and rearranging terms,

$$\frac{d^2T}{dx^2} - \left(\frac{h}{k\,t} \right) \left(T\{x\} - \frac{d\dot{Q}/dx}{\pi Dh} - T_L \right) = 0 \tag{V-2}$$

Letting

$$\alpha \equiv h/kt \tag{V-3}$$

and

$$\theta\{x\} \equiv T\{x\} - \frac{d\dot{Q}/dx}{\pi Dh} - T_L \tag{V-4}$$

reduces equation V-2 to

$$\frac{d^2\theta}{dx^2} - \alpha\theta = 0 \tag{V-5}$$

It is assumed, and later established, that the tube is essentially infinite in length for this problem. The boundary conditions thus become:

$$T = T_L, \; x = 0$$

and

$$dT/dx = 0, \; x = \infty$$

or, written in terms of equation V-4,

$$\theta = - \frac{d\dot{Q}/dx}{\pi Dh}, \; x = 0 \tag{V-6}$$

and

$$d\theta/dx = 0, \ x = \infty \tag{V-7}$$

The general solution to equation V-5 is

$$\theta = M \exp\left\{-\sqrt{\alpha}\,x\right\} + N \exp\left\{\sqrt{\alpha}\,x\right\} \tag{V-8}$$

Using the conditions V-6 and V-7 to evaluate the arbitrary constants M and N in equation V-8 and reverting to the original variables, one obtains

$$T\{x\} = T_L + \frac{(d\dot{Q}/dx)}{\pi Dh}\left[1 - \exp\left\{-\sqrt{h/kt}\,x\right\}\right] \tag{V-9}$$

The equation V-9 result is first used to determine the distance from either of the electrode blocks beyond which the presence of the blocks has an inconsequential effect on the C_H determination. The Stanton number determined from the wall temperature measurements in the present experiments is written

$$C_{Hm} \equiv \frac{(d\dot{Q}/dx)/\pi D}{\rho\, u_m\, c_p\, (T - T_L)} \tag{V-10}$$

and the true C_H sought is written

$$C_H \equiv \frac{h}{\rho\, u_m\, c_p} \tag{V-11}$$

Using the definitions V-10 and 11 with the result from equation V-9, one can write for large values of the exponential argument

$$\frac{C_H - C_{Hm}}{C_H} \cong -\exp\left\{-\sqrt{h/kt}\,x\right\} \tag{V-12}$$

From this expression it can be shown that the percentage error in C_{Hm} due to end-conduction effects will be less than one percent if

$$x\,(h/kt)^{1/2} \geqslant 5.0$$

This criterion can be rewritten

$$x \geqslant 5 \left(\frac{\pi \, kt \, D^2}{4 \, C_H \, c_p \dot{w}}\right)^{1/2} \tag{V-13}$$

wherein the identity V-11 has been used to eliminate "h", and the mass continuity equation,

$$\dot{w} = (\pi/4) \, D^2 \, \rho \, u_m \tag{V-14}$$

has been employed. For the present experiments, the term on the right in expression V-13 is a maximum for the lowest flow rate ($\dot{w}$) and for the smooth tube operating at low fluid bulk temperature to give minimum C_H. Using the criterion of expression V-13, it is thus found that, if the distance from the nearest electrode is greater than 0.38 inches, the error in the C_{Hm} determination due to end conduction is less than one percent. At the location of the wall thermocouples placed closest to the electrodes, approximately 2.0 inches, this error is thus computed to be completely negligible.

The equation V-9 result is next used to estimate the net heat conducted to the electrodes along the tube walls. The heat conducted to the electrodes due to the electrodes being at a temperature other than the liquid bulk temperature (T_L) is supposedly compensated in the data reduction procedure for the hot tests. However that heat is not compensated which is conducted to the electrodes when the electrodes are held at T_L and the tube is electrically heated. This net electrode heat conduction represents a potential source of discrepancy between the heat rate received by the flowing water and the electrical power supplied to the system. Differentiating equation V-9 and evaluating (dT/dx) at the electrode, $x = 0$, there is obtained

$$(dT/dx)\{0\} = (h/kt)^{1/2} \; \frac{d\dot{Q}/dx}{\pi \, Dh} \tag{V-15}$$

Then it is noted that

$$\dot{Q}_E = \pi D t\, k\, (dT/dx)\, \{0\} \tag{V-16}$$

where $\dot{Q}_E$ is the heat conducted to the electrode. Also,

$$\dot{Q} = (d\dot{Q}/dx)\, L \tag{V-17}$$

where $\dot{Q}$ is the total energy delivered to the tube. Using equations V-15 and 17 with equation V-16 and making the same parameter substitutions used in expression V-13, the result is obtained,

$$\frac{2\dot{Q}_E}{\dot{Q}} = \frac{2}{L}\left(\frac{\pi k t D^2}{4\, C_H c_p \dot{w}}\right)^{1/2} \tag{V-18}$$

where the factor 2 is applied to account for the heat loss to both electrodes. Using the same maximum parameters on the right hand side of equation V-18 as were used in evaluating expression V-13, the portion of the total heat supplied to the tube that is lost to the electrodes is computed as 0.8 percent for the most adverse test conditions. For the majority of the test conditions investigated in the present work, the computed power discrepancy is much less than this maximum value.

APPENDIX VI

Effects of Errors in the Calorimetric Power Determination

To an acceptably good approximation, the data reduction equation (Cf. Eq. 80 of the text) used to obtain the heat transfer coefficient can be expressed by

$$C_H = \frac{D \, W_{TS}}{4L \, \dot{w} \, c_p \, \Delta T_f} \qquad * \qquad \text{(VI-1)}$$

where W_{TS} is the total heating power generated in the tube and where

$$\Delta T_f \cong (T_x - T_{11}) + (1 - \frac{x}{L}) \Delta T_c - \Delta T_w \qquad \text{(VI-2)}$$

Since W_{TS} is measured electrically, errors in the calorimetric power measurement affect C_H through ΔT_f only, and one can write

$$\% \, \delta C_H = -\% \delta \, \Delta T_f \qquad \text{(VI-3)}$$

where δ is taken here to infer the computed value minus the correct value. It is now assumed that a small heat loss rate, not apparent in the non-heating calibration tests, occurs in the hot tests leading to a shortage in the measured calorimetric power. Two cases are of interest.

Case I: Consider the existence of an anomalous heat loss between the wall thermocouple station and the exit as illustrated by the diagram in Figure A-VI-1-a. It is assumed that the exit bulk temperature without the heat loss would be T_{11}' as determined from the known electrical power added to the fluid. Thus,

$$(T_{11}' - T_o) = W_{TS}/\dot{w} c_p \qquad \text{(VI-4)}$$

*The nomenclature used in the text will be followed in this appendix unless otherwise noted.

The calorimetric power is defined by

$$(T_{11}-T_o) \, \dot{w} \, c_p \equiv \Delta T_c \, \dot{w} \, c_p \equiv W_{TSC} \tag{VI-5}$$

Equations VI-4 and 5 can be combined to give

$$\frac{T'_{11}-T_{11}}{\Delta T_c} = \frac{W_{TS}-W_{TSC}}{W_{TSC}} \tag{VI-6}$$

Referring again to the definitions in Figure A-VI-1-a and to equation VI-2,

$$\Delta T_f' = (T_x-T_{11}) + (1 - \frac{x}{L})(T_{11}-T_o) - \Delta T_w \tag{VI-7}$$

and

$$\Delta T_f = (T_x-T'_{11}) + (1 - \frac{x}{L})(T'_{11} - T_o) - \Delta T_w \tag{VI-8}$$

Subtracting equation VI-8 from VI-7 and dividing by ΔT_f gives

$$\% \, \delta\Delta T_f \equiv (100) \frac{\Delta T_f'-\Delta T_f}{\Delta T_f} = (100) \frac{x}{L} \frac{(T'_{11}-T_{11})}{\Delta T_f} \tag{VI-9}$$

or

$$\% \, \delta\Delta T_f = (100) \frac{x}{L} \frac{(T'_{11}-T_{11})}{\Delta T_c} \frac{\Delta T_c}{\Delta T_f} \tag{VI-10}$$

From equations VI-1 and 5,

$$\frac{\Delta T_c}{\Delta T_f} = 4 \frac{L}{D} C_H \frac{W_{TSC}}{W_{TS}} \tag{VI-11}$$

Then combining equations VI-3, 10, 6 and 11, the result is obtained:

$$\% \, \delta C_{HI} = - (400) \frac{x}{D} C_H (\frac{W_{TS}-W_{TSC}}{W_{TS}}) \tag{VI-12}$$

where the subscript I refers to Case I.

Clearly, if the exit thermocouple indicates too low a value for bulk

temperature due to poor mixing of the fluid, equation VI-12 would still yield the C_H error.

Case II: Assume next that an anomalous heat loss occurs between the entrance and the wall thermocouple station. This case is portrayed in Figure A-VI-1-b. Equations VI-1 through 7 and VI-11 are still applicable, but the equation for the correct ΔT_f becomes

$$\Delta T_f = (T_x - T_{11}) + (1 - \frac{x}{L})(T'_{11} - T_o) - \Delta T_w \qquad (VI-13)$$

Then subtracting equation VI-13 from VI-7 and dividing by ΔT_f gives

$$\% \delta \Delta T_f \equiv (100) \frac{\Delta T'_f - \Delta T_f}{\Delta T_f} = -(100)(1 - \frac{x}{L}) \frac{(T'_{11} - T_{11})}{\Delta T_f} \qquad (VI-14)$$

or

$$\% \delta \Delta T_f = -(100)(1 - \frac{x}{L}) \frac{(T'_{11} - T_{11})}{\Delta T_c} \frac{\Delta T_c}{\Delta T_f} \qquad (VI-15)$$

Then, combining equations VI-3, 15, 6 and 11 gives the result for Case II:

$$\% \delta C_{HII} = (400) \frac{(L-x)}{D} C_H (\frac{W_{TS} - W_{TSC}}{W_{TS}}) \qquad (VI-16)$$

As a numerical example of the application of equations VI-12 and 16, the heat transfer test yielding the highest computed error will be considered. For the rough tubes the calorimetric power discrepancy, $(W_{TS} - W_{TSC})/W_{TS}$, was computed to be approximately $+0.03$. The highest C_H value occurs for tube A-4 at the lowest flow rate (0.2 lb/sec) and the highest fluid temperature ($290°F$). For this condition,

$$C_H \tilde{=} 5 \times 10^{-3}$$

For tube A-4,

$$D \cong 0.40 \text{ in.}$$

$$L \cong 17.4 \text{ in.}$$

and the downstream wall thermocouple station is located at

$$x \cong 15.0 \text{ in.}$$

Then if the heat loss occurs at a point downstream of the wall thermocouple station, Case I (Eq. VI-12) applies so that

$$\% \delta \ C_{HI} \cong -(400) \frac{15.0}{0.40} \ 5 \times 10^{-3} \ (0.03)$$

$$\% \delta \ C_{HI} = -2.25\% \tag{VI-17}$$

If the observed heat loss occurs upstream of the wall thermocouple station, Case II (Eq. VI-16) applies so that

$$\% \delta \ C_{HII} \cong (400) \frac{(17.4-15)}{0.40} \ 5 \times 10^{-3} \ (0.03)$$

$$\% \delta \ C_{HII} \cong +0.36\% \tag{VI-18}$$

Thus the maximum error in the C_H determination due to the observed calorimetric power discrepancy is -2.25% or +0.36% depending where the heat loss or temperature measurement error occurs. For most cases, this error is somewhat less than these maximum values since the C_H values are lower than 5×10^{-3}.
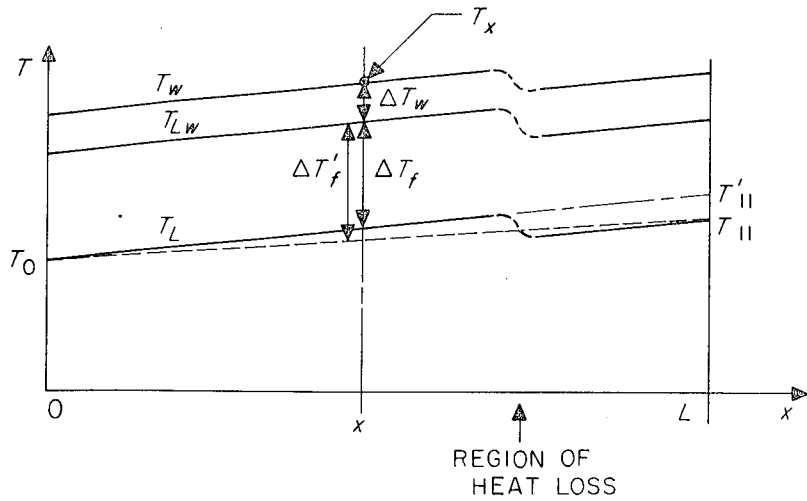
a. ANOMALOUS HEAT LOSS BETWEEN THERMOCOUPLE
STATION AND EXIT
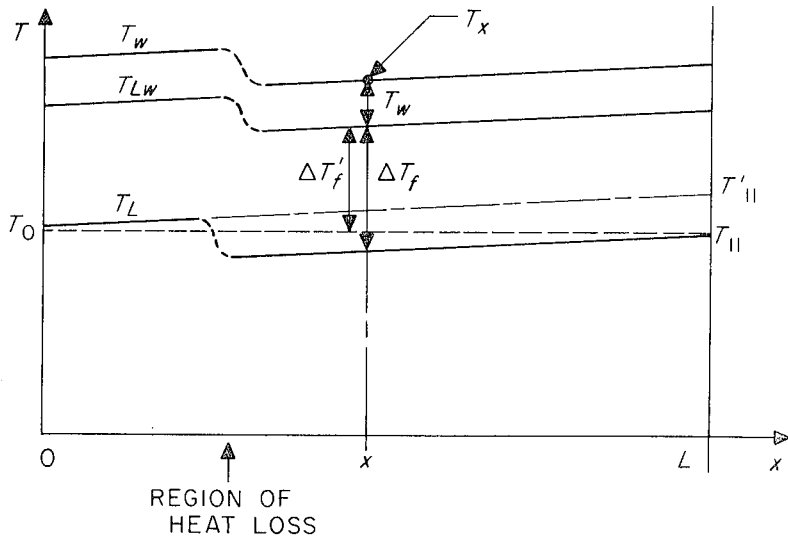
b. ANOMALOUS HEAT LOSS BETWEEN ENTRANCE
AND THERMOCOUPLE STATION

FIG. A-$\overline{\text{VI}}$-I. SCHEME OF LONGITUDINAL TEMPERATURE
PROFILES WITH ANOMALOUS HEAT LOSS

APPENDIX VII

A Turbulent Vortex Model for the Cavity Heat Transfer

It was shown in Section II of the text that, for pipes having geometrically similar roughness elements and operating in the fully rough region, the heat transfer similarity law can be written

$$\left[\frac{(C_F/2C_H)-1}{\sqrt{C_F/2}} + A\right]_{F.R.} \equiv g_{F.R.} = \frac{1}{AC_{Hc}\{A\epsilon*, Pr\}} \qquad (VII-1)$$

In this equation, "A" is the fully rough friction similarity parameter which is equal to 8.48 for the hydraulic equivalent sand-grain roughness ratio used to describe the tubes of the present experiments. The term C_{Hc} is the so-called cavity Stanton number having the pertinent Reynolds number $A\epsilon*$. The exact meaning of the term C_{Hc} will be defined presently.

From equation VII-1, it is seen that an understanding of the dependence of the cavity Stanton number on the pertinent Reynolds number and Prandtl number will lead directly to an understanding of the complete C_H, Re, Pr, ϵ/D dependence for rough pipes in fully rough operation. A possible model for the cavity flow, to be examined in this appendix, will be referred to as the turbulent vortex hypothesis. To the extent that it correctly describes the cavity flow conditions, it should be useful in guiding future theoretical and experimental investigations leading to a description of the cavity heat transfer relations.

Following the discussion in Section II of the text by which equation VII-1 was developed, the mean flow is imagined to be divided into an "external flow" and a "cavity flow" by a cylinder passing through the tips of the roughness elements. The mean axial velocity

of the flow at the interface cylinder is deduced in the discussion

leading to equation 56 of the text. The result is

$$u_g \approx \sqrt{\tau_o/\rho} \; A \equiv u_\tau A \qquad\qquad \text{(VII-2)}$$

where ''A'' is again the similarity constant for the given roughness

geometry, u_g* is the temporal and spatial mean axial velocity at

the interface, and τ_o is the temporal and spatial mean shear stress

at the interface. A temporal mean cavity flow pattern is then as-

sumed to exist which conforms to the cavity wall profile with a finite

number of stagnation points. Several examples of visualized flow

patterns over two-dimensional elements are given by Wieghardt

(Ref. 40)**. For purposes of discussion, a sketch of an assumed

cavity flow pattern is presented in Figure A-VII-1. The interface

is assumed to be located just far enough from the element tips so

that it is outside of the laminar flow boundary layer induced by any

exposed wall segments.

For the fully rough conditions being assumed in this discus-

sion, the friction coefficient of the pipe is independent of Re. Thus

the surface shear stress (τ_o) is independent of viscosity, and it is

assumed that the integrated axial component of the pressure forces

on the cavity walls due to the dynamics of the cavity flow is

very much greater than the effect of the viscosity-dependent shear

stresses at the cavity walls. Roshko (Ref. 33) demonstrated,

by direct measurement, the validity of this assumption for the case

of single, two-dimensional, rectangular cavities. It is also assumed

from the independence of τ_o from viscosity that the entire mean flow

*The nomenclature of the text will be used in this appendix except
where otherwise noted.
**Reference numbers in this appendix refer to the list of references
in the text.

pattern of the cavity is independent of viscosity. It follows that, if

the depth of the cavity (ϵ) is used as a scaling factor to define a loca-

tion in the cavity, the ratio of any local mean velocity in the cavity

to the mean external velocity (u_g) is fixed with respect to the pipe

Reynolds number and the roughness ratio (ϵ/D). The fact that the

vortices may be unstable and change form intermittently is assumed

not to affect the present reasoning since the temporal mean flow is

being discussed, and such time dependent variations are considered

as being a part of the turbulence. Thus, one can write

$$\frac{\vec{u}_v}{u_g} = f_1 \left\{ \frac{\vec{r}}{\epsilon} \right\} \tag{VII-3}$$

where $\vec{u}_v$ is the mean velocity at any arbitrary point in the cavity

given by the locating vector $\vec{r}$.

A high degree of turbulence must exist in the neighborhood

of the interface in order to transmit the large net pressure forces

on the cavities to the main flow via the turbulent shear stresses (τ_o).

From this it is inferred that the entire cavity flow carries a high

turbulence level which is damped out to form laminar boundary layers

only in the immediate vicinity of the walls.

If equation VII-3 is to hold true throughout the cavity, those

turbulent components which are effective in transferring momentum

between adjacent parts of the cavity flow must also be independent

of the pipe Reynolds number and of pipe diameter. Thus,

$$\frac{\overline{u'_i u'_j}}{u_g^2} = f_{ij} \left\{ \frac{\vec{r}}{\epsilon} \right\} \tag{VII-4}$$

where ($\rho \overline{u'_i u'_j}$) is any of the components of the turbulent shear stress

tensor. In addition, a comparison of equations VII-3 and 4 implies

that the ratio of any of the local mean turbulent velocity terms to the local mean translational velocity squared is a function only of position in the cavity.

The way in which this turbulent vortex model of the cavity flow can be used to develop relationships for the cavity heat transfer will now be considered. A segment of the wall between any two stagnation points is assumed to form a boundary layer out of a turbulent external flow. This boundary layer of laminar and partially damped turbulent flow is assumed to constitute essentially the entire thermal resistance of the cavity. The heat transmitted through the thin boundary is thought to be convected freely around the cavity flow vortex or vortices to the interface region. Thus even though the local boundary layers have a negligible effect on the main cavity flow, they are of principal importance in determining the cavity heat transfer. The assumed heat transfer conditions are analogous to those near a stagnation point on a surface placed in a turbulent free stream.

It will be assumed for the discussion that follows that the dependence of the pertinent cavity Stanton number on a Reynolds number, based on distance from the stagnation point, and on Prandtl number can be represented by a simple power law relation. Thus the local Stanton number for one of the wall segments between a pair of stagnation points is written

$$C_{Hvi} = K_{li} \, (Re_{vLi})^{-p} \, (Pr)^{-m} \qquad\qquad (VII-5)$$

where the subscript "i" refers to one of "n" segments of the wall and the exponents "p" and "m" are empirical. All K's used in this discussion refer to dimensionless constants for a given type of pipe

roughness. The new terms in equation VII-5 are:

$$C_{Hvi} \equiv \frac{\dot{Q}_{vi}/A_{vi}}{\rho\, u_{vi}\, c_p\, (T_w - T_{vi})} \qquad\qquad \text{(VII-6)}$$

and

$$Re_{vLi} \equiv \frac{L_{vi} u_{vi}}{\nu} \qquad\qquad \text{(VII-7)}$$

where $\dot{Q}_{vi}$ is the mean heat transfer rate through the wall segment

area A_{vi}; L_{vi} is the length of the segment along the streamline; u_{vi}

and T_{vi} are respectively the local mean velocity and temperature

external to the boundary layer; and T_w is the cavity wall temperature,

assumed to be the same for all segments. From the preceding dis-

cussion, the fluid temperature drop between the region just outside

of the boundary layer and the cavity interface region is assumed to

be negligible; hence,

$$T_{vi} = T_g \qquad\qquad \text{(VII-8)}$$

where T_g is defined as the average temperature at the interface.

From the assumed similarity for the cavity flow given by equation

VII-3,

$$L_{vi} = K_{2i}\epsilon \qquad\qquad \text{(VII-9)}$$

$$A_{vi} = K_{3i} A_c \qquad\qquad \text{(VII-10)}$$

and

$$u_{vi} = K_{4i} u_g \qquad\qquad \text{(VII-11)}$$

where A_c is the projected area of each element of the roughness on

the interface. Further,

$$\sum_{i=1}^{n} \dot{Q}_{vi} = \dot{Q}_{c} \tag{VII-12}$$

where $\dot{Q}_{c}$ is the total heat transferred from a given element. Then using equations VII-9 and 11 in expanding the definition given in equation VII-7,

$$Re_{vLi} = K_{2i} K_{4i} \frac{\epsilon u_{g}}{\nu} \tag{VII-13}$$

and, since $\epsilon^* \equiv \epsilon u_{\tau}/\nu$, equation VII-2 substituted into equation VII-13 gives

$$Re_{vLi} = K_{2i} K_{4i} A\epsilon^* \tag{VII-14}$$

Next, substituting equations VII-8, 10 and 11 in the definition VII-6 gives

$$C_{Hvi} = \frac{\dot{Q}_{vi}}{K_{3i} K_{4i} A_{c} \rho c_{p} u_{g} (T_{w} - T_{g})} \tag{VII-15}$$

The cavity Stanton number (C_{Hc}) is defined in Section II of the text for use in equation VII-1. This C_{Hc} is based on the total heat flow from the roughness element ($\dot{Q}_{c}$), the projected area of the element on the cylindrical interface (A_{c}), the average axial velocity at the interface (u_{g}) and the difference between the wall temperature and the average fluid temperature at the interface ($T_{w} - T_{g}$). Thus,

$$C_{Hc} = \frac{\dot{Q}_{c}/A_{c}}{u_{g} c_{p} \rho (T_{w} - T_{g})} \tag{VII-16}$$

From this definition and equations VII-12 and 15, C_{Hc} can be written

$$C_{Hc} = \sum_{i=1}^{n} K_{3i} K_{4i} C_{Hvi} \tag{VII-17}$$

and using equations VII-5 and 14 in VII-17, the result is obtained,

$$C_{Hc} = K'(A\epsilon*)^{-p} (Pr)^{-m} \qquad \text{(VII-18)}$$

where the constant K', which depends only on the form of the roughness, is defined

$$K' \equiv \sum_{i=1}^{n} K_{3i} K_{4i} K_{1i} (K_{2i} K_{4i})^{-p} \qquad \text{(VII-19)}$$

Putting equation VII-18 into VII-1 gives the final result

$$g_{F.R.} = K_f(\epsilon*)^p (Pr)^n \qquad \text{(VII-20)}$$

where

$$K_f \equiv \frac{1}{K'A^{(1-p)}} \qquad \text{(VII-21)}$$

Thus the turbulent vortex hypothesis, for the flow in the roughness cavities under fully rough conditions, leads to two predictions concerning the heat transfer similarity parameter, $g_{F.R.}\{\epsilon*, Pr\}$: First, this parameter should have the same $\epsilon*$ and Prandtl number dependence for different types of roughness elements. That is, the $g_{F.R.}$ function should change only by a constant factor (K_f in equation VII-20) if the form of the pipe surface is changed. Secondly, the $\epsilon*$ and Pr dependence of the $g_{F.R.}$ function for a fixed type of pipe roughness is the reciprocal of that expected for the Stanton number of a free boundary layer developed on a surface immersed in a turbulent external flow. This second prediction is understood by recalling that the exponents "p" and "m" in equation VII-20 were introduced in equation VII-5 as part of an assumed relation between the

Stanton number for a free boundary layer and a Reynolds number based on distance along the surface.

The next discussion is presented only to show that reasonable guesses concerning the heat transfer characteristics of the assumed cavity boundary layers will lead to values for "p", "m" and K_f in equation VII-20 that are of the right order-of-magnitude with respect to the results of the present experiments. The conjectures leading to estimates for the exponents "p" and "m" will be considered first. Reference to the smooth tube measurements, Cf. Eq. 122 in Sec. IV-B of the text, shows that, for Prandtl numbers between 1.0 and 10, the ratio C_H/C_F can be approximated by the power law

$$\frac{C_H}{C_F} = K_5 \, Pr^{-0.48} \tag{VII-22}$$

It is now assumed that this relation (with the appropriate re-definition of terms) will also represent, at least in an approximate way, the relation between the local values of C_H and C_F in a boundary layer with free stream turbulence. A similar assumption is often made in relating pipe flow results to boundary layer flow (Cf. e.g., Ref. 12, p. 215). Next, it is assumed that the local friction factor in the cavity can be approximated by the expression

$$C_{Fx} = K_6 \, Re_x^{-0.2} \tag{VII-23}$$

which is applicable to a flat plate in a free boundary layer having only self-induced turbulence. The subscript "x" in equation VII-23 refers to a particular distance from the stagnation point. The C_{Fx} and Re_x are here defined in terms of the local wall shear stress

and the velocity outside of the boundary layer. It is conjectured that, in the case of a highly turbulent free stream, equation VII-23 could represent the friction even close to the stagnation point, i.e., down to Reynolds numbers of a few hundred based on distance from the stagnation point. Substituting then equation VII-23 into VII-22 and integrating over a segment of the cavity wall, starting from a location near the stagnation point, leads to the mean Stanton number for a cavity boundary layer,

$$C_H = K_7 \, Pr^{-0.48} \, Re^{-0.20} \qquad \text{(VII-24)}$$

This Stanton number is defined in the sense of equation VII-6.

Next, an attempt is made to predict the order of magnitude of the coefficient K' in equation VII-18. For this, a square two-dimensional cavity with a single vortex such as that studied by Roshko (Ref. 33) has been assumed. A small separation region is assumed to exist at each corner of the cavity. This then causes the respective boundary layers to re-start near the corners in such a way that essentially identical layers are formed on each of the three walls. Thus, for the square cavity, K_{2i} and K_{3i} in equations VII-9 and 10 respectively are taken as 1.0. The ratio of the velocity in the vortex near the walls (u_{vi}) to the external velocity (u_g) in equation VII-11 is assumed to be 1/3 on the basis of Roshko's observations. The K_1 coefficient from equation VII-5, which is essentially the K_7 coefficient in equation VII-24, is taken from experimental results for turbulent boundary layers over flat plates. Assuming, furthermore, that the exponent "p" is 0.20 (compare equations VII-5 and 24), the K' coefficient defined in equation VII-19 can be evaluated.

This computed value for K' is then put into the definition for K_f in equation VII-21. The value for the similarity parameter "A" is taken as 8.48 which is correct for sand grain roughness and which is also a good approximation to the measured factor for Roshko's square cavity. The final result of these crude approximations for the coefficient K_f, taken together with the exponents estimated in equation VII-24, yields the evaluation of equation VII-20, as follows:

$$g_{F.R.} \cong 4.0 \, (\epsilon *)^{0.20} \, (Pr)^{0.48} \qquad\qquad (VII-25)$$

Equation VII-25 may be compared with the results of the present experiments with a three-dimensional type of roughness given by equation 129 of the text,

$$g_{F.R.} = 5.19 \, (\epsilon *)^{0.20} \, (Pr)^{0.44}$$

The fact that reasonable assumptions regarding the cavity boundary layers lead to a correct order-of-magnitude prediction of the rough tube experimental results lends credence to the simple physical model of the cavity flow process implied by the turbulent vortex hypothesis. Again it should be emphasized that the exact relationships assumed for C_H/C_F and C_F in the above development are of secondary importance. Slightly different exponents and coefficients — including even those corresponding to laminar flow — would have led to the same conclusion as to the acceptability of the flow model postulated for the cavity.

The reasoning leading to the turbulent vortex hypothesis is, of course, subject to limitations and criticisms. First, the results are limited in application by the assumption of similar cavity flow

patterns, and this assumption is based on the pipe C_F value being independent of Reynolds number. Two of the ring configurations used as roughness elements by Nunner (Ref. 5) showed a marked tendency for the C_F to rise with increasing Re at high Re values even though C_F assumed a constant value in a lower Re region. This implies, in terms of the hypothesis, that a new flow pattern must have begun to evolve at high Reynolds number. Nevertheless, a wide variety of roughness types do yield constant C_F over a large range of Re values (Cf., e.g., Refs. 49, 10, 5 and 13).

Secondly, the assumption that nearly stationary flow patterns exist may be criticized. If large scale vortex shedding takes place, the local boundary layers are in a continual transient state and the simple steady relations for the cavity boundary layers could not be expected to hold. It is noted that in many flow visualization experiments, mostly limited to flow over various two-dimensional elements, standing vortex patterns are observed (Cf. Refs. 39, p. 196; 2 and 40). Roshko (Ref. 33) made pressure measurements in various two-dimensional rectangular wells placed in the floor of a wind tunnel. In the case of the square well, a single vortex formed in the cavity.

Another and perhaps the greatest limitation of the turbulent vortex hypothesis is that the cavity flow model in itself offers little insight into the characteristics of the cavity boundary layers. Since the flow, external to the cavity, is assumed to be unaffected by these local shear layers, no information concerning the shear stresses at the walls is available from the pipe friction (C_F) measurement.

Some qualitative description of the conditions for the cavity boundary layers is possible however. For example, the Reynolds number for the boundary layers are seen from equation VII-14 to be of the order of $(A\epsilon^*)$. For the present experiments, A is 8.48 and the ϵ^* values range from 70 to 2000 for the fully rough region. Thus the cavity flow Reynolds numbers based on distance along the wall can be assumed to range from about 600 to 17,000.

In summary, the essential points of the turbulent vortex hypothesis for fully rough conditions in pipes having geometrically similar roughness elements are the following:

i) The mean flow in the cavities between the elements is composed of a finite number of discrete vortices.

ii) The pattern and velocity distributions of these vortices, for a given type of roughness form, are independent of of the Reynolds number of the pipe flow, independent of the roughness ratio of the pipe, and independent of the presence of thin shear layers at the cavity walls.

iii) The heat transfer in the cavities is controlled by the thin shear layers at the walls.

iv) The Reynolds numbers, based on distance from the stagnation point, for the boundary layers at the cavity walls are very small (of the order of 10^2 to 10^4) for cases of interest.

v) The flow external to the cavity boundary layers is highly turbulent with turbulent velocity components estimated to be in the range of 1 to 10 percent of the mean velocity.

The heat transfer characteristics of the cavity boundary layers still remain to be understood before the turbulent vortex model will be useful in completely describing the heat transfer characteristics of rough pipes. Such understanding could be gained from heat transfer measurements near the stagnation points on blunt bodies immersed in turbulent free streams. To be of greatest use, these measurements should be taken at various Prandtl numbers and Reynolds numbers and with differing amounts of free stream turbulence. If the points just listed represent a correct model of the cavity conditions and if the cavity boundary layer behavior can be adequately described, the information obtained from visualization of the flow patterns in large scale roughness elements can be used as an effective means for predicting which roughness types will yield the most desirable heat transfer characteristics for rough pipes.

An immediately useful result of the turbulent vortex hypothesis comes from making the additional assumption that the Stanton number dependence on the local Reynolds number and Prandtl number for cavity boundary layers can be represented by a power law. The result in equation VII-20 then predicts that the $g_{F.R.}\{\epsilon^*, Pr\}$ function would change only by a multiplicative factor as the type of roughness is changed.
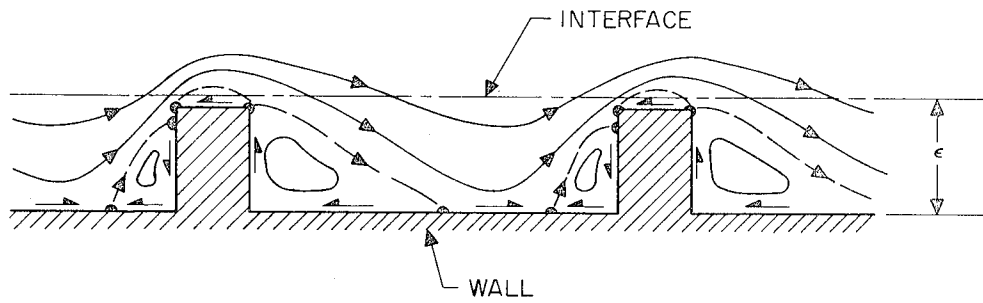
FIG. A-$\overline{VII}$-I. SCHEMATIC ILLUSTRATION OF A
ROUGHNESS-CAVITY FLOW PATTERN